Neutron Data Evaluation of ^{233}U

V.M. Maslov[1], M. Baba[2],
A. Hasegawa[3], A.B. Kagalenko[1*], N.V. Kornilov[1*],
N.A. Tetereva[1]

[1])   Joint Institute of Nuclear and Energy Research – SOSNY
220109, Minsk-Sosny, Belarus

[2])   Cyclotron and Radioisotope Center, Tohoku University,
Sendai, Japan

[3])   Department of Nuclear Energy System, Tokai Research
Establishment, Japan Atomic Energy Research Institute,
Tokai-mura, Naka-gun, Ibaraki-ken

*)   Permanent address: Institute of Physics and Power Engineering,
249020, Obninsk, Russia

August 2003

Neutron Data Evaluation of ^{233}U

V.M. Maslov[1], M. Baba[2],
A. Hasegawa[3], A.B. Kagalenko[1*], N.V. Kornilov[1*],
N.A. Tetereva[1]

[1])   Joint Institute of Nuclear and Energy Research – SOSNY
220109, Minsk-Sosny, Belarus

[2])   Cyclotron and Radioisotope Center, Tohoku University,
Sendai, Japan

[3])   Department of Nuclear Energy System, Tokai Research
Establishment, Japan Atomic Energy Research Institute,
Tokai-mura, Naka-gun, Ibaraki-ken

[*])   Permanent address: Institute of Physics and Power Engineering,
249020, Obninsk, Russia

Abstract

Consistent evaluation of ^{233}U measured data base is performed. Hauser-Feshbach-Moldauer theory, coupled channel model and double-humped fission barrier model are employed. Total, differential scattering, fission and (n,xn) data are calculated using fission cross section data description as a major constraint. The direct excitation of ground state is calculated within rigid rotator model. Average resonance parameters are provided, which reproduce evaluated cross sections in the range of 0.6-40.5 keV.

August 2003

Contents

1 Introduction

Uranium-233 plays an important role in uranium-thorium-fueled nuclear reactors. It turns out that theoretical fission data description maintains major constraint for ^{233}U capture, neutron elastic and inelastic scattering, (n,2n), (n,3n) reaction crosss sections and secondary neutron spectra evaluation. Current theoretical approach to measured data analysis was validated recently in case of ^{238}U and ^{232}Th neutron data description [1, 2, 3].

2 Resolved resonance energy range

Here we will briefly review the status of resolved neutron resonance parameters of ^{233}U. Resolved resonance region of ENDF/B-VI [4] data file extends up to 60 eV, multi-level resonance parameters in Adler-Adler formalism are adopted. Region of resolved resonances in JENDL-3.3 [5] extends up to 150 eV. Reich-Moore formalism parameters, recommended by Derrien [6] are adopted.

The Reich-Moore formalism resonance parameters by Leal et al. [7], basically accepted in present data file of ^{233}U, might provide a test of neutron width and resonance spacing distributions (see Figs. 3, 4 and 5). Leal et al. [7] observed/extracted parameters of 739 resonances up to $\sim$600 eV, they noticed that in the upper region of the analysis the resonances are actually pseudo-resonances. They estimated $\langle D_{l=0} \rangle$ =0.7 eV for the energy range of 0-70 eV, but the fit to the staircase plot up to 600 eV predicts $\langle D_{l=0} \rangle$ =0.82 eV (see Fig. 1). They assumed, however, that 96 resonances up to 70 eV comprise the best sample of $s-$wave resonances. Cumulative sum of reduced neutron widths of $s-$resonances Γ_n^o up to 70 eV was fitted with $S_o = (0.88 \pm 0.128) \times 10^{-4}$, while for the range 0-600 eV it increases to $S_o = (0.895 \pm 0.047) \times 10^{-4}$ (see Fig. 2). It seems that the strength function estimate is much less sensitive to the missing of resonances than the estimate of average spacing. The severe missing of small resonances even up to $\sim$70 eV was predicted by comparison of measured and Porter-Thomas integral distributions of reduced neutron widths. Figure 5 shows a comparison of experimental distribution of $2g\Gamma_n^o$ reduced neutron widths with cumulative Porter-Thomas distribution. Cumulative Porter-Thomas distribution of reduced neutron widths without resonance missing correction (solid line on Fig. 5) is plotted, normalized for the number of resonances N =135, which takes into account estimate of missing of $\sim$30% levels [7]. This estimate of total number of resonances gives $\langle D_{l=0} \rangle$ =0.52 eV, which means that $\sim$30% of resonances are missing up to $\sim$70 eV, however, in that case the staircase plot on Fig. 1 is not fitted.

We performed an analysis of resonance parameters recommended by Leal et al. [7], based on maximum likelihood estimates [8] both of mean level spacing $\langle D_{l=0} \rangle$ and neutron strength function S_o. Correction for the missing of levels based on simultaneous analysis of level spacing distribution and neutron width distribution shows that estimates of average $s-$wave neutron resonance spacing $\langle D_{l=0} \rangle$ =0.52 eV and strength function estimate $S_o = (0.895) \times 10^{-4}$ are

quite compatible with relevant expperimental distributions. This $\langle D_{l=0} \rangle$ estimate is lower than that of Reference Input Parameter Library File [9] ($\langle D_{l=0} \rangle =$ 0.55±0.05 eV) and $\langle D_{l=0} \rangle$ =0.68 of ENDF/B-VI [4], but higher than $\langle D_{l=0} \rangle$ =0.44 eV, adopted in JENDL-3.3 [5]. Figure 3 shows the comparison of predicted level spacing $D_{l=0}$ distributions with recommended by Leal et al. [7] resonance parameter set. Deciles on Fig. 3 show ten equal probability intervals ($P(x \leq x_{0.1} = \int p(x)dx = 0.1$) for observeded level spacing distribution of $s-$wave resonances $D_{l=0}$ up to $\sim$70 eV and up to $\sim$600 eV. Relevant predicted distributions are also shown. Measured and predicted neutron resonance spacings for resonance sample up to $\sim$70 eV are more compatible than those for resonance sample up to $\sim$600 eV. We estimate $\sim$7% of missed levels up to $\sim$70 eV and $\sim$30 % up to $\sim$600 eV. The former estimate of level missing is at variance with that, based on cumulative Porter-Thomas distribution of reduced neutron widths, being much lower. The experimental resolution function parameters are obtained by maximum likelihood method when comparing ^{238}U experimental distributions of reduced neutron width and resonance spacing with Porter-Thomas and Wigner distributions, modified for the resonance missing [2]. Predicted level spacing distribution, which takes into account missing of weak resonances and unresolved doublets, is compatible with experimental distribution. Expected distribution is qualitatively similar to the Wigner distribution.

Figure 4 demonstrates the comparison of predicted reduced neutron width Γ_n^o distribution resonance parameter set, recommended by Leal et al. [7]. Deciles on Fig. 4 show ten equal probability ($P(x \leq x_{0.1} = \int p(x)dx$ =0.1) intervals for Γ_n^o expected distribution. It demonstrates that reduced neutron width distribution with account of missing is compatible with observed distribution for resonance set up to 70 eV, in the range of small reduced neutron width values some missing of resonances is predicted. For the resonance sample up to $\sim$600 eV theoretical and measured distributions are quite compatible. It seems that the experimental resolution function parameters, obtained by maximum likelihood method when comparing ^{238}U experimental distributions of reduced neutron width and resonance spacing with predicted distributions [8], modified for the resonance missing [2], is valid.

Table 1

Average $s-$resonance parameters for ^{233}U

	$D_{l=0}$,	Γ_γ,	S_0	S_1	S_2	Γ_f^{2+},	Γ_f^{3+},
	eV	meV	$\times 10^{-4}$	$\times 10^{-4}$	$\times 10^{-4}$	meV	meV
Leal et al. [7]	0.52	39	0.895			760±60	296±30
RIPL	0.55	40	1.04±0.07				
Present	0.52	39	.893	2.3349	1.2005	818	370

Integral distribution of total fission widths (up to 70 eV) (41 of 2^+ resonances, and 54 of 3^+ resonances) was nicely described by the sum of two

Porter-Thomas distributions with $\langle \Gamma_f^{2+} \rangle$ =0.760 eV, ν_f^{2+} =5 and $\langle \Gamma_f^{3+} \rangle$ =0.296 eV, ν_f^{2+} =4 by Leal et al. [7], though about 30% of resonances are assumed to be missing. Present and recommended by Leal et al. [7] average resonance parameters are given in Table 1.

3 Unresolved resonance region

Here we will briefly review the status of unresolved neutron resonance parameters of ^{233}U and provide a cross section parameterization of total, capture and elastic scattering cross sections.

The unresolved resonance energy region of ENDF/B-VI [4] extends from 60 eV up to 10 keV. Provided are energy independent average resonance parameters $\langle D_{J=2} \rangle = 1.632$ eV, $\langle D_{J=3} \rangle = 1.166$ eV, $\langle D_{J=1} \rangle = 2.72$ eV $\langle D_{J=4} \rangle = 0.9067$ eV and $\langle \Gamma_\gamma \rangle = 0.045$ eV, reduced neutron and fission widths are energy dependent. In JENDL-3.3 [5] unresolved resonance region extends from 150 eV up to 30 keV, only $s-$ and $p-$ wave neutron-nucleus interactions are assumed to be effective. Provided are energy dependent average resonance parameters $\langle D_J \rangle$, which fluctuate wildly over the energy range of interest, reduced neutron and fission average widths are also fluctuating, while $\langle \Gamma_\gamma \rangle$ =0.040 eV.

We assume that lower energy of unresolved resonance energy region in present evaluation is the end-point of resolved resonance region, i.e. 600 eV, the upper energy is 40.5 keV. We suppose $s-$, $p-$ and $d-$wave neutron-nucleus interactions to be effective.

3.1 Average resonance parameters

Average resonance parameters , $\langle D_{obs} \rangle = \langle D_{l=0} \rangle$ = 0.52 eV, $\langle \Gamma_\gamma \rangle$ =39 meV are adopted for the cross section calculation from 600 eV up to 40.5 keV. Neutron strength functions S_l ($S_o = 0.893 \times 10^{-4}$, $S_1 = 2.2335 \times 10^{-4}$, $S_2 = 1.2 \times 10^{-4}$ at 0.6 keV) were calculated with the optical model, using the deformed optical potential, described below.

3.1.1 Neutron resonance spacing

Neutron resonance spacing $\langle D_J \rangle$ was calculated with the phenomenological model [10], which takes into account the shell, pairing and collective effects. The main parameter of the model, asymptotic value of level density parameter $\widetilde{a}$, was normalized to the observed neutron resonance spacing $\langle D_{l=0} \rangle = 0.52$ eV.

3.1.2 Neutron width

Average neutron width is calculated as follows

$$\langle \Gamma_n^{lJ} \rangle = S_l \langle D_J \rangle E_n^{1/2} P_l \nu_n^{lJ}, \tag{1}$$

where E_n is the incident neutron energy, P_l is the transmission factor for the $l-$th partial wave, which was calculated within black nucleus model, ν_n^{lJ} is the number of degrees of freedom of Porter-Thomas distribution (see Table 2).

3.1.3 Radiative capture width

Energy and angular momentum dependence of radiative capture width are calculated within a two-cascade γ-emission model with allowance for the (n,γn') [11] and (n,γf) [12] reactions competition to the (n,$\gamma\gamma$) reaction. The (n,$\gamma\gamma$) reaction is supposed to be a radiative capture reaction. The radiative capture width was normalized to the value of $\langle \Gamma_\gamma \rangle = 39$ meV.

3.1.4 Fission width

Fission widths are calculated within a double-humped fission barrier model. Energy and angular momentum dependence of fission width is defined by the transition state spectra at inner and outer barrier humps. We constructed transition spectra by supposing the axiality of inner saddle and mass asymmetry at outer saddle [9, 13]. Numbers of degrees of freedom ν_f^{lJ} of Porter-Thomas distribution is defined in Table 2. Transition spectra and number of degrees of freedom will be described in more detail below.

Table 2
Number of degrees of freedom

l, J	ν_n^{lJ}	ν_f^{lJ}	$\nu_f^{lJ}[7]$	$\nu_f^{lJ}[5]$
0,2	1	4	4	4
0,3	1	3	3	2
1,1	1	2		3
1,2	2	2		3
1,3	2	3		4
1,4	1	3		3
2,0	1	3		
2,1	2	1		
2,2	2	4		
2,3	2	3		
2,4	2	4		
2,5	1	3		

3.2 Average cross sections in the region 0.6-40.5 keV

3.2.1 Total cross section section

There are quite a number of ^{233}U total cross section measurements in keV-energy region. Data by Stupegia [14] above 3.4 keV define the lowest cross

section level below $E_n \sim 1.5$ MeV (see Fig. 6), while the data by Pattenden and Harvey [15] in the 0.07 eV-10 keV energy range define the highest total cross section level. However, recent data by Guber et al. [16] are compatible with data by Stupegia [14] from ~ 30 keV up to ~ 300 keV, below ~ 30 keV data by Guber et al. [16] predict systematically higher cross section level.

Total cross section for $E_n =600$ eV -20 MeV was calculated with the optical model, using the deformed optical potential, described below. Above 10 keV total cross section was approximated within the formalism, adopted in ENDF/B processing codes [17, 18], assuming a linear trends of S_o and S_1 neutron strength function values. They, as well as potential radius, were adopted from the optical model calculations. To reproduce total cross section, calculated with the optical model, we assume S_o value linearly decreasing to 0.8735×10^{-4} at 10 keV and then to 0.8613×10^{-4} at 40.5 keV. We assume S_1 value linearly increasing to 2.3445×10^{-4} at 10 keV and then decreasing to 2.0560×10^{-4} at 40.5 keV. The d-wave neutron strength function was assumed to be equal to $S_2 = 1.200 \times 10^{-4}$. In JENDL-3.3 [5] evaluation potential scattering radius is $R =0.96786$ fm, while in ENDF/B-VI [4] $R = 0.9893$ fm, we assumed $R = 0.9473$ fm, that is consistent with coupled channel optical model calculations, which fit data by Guber et al. [16].

3.2.2 Elastic scattering cross section

Elastic scattering cross section estimate is rather insensitive to the fission cross section estimate. The discrepancy of present, ENDF/B-VI [4] and JENDL-3.3 [5] estimates is shown on Fig. 7.

3.2.3 Fission cross section

A number of sets of the measured fission cross section data are available below ~ 40 keV. Here are briefly described those on which our evaluation is based.

Pfletchinger and Kappeler [19] have measured the ^{233}U and ^{235}U fission cross-section ratio with an accuracy of 1.6-2.7% in the 0.005-1 MeV neutron energy range using the time-of-flight method. The fission fragments were recorded using a gas scintillation detector in 4π geometry. ^{7}Li(p,n) reaction neutrons were used. The masses of the ^{233}U and ^{235}U layers were determined by alpha counting. The ^{233}U layer contained 11.25% ^{238}U.

Weston et al. [20] have measured fission cross section up to 2 keV. The reported cross section data are based on the $1/E^{1/2}$ energy dependence of the ^{10}B(n,α) cross section. For normalization purposes, total cross section data by Pattenden and Harvey [15] were used.

Blons [21] have measured fission cross section up to 30 keV. Neutron flux was monitored using ^{10}B(n,α) cross section. Fission cross section was normalized to the fission resonance integral of 168.31 barns from 8.32 to 101.2 eV.

Gwin et al. [22] have measured the cross-section for ^{233}U fission by 5-200 keV neutrons. The neutrons were produced by a linac. A boron counter was used to calibrate neutron flux. An ionization chamber was used to detect fission

fragments. The data were normalized to the resonance integral in the 22.6-l0l.3 eV region [20]. The uncertainty of such normalization was ~5%.

Zhuravlev et al. [23] have measured the ratio of ^{233}U and ^{235}U fission cross sections by filtered beams of reactor neutrons at 2.24, 55 and 144 keV. An ionization chamber was used to detect fission fragments. The ^{235}U fission cross-section was measured using this technique [24], with normalization to the ^{235}U fission cross-section value at thermal σ_f^0 [25]. The ^{233}U fission cross-section values can therefore be regarded as a normalized to this σ_f^0 value of ^{235}U. The σ_f^0 value of ^{233}U, which was obtained relative to σ_f^0 of ^{235}U, is in good agreement with that recommended by Divadeenam et al. [26].

Mostovaya et al. [27] have measured the ^{233}U fission cross-section in the 0.1-100 keV neutron energy region. A linac was used as a neutron source. The reaction ^{10}B(n, α) was used for determining the energy dependence of the neutron flux. An ionization chamber with a high time resolution was used to detect fission fragments. The measured data were normalized in the 166.9-1223.3-eV region to the resonance integral of 32.95 barn, defined by Gwin et al. [22].

Using a neutron slowing down spectrometer in lead, Bergman et al. [28] have measured ^{233}U fission cross section and its ratio to the ^{235}U fission cross section in the 0.2-50 keV range. The neutron flux was determined relative to the reaction ^{10}B(n, α). An ionization chamber was used to detect fission fragments. The thermal calibration method was used for the cross section ratio absolutization.

Recently fission cross section measurement was accomplished by Guber [29] over a 0.4 eV to 700 keV incident neutron energy range. Average fission cross sections were obtained in this energy range. Neutron flux was monitored using ^{6}Li(n,α) reaction. Data were normalized using an integral fission cross section by Deruytter and Wagemans [30] in the 8.1- to 17.7-eV neutron energy range, revised by Wagemans et al. [31].

In the 10-100 keV neutron energy region, the results of direct measurements of the ^{233}U fission cross sections were renormalized to Deruytter's fission integral [30] (data by Gwin et al.[22] and Mostovaya et al. [27]); data by Bergman et al. [28] and Zhuravlev et al. [23] were renormalized to the ^{233}U and ^{235}U thermal fission cross section [26]. The data by Gwin et al. [22] and by Bergman et al. [28] are quite compatible, but within the error bars they also agree with the data by Zhuravlev et al. [23], which are systematically ($\sim$5%) lower than the data by Gwin et al. [22]. The energy dependencies of the data by Gwin et al.[22] and Mostovaya et al. [27] are in agreement. However, in view of the fact that the results of the relative measurements of the ^{233}U and ^{235}U fission cross sections by Carlson and Behrens [32] and Fursov et al. [33] better agree with the ratio of the average ^{233}U and ^{235}U cross sections by Gwin et al. [22], than with the data by Mostovaya et al. [27], we give preference to the data by Gwin et al. [22].

Observed fission cross section is calculated as a sum of (n,f) and (n,γf) fission reactions, the latter contribution is defined by pre-fission $\gamma-$ray spectra

and transition spectra at saddle deformations [12]:

$$\sigma_{nF} \;=\; \sigma_{nf} + \sigma_{n,\gamma f}. \tag{2}$$

$$\sigma_{nF} \;=\; \frac{\pi \,\acute{\lambda}^2}{2(2I+1)} \left(\sum_{J\pi} \left\langle \frac{\Gamma_n^{J\pi}\Gamma_f^{J\pi}}{\Gamma} \right\rangle + \left\langle \frac{\Gamma_n^{J\pi}\Gamma_{\gamma f}^{J\pi}}{\Gamma} \right\rangle \right). \tag{3}$$

$$\sigma_{nF} \;\cong\; \frac{\pi \,\acute{\lambda}^2}{2(2I+1)} \sum_{J\pi} \left\langle \frac{\Gamma_n^{J\pi}(\Gamma_f^{J\pi} + \Gamma_{\gamma f}^{J\pi})}{\Gamma} \right\rangle. \tag{4}$$

Statistical properties of fission $\Gamma_f^{J\pi}$ and (n,γf) reaction $\Gamma_{\gamma f}^{J\pi}$ are rather different, the latter width they are assumed to be similar to those of radiation widths. To comply with ENDF/B [4] format rules, we would add (n,γf) reaction width $\Gamma_{\gamma f}^{J\pi}$, which is less than $\sim$10 meV, to the "prompt" fission width $\Gamma_f^{J\pi}$. Figures 8 and 9 show the comparison of calculated fission cross section with measured data base. Figure 8 shows the contribution of (n,γf) reaction to the observed fission cross section. Figure 9 shows the contribution of $s-, p-$ and $d-$waves to the observed fission cross section. Total and fission cross sections are described consistently within statistical Hauser-Feshbach-Moldauer model. The details of fission width calculation would be described below. Here we would stress that average fission widths of compound nuclide ^{234}U are defined by transition states structure at saddle deformations. Calculated fission widths Γ_f^{2+} and Γ_f^{3+} are consistent with those, estimated by Leal et al. [7] (see below). For width fluctuation correction calculation only Porter-Thomas fluctuations are taken into account. Effective number of degrees of freedom for fission channel is defined at the higher (outer) fission barrier saddle as $\nu_f^{J\pi} = T_f^{J\pi}/T_{f\,\max}^{JK\pi}$, where $T_{f\,\max}^{JK\pi}$ is the maximum value of the fission transmission coefficient $T_{f\,\max}^{JK\pi}$ for the $(JK\pi)$ collective state. Effective numbers of degrees of freedom for entrance channels (l, J) are compared in Table 3. Leal et al. [7] defined $\nu_f^{J\pi}$ as an effective number of fission channels $N_f^{J\pi} = 2\pi\langle\Gamma_f^{J\pi}\rangle/\langle D^{J\pi}\rangle$. Both estimates of ν_f^{2+} and ν_f^{3+} are consistent with our estimates. In case of 2^+ and 3^+ channels, contributing $K^\pi-$channels are almost fully open (for more details see discussion below).

3.2.4 Capture cross section

We adopted $s-$wave radiative strength function $S_{\gamma 0} = 0.075$ ($\Gamma_\gamma = 39$ meV and $\langle D_{l=0}\rangle = 0.52$ eV). Calculated cross section is compared with measured data by Weston et al. [20] and Hopkins and Diven [34] and other evaluations on Figs. 10 and 11. The pattern of $s-, p-$ and $d-$wave channel contributions to the capture cross section in the energy range of 0.6 - 40.5 keV is rather different than in case of ^{238}U target nuclide. The $p-$wave contribution is higher than that of $s-$wave above $\sim$8 keV, while that of $d-$wave neutrons is the lowest. In case of ^{233}U(n,γ) reaction main contribution comes from $p-$wave neutrons only above $\sim$25 keV, while that of $d-$wave neutrons is lower than in case of $s-$ and $p-$waves below $\sim$40 keV. These peculiarities might be attributed to the increased fission

competition in $s-, p-$ and $d-$wave entrance channels. Competition of (n,γf) reaction [12] to capture reaction is rather essential (see Fig. 11). Capture cross sections in present data file and those of JENDL-3.3 [5] and ENDF/B-VI [4] are of rather different shapes. It seems that only present evaluation is consistent both with data by Weston et al. [20] and Hopkins and Diven [34]. The capture cross section estimate of JENDL-3.3 [5] is systematically lower than present and ENDF/B-VI [4] estimates. The discrepancies could be attributed to the fission competition, energy dependence of radiative strength functions, which is missing in JENDL-3.3 [5] and ENDF/B-VI [4] files, as well as to different estimates of reduced neutron widths.

3.2.5 Comparison of average resonance parameters

Figures 12-17 compare reduced neutron widths $\langle \Gamma_n^{lJ} \rangle$ for $s-$ and $p-$wave channels. Differences are pronounced either in $s-$wave, $p-$wave and $d-$wave reduced neutron widths. Non-smooth energy dependence of ENDF/B-VI [4] $s-$ and $p-$wave reduced neutron widths seems to be unnecessary to reproduce total, fission and capture cross sections data trends in the energy range of 600 eV - 40.5 keV.

Table 3
Average resonance parameters for ^{233}U

	$D_{l=0}$,	Γ_γ,	$S_0 \times 10^{-4}$	Γ_f^{2+},	Γ_f^{3+},	R, fm
	eV	meV		meV	meV	
JENDL-3.3	0.44	40				0.96786
ENDF/B-VI	0.68	45				0.9893
BROND	0.42		.99			0.96
ORNL	0.52	39	0.895	760$\pm$60	296$\pm$30	
RIPL	0.55	40	1.04$\pm$0.07			
Present	0.52	39	.89258	818	370	0.947284

Figures 18-23 compare present fission widths $\langle \Gamma_f^{lJ} \rangle$ with those of ENDF/B-VI [4] and JENDL-3.3 [5] for $s-$ and $p-$wave channels. In case of 2^+ and 3^+ $s-$wave channels our estimates are consitent with those by Leal et al. [7] (see Figs. 18, 19). In case of $p-$wave channels our estimates are much lower than both ENDF/B-VI [4] and JENDL-3.3 [5] estimates (see Figs. 20 -23).

Figures 24-27 compare present average level spacing $\langle D^{lJ} \rangle$ with those of ENDF/B-VI [4] and JENDL-3.3 [5] for $s-$ and $p-$wave channels. In case of 2^+ and 3^+ compound states our estimates are consitent with those by Leal et al. [7] (see Figs. 24, 25). In case of 2^- and 3^- compound states, excited by $p-$wave neutrons, our estimates are much lower than those of ENDF/B-VI [4] and JENDL-3.3 [5] estimates. For $E_n \gtrsim 20$ keV, our estimates and those of JENDL-3.3 [5] are rather similar.

The advantage of present evaluation is that it provides smooth average energy dependent resonance parameters which reproduce evaluated total, elastic, fission and capture cross sections, using conventional ENDF/B processing codes [17, 18] up to 40.5 keV.

4 Optical Potential

A coupled channel model is employed for estimating differential scattering and total cross sections. Another important application of coupled channel model is calculation of direct inelastic scattering contribution of discrete levels. The direct excitation of ground state rotational band levels 0^+-2^+-4^+-6^+ is estimated within rigid rotator model, four levels of ground state band are assumed coupled.

We adopted here the optical potential parameters obtained for ^{232}Th [?] by fitting total cross section data, angular distributions and $s-$wave strength function. Then we fitted ^{233}U $s-$wave strength function $S_o = (0.895\pm 0.0.047)\times 10^{-4}$ with β_2 and β_4 deformation parameters. The total data were desribed acceptably without any further parameter variation. The optical potential parameters adopted are as follows:

$$V_R = 45.722 - 0.334E_n, MeV, r_R = 1.2668 \ fm, a_R = 0.6468 \ fm$$
$$W_D = \begin{cases} 3.145 + 0.455E_n, MeV, \quad E_n \leq 10 MeV, r_D = 1.25 \ fm, a_D = 0.5246 \ fm \\ 7.695 \ MeV, \qquad\qquad\quad 10 < E_n < 20 \ MeV \end{cases}$$
$$V_{SO} = 6.2 \ MeV, r_{SO} = 1.120 \ fm, a_{SO} = 0.47 \ fm,$$
$$\beta_2 = 0.190, \beta_4 = 0.072$$

4.1 Total and elastic cross sections

There are quite a number of ^{233}U total cross section measurements, but there are a number of systematic discrepances. Nonetheless, optical model provides reasonable fit of selected data sets, which seem to be the most reliable.

Total cross section was measured by Stupegia [14] in the 3.4 keV- 1.6 MeV incident neutron energy range, Pattenden and Harvey [15] in the 0.07 eV-10 keV energy range, Foster and Glasgow [35] in the 2.25 - 14.95 MeV energy range, Green and Mitchell [36] in the 0.899 - 9.887 MeV energy range, Poenitz et al.[37] in the 0.058 - 4.43 MeV energy range, Poenitz et al.[38] in the 0.048 - 4.807 MeV energy range and Poenitz et al.[39] in the 1.87 - 20.25 MeV energy range.

Data by Stupegia [14] in the 3.4 keV - 1.6 MeV energy range define the lowest cross section level for incident neutron energies below E_n ~1.5 MeV (see Fig. 28), while the data by Pattenden and Harvey [15] in the 0.07 eV-10 keV energy range - the highest total cross section level. However, recent data by Guber et al. [16] are compatible with data by Stupegia [14] from ~30 keV up to ~300 keV, below ~30 keV data by Guber et al. [16] predict systematically higher cross section level. Data by Foster and Glasgow [35] above ~2.25 MeV look like a continuation of the data by Stupegia [14], since they predict somewhat lower cross section, than do other data sets in the energy range of 2.25 - 4 MeV (see Fig. 29). Data by Poenitz et al.[38] in the 0.048 - 4.807 MeV energy range

define higher cross section level, they are systematically higher than the data by Guber et al. [16] (see Fig. 28). Data by Green and Mitchell [36] define the highest cross section level from ∼1.5 Mev up to ∼4 MeV, while in in the energy range of 5-10 MeV they scatter a lot. Data by Foster and Glasgow [35] are compatible with data by Poenitz et al.[39] up to ∼6 MeV, while at higher energies the latter data define a higher total cross section level in the 6 - 20 MeV energy range.

Calculated total cross section is compared with measured data below 1 MeV on Fig. 28. Calculated cross section is compatible with data by Guber et al. [16] up to ∼40 keV. At higher incident neutron energies calculated cross section is compatible with data by Poenitz et al. [38] and Poenitz et al.[39] up to 5.5 MeV (see Figs. 28 and 29). Data by Foster and Glasgow [35] are somewhat lower than calculated total cross section up to ∼4 MeV, while at higher energies calculated curve is compatible with them up to ∼15 MeV (see Fig. 30). At higher neutron energies calculated cross section is somewhat higher than data by Poenitz et al.[39] predict (see Fig. 31). It is rather easy to follow the data by Poenitz et al.[39] above ∼15 MeV slightly varying real term V_R of the optical potential, but we refrain from doing that by the following reason. The data by Poenitz et al.[39] are inconsistent with the data by Foster and Glasgow [35] starting from ∼5.5 MeV, while our optical potential nicely describes the latter data in the energy range of ∼3 - 15 MeV.

Figure 32 compares total cross sections estimates of present coupled channels optical potential and that of JENDL-3.3 [5] with estimate of total scattering cross section of ENDF/B-VI [4]. Present and JENDL-3.3 [5] estimates are not much different below ∼6 MeV, while at higher energies JENDL-3.3 [5] follows data by Poenitz et al.[39]. Total cross section of recent evaluation by Young et al. [40] follows data by Green and Mitchell [36] from ∼1 MeV up to ∼3 MeV, Poenitz et al.[39] and Foster and Glasgow [35] from ∼5 MeV up to ∼20 MeV, is somewhat lower than data by Poenitz et al. [38] below ∼1 MeV. In the incident neutron energy range from ∼4 to ∼5 MeV estimate by Young et al. [40] is lower than the bulk of the measured data.

Figure 33 compares elastic cross sections estimates of present coupled channels optical potential and that of JENDL-3.3 [5] with estimate of elastic scattering cross section of ENDF/B-VI [4]. Present and JENDL-3.3 [5] estimates are compatible with data by Haouat et al. [41]

4.2 Angular distributions

Elastic and inelastic scattering angular distributions were measured by Haouat et al. [41] at 0.7 (see Fig. 34) and 1.5 MeV (see Fig. 35). At E_n =1.5 MeV coupling of four ground state band levels allows to reproduce measured angular distribution data, while at E_n =0.7 MeV measured data predict much more backward scattering. That high level of backward scattering can not be reproduced neither with 3 or 5 coupled levels, Fig. 34 shows direct scattering components for different number of coupled levels. Solid curves on Figs. 34 and 35 correspond to the summed contribution of isotropic compound scattering and

direct anisotropic scattering for 4 coupled levels.

Differential cross sections of inelastic scattering to the first excited $J^\pi = 7/2^+$ level of the ^{233}U ground state band is shown on Figs. 36 and 37. Varying number of coupled levels we can not reproduce the Haouat et al. [41] measured data shape for $E_n = 0.7$ MeV, direct scattering components for different number of coupled levels are shown. For $E_n = 1.5$ MeV coupling of 4 levels is roughly consistent with measured data by Haouat et al. [41].

Differential cross sections of inelastic scattering to the second excited $J^\pi = 9/2^+$ level of the ^{233}U ground state band for $E_n = 1.5$ MeV is shown on Fig. 38. Here also is shown the effect of varying number of coupled levels on the direct scattering component. Coupling of 4 levels is also roughly consistent with measured data.

5 Statistical Model

As distinct from the previous evaluations of JENDL-3.3 [5] and ENDF/B-VI [4] we use calculated cross sections for evaluated data file compilation. We calculate neutron cross sections within Hauser-Feshbach-Moldauer theory, coupled channel optical model and double-humped fission barrier model. The relative importance of direct excitation of rotational ground state band levels is higher, as compared with ^{238}U+n interaction, due to the lower compound neutron scattering to the ^{233}U discrete and continuum levels.

Hauser-Feshbach-Moldauer [42] statistical theory is employed for partial cross section calculations below emissive fission threshold, at higher incident neutron energies Hauser-Feshbach statistical theory is used. Fissioning and residual nuclei level densities as well as fission barrier parameters are key ingredients, involved in actinide neutron-induced cross section calculations. First, level density parameters are defined, using neutron resonance spacing $\langle D_{l=0} \rangle$ estimate for ^{233}U target nuclide. Constant temperature level density parameters T_o, E_o, U_c are defined by fitting cumulative number of low-lying levels of ^{232}U, ^{233}U and ^{234}U (see Figs. 39, 40) [8].

In case of fast neutron interaction with ^{233}U target nuclide, the main reaction channel is fission, fission cross section description serves as a major constraint for the neutron inelastic scattering and radiative neutron capture cross section estimate. Below there is an outline of the statistical model [43, 44] employed.

Neutron-induced reaction cross section (n, x) for excitation energies up to emissive fission threshold is defined as

$$\sigma_{nx}(E_n) = \frac{\pi \, \acute\lambda^2}{2(2I+1)} \sum_{ljJ\pi} (2J+1) T_{lj}^{J\pi}(E_n) P_x^{J\pi}(E_n) S_{nx}^{ljJ\pi}, \qquad (5)$$

the compound nucleus decay probability $P_x^{J\pi}$ $(x = n, f, \gamma)$ is

$$P_x^{J\pi}(E_n) = \frac{T_x^{J\pi}(U)}{T_f^{J\pi}(U) + T_n^{J\pi}(U) + T_\gamma^{J\pi}(U)}, \qquad (6)$$

17

where $U = B_n + E_n$ is the excitation energy of the compound nucleus, B_n is the neutron binding energy, $T_{lj}^{J\pi}$ are the entrance neutron transmission coefficients for the channel $(ljJ\pi)$, I is the target nucleus spin. Decay probability $P_x^{J\pi}(E_n)$ of the compound nucleus with excitation energy U for given spin J and parity π, depends on $T_f^{J\pi}$, $T_n^{J\pi}(U)$ and $T_\gamma^{J\pi}(U)$, transmission coefficients of the fission, neutron scattering and radiative decay channels, $S_{nx}^{ljJ\pi}$ denotes partial widths Porter-Thomas fluctuation factor. Below incident neutron energy equal to the cut-off energy of discrete level spectra, neutron cross sections are calculated within Hauser-Feshbach approach with correction for width fluctuation by Moldauer [42]. For width fluctuation correction calculation only Porter-Thomas fluctuations are taken into account. Effective number of degrees of freedom for fission channel is defined at the higher fission barrier saddle as $\nu_f^{J\pi} = T_f^{J\pi}/T_{f\,\text{max}}^{J\pi}$, where $T_{f\,\text{max}}^{J\pi}$ is the maximum value of the fission transmission coefficient $T_f^{J\pi}$. At higher incident neutron energies the Tepel et al. [45] approach is employed, it describes cross section behavior in case of large number of open channels correctly.

5.1 Level Density

Level density is the main ingredient of statistical model calculations. Level density of fissioning, residual and compound nuclei define transmission coefficients of fission, neutron scattering and radiative decay channels, respectively. We will briefly discuss here level densities of even-even ^{234}U and even-odd ^{233}U nuclides.

The level densities were calculated with a phenomenological model by Ignatyuk et al. [10], which takes into account shell, pairing and collective effects in a consistent way

$$\rho(U, J, \pi) = K_{rot}(U, J)K_{vib}(U)\rho_{qp}(U, J, \pi), \tag{7}$$

where quasiparticle level density

$$\rho_{qp}(U, J, \pi) = \frac{(2J+1)\omega_{qp}(U)}{4\sqrt{2\pi}\sigma_\perp^2\sigma_\parallel} \exp\left(-\frac{J(J+1)}{2\sigma_\perp^2}\right), \tag{8}$$

$\omega_{qp}(U, J, \pi)$ is state density, $K_{rot}(U, J)$ and $K_{vib}(U)$ are factors of rotational and vibrational enhancement of the level density. The collective contribution of the level density of deformed nuclei is defined by the nuclear deformation order of symmetry. The actinide nuclei at equilibrium deformation are axially symmetric. The order of symmetry of nuclear shape at inner and outer saddles were adopted from calculations within shell correction method (SCM) by Howard & Möller [46], uranium nuclei of interest ($A \leq 235$) are assumed to be axially symmetric, then

$$K_{rot}(U) = \sigma_\perp^2 = F_\perp t, \tag{9}$$

where $\sigma_\perp^2$ is the spin cutoff parameter, $F_\perp$ is the nuclear momentum of inertia (perpendicular to the symmetry axis), which equals the rigid-body value at high

excitation energies, where the pairing correlations are destroyed, experimental value at zero temperature and is interpolated in between, using the pairing model, $F_{\parallel} = 6/\pi^2 < m^2 > (1 - 2/3\varepsilon)$, where $< m^2 >$ is the average value of the squared projection of the angular momentum of the single-particle states, and ε is quadrupole deformation parameter. The closed-form expressions for thermodynamic temperature and other relevant equations which one needs to calculate $\rho(U, J, \pi)$ are provided by Ignatyuk et al. model [10].

To calculate the residual nucleus level density at the low excitation energy, i.e. just above the last discrete level excitation energy, where $N^{exp}(U)$ $\sim N^{theor}(U)$, we employ a Gilbert-Cameron-type approach. The constant temperature approximation of

$$\rho(U) = dN(U)/dU = T^{-1} \exp((U - U_o)/T) \tag{10}$$

is extrapolated up to the matching point U_c to the $\rho(U)$ value, calculated with a phenomenological model by Ignatyuk et al. [10] with the condition

$$U_c = U_o - T ln(T\rho(U_c)). \tag{11}$$

In this approach $U_o \simeq -n\triangle_o$, where $\triangle_o$ is the pairing correlation function, $\triangle_o = 12/\sqrt{A}$, A is the mass number, $n = 0$ for even-even, 1 for odd nuclei, i.e. U_o has the meaning of the odd-even energy shift. The value of nuclear temperature parameter T is obtained by the matching conditions at the excitation energy U_c.

In present approach the modelling of total level density

$$\rho(U) = K_{rot}(U) K_{vib}(U) \frac{\omega_{qp}(U)}{\sqrt{2\pi}\sigma} = T^{-1} \exp((U - U_o)/T) \tag{12}$$

in Gilbert-Cameron-type approach looks like a simple renormalization of quasiparticle state density $\omega_{qp}(U)$ at excitation energies $U < U_c$. The cumulative number of observed levels for even-even ^{234}U and even-odd ^{233}U are compared with constant temperature approximation on Figs. 39 and 40. In case of ^{234}U nuclide missing seems to be pronounced above excitations of $\sim$1.3 MeV. In case of ^{233}U missing of levels above pairing gap ($\sim$0.6 MeV) is markedly pronounced.

Few-quasiparticle effects, which are due to pairing correlations are essential for state density calculation at low intrinsic excitation energies either for equilibrium (^{233}U) or saddle (^{234}U) deformations. The step-like structure in ^{235}U(n,f) reaction cross section above fission threshold was shown to be a consequence of threshold excitation of two-quasiparticle states in fissioning ^{236}U nuclide and three-quasiparticle configurations in residual even-even nuclide ^{235}U [47]. A step-like structure is observed in the reaction ^{235}U(n,f) around $\sim$0.8 MeV. However the step-like structure in case of ^{233}U(n,f) reaction, which could be correlated with threshold excitation of two-quasiparticle states in fissioning ^{234}U nuclide and three-quasiparticle configurations in residual even-odd nuclide ^{233}U, is observed at lower energies, i.e., $\sim$0.3 MeV. We argue that few-quasiparticle effects are important also for reasonable prediction of inelastic scattering cross section for even-odd target nuclide ^{233}U at low energies.

19

The partial $n-$quasiparticle state densities, which sum-up to intrinsic state density of quasiparticle excitations could be modelled using the Bose-gas model prescriptions [48, 49]. The intrinsic state density of quasiparticle excitations $\omega_{qp}(U)$ could be represented as a sum of $n-$quasiparticle state densities $\omega_{nqp}(U)$:

$$\omega_{qp}(U) = \sum_n \omega_{nqp}(U) = \sum_n \frac{g^n(U - U_n)^{n-1}}{((n/2)!)^2(n-1)!}, \qquad (13)$$

where $g = 6a_{cr}/\pi^2$ is a single-particle state density at the Fermi surface, n is the number of quasiparticles. The important model parameters are threshold values U_n for excitation of $n-$quasiparticle configurations $n = 2, 4...$ for even-even nuclei and $n = 1, 3...$ for odd-A nuclei [49]. The detailed treatment of this approach and approximations employed, as applied for fission, inelastic scattering or capture reaction calculations, is provided in [13, 50].

Nuclear level density $\rho(U)$ of even-even nuclide ^{234}U above the pairing gap up to the four-quasiparticle excitation threshold was extracted by fitting fission cross section data of ^{233}U(n,f) reaction. The total level density for even nuclide ^{234}U at outer saddle deformation, as compared with the Gilbert-Cameron-type approximation of $\rho(U)$ is shown on Fig. 41. The arrows on the horizontal axis of Fig. 41 indicate the excitation thresholds of even $n-$quasiparticle configurations. Below the excitation threshold U_2, i.e. within pairing gap the constant temperature model fits cumulative number of ^{234}U levels [51].

In case of and even-odd nucleus ^{233}U the partial contributions of $n-$quasiparticle states $\omega_{nqp}(U)$ to the total intrinsic state density $\omega_{qp}(U)$ produces distinct "jump" only below three-quasiparticle excitation threshold U_3 (see Fig. 42). The arrows on the horizontal axis of Fig. 42 indicate the excitation thresholds of odd $n-$quasiparticle configurations. Nuclear level density $\rho(U)$ up to the three-quasiparticle excitation threshold U_3 is virtually independent on the excitation energy, since the intrinsic state density ($\omega_1 \sim g$) is constant. The numerical values of nuclear level density $\rho(U)$ parameters of ^{233}U, defining one- and three quasiparticle state densities, are fitted to ^{233}U(n,f) cross section data.

Table 4

Level density parameters of fissioning ^{234}U nucleus and residual ^{233}U nucleus

Parameter	inner saddle	outer saddle	neutron channel
δW, MeV	1.5	0.6	LDM
$\triangle$, MeV	$\triangle_o + \delta^*$	$\triangle_o + \delta^*$	$\triangle_o$
ε	0.6	0.8	0.24
$F_0/\hbar^2$, MeV^{-1}	100	200	73

*)$\delta = \Delta_f - \Delta$ value is defined by fitting fission cross section in the plateau region.

Main parameters of the level density model for equilibrium, inner and outer saddle deformations are as follows: shell correction δW, pairing correlation

functions Δ and Δ_f, at equilibrium deformations $\Delta = 12/\sqrt{A}$, quadrupole deformation ε and momentum of inertia at zero temperature $F_o/\hbar^2$ are given in Table 4. For ground state deformations the shell corrections were calculated as $\delta W = M^{exp} - M^{MS}$, where M^{MS} denotes liquid drop mass (LDM), calculated with Myers-Swiatecki parameters [52], and M^{exp} is the experimental nuclear mass. Shell correction values at inner and outer saddle deformations $\delta W_f^{A(B)}$ are adopted following the comprehensive review by Bjornholm and Lynn [53].

5.2 Fission Channel

Neutron-induced fission in a double humped fission barrier model could be viewed as a two-step process, i.e. a successive crossing over the inner hump A and over the outer hump B. Hence, the transmission coefficient of the fission channel $T_f^{J\pi}(U)$ can be represented as

$$T_f^{J\pi}(U) = \frac{T_{fA}^{J\pi}(U)T_{fB}^{J\pi}(U)}{(T_{fA}^{J\pi}(U) + T_{fB}^{J\pi}(U))}. \tag{14}$$

The transmission coefficient $T_{fi}^{J\pi}(U)$ is defined by the level density $\rho_{fi}(\varepsilon, J, \pi)$ of the fissioning nucleus at the inner and outer humps (i = A,B, respectively):

$$T_{fi}^{J\pi}(U) = \sum_{K=-J}^{J} T_{fi}^{JK\pi}(U) + \int_0^U \frac{\rho_{fi}(\epsilon, J, \pi)d\epsilon}{(1 + \exp(2\pi(E_{fi} + \epsilon - U)/h\omega_i))}, \tag{15}$$

where the first term denotes the contribution of low-lying collective states and the second term - contribution from the continuum levels at saddle deformations, ϵ is the intrinsic excitation energy of fissioning nucleus. The first term contribution due to discrete transition states depends upon saddle symmetry. The total level density $\rho_{fi}(\epsilon, J, \pi)$ of the fissioning nucleus is determined by the order of symmetry of nuclear saddle deformation.

Inner and outer fission barrier heights and curvatures as well as level densities at both saddles are the model parameters. They are defined by fitting fission cross section data at incident neutron energies below emissive fission threshold. Fission barrier height values and saddle order of symmetry are strongly interdependent. The order of symmetry of nuclear shape at saddles was defined by Howard and Möller [46] within shell correction method (SCM) calculation. We adopt the saddle point asymmetries from SCM calculations. According to shell correction method (SCM) calculations of Howard and Möller [46] the inner barrier of ^{234}U was assumed axially symmetric. This helped to interpret also the non-threshold fission cross section behavior of ^{232}U(n,f) [54] assuming a lowered height of axially symmetric inner hump of ^{233}U, as anticipated by Howard and Möller [46] with SCM calculations. Outer barrier for asymmetric fission of uranium nuclei is assumed to be mass-asymmetric.

5.2.1 Fission transmission coefficient, level density and transition state spectrum

Fission cross section of ^{233}U for incident neutron energies $E_n \lesssim U_2 + E_{fB} - B \sim 200$ keV, correspondent to the excitation of two-quasiparticle states at higher (outer) saddle deformations, is defined by the collective states lying within pairing gap, up to the two-quasiparticle excitation threshold U_2. Each collective state in even fissioning nucleus ^{234}U is assumed to have a rotational band built on it with a rotational constant, dependent upon the respective saddle deformation. Saddle symmetries are similar to that of ground state deformation, i.e., they are axially symmetric, the difference is due to mass asymmetry at outer saddle. That would lead to the lowering of negative parity octupole vibration bands at outer saddle B deformations. Positions of other collective bands could be lowered due to higher quadrupole and hexadecapole deformations at saddles. Generally, the structures of collective bands of ^{234}U at saddles and at ground state deformations would be rather similar. Collective bands structure of ^{234}U was described within soft rotator model [55]. For excitation energies up to ~ 1.35 MeV six bands with $K^\pi = 0_1^+$, 0_2^+, 0_3^+, $K^\pi = 0^-$, $K^\pi \simeq 2^-$ and $K^\pi \simeq 2^+$ were distinguished in ^{234}U level scheme [56] within a soft rotator model [55] (marked by (*) in Table 5). Excitation energies of members of even parity collective bands $K^\pi = 0_1^+$, 0_2^+, 0_3^+, $K^\pi \simeq 2^+$ and first octupole band $K^\pi = 0^-$ as well as second octupole band $K^\pi \simeq 2^-$ of ^{234}U were reproduced. Levels of $K^\pi = 0_2^+$ band ($E_{0_2^+} = 0.810$ MeV) were classified as quadrupole longitudinal β-vibrations, while levels of $K^\pi = 0_3^+$ band ($E_{0_3^+} = 1.0445$ MeV) as quadrupole γ-transversal vibrations. Levels of negative parity band with $K^\pi = 0^-$ were defined by octupole deformation parameter β_3 and parameter of softness to the octupole vibrations μ_{β_3}. Quadrupole longitudinal β-vibration $K^\pi = 0^+$ band levels and quadrupole transversal γ-vibration $K^\pi = 0^+$ band levels were defined by the softness parameters to respective vibrations μ_{β_2} and μ_γ. Anomalous rotational $K^\pi \simeq 2^+$ γ-band levels were defined by the non-axiality parameter γ_o, which is correlated with position of $K^\pi \simeq 2^+$ level. We construct the discrete transition spectra up to ~ 1.2 MeV, using collective band heads shown in Table 5. In the sixth column sequences of spins of collective bands are shown. Except $K^\pi = 0_1^+$, 0_2^+, 0_3^+, $K^\pi \simeq 2^+$, $K^\pi = 0^-$ and $K^\pi \simeq 2^-$ bands, identified in ^{234}U scheme with soft rotator model, collective states with $K^\pi = 2_2^+$, 2_3^+ and 1_1^- were added to fit fission cross section for 600 eV $\lesssim E_n \lesssim 300$ keV. Only $K^\pi = 2_3^+$ extra band is not observed at equilibrium deformations. With transition state spectra thus defined the fission barrier parameters are obtained by fitting fission cross section.

Incident neutron energy $E_2 = U_2 + E_{fA(B)} - B$ is correspondent to the excitation of two-quasiparticle states. The two-quasiparticle neutron states of even fissioning nuclide, lying below the four-quasiparticle states excitation threshold define the shape of fission cross section below incident neutron energy of $E_n \leq E_{fA(B)} + U_4 - B_n$. At higher excitation energies four-quasiparticle states are excited.

Three-quasiparticle states in even-odd residual nuclide ^{233}U could be excited at incident neutron energies $E_n > U_3$. At lower energies fission cross section shape is controlled by one-quasiparticle state density. The transition state spectra were constructed using values of $F_0/\hbar^2$ at the inner and outer saddles shown in Table 5. Adopted level density description allows to describe shape of measured fission cross section data of ^{233}U (see Figs. 43 - 47).

Table 5
Transition spectra band-heads, Z-even, N-odd nuclei

inner saddle		outer saddle		ground state deformation	
K^π	E_{K^π},	K^π	E_{K^π},	K^π	E_{K^π},
	MeV		MeV		MeV
0^+	0.0	0_1^+	0.0	$*0_1^+$	0.0; $J^\pi=0^+,2^+,4^+,6^+...$
2_1^+	0.3	2_1^+	0.3	$*2_1^+$	0.9269(γ-vib.); $J^\pi=2^+,3^+,4^+,...$
2_2^+	0.3	2_2^+	0.3	2_2^+	1.126(γ-β-vib.);$J^\pi=2^+,3^+,4^+,...$
0_1^-	0.4	0_1^-	0.2	$*0_1^-$	0.7862(oct-vib.);$J^\pi=1^-,3^-,5^-...$
1_1^-	0.4	1_1^-	0.1	1_1^-	1.4354(oct-vib.);$J^\pi=1^-,2^-,3^-...$
2_3^+	0.5	2_3^+	0.5	2_3^+	$J^\pi=2^+,3^+,4^+,5^+,6^+$
2_1^-	0.4	2_1^-	0.3	$*2_1^-$	0.989(oct-vib.);$J^\pi=2^-,3^-,4^-,5^-...$
0_2^+	0.5	0_2^+	0.5	$*0_2^+$	0.810(β-vib.); $J^\pi=0^+,2^+,4^+,6^+...$
0_3^+	0.8	0_3^+	0.8	$*0_3^+$	1.0445(γ-vib.); $J^\pi=0^+,2^+,4^+,6^+...$

5.3 Fission Data Analysis

5.3.1 Measured fission data

Measurements for ^{233}U are difficult due to alpha activity and isotopic impurity of the layers. Rather low data errors, claimed in the measurements, do not correspond to the systematic differences evident in the data base. The absolute fission cross section measurements are an important addition to the experimental data base. Neutron-induced fission cross section of ^{233}U has been studied experimentally in numerous experiments (see Figs. 43-47). The most measurements of fission cross sections were done relative to the ^{235}U fission cross-section, with only one data set by Carlson and Behrens [32], covering the neutron energy range up to 20 MeV. In addition, there are some absolute measurements at E_n = 1.9 MeV [57], E_n = 14-15 MeV [58, 59, 60] and in the 0.13-8 MeV energy range [61]. There are systematic differences in measured fission data, however, it is possible to select a representative set of measurements, which are mutually consistent. Below is given a short description of the measurements.

Using time-of-flight method, Carlson et al. [32] have measured ratio of the ^{233}U and ^{235}U fission cross-sections from ~1 keV up to ~30 MeV. A linac was used for producing the neutrons, fission events were detected with ionization chamber. Two methods were used for normalizing the ratios: the thermal calibration method and the isotopic impurity method. With the latter method, the ratio of the cross-sections for ^{233}U and ^{235}U was obtained from the ratios of

the cross-sections for ^{238}U and ^{233}U and for ^{238}U and ^{235}U. In the 1.75-4 MeV normalization range, the normalization coefficients for the energy dependence of the ^{233}U and ^{235}U fission cross-section ratio for these two methods are different: thermal calibration gives ratios ~3.6% higher than those given by the isotopic impurity method. The final normalization coefficient was defined as an average value.

Poenitz [61] has measured the fission cross-section in the 0.l3-8.0 MeV energy range. This is the only measurement in which the absolute fission cross-section values have been obtained over a wide energy range. An ionization chamber was used to detect the fission fragments. A total absorption detector was used to measure the neutron flux. The number of nuclei in the layer was determined by alpha counting.

Meadows has measured the ^{233}U and ^{235}U fission cross section ratio in the 0.1-7.5 MeV neutron energy range [62]. The ionization technique was used to study the energy dependence of the ratio. Absolute ratios were obtained at four energy points: 1.5, 2.0, 2.5 and 3.0 MeV. The thermal calibration method was used for normalization of the ratio. Calibration by comparing the alpha activity levels of the ^{233}U and ^{235}U layers yields results which agree within the limits of statistical error.

Fursov et al. [33] have measured the ^{233}U and ^{235}U fission cross section ratio in the 0.024-7.4 MeV neutron energy range. The ionization technique was used to define the energy dependence of the ratio. The normalization was accomplished using the glass detector technique. The thermal calibration method was also used to convert the data to the absolute values.

Kanda et al. [63, 64] have measured the ^{233}U and ^{235}U fission cross-section ratio in the 0.5-7 MeV neutron energy range. The number of nuclei in the ^{233}U layer was determined by alpha counting; the number of nuclei in the ^{235}U layer was determined using the thermal calibration method.

Shpak et al.[65] have measured the ^{233}U and ^{235}U fission cross section ratio in the 0.06-3.28 MeV neutron energy range. The fission fragments were recorded using glass detectors in 4π geometry. The thermal calibration method was used for absolutization purposes.

White et al. have measured the ^{233}U and ^{235}U fission cross- section ratio at 0.04, 0.067, 0.127, 0.312, 0.415 and 0.505 MeV [66] and at 1.0, 2.25, 5.4 and 14.1 MeV [67]. An ionization chamber was used to detect fission fragments. The ratio of the numbers of nuclei was determined by alpha counting. In the renormalization of the data, account must be taken of the new half-life value $T^\alpha_{1/2}$. It increases the ratio by 3.6%.

Smirenkin and Nesterov [68] have measured the ^{233}U and ^{235}U fission cross-section ratio in the 0.3-2.5 MeV energy range. The measurement technique was similar to the one used later by Fursov et al. [33] for a wider neutron energy range.

Adamov et al. [58] have measured the cross section for ^{233}U fission by 14.7 MeV neutrons using the time-correlated associated particle method. The reaction ^{3}H(d,n)^{4}He was used to produce the neutrons, and a plastic scintillator

was used to detect the helions, correlated with neutrons. An ionization chamber was used to detect the fission fragments. Layer calibration was done by alpha counting.

Dushin et al. [58] have measured the cross section for ^{233}U fission by 14.7 MeV neutrons using the time-correlated associated particle method. The reaction ^{3}H(d,n)^{4}He was used to produce the neutrons, and a plastic scintillator was used to detect the helions, correlated with neutrons. An ionization chamber was used to detect the fission fragments. Layer calibration was done by alpha counting.

Zasadny et al. [60] have measured the absolute value of ^{233}U fission cross section for by ~14.62 MeV neutrons. A track detector was used to detect fission fragments. The neutron flux was determined relative to the ^{56}Fe(n,p)^{56}Mn activation cross section, measured with 4π proportional counter. Time variations in the neutron flux were taken into account with a boron counter.

Kalinin et al. [57] have measured the cross-section for ^{233}U fission by 1.9-MeV neutrons using the time-correlated associated particle method. The reaction D(α,n)^{3}He was used to produce the neutrons. A silicon surface-barrier detector was used to detect the helions. The uniformity of the layer was determined from the alpha activity.

Iyer et al. [69] have measured the ratio of the ^{233}U and ^{238}U fission cross-sections at E_n = 14.1 MeV. Plastic track detectors were used to record the fission fragments. No information is given about the calibration of the fissile layers. The error level for the ratio was 18%.

Meadows has measured the fission cross-section ratio at E_n = 14.74 MeV [70] using the method described in [62]; the reaction T(D,n)^{4}He was used to produced the neutrons.

Recently fission cross section ratio was measured by Shcherbakov et al. [71] in a wide energy range, from 0.58 MeV up to ~196 MeV. Spallation neutron source and neutron time-of-flight spectrometer were used. method. It seems the cross section ratios for ^{233}U and ^{235}U were normalized measuring the ratios of the cross-sections for ^{238}U and ^{233}U and for ^{238}U and ^{235}U. The latter two were defined by the isotopic impurity method [32].

5.3.2 Analysis of the measured data

From the measured data base for neutrons with energies greater than ~0.5 MeV, it is possible to define two groups of data sets, which predict different behavior of ^{233}U fission cross section. Data by Carlson and Behrens [32], Fursov et al. [33], Shpak et al. [65], White et al. [67], Pfletchinger et al. [19] and Iyer[69], absolute measurements performed by Kalinin et al. [57] and the data obtained at the Radium Institute and the Technical University in Dresden [58] are mutually consistent. The data obtained by Meadows [62, 70] and Kanda et al. [64] and the results of absolute measurements at 14.62 MeV performed by Zasadny et al. [60] comprize the second group. Data of the second group [60, 62, 70] are systematically higher than the data of the first group, while the data by Kanda et al. [64] are higher than the data in both groups and have a

significantly different shape. Absolute data by Poenitz [61] are scattering a lot, but generally they agree better with the data of the first group.

The largest discrepancies ($\sim$10%) are observed at the 'step' around $\sim$300 keV. Data by Fursov et al. [33] define the lowest level and data by Poenitz [61] - the highest. In the 0.4-2.0 MeV region, the data by Fursov et al. [33] and Carlson and Behrens [32] are in good agreement. The data by Meadows [62] for the 0.4-2.0 MeV region are systematically higher than the data in the first group, but they reproduce the 'step' observed by Carlson and Behrens [32] and by Fursov et al.[33]. The data by Kanda et al. [64] have a comparatively large spread in this region and are systematically higher than the data by Meadows [62].

The calculated curve in the 0.04-2 MeV region is fitted to the data of the first group. For the incident neutron energies up to $\sim$200 keV the calculated cross section is defined mostly by the discrete transition states (see Figs. 43-46). Figure 43 demonstrates the influence of removing one collective band $K^\pi = 2_2^+$ at at 0.3 MeV excitation above saddle point. The calculated curve in the 0.1-0.4 MeV range follows the data by Fursov et al. [33]. For the incident neutron energies higher than $E_2 = U_2 + E_{fA(B)} - B$ $\sim$200 keV the steplike-structure could be reproduced modelling the level density of ^{234}U due to excitation of two-quasiparticle states (see Fig. 41). Figure 46 shows the calculated cross section when the level densities of either fissioning ^{234}U and residual ^{233}U nuclides are calculated with smooth Gilbert-Cameron-type functions (see Fig. 41). The two-quasiparticle neutron states of even fissioning nuclide, lying below the four-quasiparticle states excitation threshold U_4 define the shape of fission cross section below incident neutron energy of $E_n \leq E_4 = E_{fA(B)} + U_4 - B_n$. At higher excitation energies four-quasiparticle states are excited. Calculated fission cross section in the incident neutron energy range 1.5$\leq E_n \leq$2.5 MeV is sensitive to the level density of ^{234}U due to the excitation of four-quasiparticle states. At higher incident neutron energies $E_n \gtrsim$2.5 MeV the level density structure is no longer important. The steep slope of calculated ^{233}U(n,f) reaction cross section is defined by the pairing correlation function at inner and outer saddles $\Delta_f = \triangle_o + \delta$, the value of $\delta =$0.06 MeV is defined by fitting fission data from $\sim$2.5 MeV up to emissive fission threshold. Fission barrier parameters are as follows: inner and outer barrier heights: $E_f^A =$4.8 MeV, $E_f^B =$5.744 MeV; inner and outer barrier curvatures $\hbar\omega_f^A =$0.9 MeV, $\hbar\omega_f^B =$0.6 MeV.

In the neutron energy region between $\sim$2 MeV and the (n,n'f) reaction threshold data by [64] gives the highest fission cross section level. The data by Meadows [62] for the 1.5-3 MeV range have an energy dependence different from the data by Kanda et al. [64]; they are 2-3% lower, but systematically higher than the data in the first group. Data by [33] give the most detailed cross section shape in this neutron energy range. The data by Smirenkin et al. [68] have a comparatively large dispersion and are not shown in Figs. 43 - 47, but on the whole they agree with data by Fursov et al. [33]. The other data sets [61, 62, 64] have different energy dependencies in this region, while the absolute differences are as high as $\sim$7%. Data by Shcherbakov et al. [71] are systemati-

cally higher than the data of the first group, however, when normalized to the absolute measurement by Kalinin et al. [57] at $E_n =$1.9 MeV they predict the same cross section shape as data of the first group.

Thus, in the 2.0-5.5 MeV energy range the calculated curve is based to the data is fitted to the data of first group. It agrees with the absolute measurement by Kalinin et al. [57] at $E_n =$1.9 MeV.

Fission data fit is used as a major constraint for capture, elastic and inelastic scattering, (n,2n) and (n,3n) cross sections as well as secondary neutron spectrum estimation.

5.4 Inelastic Scattering

Fission data fit defines the compound inelastic neutron scattering contribution to the total inelastic scattering cross section. The relative contribution of direct discrete level excitation cross sections is much higher than in case of ^{238}U target nuclide because of stronger fission competition to the compound neutron scattering in case of ^{233}U target nuclide.

5.5 Neutron Channel

The lumped transmission coefficient of the neutron scattering channel is given by

$$T_n^{J\pi}(U) = \sum_{l'j'q} T_{l'j'}^{J\pi}(E_n - E_q) + \sum_{l'j'I'} \int_0^{U-U_c} T_{l'j'}^{J\pi}(E_n')\rho(U - E_n', I', \pi)dE_n', \quad (16)$$

where $\rho(U - E_n', I', \pi)$ is the level density of the residual nucleus. Levels of residual nuclide ^{233}U [51] are provided in Table 6. The entrance channel neutron transmission coefficients $T_{lj}^{J\pi}$ are calculated within a rigid rotator coupled channel approach. For the compound nucleus formation cross section calculation, the cross sections of the direct excitation of ground state band levels were subtracted from the absorption cross section. The compound and direct inelastic scattering components are added incoherently.

The exit neutron transmission coefficients $T_{l'j'}^{J\pi}(E_n')$ were calculated using the re-normalized deformed optical potential of entrance channel without coupling, which describes a neutron absorption cross section.

5.6 Discrete level excitation cross section

Predicted discrete level excitation cross section shape, calculated within a rigid rotator model, depends upon the optical potential used. Calculated compound contribution is controlled mainly by the fission competition. Due to the lower fission threshold of ^{234}U fissioning nuclide, as compared with that of ^{239}U, compound inelastic scattering makes much lower contributions to the excitation cross sections of 1st, 2nd and 3d levels of ^{233}U around $E_n \sim$1 MeV (see Figs.

48, 49 and 50). Figures show that direct scattering essentially defines the excitation cross section of levels above ∼2 MeV.

The compound component tends to be zero above ∼3 MeV incident neutron energy. We assume strong missing of levels above excitations of ∼0.598 MeV (see Fig. 40), so only levels up to this excitation energy were included when calculating inelastic scattering cross sections. Figures 51 - 61 show the comparison of discrete level excitation cross sections.

Table 6
Levels of ^{233}U

E, MeV	J^π	K^π
0.59720	$7/2^+$	
0.57200	$1/2^-$	
0.56150	$9/2^-$	
0.54660	$5/2^+$	
0.52220	$15/2^-$	
0.51770	$19/2^+$	
0.50380	$7/2^-$	
0.49700	$11/2^+$	
0.45600	$5/2^+$	
0.43200	$9/2^+$	
0.41580	$3/2^+$	
0.41110	$17/2^+$	
0.39850	$1/2^+$	
0.39760	$11/2^-$	
0.37900	$7/2^+$	
0.35380	$9/2^-$	
0.34068	$5/2^+$	
0.32070	$7/2^-$	
0.31470	$15/2^+$	
0.31217	$3/2^+$	
0.29885	$5/2^-$	
0.22940	$13/2^+$	
0.15527	$11/2^+$	
0.09219	$9/2^+$	
0.04035	$7/2^+$	
0	0^+	

5.7   Total inelastic cross section

Calculated total inelastic cross section is compared with previous evaluated data on Fig. 62. Lumped contribution of direct excitation of ground state band levels is shown to attain ∼20% of total inelastic cross section at $E_n \gtrsim 2$

MeV. Present calculated curve is higher than JENDL-3.3 evaluation [5] above $E_n \sim 1.5$ MeV. Our estimate is much higher than ENDF/B-VI [4] evaluation above $E_n \sim 0.5$ MeV, this inconsistency is explained by rather high estimate of continuum inelastic scattering in present evaluation (see Fig. 63).

Shape of calculated continuum inelastic scattering cross section is rather similar to that of JENDL-3.3 [5] up to $E_n \sim 6$ MeV, but the absolute values are rather different (see Fig. 63). The pre-equilibrium contribution continuum inelastic scattering cross section in present is also rather different from previous estimates. Continuum inelastic scattering cross section of ENDF/B-VI [4] evaluation seems to be too low, though it is compatible with present estimate up to $E_n \sim 1.5$ MeV .

Above emissive fission threshold evaluations of inelastic scattering cross section differ severely, present estimate being the highest (see Fig. 64). In our calculations pre-equilibrium neutron emission contribution is defined by description of ^{238}U secondary neutron spectra and consistent description of ^{238}U(n,f), ^{238}U(n,2n) and ^{238}U(n,3n) reaction cross sections [50]. At $E_n \sim 10$ MeV it is ~ 1.5 times higher than that of JENDL-3.3 evaluation [5]. Pre-equilibrium neutron emission contribution allowed to reproduce also observed fission cross section of ^{233}U(n,f) up to $E_n \sim 20$ MeV.

6 Capture cross section

We have demonstrated by the analysis of measured capture cross sections of ^{238}U(n,γ) and ^{232}Th(n,γ) [72] that neutron capture data could be described within a Hauser-Feshbach-Moldauer statistical model. Specifically, in a few keV energy region calculated capture cross section is defined by the radiative strength function value $S_\gamma = \Gamma_\gamma/D$. At incident neutron energies above ~ 100 keV calculated capture cross section shape is defined by the energy dependence of radiative strength function S_γ. Energy dependence of S_γ is controlled mainly by the energy dependence of the level density of the compound nuclide ^{234}U. Low fission threshold for the ^{234}U nuclide necessitates the inclusion of the competition of fission [12] alongside with neutron emission [11] at the second $\gamma-$cascade, i.e. after first $\gamma-$quanta emission . Then "true" capture reaction cross section (n,$\gamma\gamma$) is defined using transmission coefficient $T_{\gamma\gamma}^{J\pi}(U)$ defined in a two-cascade approximation as

$$T_{\gamma\gamma}^{J\pi} \; = \; \frac{2\pi C_{\gamma 1}}{3(\pi hc)^2} \int \varepsilon_\gamma^2 \sigma_\gamma(\varepsilon_\gamma) \sum_{I=|J-1|}^{I=J+1} \rho(U-\varepsilon_\gamma, I, \pi) \frac{T_\gamma^{I\pi}}{T_f^{I\pi} + T_{n'}^{I\pi} + T_\gamma^{I\pi}} d\varepsilon_\gamma \; , \; (17)$$

The last term of the integrand describes the competition of fission, neutron emission and γ-emission at excitation energy $(U - \varepsilon_\gamma)$ after emission of first γ-quanta, $C_{\gamma 1}$ is the normalizing coefficient. That means that transmission coefficients $T_\gamma^{I\pi}$, $T_{n'}^{I\pi}$ and $T_f^{I\pi}$ are defined at excitation energy $(U - \varepsilon_\gamma)$. The neutron emission after emission of first $\gamma-$quanta strongly depends on the ^{233}U residual nuclide level density at excitations just above paring gap U_2. The

contribution of (n,γf)−reaction [12] to the observed fission cross section is defined by $T_{\gamma f}^{J\pi}$ coefficient. The energy dependence of (n,γf) reaction transmission coefficient $T_{\gamma f}^{J\pi}$ was calculated with the expression

$$T_{\gamma f}^{J\pi} \;=\; \frac{2\pi C_{\gamma 1}}{3(\pi hc)^2} \int \varepsilon_\gamma^2 \sigma_\gamma(\varepsilon_\gamma) \sum_{I=|J-1|}^{I=J+1} \rho(U-\varepsilon_\gamma, I, \pi) \frac{T_f^{I\pi}}{T_f^{I\pi}+T_{n'}^{I\pi}+T_\gamma^{I\pi}} d\varepsilon_\gamma \;, \;\; (18)$$

The capture cross section is shown on Figs. 65 and 66. The (n,γf) reaction competition to the "true" capture (n,γγ) reaction competition is rather strong above $E_n \sim 3$ MeV. The competition of (n,γn') reaction to the "true" capture (n,γγ) reaction is essential above $E_n \sim 1$ MeV. We adopted here radiative capture strength function $S_{\gamma o}$, which actually corresponds to $\langle \Gamma_\gamma \rangle = 39$ meV and $\langle D_{l=0} \rangle = 0.52$ eV. Above $E_n \sim 1$ MeV capture cross section decrease is defined by (n,γf) and (n,γn') reactions competition.

Previous evaluated capture cross sections are drastically discrepant with present calculation (see Fig. 66). Some consistency is observed only with ENDF/B-VI [4] up to ~15 keV. For higher incident neutron energies competition of fission and inelastic scattering with γ−emission seems to be modelled correctly within present approach. A consistent description of a most complete set of measured data on the (n,γ), (n,f) and (n,n') reaction cross sections for the ^{238}U and ^{232}Th target nuclides [1, 2, 3, 72] enables one to consider the statistical theory estimates of ^{233}U(n,γ) reaction as fairly realistic.

7   Cross sections above emissive fission threshold

At incident neutron energies when fission reaction of ^{233}U or ^{232}U nuclides is possible after emission of 1 or 2 pre-fission neutrons, the observed ^{233}U(n,f) fission cross section being a superposition of non-emissive or first chance fission of ^{234}U and xth-chance fission contributions. These contributions are weighted with a probability of x neutron emission before fission. For fixed statistical model parameters of residual nuclei ^{233}U and ^{232}U, fissioning in ^{233}U(n,nf) or ^{233}U(n,2nf) reactions, the behavior of the first-chance fission cross section σ_{nf} should make it possible to reproduce the observed fission cross section σ_{nF} of ^{233}U(n,f) reaction. A consistent description of a most complete set of measured data on the (n,f), (n,2n), (n,3n) and (n,4n) reaction cross sections for the ^{238}U target nuclide up to 20 MeV enables one to consider the estimates of first neutron spectra of initial ^{234}U nuclide as fairly realistic.

7.1   Fission cross section

Above emissive fission threshold contributions of emissive fission to the observed fission cross section coming from (n,$x$nf), $x = 1, 2, 3...X$, fission reactions of relevant equilibrated uranium nuclei, could be calculated as

$$\sigma_{nF}(E_n) = \sigma_{nf}(E_n) + \sum_{x=1}^{X} \sigma_{n,xnf}(E_n), \qquad (19)$$

emissive fission contributions could be calculated using fission probability estimates $P_{fi}^{J\pi}(U)$ as

$$\sigma_{n,xnf}(E_n) = \sum_{J\pi} \int_0^{U_{max}} W_{x+1}^{J\pi}(U) P_{f(x+1)}^{J\pi}(U) dU, \qquad (20)$$

where $W_x^{J\pi}(U)$ is the population of $(x+1)-$th nucleus at excitation energy U after emission of x neutrons, excitation energy U^{max} is defined by the incident neutron energy E_n and energy, removed from the composite system by ^{233}U(n,$x$nf) reaction neutrons. Fission probabilities $P_{fx}^{J\pi}$ for fissioning $x-$th nuclei, could be estimated by fitting neutron-induced fission cross sections of ^{232}U target nuclide [73]. Neutron-induced fission cross section of ^{233}U, shown on the Fig. 67 demonstrates a step-like structures, relevant to the contributions of (n,$x$nf) reactions to the total fission cross section. For these calculations modified version of Hauser-Feshbach code STAPRE [74] is employed.

Contribution of first-chance fission is defined by the pre-equilibrium emission of first neutron and level densities of fissioning ^{234}U and residual ^{233}U nuclides. The behavior of the first-chance fission cross section σ_{nf} is obviously related to the energy dependence of the fission probability of the ^{234}U nuclide P_{f1}:

$$\sigma_{nf} = \sigma_r(1 - q(E_n))P_{nf}. \qquad (21)$$

Once the contribution of first neutron pre-equilibrium emission $q(E_n)$ is fixed, the first-chance fission probability P_{nf} of the ^{234}U composite nuclide depends only on the level density parameters of fissioning and residual nuclei. Actually, it depends on the ratio of shell correction values $\delta W_{fA(B)}$ and δW_n. The results of different theoretical calculations of the shell corrections as well as of the fission barriers vary by $1 \sim 2$ MeV. The same is true for the experimental shell corrections, which are obtained with a smooth component of potential energy, calculated according to the liquid-drop or droplet model. However the isotopic changes of $\delta W_{fA(B)}$ and δW_n [53] are such that P_{nf} viewed as a function of the difference $(\delta W_{fA(B)} - \delta W_n)$ is virtually independent on the choice of smooth component of potential energy. Therefore, we shall consider the adopted $\delta W_{fA(B)}$ estimates (see Table 4) to be effective, provided that δW_n are obtained with the liquid drop model.

It should be noted that from the ^{233}U(n,n'f) reaction threshold up to $\sim$8 MeVdata of the first and second groups are in fairly good agreement. Over a wider range the fission cross-section energy dependencies derived from the data in the two groups and in Ref. [61] differ. At energies above 8.0 MeV, where the data in Refs [62, 70] predict a fission cross section, which is $\sim$5% higher than the cross sections of the first group data predict.

Above (n,nf) reaction threshold (see Fig. 67) calculated curve is compatible with measured data by Carlson and Behrens [32] and Fursov et al. [33]. At

higher energies the calculated curve is compatible with the data by Carlson [32]. Above (n,2nf) reaction threshold calculated curve is compatible with measured data by Adamov et al. [59] (E_n ∼14.7 MeV). Data point by Zasadny et al. [60] at E_n ∼14.7 MeV predicts higher cross section level, the other data point by Dushin et al. [58] lies a bit lower. Data by Shcherbakov et al. [71] are systematically higher than the data of the first group, at ∼15 MeV they are compatible with data by Zasadny et al. [60]. However, when normalized to the absolute measurement by Kalinin et al. [57] at E_n =1.9 MeV they predict the same cross section shape as the data of the first group below and above emissive fission threshold. At E_n ∼14.8 MeV normalized data by Shcherbakov et al. [71] are compatible with data by Dushin et al. [58].

The trend of the first-chance fission cross section σ_{nf}, shown in Fig. 67 corresponds to the estimate of σ_{nf}, obtained by the fit of ^{238}U(n,f), ^{238}U(n,2n), ^{238}U(n,3n) and ^{238}U(n,4n) reaction cross section data [75]. Contribution of second-chance fission of ^{233}U nuclide is defined by the pre-equilibrium contribution of first neutron spectrum and subsequent sharing of $\sigma_r = \sigma_{nf} + \sigma_{n,nx}$ reaction cross section into first-chance fission and neutron emission cross sections. First-, second- and third-chance fission contributions to the total neutron-induced fission cross section of ^{233}U are compared with relevant contributions for neutron-induced fission of ^{238}U target nuclide on Fig. 68. The contribution of first-chance fission to the observed ^{233}U(n,f) reaction cross section is rather smooth function of incident neutron energy, as distinct from ^{238}U(n,f) reaction. In the latter case a local minimum is observed near ^{238}U(n,nf) reaction threshold. The second-chance fission contribution ^{233}U(n,nf) is a smooth increasing function of excitation energy up to E_n ∼12 MeV. It corresponds to neutron-induced fission cross section of ^{232}U(n,f) reaction. Calculated with present level density approach cross section of ^{232}U(n,f) reaction is shown on Fig. 69. The contribution of ^{233}U(n,2nf) third chance fission reaction to the observed fission cross section is somewhat higher near the threshold, than in case of ^{238}U(n,2nf) reaction. Fission barrier parameters of relevant U nuclei, i.e. inner and outer barrier heights E_f^A, E_f^B and $\hbar\omega_f^A$, $\hbar\omega_f^B$ are given in Table 7.

Table 7

Fission barrier parameters of U nuclei

Nuclide	E_f^A,MeV	E_f^B,MeV	$\hbar\omega_f^A$,MeV	$\hbar\omega_f^B$,MeV
^{234}U	4.8	0.6	0.9	0.6
^{233}U	4.15	5.85	.7	.5
^{232}U	4.4	5.1	1.0	0.6
^{231}U	4.8	6.0	.7	.5

7.2 ^{233}U(n,xn) cross section

There is no measurements of ^{233}U(n,2n) or ^{233}U(n,3n) reaction cross section. These cross sections would be estimated using ^{233}U(n,f) fission cross section

fit up to E_n =20 MeV as the only constraint. Present estimate of ^{233}U(n,2n) cross section for $E_n \gtrsim$11 MeV is much lower than those of JENDL-3.3 [5] and ENDF/B-VI [4] (Fig. 70). For $E_n \gtrsim$11 MeV calculated (n,2n) reaction cross section shape corresponds to pre-equilibrium emission contribution to the first neutron spectrum.

Present estimate of ^{233}U(n,3n)^{232}U cross section is much lower than those of JENDL-3.3 [5] and ENDF/B-VI [4], both seem to be unrealistically high (see Fig. 71).

8   Neutron emission spectra

First we will describe the approach used for the prompt fission neutron number ν_p and prompt fission neutron spectra (PFNS) calculation and then return to the discussion of secondary neutron spectra of (n,xn) reactions. A brief survey of the model used to estimate prompt fission neutron number ν_p value and PFNS is provided below.

8.1   Prompt fission neutron number ν

Number of prompt fission neutrons for ^{233}U was measured rather extensively. Below is given a brief survey of the measurements.

8.1.1   Measured ν data

At thermal energy point the total neutron multiplicity (prompt plus delayed) is known with accuracy better than $\sim$0.2%, ν_t =2.4946±0.0040 [76]. At higher incident neutron energies most of the measurements used similar experimental techniques: multilayer ionization chamber as a fission fragments detector and a large scintillator tank (or BF$_3$ counters placed into moderator) as a prompt fission neutrons detector. The energy dependence in a wide energy range has been measured relative to ^{252}Cf(sf) $\nu-$value. We renormalized data to modern value $\nu = 3.756$ when another value was originally used.

Hopkins and Diven [77] used large scintillation tank as a prompt fission neutrons detector and ν_{Cf} =3.78, incident neutron enrgy range of 0.28 - 3.93 MeV was investigated.

Gwin et al. [78] used linac as a neutron source and Gd-loaded large scintillation tank as a prompt fission neutrons detector. Corrections were made for delayed $\gamma-$rays from fission, error fission events, background in neutron detector, displacement of samples, foil thickness, spontaneous fission events, anisotropy of fission-fragment distribution, differences in fission neutron energies. Incident neutron energy range of 0.0005 - 10 MeV was investigated.

Mather et al. [79] used 6 MeV Van De Graaff accelerator as neutron source and Gd-loaded large scintillation tank as a prompt fission neutrons detector. Monitor value was $\nu_{Cf} = 3.782$.Incident neutron enrgy range of 0.96 - 4 MeV was investigated.

Boldeman and Walsh [80] used 3 MeV Van De Graaff accelerator and ^{7}Li(p,n) and T(p,n) reactions as neutron source and Gd-loaded large scintillation tank as a prompt fission neutrons detector. Monitor value was $\nu_{Cf} = 3.782$. Incident neutron energy range of 0.3 - 1.87 MeV was investigated.

Nurpeisov et al. [81] used Van De Graaff accelerator and T(p,n) reaction as neutron source, 24 ^{3}He counters, placed into paraffin block, were used for for neutron registration. They measured ratio of ν_U/ν_{Cf}. Incident neutron energy range of 0.08 - 1.4 MeV was investigated.

Nurpeisov et al. [82] used the same experimental technique as in measurement by Nurpeisov et al. [81] . Monitor value was $\nu_{Cf} = 3.756$. Incident neutron energy range of 0.0254 eV - 4.89 MeV was investigated.

Colvin and Sowerby [83] used ^{3}He counters, placed into moderator for neutron registration. Monitor value was $\nu_{Cf} = 3.78$. Incident neutron energy range of 0.57 - 2.6 MeV was investigated.

Sergachev et al. [84] used for absolute measurements reactor beam as thermal neutrons source and Van De Graaff accelerator (^{7}Li(p,n), T(p,n) and D(d,n) reactions) as a fast neutron source. They measured fission fragments kinetic energies by silicon detector, ν-values were estimated from the fission energy balance. Incident neutron energy range of 0.0254 eV - 2.14 MeV was investigated.

Kolosov et al. [85] measured fission fragments kinetic energies by silicon detector, ν-values were obtained on the basis of fission energy balance. Monitor value was $\nu = 2.48$ for thermal fission of ^{233}U. However, one should have in mind that data by Sergachev et al. [84] and Kolosov et al. [85] are not purely experimental. The ν-data were based on the measured fission fragment kinetic energy and model calculations.

Smirenkin et al. [86] have measured prompt fission neutron number at ~ 4 MeV and ~ 15 MeV. Coincidence in double ionization chamber were registered to detect fission fragments. Data were normalized to ^{233}U thermal prompt neutron number $\nu = 2.497$. Corrections were made for the detector efficiency, inelastic scattering, detection efficiency differences for slow and fast neutrons. We renomalized these data to the thermal prompt neutron number $\nu = 2.486$.

8.1.2 Prompt fission neutron number ν above emissive fission threshold

At incident neutron energies above emissive fission threshold the number of prompt fission neutron $\nu(E_n)$ was calculated as

$$
\begin{aligned}
\nu(E_n) &= \beta_o \nu_o(E_n) + \beta_1(1 + \nu_1(E_n - B_{nA} - \langle E_1 \rangle)) + \\
&\quad \beta_2(2 + \nu_2(E_n - B_{nA} - B_{nA-1} - \langle E_1 \rangle - \langle E_2 \rangle)). \quad (22)
\end{aligned}
$$

Here, $\nu_i(E_n)$ is a prompt fission neutron number for ith fissioning nucleus, B_{nA} - neutron binding energy for the A nucleus, $\langle E_i \rangle$- average energy of ith neutron. To calculate the ν-value energy dependence for ^{233}U(n,f) up to 20 MeV we should know also ν-values for ^{232}U and ^{231}U target nuclides, which contribute

to the observed ν-value via emissive fission processes (see Figs. 67, 68). We assume that excitation energy:

$$U_i = E_n - \sum_j (B_{nj} + \langle E_{ij} \rangle),$$ (23)

is brought into A_i nucleus with the reaction: $n + (A_i - 1) \rightarrow fission$. Incident neutron energy in this hypothetical reaction equals to $U_i - B_{nA_i}$. In this way the $\nu_i(E_n)$ functions for all isotopes in the chain $A+1, A, A-1$ were calculated.

8.1.3 $\nu-$value analysis

Experimental data are shown on Figs. 72 and 73. One can see that data by Colvin [83] and some "single energy point" measurements ([77] and [87]) disagree with the other measurements. The other data are in a reasonable agreement.

Low energy data are shown in Fig. 72. Some shift between time-of-flight experiment by Gwin et al. [78] and other "monoenergetic" data data is visible. In the energy around $\sim$0.1 MeV five "monoenergetic" data points [81],[82],[84],[85] average to $\langle \nu \rangle = 2.489 \pm 0.015$, 23 data points from time-of-flight experiment by Gwin et al. [78] ($\langle \nu \rangle = 2.485 \pm 0.020$) are in good agreement with them. Average ν-value for this energy interval and its standard deviation per one experimental point could be used to estimate thermal energy value as $\nu = 2.486 \pm 0.004$. This value agrees with experimental data from [88] (2.449 ± 0.054) and [89] (2.480 ± 0.013), measured relative to ^{235}U and ^{239}Pu. The absolute values were calculated with $\nu_{235U} = 2.408$, and $\nu_{239Pu} = 2.876$ [90].

The energy dependence of ν versus incident neutron energy is compared on Fig. 73 with experimental data and previous evaluations. The behavior of the ν-function above (n,nf) reaction threshold is determined by the fissility of ^{233}U nuclide after emission of first pre-fission neutron. As a result, the energy dependence of the neutron multiplicity may be a linear function as for ^{238}U(n,f) [75] or a bump-like function as for ^{232}Th(n,f) reaction [91]. ^{233}U(n,nf) reaction demonstrates an intermediate case. The first-chance ν-values for ^{231,232,233}U target nuclides are shown in Table 8. The incident neutron energy dependences for partial ν-values were taken from [92]. Only for ^{233}U(n,f) reaction parameters were corrected to improve agreement with the experimental data. The delayed neutrons yield and decay parameters were taken from JENDL-3.3 [5].

Table 8
First chance ν-values for ^{231,232,233}U target nuclides.

Target	ν^{th}	$\nu(E_n)$	$\nu(6$ MeV$)$
^{231}U	2.632	2.679 (0.57 MeV)	3.370
^{232}U	2.506	2.677 (1.92 MeV)	3.196
^{233}U	2.486	2.560 (1.02 MeV)	3.240

In the incident neutron energy range $0 \lesssim E_n \lesssim 5$ MeV all evaluations give very close absolute values, ν-dependences on the incident neutron energy are

also rather similar. At the energy range $6 \lesssim E_n \lesssim 11$ MeV evaluation of JENDL-3.3 [5] is somewhat higher than experimental data by Gwin et al. [78]. The partial ν-functions for (n,f), (n,nf) and (n,2nf) estimated in this work are also shown in Fig. 73.

8.2   Prompt fission neutron spectra

Prompt Fission Neutron Spectra (PFNS) for ^{233}U have been calculated with the model that was previously applied for ^{238}U and ^{232}Th PFNS data analysis [1, 75, 91, 93]. Here is enclosed a brief description of the PFNS model.

8.2.1   Model for PFNS evaluation

In the energy range of first chance fission ($E_n \lesssim 5$ MeV) the PFNS are calculated as sum of two Watt distributions [94]:

$$
S(E, E_n) = 0.5 \cdot \sum_i W_i(E, T_i(E_n), \alpha), \tag{24}
$$

$$
E_{vl} = \frac{A_h}{A_l \cdot A} \cdot \alpha \cdot TKE, E_{vh} = \frac{A_l}{A_h \cdot A} \cdot \alpha \cdot TKE,
$$

where

$$
W(E, T, E_\nu) = M(E, T) \cdot \exp(\frac{-E_\nu}{T}) \cdot \frac{sh(\sqrt{b \cdot E})}{\sqrt{b \cdot E}}, b = \frac{4 \cdot E_\nu}{T^2}, \tag{25}
$$

$$
M(E, T) = \frac{2\sqrt{E}}{\sqrt{\pi}T^{3/2}} \cdot \exp(-\frac{E}{T}). \tag{26}
$$

$$
T_{ij} = k_{ij} \cdot \sqrt{E^*} = \sqrt{E_r + E_n + B_n - TKE} \tag{27}
$$

T_{ij} is the temperature parameters for nucleus "i", light and heavy fragments ($j = 1,2$) , α is the ratio of the total kinetic energy (TKE) at the moment of the neutron emission to the TKE value at full acceleration. Free parameter α was fitted to the PFNS experimental data for a number of nuclei. The ratio of "temperatures" for light and heavy fragment $r = \frac{T_{i1}}{T_{i2}}$ is the second semi-empirical fitting parameter, it varies from one target nucleus to another only slightly, so we assumed $r = 1.248$ for uranium nuclei.

Above emissive fission threshold the PFNS are described by the equation:

36

$$
\begin{aligned}
S(E, E_n) &= \nu^{-1}(E_n)(\nu_o(E_n) \cdot \beta_o(E_n) \cdot S_o(E, E_n) + && (28)\\
&\quad \nu_1(E_n) \cdot \beta_1(E_n) \cdot S_1(E, E_n) + \beta_1(E_n) \cdot P_{11}(E, E_n) + \\
&\quad \nu_2(E_n) \cdot \beta_2(E_n) \cdot S_2(E, E_n) + \\
&\quad \beta_2(E_n) \cdot [P_{21}(E, E_n) + P_{22}(E, E_n)] + ...),
\end{aligned}
$$

$$
\int P_{ij}(E, E_n)dE = 1,
$$

$$
\nu(E_n) = \sum_{i=0}[(\nu_i(E_n) + i) \cdot \beta_i(E_n)], \qquad (29)
$$

where subscript i =0, 1, 2 denotes i-th chance fission reaction of the $A + 1$, A, $A - 1$ nucleus after emission of i pre-fission neutrons, $\beta_i(E_n)$ is the i-th chance fission contribution to the observed fission cross section (see Fig. 68), $\nu_i(E_n)$ is the number of the prompt fission neutron for these nuclei, $S_i(E, E_n)$ is PFNS spectrum without pre-fission neutrons, $P_{ik}(E, E_n)$ is the spectrum of k-th pre-fission neutron for $i-$th chance fission. To calculate total PFNS, $\nu_i(E_n)$, $\beta_i(E_n)$ and T_{ij} values should be known.

The pre-fission neutron spectra $P_{ik}(E, E_n)$ and average neutron energy $\langle E_{ik} \rangle$ were calculated taking into account pre-equilibrium pre-fission neutron emission.

The excitation energy U_i of the nucleus $A_i = A + 1 - i$ after emission of i-neutrons was calculated as:

$$
U_i = B_n + E_n - \sum_j (B_j + \langle E_{ij} \rangle), \qquad (30)
$$

where B_j is the neutron binding energy. This allows to estimate the excitation energy of fission fragments as $E^* = E_r + U - TKE$ and calculate the $T_{ij}(E_n)$ energy for each uranium nuclide in the chain. The formula for $\nu_i(E_n)$ calculation is given in previous section.

For incident neutron energies $E_n \gtrsim 10$ MeV we incorporated an additional correction to diminish the discrepancy between measured and calculated data for PFNS of ^{238}U(n,f) and ^{232}Th(n,f) reactions [1]. The same tendency was observed for ^{235}U(n,f) reaction [93]. We introduce the same correction for CMS energy per one nucleon E_{v0} for ^{233}U(n,f) reaction. The CMS energy was calculated according to the equation:

$$
E_v = \alpha \cdot \alpha_1 \cdot E_{v0}, \qquad (31)
$$

α_1=1 for E_n <10 MeV and α_1=0.8 for E_n >12 MeV and linearly interpolated for $10 \leq E_n \leq 12$ MeV. This correction was made either for non-emissive and emissive fission reactions.

Available data on PFNS are obtained in so-called shape experiments, i.e. they provide relative data without absolute normalization. To compare experimental and calculated data both should be normalized to unity. The normalization coefficient for measured data was calculated by least squares method using following equation:

$$F(C) = \sum_i (N_i - C \cdot S_i)^2 \cdot \omega_i, \quad \omega_i = \frac{1}{\delta N_i^2}, \qquad (32)$$

where S_i is the calculated value at energy E_i, ω_i is weight of the i-th experimental point, δN_i is absolute error of the experimental value N_i. The C value was estimated from condition $dF/dC = 0$, which gives the following relation:

$$C = \frac{\sum S_i \cdot N_i \cdot \omega_i}{\sum S_i^2 \cdot \omega_i} \qquad (33)$$

The experimental data were normalized to unity using predicted(calculated) shape $S(E, E_n)$.

The experimental average neutron energies $\langle E \rangle$ for PFNS was calculated with the following procedure. The lower energy tail of PFNS from lowest energy E_1 up to $(E_1 + 1)$ MeV and higher energy tail from $(E_2 - 2)$ up to E_2 MeV were fitted with Maxwellian. The respective parameters were used for extrapolation to 0 and 20 MeV.

8.2.2 Pre-fission (n,$x$nf) neutron spectra

Partial neutron energy distributions $P_{ik}(E, E_n)$ of (n,$x$nf), $x = 1$, 2, 3, reactions are calculated with Hauser-Feshbach model taking into account fission and $\gamma-$emission competition to neutron emission, actually exclusive neutron spectra are calculated simultaneously with fission and (n,xn) reaction cross sections [93, 96]. The pre-equilibrium emission of first neutron is fixed by the description of high energy tails of (n,2n) reaction cross sections and (n,f) reaction cross sections for ^{238}U and ^{232}Th target nuclides. First neutron spectrum of the ^{233}U(n,nf) reaction is the sum of evaporated and pre-equilibrium emitted neutron contributions. Second and third neutron spectra for ^{233}U(n,$x$nf) fission reactions are assumed to be evaporative. Pre-fission neutron spectrum of ^{233}U(n,nf) reaction, especially its hard energy tail, is sensitive to the description of fission probability of ^{233}U nuclide near fission threshold (see below).

Partial neutron spectra are shown on Figs. 74-82. Components of first, second, third and fourth neutron spectra for E_n =20 MeV are shown on Figs. 74, 75, 76 and 77. Components of first, second and third neutron spectra for E_n =14 MeV are shown on Figs. 78, 79 and 80, for E_n =8 MeV - on Figs. 71 and 82.

At E_n =20 and 14 MeV major contribution to the first neutron spectrum comes from (n,nf) and (n,2nf) reaction spectra (see Figs. 74 and 78), at lower energy E_n =8 MeV soft part of (n,nf) reaction neutron spectrum is much higher than the first neutron component of (n,2nγ) reaction, while hard part of (n,nf) reaction neutron is comparable with soft energy tail of (n,nγ) reaction spectrum (see Fig. 81). Spectrum of (n,nγ) reaction actually is just hard energy tail of 'pre-equilibrium' component of first neutron spectrum. Shapes of first neutron spectra of (n,nγ) and (n,2nγ) reactions at E_n =20 (Fig. 74) and 14 MeV (Fig. 78) are rather similar, soft part being defined by neutron emission competition of

higher neutron multiplicity reactions. This lowering of soft part of first neutron spectrum of (n,2nγ) reaction disappears at E_n =8 MeV.

At E_n =20 MeV major contribution to the second neutron spectrum (up to $E \sim 9$ MeV) comes from (n,2nf) reaction (see Fig. 75), it is defined by the fission probability of ^{233}U. Soft parts of the second neutron spectra of (n,2n) and (n,3n) reactions are comparable. At lower incident neutron energy E_n =14 MeV major contribution to the second neutron spectrum comes from (n,2nγ) reaction (see Fig. 79). At lower energy E_n =8 MeV major contribution to the second neutron spectrum also comes from (n,2nγ) reaction (see Fig. 82)

At E_n =20 MeV largest contribution to the third neutron spectrum comes from (n,3nγ) reaction (see Fig. 76), those of the (n,3nf) and (n,4n) reactions being rather low.

8.2.3   Comparison with previous evaluations

Prompt fission neutron spectra of ^{233}U(n,f) reaction were measured at thermal incident neutron energy be Lajtai et al. [97] and Starostov et al.[98], at E_n =0.5, 1.9 and 4.1 MeV measurements were carried out by Baba et al. [99] and Miura et al. [100]. The peculiarities similar to the PFNS for ^{238}U(n,f) and ^{232}Th(n,f) reactions that were analyzed recently [93], are visible also (see Figs. 83-87). The PFNS calculated with present model demonstrate more complicated shape as compared with Watt spectrum of ENDF/B-VI [4]. At the other hand, the Madland-Nix model prediction of JENDL-3.3 [5] drops in the energy range $E \lesssim 2$ MeV and overestimates the high energy tail of the spectrum.

The PFNS for the ENDF/B-VI [4] evaluation were calculated as Watt spectrum, while for the JENDL-3.3 [5] - on the basis of the Madland-Nix model [95]. Previous evaluations of JENDL-3.3 [5] and ENDF/B-VI [4] overestimate the average energy of PFNS at thermal energy. As it was shown earlier by Kornilov et al. [101], there is a contradiction between microscopic experimental ($\langle E \rangle = 1.98$ MeV) and macroscopic ($\langle E \rangle$ =2.05 MeV) data for ^{235}U(n,f) PFNS at thermal energy. The model, adjusted to the macroscopic data overestimates the average energy of PFNS for ^{235}U(n,f). As a result, the PFNS calculated with similar model parameters for ^{233}U(n,f) reaction, which has similar neutron multiplicity and fission fragment kinetic energies, will predict higher average energy as compared with microscopic data. Our evaluation being in good agreement with experimental data predicts ~ 70 keV reduction of the $\langle E \rangle$ as compared with JENDL-3.3 [5] and ENDF/B-VI [4] evaluations (see Fig. 88).

Above emissive fission threshold at $E_n \sim 7$-10 MeV the contribution of the second chance fission reaction ^{233}U(n,f) is comparable with that of non-emissive fission (see Figs. 67, 68). The average energy removed by first pre-fission neutron is much smaller than the average energy of post-fission neutrons. This peculiarity explains appearance of low energy bump in the spectrum of fission neutrons (Fig. 89). At higher incident neutron energies of E_n =14 and 20 MeV (see Figs. 90 and 91), the PFNS also consists of several components. One of them is connected with pre-equilibrium first neutron emission and produces bump at $E_{th} \sim E_n - B_{fA} \sim 8$ MeV prompt fission neutron energy for E_n =14

MeV or $E_{th} \sim 14$ MeV for $E_n = 20$ MeV, B_{fA} is the effective fission barrier of ^{233}U. Soft neutron component connected with pre-fission neutrons from (n,2nf) reaction is noticed on Fig. 90 for $E_n = 14$ MeV. Irregularity around 8 MeV for PFNS for $E_n = 20$ MeV (see Fig. 91) might be correlated with the first neutron spectrum of ^{233}U(n,2nf) reaction, $P_{21}(E, E_n)$ ((n,2nf)^1), it is sensitive to the description of fission probability of ^{233}U near fission threshold.

The dependence of the average energy of fission neutrons $\langle E \rangle$ versus incident energy also demonstrates all these peculiarities (Fig. 88). At incident neutron energies $E_n \lesssim 6$ MeV the average energy dependence is proportional to the square root of fission fragments excitation energy $\sqrt{U_i}$ or ν value. At $E_n \gtrsim E_{nnf} 6$ MeV (threshold of ^{233}U(n,nf) reaction $E_{nnf} \sim 6$ MeV) the average energy drops due to the contribution of low energy pre-fission neutrons. The increase of incident neutron energy gives the proper increase of average energy for PFN. This tendency (solid line in Fig. 88) is reduced at $E_n \sim 10$ MeV due to inclusion of additional correction $\alpha_1$to the secondary neutron energy. At higher neutron energies ($E_n > 13$ MeV) the stable increase of the average energy $\langle E \rangle$ was predicted in the framework of present model. Somewhat different behavior as compared with prediction for ^{238}U(n,f) reaction, may be explained by the lower share of the (n,3nf) reaction for ^{233}U(n,f) reaction.

Calculated PFNS of ^{238}U(n,f) reaction reproduce available measured data. We will compare with them calculated PFNS of ^{233}U(n,f) to define the influence of different partial chance fission contributions. In the domain of emissive fission rather different contribution of (n,nf) reaction for the ^{233}U(n,f) reaction, than in case of ^{238}U(n,f) reaction [1] is observed (see Figs. 67, 68). Figure 69 shows the comparison of emissive chance fission contributions to the total fission cross section of ^{233}U (n,f) and ^{238}U (n,f) reactions. Relative contribution of ^{233}U (n,nf) reaction is higher than in case of ^{238}U (n,nf) reaction for $E_n \gtrsim 8$ MeV, while they are similar for $E_n \lesssim 8$ MeV. The low energy spectrum component due to pre-fission neutrons makes a strong influence on the PFNS shape. For ^{233}U(n,f) reaction the contribution of pre-fission neutrons from (n,nf) reaction to the observed PFNS in fission neutron energy range $E_{th} \sim E_n - B_f$ should much more pronounced than in case of ^{238}U(n,f) for $E_n \gtrsim 8$ MeV. The contribution of ^{233}U(n,nf) reaction cross section to the observed fission cross section ^{233}U(n,f) is shown on Fig. 68.

Partial contributions of chance fission reactions to the observed prompt fission neutron spectra are shown on Figs. 92, 93 and 94 for $E_n = 20$ MeV, $E_n = 14$ MeV and $E_n = 7$ MeV, respectively. On the figures are shown normalized to unity observed prompt fission neutron spectra of ^{233}U(n,f) reaction and its partial contributions from chance fission reactions, multiplied by respective contributions to the observed fission cross section.

8.3 Neutron spectra of (n,xn) reactions

For incident neutron energies higher than emissive fission threshold we have calculated 1st, 2nd and 3d neutron spectra for the (n,nγ), (n,2n) and (n,3n) reactions. According to the ENDF/B-VI format specifications the secondary

neutron spectra are included in the following way. Calculated spectra were summed up and tabular spectra for the (n,nγ), (n,2n) and (n,3n) reactions were obtained.

Spectrum of (n,nγ) reaction actually is just hard energy tail of 'pre-equilibrium' component of first neutron spectrum. Spectrum of the first neutron of (n,2n) reaction is much softer, although 'pre-equilibrium' component still comprise appreciable part of it. First neutron spectrum of (n,3n) reaction is actually of evaporative nature. First neutron spectrum of (n,nf) reaction has rather long pre-equilibrium high-energy tail. First neutron spectrum of (n,2nf) reaction, as that of (n,3n) reaction, is of evaporative nature.

Figures 95, 96, 97, 98 and 99 compare neutron spectra of (n,nγ) reaction of JENDL-3.3 [5] and ENDF/B-VI [4] with present calculation. Neutron spectra ENDF/B-VI [4] are evaporative, in JENDL-3.3 spectra were calculated with FKK model by Kawano et al. [102]. At E_n =20 and E_n =14 MeV hard energy tails of 'pre-equilibrium' component of first neutron spectrum of JENDL-3.3 [5] and present evaluation are rather similar, for lower energies E_n =10 and E_n = 8 MeV the former estimate is much softer. Average energies of first neutron spectra for ENDF/B-VI [4] are much lower than that of present evaluation.

Table 9

Average energies of secondary neutron spectra for ^{233}U+n

1st neutron average energy $\langle E \rangle$, MeV						(n,2n)	(n,nf)	(n,3n)	(n,2nf)
E_n,			(n,n')						
MeV	Pres.	B-VI	J-3.3	JEF-2	BROND			Present	
6.0	1.261		0.936		1.185	0.090	0.402		
8.0	2.865		1.649		3.534	0.774	1.027		
10.0	4.461		5.896		5.888	1.217	1.471		0.214
14.0	8.451		9.122		9.910	4.032	2.466	0.427	1.310
20.0	14.35	1.924	14.274	2.8	15.905	9.988	3.697	2.662	2.714

Table 9 (continued)

Average energies of secondary neutron spectra for ^{233}U+n

$\langle E \rangle$ for (n,2n), MeV					
E_n,MeV	Present	J-3.3	B-VI	JEF-2	BROND
8.0	0.674	0.712		0.403	0.706
10.0	0.989	0.928	0.866	0.548	0.954
14.0	2.552	1.245		0.678	1.764
20.0	5.489	2.934	1.508	0.900	5.344

Table 9 (continued)

Average energies of secondary neutron spectra for ^{233}U+n

$\langle E \rangle$ for (n,3n), MeV				
Present	J-3.2	B-VI	JEF-2	BROND
0.323	0.336	0.288	0.292	0.278
1.561	1.134	1.040	1.040	1.328

Figures 100, 101, 102 and 103 show the comparison of (n,2n) reaction spectra of JENDL-3.3 [5], ENDF/B-VI [4] and present evaluation at E_n =20, 14, 10 and 8 MeV. Again, at E_n =20 MeV present and JENDL-3.3 [5] spectra are rather similar, while at $E_n = 14$ MeV hard energy tail in our calculation is much more pronounced. The discrepancies above $\sim$5 MeV and $\sim$3 MeV, $\sim$1 MeV and $\sim$0.5 MeV respectively, are due to the first neutron spectra of (n,2n) reaction in present calculation being of hard pre-equilibrium nature. Figure 103 shows the comparison of (n,2n) reaction spectra at E_n =8 MeV. Figures 104 and 105 show spectra of (n,3n) reaction for E_n =14 MeV and E_n =20 MeV, respectively.

In summary, inclusion of pre-equilibrium emission changes significantly the average energies of emitted neutron spectra. That is shown in Table 9, where the average secondary neutron energies for current, ENDFB-VI and JENDL-3.3 evaluations are compared. The most significant is the change of neutron spectra of (n,nγ) reaction.

9   Conclusions

The statistical Hauser-Feshbach-Moldauer model calculation of neutron-induced reaction cross sections for ^{233}U target nuclide shows the fair description of available data base on fission cross section. Statistical calculations were employed for predicting total, capture, inelastic, (n,2n) and (n,3n) reaction cross sections. Rigid rotator coupled channel model was used to predict inelastic scattering cross sections for level excitation. Prompt fission neutron spectra are predicted with the model, tested on the PFNS description of ^{238}U(n,f) and ^{232}Th(n,f) reactions.

10   Acknowledgments

References

[1] Maslov V.M., Porodzinskij Yu. V., Baba M., Hasegawa A., Kornilov N.V., Kagalenko A.B., Proc. International Conference on Nuclear Data for Science and Technology, October 7-12, 2001, Tsukuba, Japan, p. 148, 2002.

[2] Maslov V.M. , Yu. V. Porodzinskij, M. Baba, A. Hasegawa, Ann. Nucl. Energy, 29, 1707 (2002).

[3] Maslov V.M., Porodzinskij Yu. V., Baba M., Hasegawa A., Nucl. Sci. Eng. 143, 188 (2003).

[4] Roussin R.W., Young P.G., McKnight R., Proc. Int. Conf. Nuclear Data for Science and Technology, Gatlinburg, USA, May 9-13, 1994, p. 692, J.K. Dickens (Ed.), ANS, 1994.

[5] JAERI-Data/Code, 98-006 (Part II), (Eds.) K. Shibata and T. Narita, 1998.

[6] Derrien H., J. Nucl. Sci. and Tech., 31, 379 (1994).

[7] Leal L.C. , et al. ORNL/TM-2000/372 (2001).

[8] Maslov V.M., Porodzinskij Yu.V. JAERI-Research 98-038, Japan, 1998.

[9] Handbook for Calculations of Nuclear Reaction Data: Reference input parameter library,IAEA-TECDOC-1034, p.81, 1998, Vienna.

[10] Ignatjuk A.V., Istekov K.K., Smirenkin G.N. Sov. J. Nucl. Phys. 29, 450 (1979).

[11] Moldauer P.A., Proc.Conf. on Neutron Cross Sections and Technology, Washington, D.C., USA, March 22-24, 1966, p. 613-622, AEC (1966).

[12] Stavinskij V.S., Shaker M.O., Nucl. Phys., 62, 667 (1965).

[13] Maslov V.M., INDC(BLR)-013, IAEA, Vienna,1998.

[14] Stupegia D.C. J. Nucl. Energ., 16, 201 (1962).

[15] Pattenden N.J., Harvey J.A. Nucl. Sci. Eng., 17, 404 (1963).

[16] Guber K. H., Spencer R. R., Leal L. C. et al., Nucl. Sci. Eng. 139, 111 (2001).

[17] Cullen D. PREPRO2000: 2000 ENDF/B Pre-Processing Codes.

[18] NJOY 94.10 Code System for Producing Pointwise and Multigroup Neutron and Photon Cross Sections from ENDF/B Data, RSIC Peripheral Shielding Routine Collection, ORNL, PSR-355, LANL, Los Alamos, New Mexico (1995).

[19] Pfletschinger E., Kaeppeler F., Nucl. Sci. Eng., 40, 375 (1970).

[20] Weston L.W., Gwin R.,.De Saussure G., Fullwood R.R., Hockenbury R.W. Nucl. Sci. Eng., 34, 1 (1968).

[21] Blons J. Nucl. Sci. Eng., 51, 130 (1973).

[22] Gwin R., Silver E.G., Ingle R.W., Weaver H. Nucl.Sci.Eng. 59, 79 (1976).

[23] Zhuravlev K.D., Kroshkin N.I., Karin L.V. 4th All Union Conf. on Neutron Physics, Kiev, USSR, 18 -22 Apr. 1977, 3, 131, (1977).

[24] Zhuravlev K.D., Kroshkin N.I., Karin L.V. Atomnaya Energiya, 42, 56 (1977).

[25] Mughabghab S.F.and Garber D.I., BNL-325, VOL. 1, BRookhaven National Laboratory (1983).

[26] Divadeenam M., Sthen J.R. Nuclear Standarts Reference Data. TECDOC-335, Vienna, 238 (1985).

[27] Mostovaya T.A., Mostovoy V.I., Biryukov S.A. et al. 5th All Union Conf. on Neutron Physics, Kiev, USSR, 15 -19 Sept. 1980, v.3, 30 (1980).

[28] Bergman A.A., Kolosovskiy, Medvedev A.N. et al. 5th All Union Conf. on Neutron Physics, Kiev, USSR, 15 -19 Sept. 1980, v.3, 54 (1980).

[29] Guber K. H., Spencer R. R., Leal L. C. et al., Nucl. Sci. Eng. 135, 141 (2000).

[30] Deruytter A.J., Wagemans C. Nucl. Sci. Eng., 54, (4), 423 (1974).

[31] Wagemans C., Schillebeeckx P., Deruytter A., Barthelemy R. Proc. Int. Conf. on Nuclear Data for Science and Technology, Mito, May 30- June 3, 1988, p. 91 (1988).

[32] Carlson G.W., Behrens J.W. Nucl. Sci. Eng., 66, 205 (1978).

[33] Fursov B.I., Kuprijanov V.M., G.N.Smirenkin., Atomnaya Energiya, 44, (3), 236, (1978).

[34] Hopkins J.C., Diven B.C. Nucl. Sci. Eng., 12, 169 (1962).

[35] Foster D.G. JR, Glasgow D.W. Phys. Rev. Part C, 3, 576 (1971).

[36] Green L., Mitchell J.A. WAPD-TM-1073 (1973).

[37] Poenitz W.P., Whalen J.F., Guenther P., Smith A.B. Nucl. Sci. Eng., 68, 358 (1978).

[38] Poenitz W.P., Whalen J.F., Smith A.B. Nucl. Sci. Eng., 78, 333 (1981).

[39] Poenitz W.P., Whalen J.F. ANL-NDM-80, 1983.

44

[40] Young P.G., Chadwick M., MacFarlane R.E., Talou P., LA-UR-03-1617, 2003.

[41] Haouat G., Lachkar J., Lagrange Ch., Jary J., Sigaud J., Patin Y.. Nucl. Sci. Eng., 81, 491 (1982).

[42] Moldauer P.A., Phys. Rev., C11, 426 (1975).

[43] Ignatjuk A.V., Maslov V.M., Proc. Int. Symp. Nuclear Data Evaluation Methodology, Brookhaven,USA, October 12-16, 1992, p.440, World Scientific, 1993.

[44] Maslov V.M., Kikuchi Y., JAERI-Research 96-030, 1996.

[45] Tepel J.W., Hoffman H.M., Weidenmuller H.A. Phys. Lett. 49, 1 (1974).

[46] Howard W.M., Möller P. Atomic Data and Nuclear Data Tables, 25, 219 (1980).

[47] Ignatyuk A.V. and Maslov V.M., Sov. J. Nucl. Phys., 54, 392 (1991).

[48] Maslov V.M., Zeit. Phys. A, Hadrons & Nuclei, 347, 211 (1994).

[49] Fu C. Nucl. Sci. Engng. 86, 344 (1984).

[50] Maslov V.M., Porodzinskij Yu.V., Hasegawa A., Shibata K. JAERI-Research 98-040, Japan, 1998.

[51] Lederer D.G. and Shirley V.S.,Table of Isotopes, 7th edition, (1978).

[52] Myers W.O., Swiatecky W.J., Ark. Fyzik, 36, 243 (1967).

[53] Bjornholm S., Lynn J.E. Rev. Mod. Phys., 52, 725 (1980).

[54] V.M. Maslov and Kikuchi Ya., Nucl. Sci. Eng. 124, 492 (1996).

[55] V.M. Maslov, Yu. V. Porodzinskij, M. Baba, A. Hasegawa,A. B. Kagalenko, N.V. Kornilov , N.A. Tetereva "Neutron Data Evaluation of ^{234}U", 135 pp., INDC(BLR)-17, IAEA, Vienna, 2003.

[56] Y.A. Ellis-Akovali , Nuclear Data Sheets, 40, 567 (1988).

[57] Kalinin V.A., Kovalenko S.S., Kuz'min V.N. et al., VANT (Ser. Yadernye Konstanty), 4, 3 (1987).

[58] Dushin V.N., Fomichev A.V., Kovalenko S.S. et al., Atomnaya Energiya, 55, (4), 218 (1983).

[59] Adamov V.M., Aleksandrov B.M., Alkhazov I.D. et al., Yadernye Konstanty 24(8) (1977).

[60] Zasadny K.R., Agrawal H.M., Mahdavi M., Knoll G.F. Trans. Amer. Nucl. Soc. 47, 425 (1984).

[61] Poenitz W.P., ANL-NDM-36 (1978).

[62] Meadows J.W., Nucl. Sci. Eng., 54, 317 (1974).

[63] Kanda K., Sato O., Yoshida K., Imaruoka H., Hirakawa N. Report JAERI-M-85-035, 220 (1985).

[64] Kanda K., Imaruoka H., Yoshida K. et al. Int. Conf. on Nuclear Data for Basic and Applied Science, Santa Fe, N.M. , 13-17 May 1985, p. 569 (1985).

[65] Shpak D.L.,.Koroljov G.G., 5th All Union Conf. on Neutron Physics, Kiev, USSR, 15 -19 Sept. 1980, 3, 35, (1980).

[66] White P.H., Hodgkinson J.C., Wall G.J. IAEA Conf. on the Physics and Chemistry of Fission, Salzburg, Austria, 22-26 Mar. 1965. Proceeding published by IAEA, Vienna as STI/PUB/101, 1, 219 (1965).

[67] White P.H., Warner G.P. J. Nucl. Energ. 21, 671 (1967).

[68] Smirenkin G.N., Nesterov V.G., Report ICD-4, (1967).

[69] Iyer R.H. Rep. BARC, 79, 55 (1978).

[70] Meadows J.W,. Ann. Nucl. Energ., 15, (8), 421 (1988).

[71] Shcherbakov O.A., Donets A., Evdokimov A., Fomichev A., Fukahori T., Hasegawa A., Laptev A., Maslov V., Petrov G., Soloviev S., Tuboltsev Yu., Vorobyev A., Proc. International Conference on Nuclear Data for Science and Technology, October 7-12, 2001, Tsukuba, Japan, p. 230, 2002.

[72] V.M. Maslov, Yu. V. Porodzinskij, M. Baba, A. Hasegawa, Proc. 11th Intern. Symp. on Capture an Gamma-ray Spectroscopy, September 2-6, 2002, Prague, Czhech Republic.

[73] Maslov V.M., Porodzinskij Yu. V., Baba M., Hasegawa A., Kagalenko A. B., Kornilov N.V., Tetereva N.A., "Neutron Data Evaluation of ^{232}U", INDC(BLR)-15, IAEA, Vienna, 2003.

[74] Uhl M., Strohmaier B., IRK-76/01, IRK, Vienna (1976).

[75] Maslov V.M., Porodzinskij Yu. V., Baba M., Hasegawa A., Kagalenko A. B., Kornilov N.V., Tetereva N.A., "Neutron Data Evaluation of ^{238}U", INDC(BLR)-14, IAEA, Vienna, 2003.

[76] NEANDC-311 "U", INDC(SEC)-101, Nuclear Standard File, Conde H. (Editor), 1992.

[77] J.C.Hopkins, B.C.Diven Nucl. Phys., 48, 433 (1963).

[78] Gwin R., Spencer R.R. and Ingle R.W. Nucl.Sci. Eng., 94, 365 (1986).

[79] Mather D.S., Fieldhouse P. and Moat A. Nucl. Phys., 66,149 (1965).

[80] Boldeman J.W. and Walsh R.L. Journal of Nucl. Energy, 25, 321 (1971).

[81] Nurpeisov B., Nesterov V.G., Prokhorova L.I. and Smirenkin G.N. Journal of Atomic Energy, 34(6), 491 (1973).

[82] Nurpeisov B., Volodin K.E., Nesterov V.G., Prokhorova L.I., Smirenkin G.N. and Turchin Ju.N. Journal of Atomic Energy, 39, 199 (1975).

[83] Colvin D.W. and Sowerby M.G. Harwell report, 1964, data scanned from curve in BNL-325, suppl.2, 1965.

[84] Sergachev A.I., Djachenko N.P., Kovalev A.M., Kuzminov B.D.Yadernaya Fizika, 16, 475 (1972).

[85] Kolosov N.P., Kuzminov B.D., Sergachev A.I., Surin V.M. Journal of Atomic Energy, 32, 83 (1972).

[86] Smirenkin G.N., Bondarenko I.I., Kutsaeva L.S., Mishchenko K.D., Prokhorova L.I. et al. Journal of Atomic Energy, 9, 155 (1959).

[87] Johnstone I. Report AERE-NP/R-1912, 1956.

[88] McMillan D.E., Jones M.E., Sampson J.B. et al., KAPL-1464, 1955.

[89] Hockenbury R.W., COO-3058-44, 4, 1973.

[90] Boldeman J.W., Frehaut J., Nucl. Sci. Eng., 76, 49 (1980).

[91] Maslov V.M., Porodzinskij Yu. V., Baba M., Hasegawa A., Kagalenko A. B., Kornilov N.V., Tetereva N.A., "Neutron Data Evaluation of ^{232}Th", INDC(BLR)-16, IAEA, Vienna, 2003.

[92] Malinovskij V.V. VANT, Nuclear Data, 1987, 2, 25,

[93] Maslov V.M., Porodzinskij Yu. V., Baba M., Hasegawa A., Kagalenko A. B., Kornilov N.V., Tetereva N.A., Proc. X International Seminar on Interaction of Neutrons with Nuclei, Dubna, Russia, May 17-20, 2002, p. 222, 2002.

[94] Kornilov N.V., Kagalenko A.B., Hambsch F.-J. Physics of Atomic Nuclei, 62, 173 (1999).

[95] Madland D.G., Nix J.R. Nucl. Sci. Eng., 81, 213 (1982).

[96] Maslov V.M., Porodzinskij Yu. V., Baba M., Hasegawa A., Kagalenko A. B., Kornilov N.V., Tetereva N.A., European Journal of Physics, A, (2003) (in print).

[97] Lajtai A., Kecskemeti J., Safar J., Dyachenko P.P., Piksaikin V.M., Proc. 6-th Meeting on Nuclear Standard Reference Data, Geel 12-16 Nov. 1984, TECDOC-335, Vienna, IAEA, 1985, p312, J,Yadernie Konstanty,1983, 2,(51), 22, (Iin Russian).

[98] Nefedov V.N., Starostov B.I., Bojkov A.A., Kiev Coference , vol. 2, 285, 1983.

[99] Baba M., Ibaraki M., Miura T., Aoki T.,Hirasawa Y., Nakashima H., Meigo S., Tanaka Su., Proc. International Conference on Nuclear Data for Science and Technology, October 7-12, 2001, Tsukuba,Japan, p. 204, 2002.

[100] Miura T., Baba M., Win T., Ibaraki M., Hirasawa Y., Hiroishi Y., Aoki T. Proc. International Conference on Nuclear Data for Science and Technology, October 7-12, 2001, Tsukuba, Japan, p. 409, 2002.

[101] Kornilov N.V., Kagalenko A.B., Zolotarerv K.I., Proc. VI International Seminar on Interaction of Neutrons with Nuclei, Dubna, Russia, May 17-20, 1998, p. 242, 1998, Dubna.

[102] Kawano T., Ohsawa T., Baba M., Nakagawa T., Phys. Rev., C, 63, 034601 (2001).

11 Figure captions

Fig. 1 Cumulative sum of levels of ^{233}U.
Fig. 2 Cumulative sum of reduced neutron widths of ^{233}U.
Fig. 3 Level spacing distribution of ^{233}U.
Fig. 4 Reduced neutron width distribution of ^{233}U.
Fig. 5 Cumulative distribution of reduced neutron widths of ^{233}U.
Fig. 6 Total cross section of ^{233}U.
Fig. 7 Elastic cross section of ^{233}U.
Fig. 8 Fission cross section of ^{233}U.
Fig. 9 Fission cross section of ^{233}U.
Fig. 10 Capture cross section of ^{233}U.
Fig. 11 Capture cross section of ^{233}U.
Fig. 12 Average reduced neutron width of ^{233}U, $l = 0, J = 2$.
Fig. 13 Average reduced neutron width of ^{233}U, $l = 0, J = 3$.
Fig. 14 Average reduced neutron width of ^{233}U, $l = 1, J = 1$.
Fig. 15 Average reduced neutron width of ^{233}U, $l = 1, J = 2$.
Fig. 16 Average reduced neutron width of ^{233}U, $l = 1, J = 3$.
Fig. 17 Average reduced neutron width of ^{233}U, $l = 1, J = 4$.
Fig. 18 Average fission width of ^{233}U, $l = 0, J = 2$.
Fig. 19 Average fission width of ^{233}U, $l = 0, J = 3$.
Fig. 20 Average fission width of ^{233}U, $l = 1, J = 1$.
Fig. 21 Average fission width of ^{233}U, $l = 1, J = 2$.
Fig. 22 Average fission width of ^{233}U, $l = 1, J = 3$.
Fig. 23 Average fission width of ^{233}U, $l = 1, J = 4$.
Fig. 24 Average neutron resonance spacing of ^{233}U, $l = 0, J = 2$.
Fig. 25 Average neutron resonance spacing of ^{233}U, $l = 0, J = 3$.
Fig. 26 Average neutron resonance spacing of ^{233}U, $l = 1, J = 1$.
Fig. 27 Average neutron resonance spacing of ^{233}U, $l = 1, J = 4$.
Fig. 28 Total cross section of ^{233}U.
Fig. 29 Total cross section of ^{233}U.
Fig. 30 Total cross section of ^{233}U.
Fig. 31 Total cross section of ^{233}U.
Fig. 32 Total cross section of ^{233}U.
Fig. 33 Elastic scattering cross section of ^{233}U.
Fig. 34 Differential elastic scattering cross section at 0.7 MeV.
Fig. 35 Differential elastic scattering cross section at 1.5 MeV.
Fig. 36 Differential scattering cross section to $7/2^+$ level at 0.7 MeV.
Fig. 37 Differential scattering cross section to $7/2^+$ level at 1.5 MeV.
Fig. 38 Differential scattering cross section to $9/2^+$ level at 1.5 MeV.
Fig. 39 Cumulative number of levels of ^{234}U.
Fig. 40 Cumulative number of levels of ^{233}U.
Fig. 41 Level density of ^{234}U.
Fig. 42 Level density of ^{233}U.
Fig. 43 Fission cross section of ^{233}U.
Fig. 44 Fission cross section of ^{233}U.

^{233}U CUMULATIVE SUM OF LEVELS

FIG. 1

^{233}U CUMULATIVE SUM OF REDUCED NEUTRON WIDTHS

LEAL ET AL., 2001
$0.895*10^{-4}*E_n$

SUM OF Γ_n^0

NEUTRON ENERGY, eV
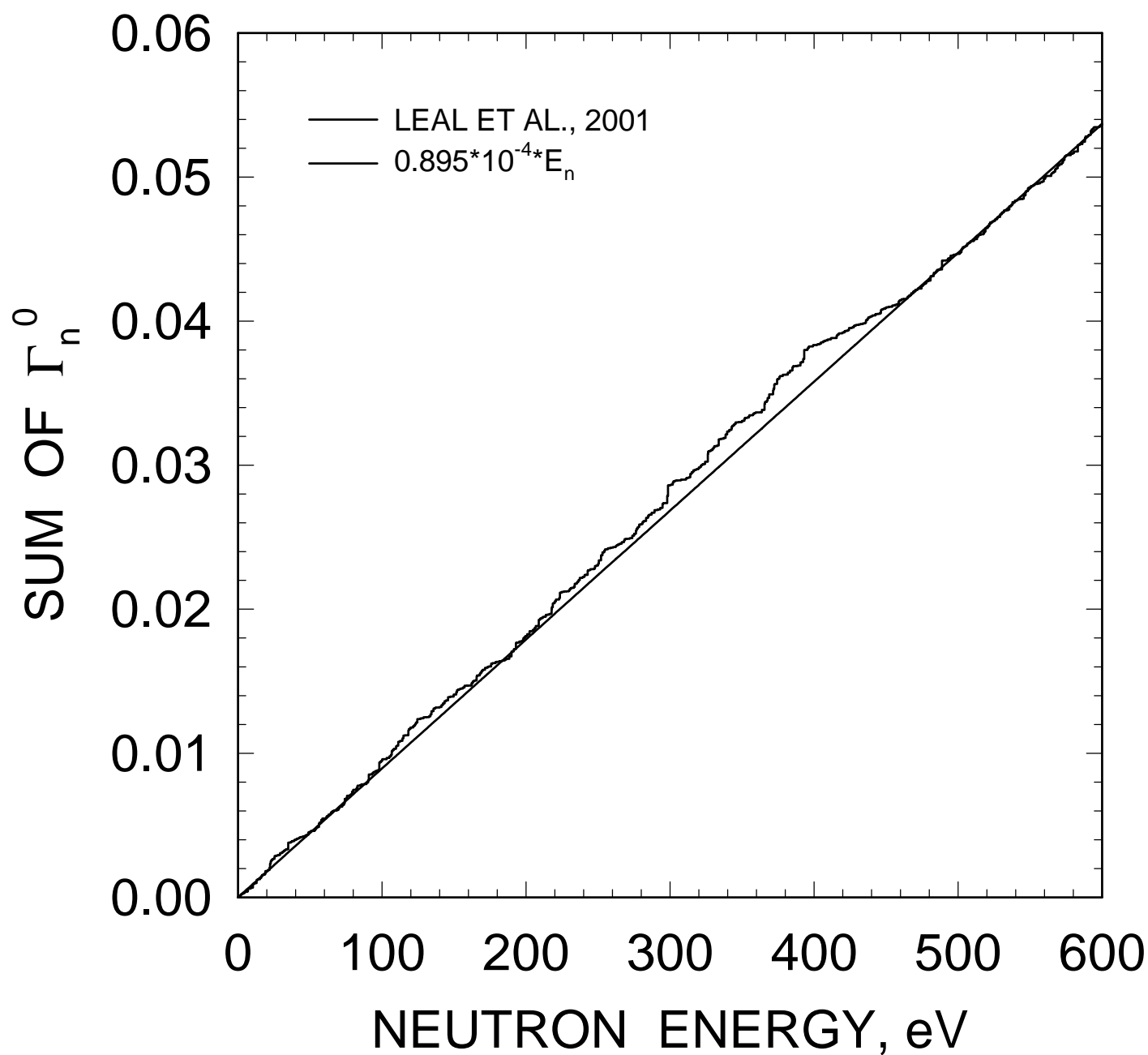
FIG. 2

^{233}U LEVEL SPACING DISTRIBUTION
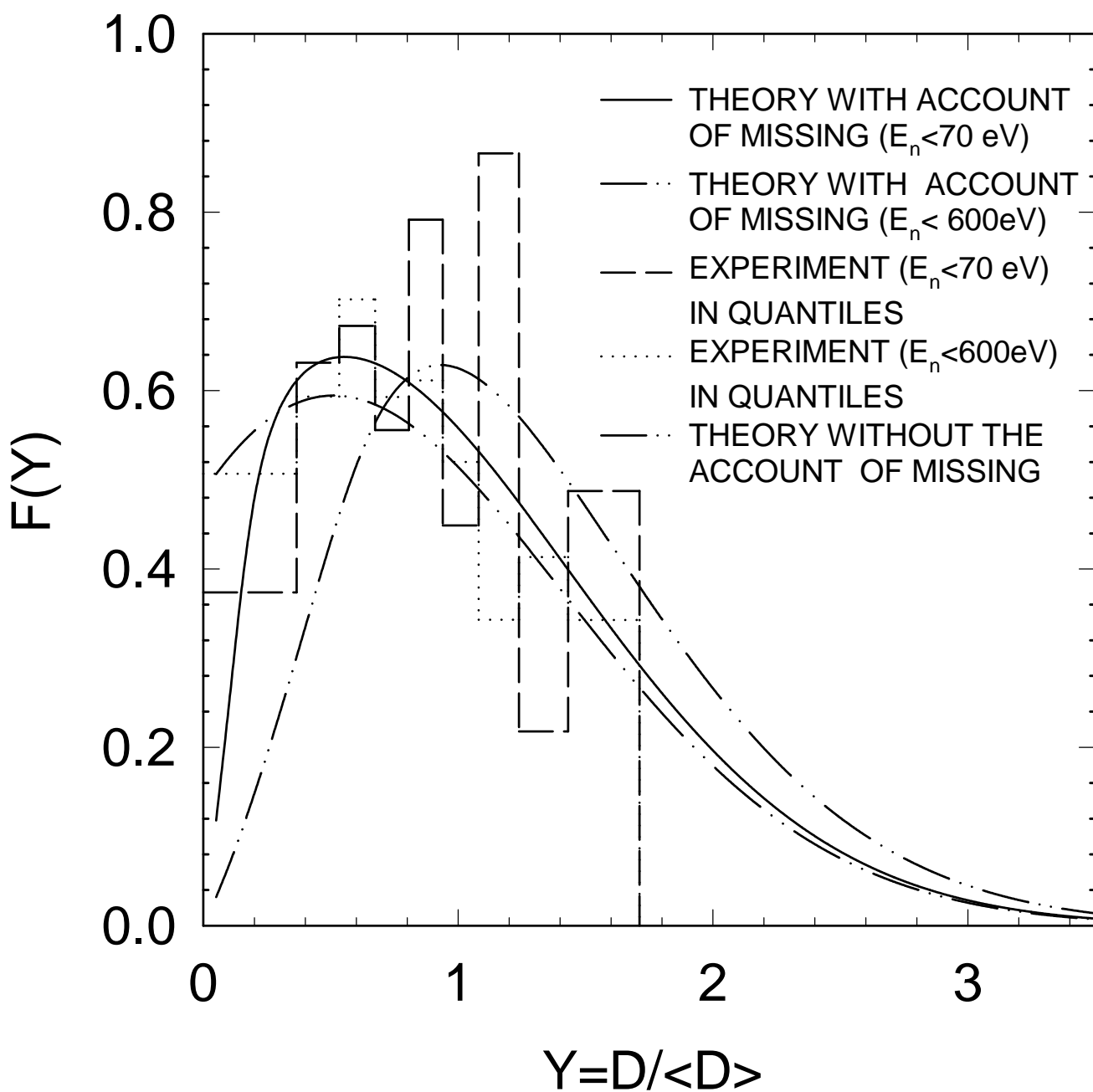
FIG. 3

^{233}U REDUCED NEUTRON WIDTH DISTRIBUTION

THEORY WITH ACCOUNT OF MISSING ($E_n < 70$ eV)

THEORY WITH ACCOUNT OF MISSING ($E_n < 600$ eV)

EXPERIMENT ($E_n < 70$ eV) IN QUANTILES

EXPERIMENT ($E_n < 600$ eV) IN QUANTILES

THEORY WITHOUT ACCOUNT OF MISSING

$X = \Gamma_n^0 / \langle \Gamma_n^0 \rangle$
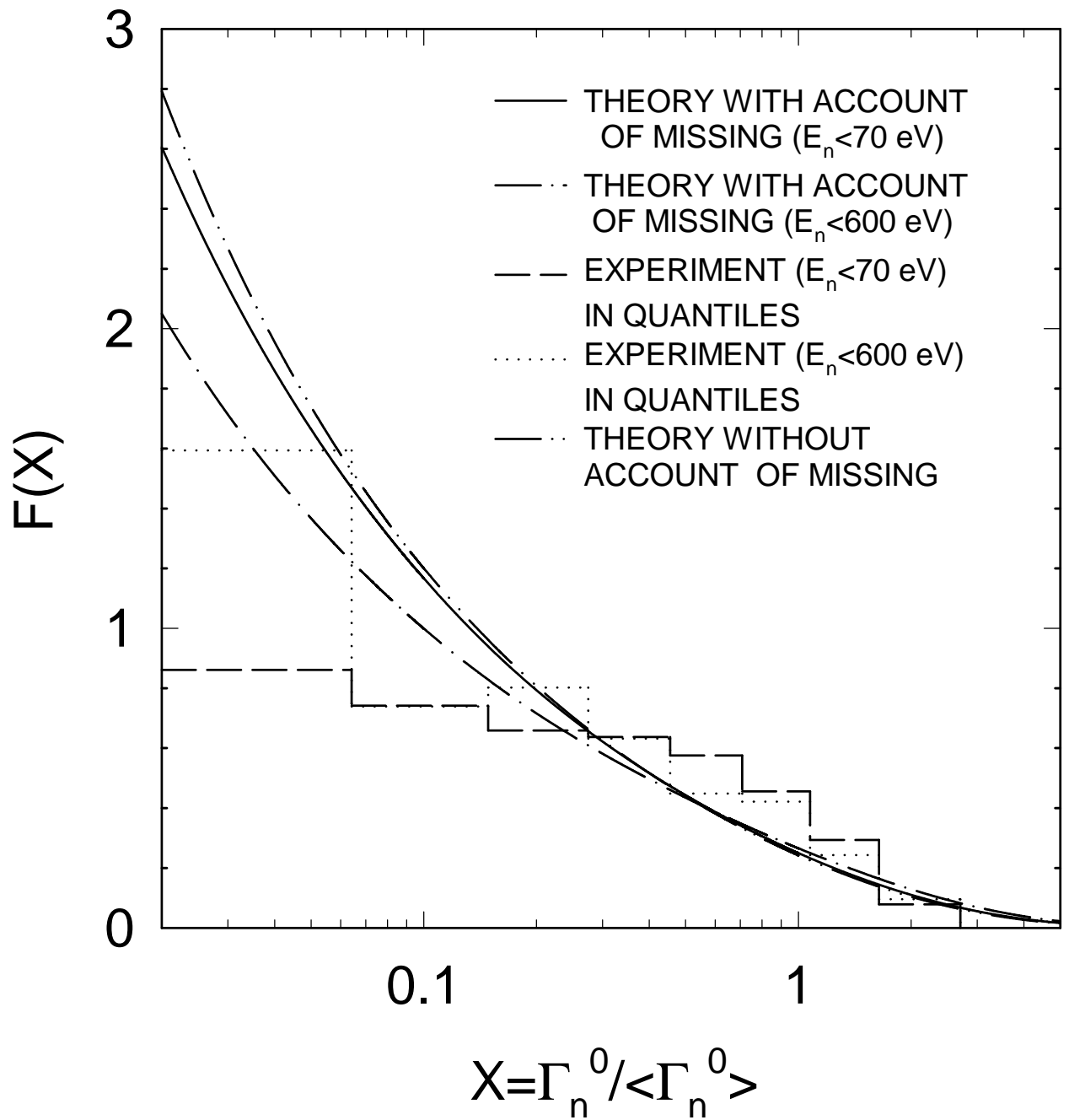
FIG. 4

CUMULATIVE PORTER-THOMAS DISTRIBUTION OF REDUCED NEUTRON WIDTHS
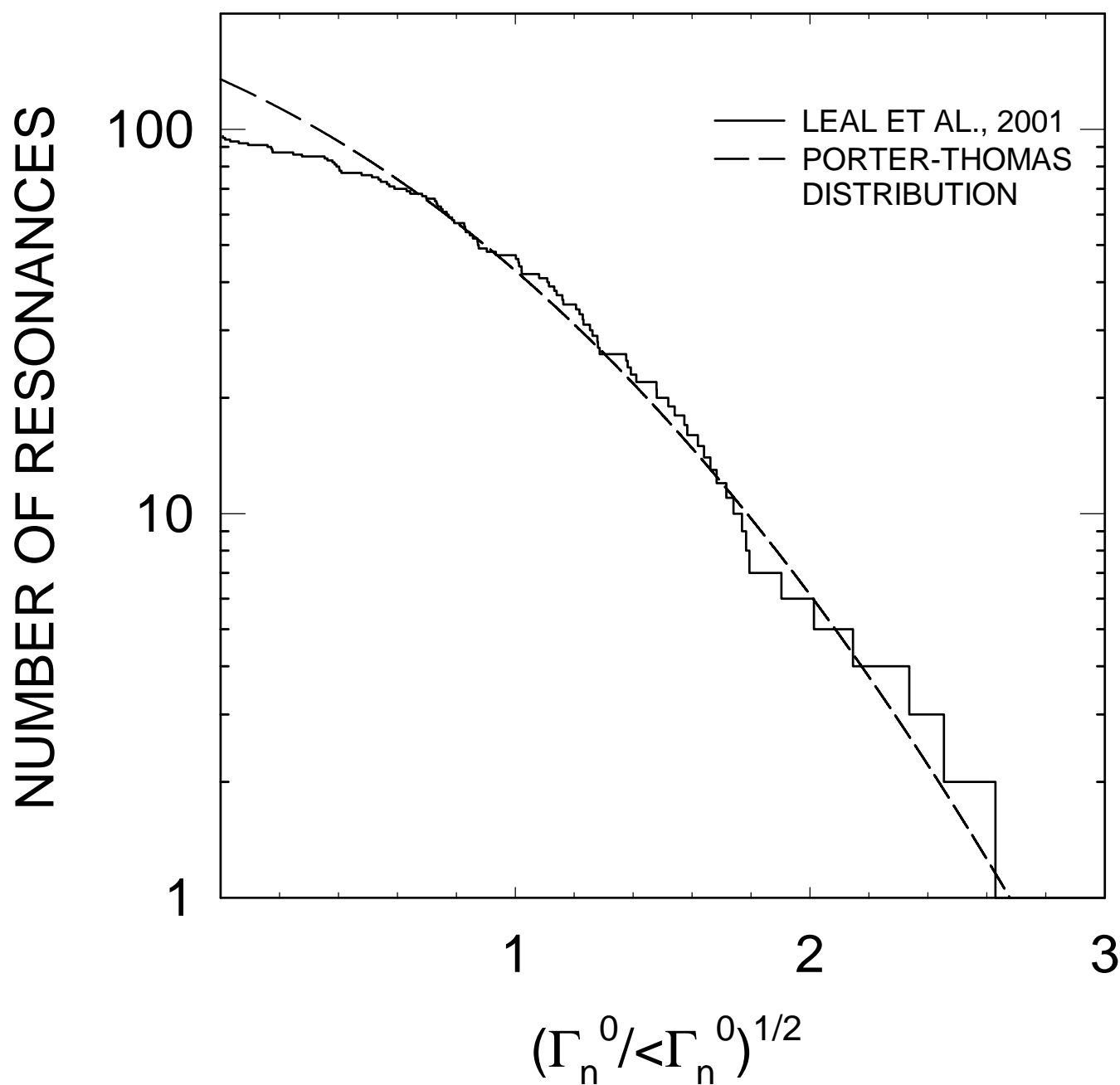
FIG. 5

^{233}U TOTAL CROSS SECTION
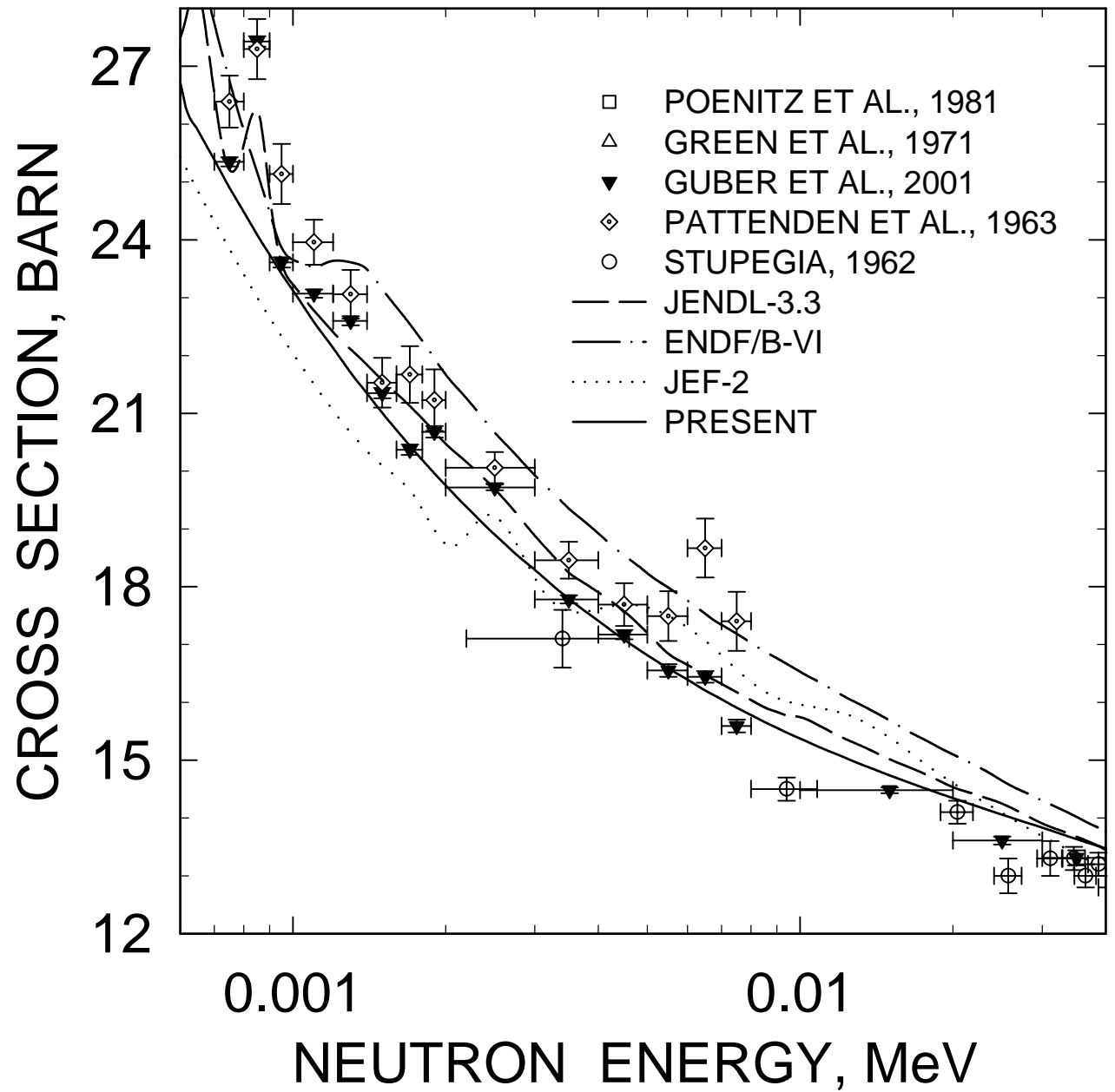
FIG. 6

^{233}U ELASTIC CROSS SECTION
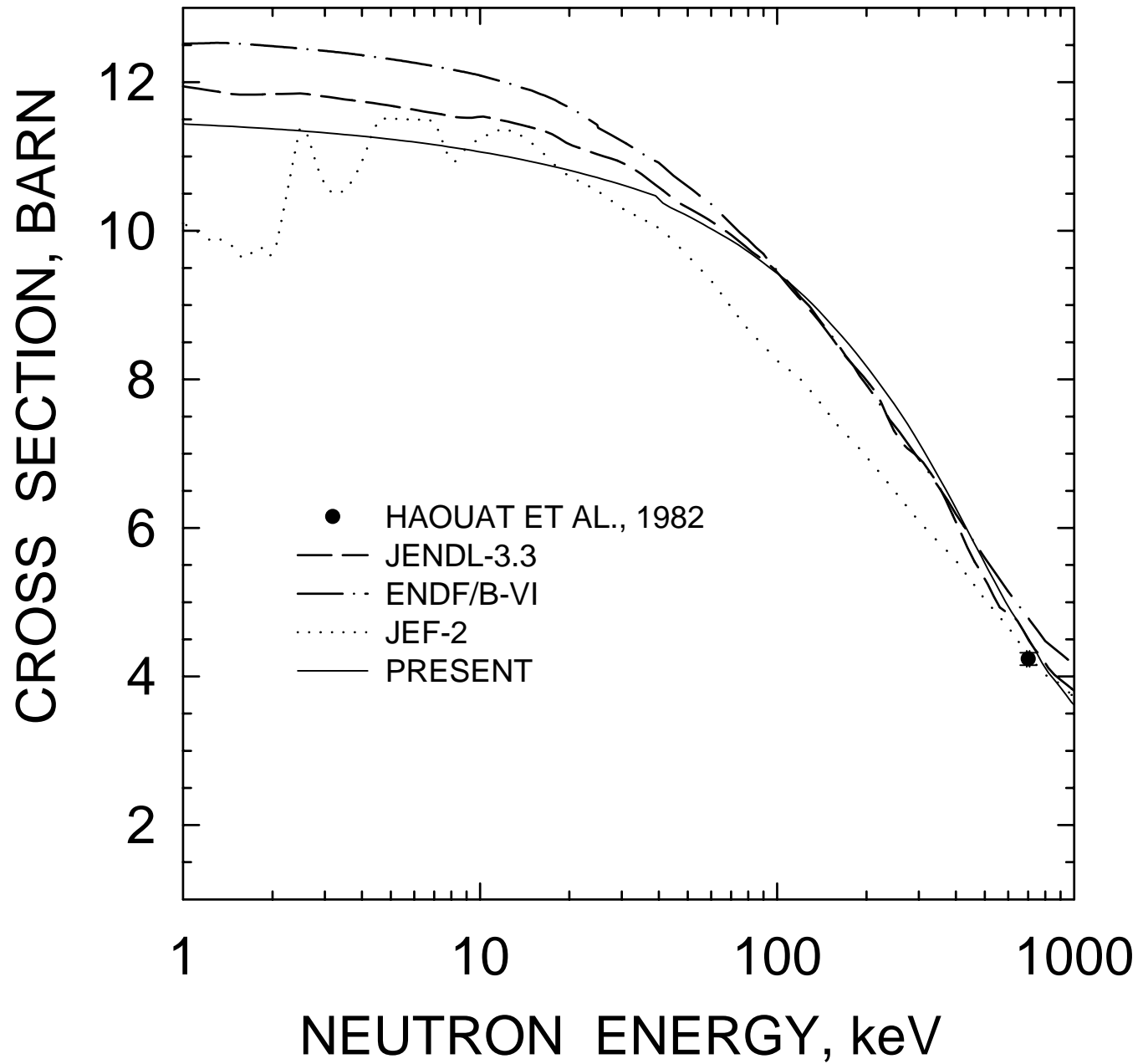
FIG. 7
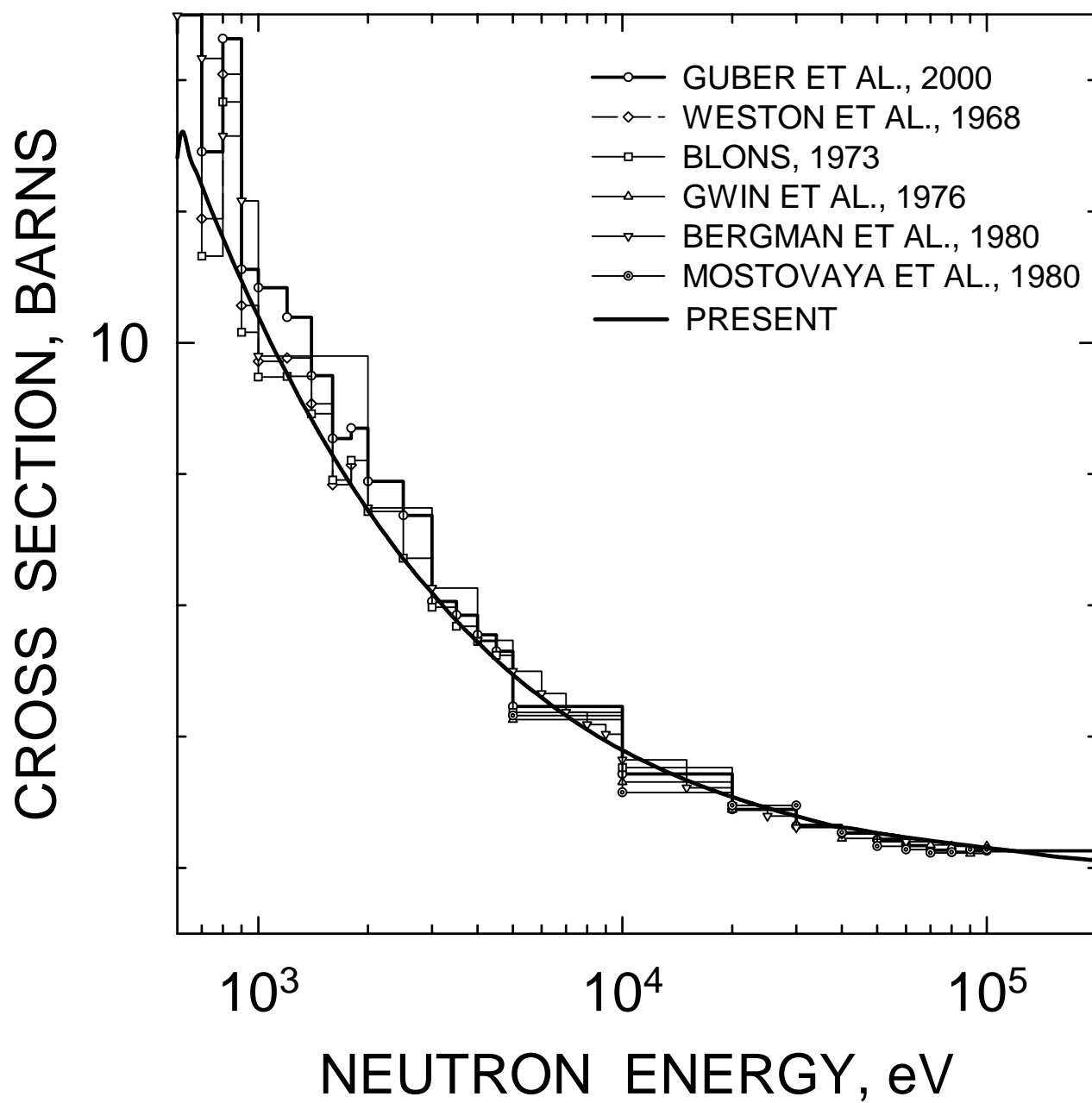
FIG. 8
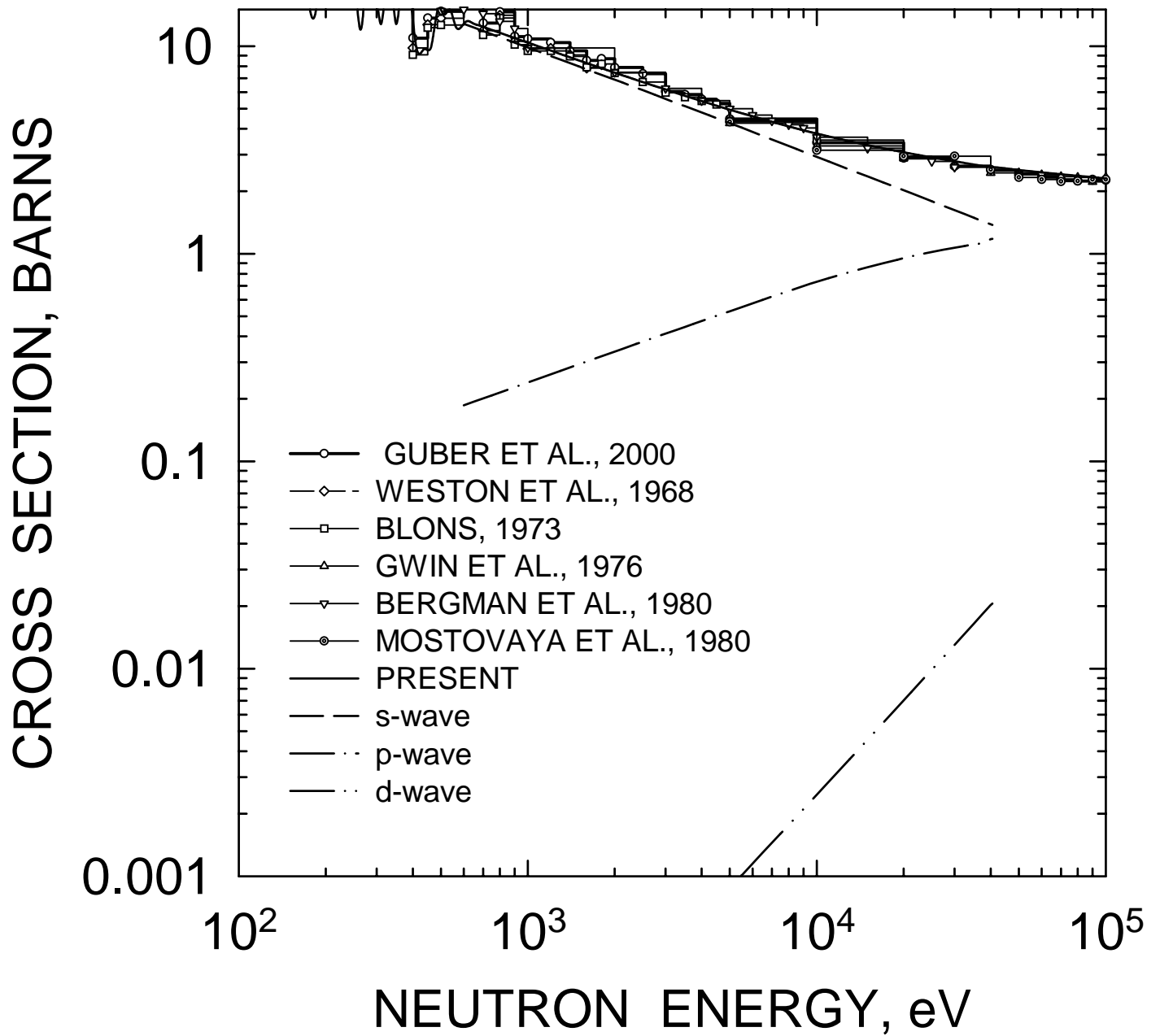
FIG. 9

^{233}U CAPTURE CROSS SECTION

FIG. 10

^{233}U (n,γ) CROSS SECTION

CROSS SECTION, BARN

- ● HOPKINS ET AL., 1962
- ▲ WESTON ET AL., 1968
- —— PRESENT
- – – s-wave
- ⋯⋯ p-wave
- –·– d-wave
- –··– (n,gf)

NEUTRON ENERGY, KeV
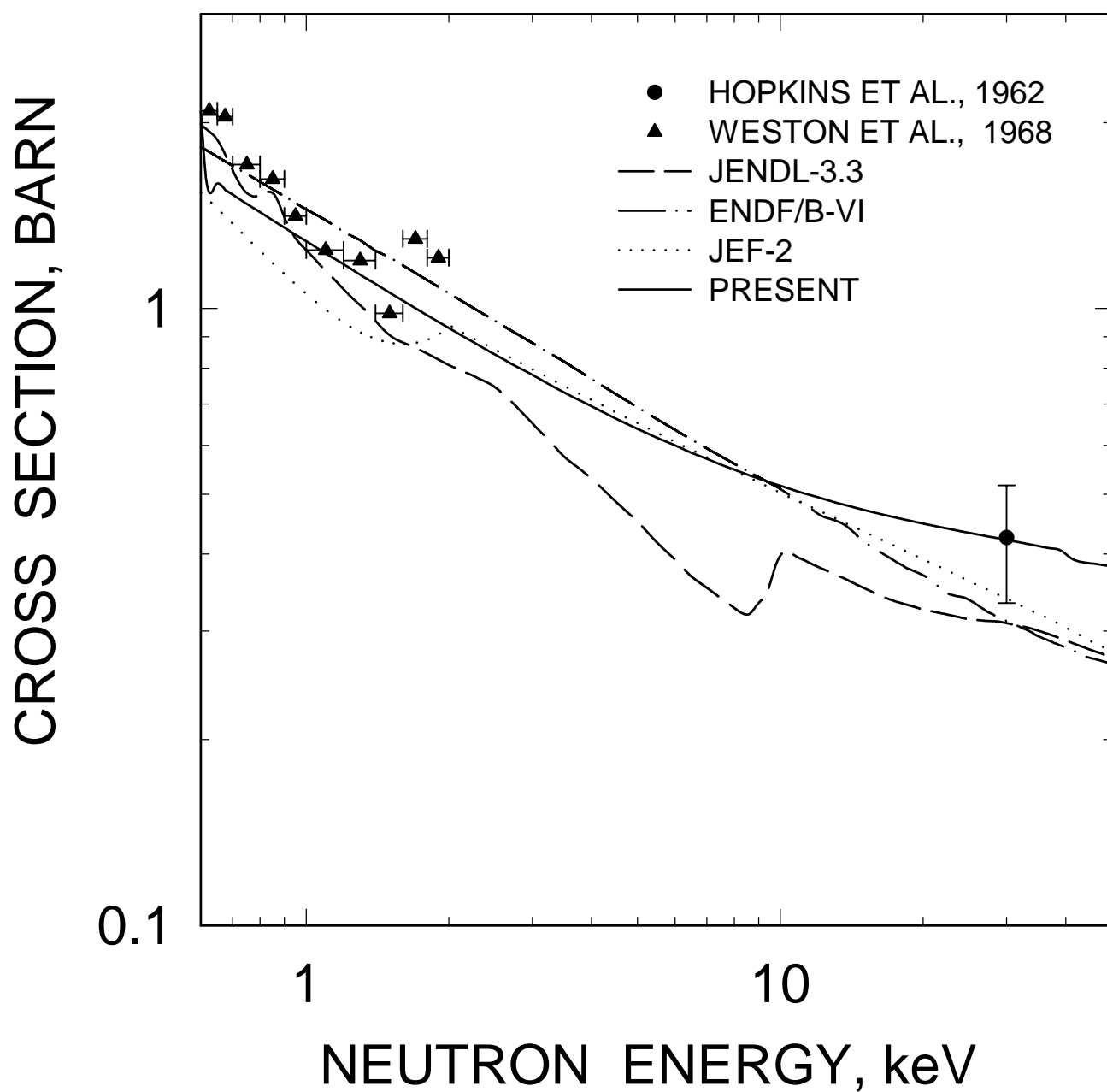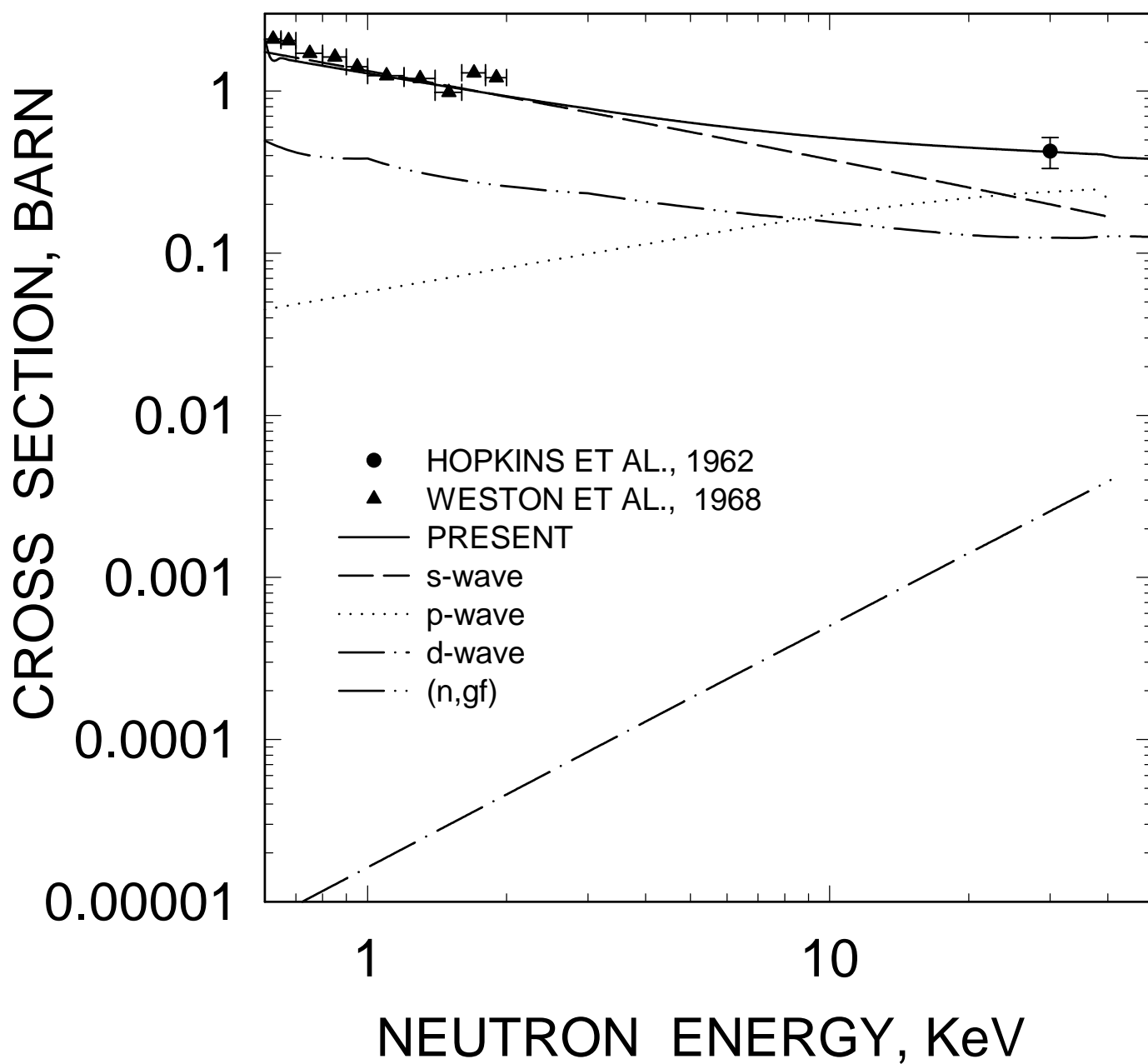
FIG. 11

^{233} U: AVERAGE REDUCED
NEUTRON WIDTH
(L=0, J=2.0)
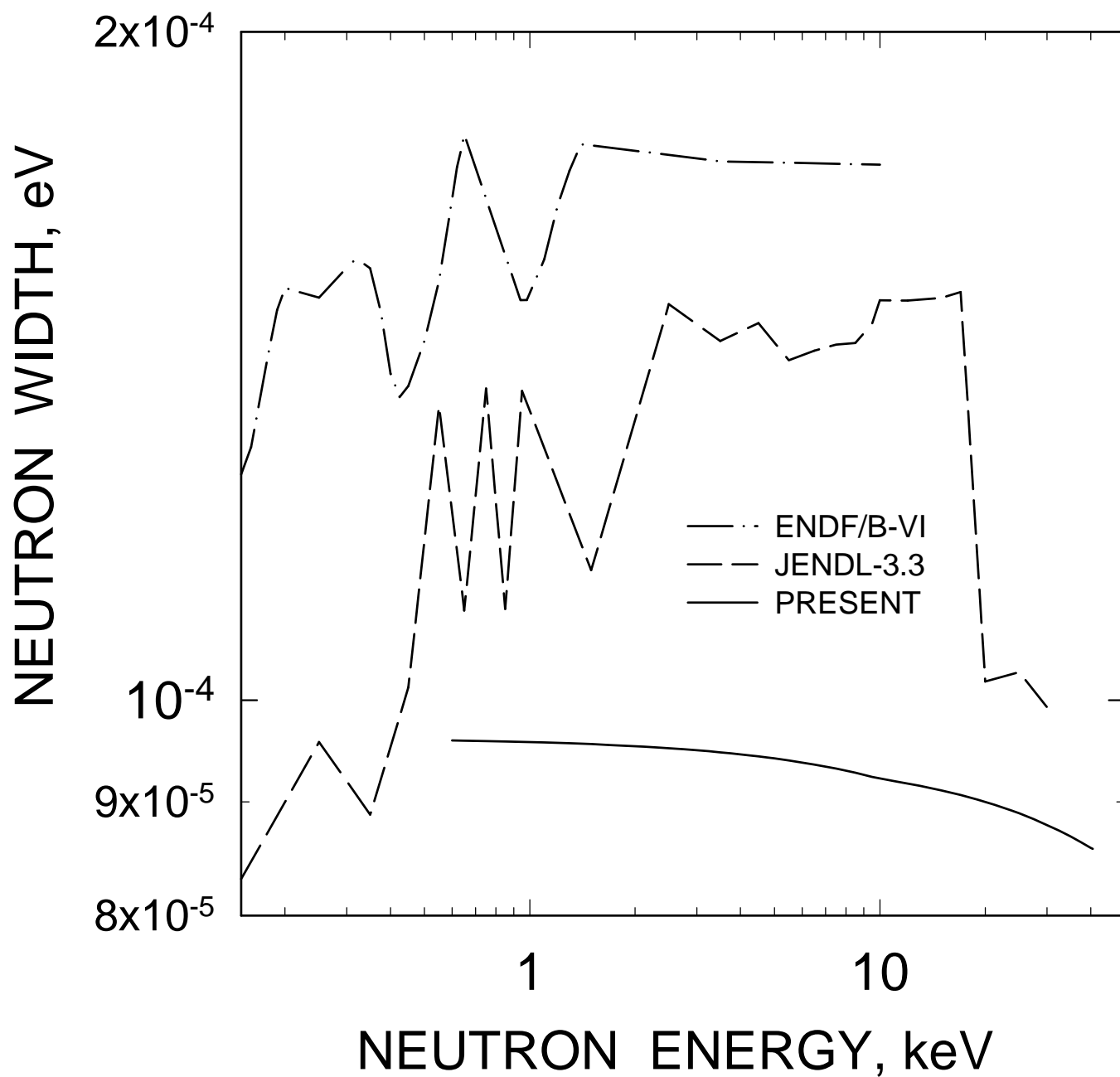
FIG. 12

²³³U: AVERAGE REDUCED
NEUTRON WIDTH
(L=0, J=3.0)
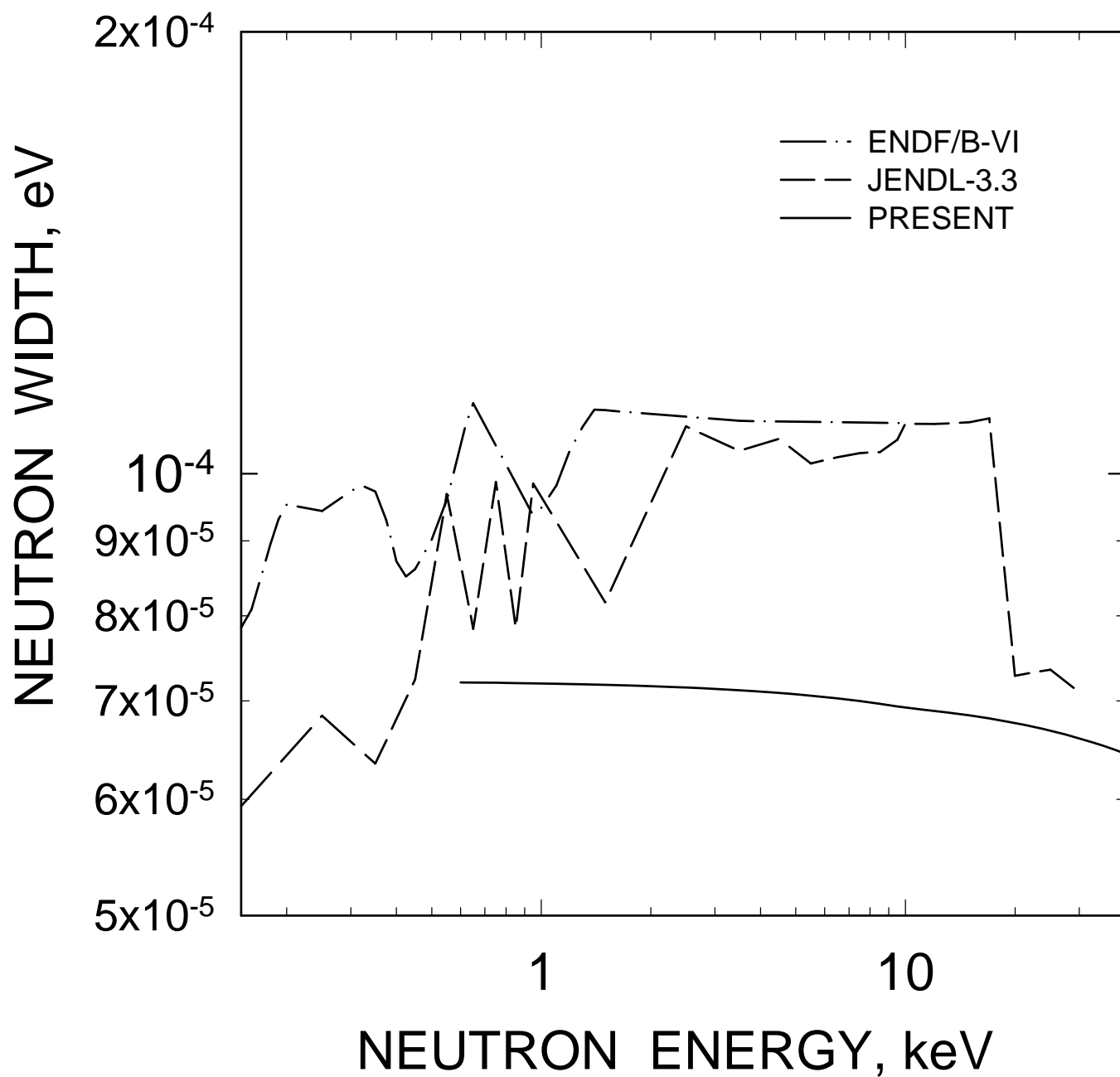
FIG. 13

^{233} U: AVERAGE REDUCED NEUTRON WIDTH (L=1, J=1.0)
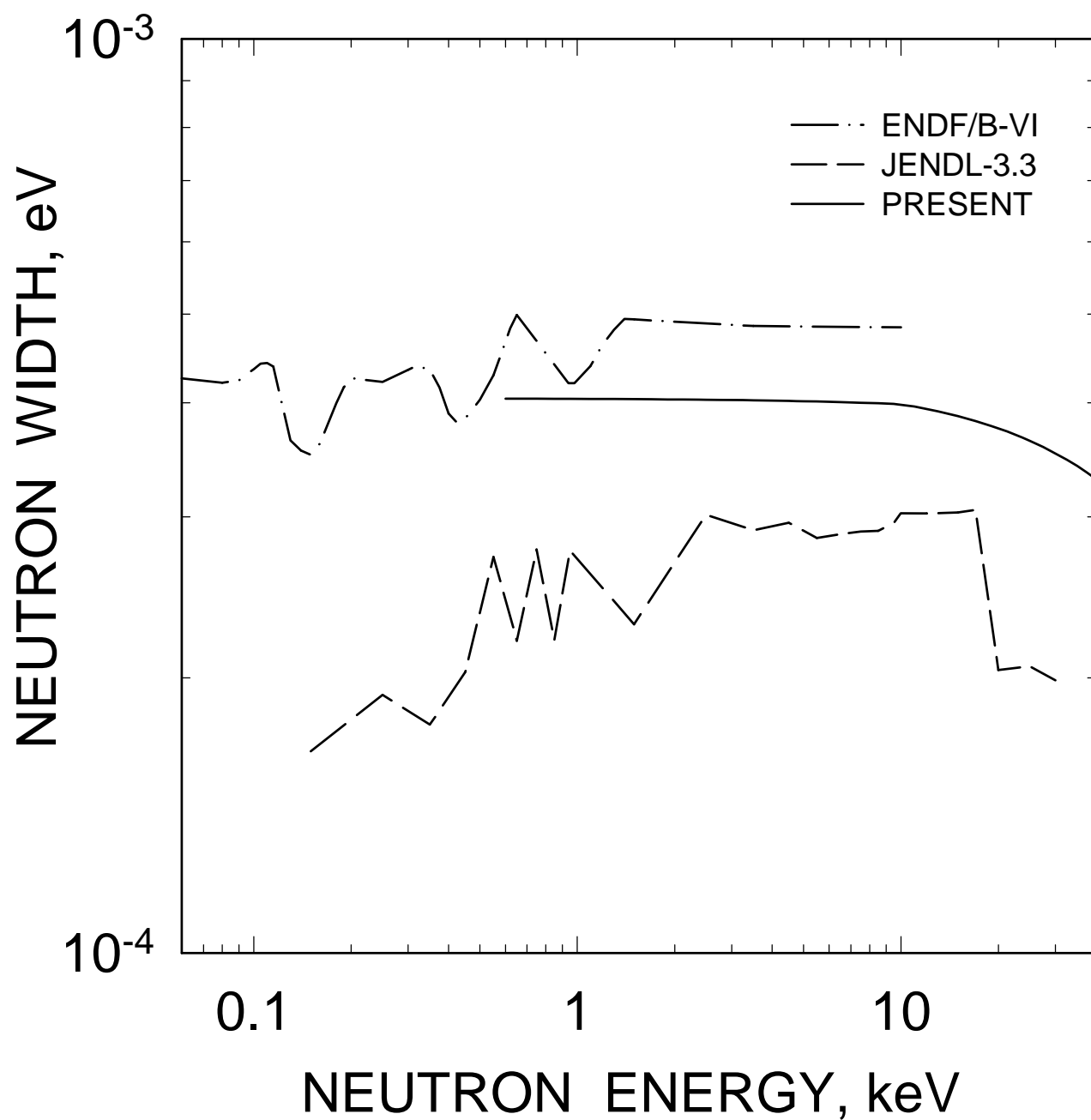
FIG. 14

^{233}U: AVERAGE REDUCED
NEUTRON WIDTH
(L=1, J=2.0)
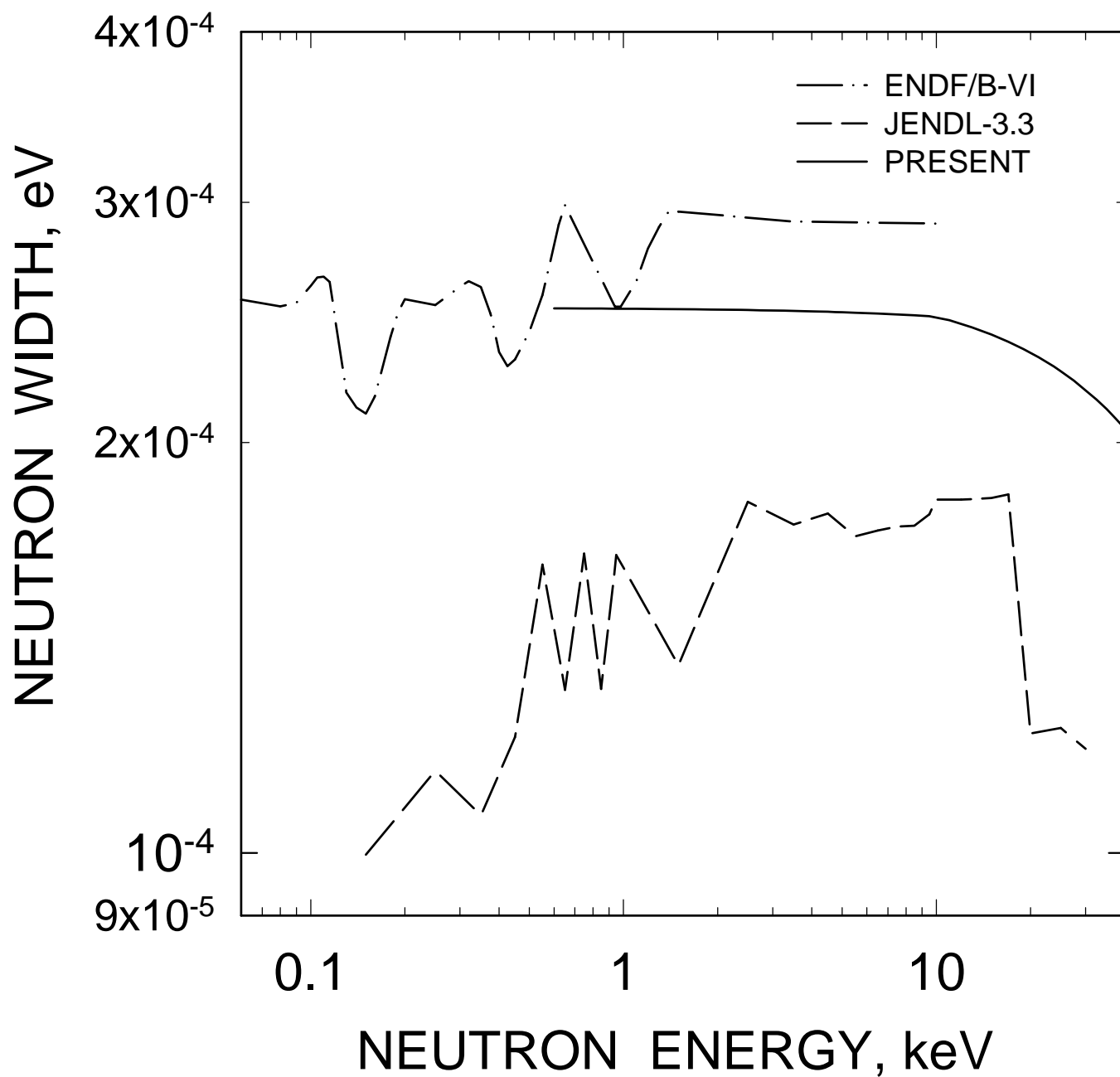
FIG. 15

^{233}U: AVERAGE REDUCED
NEUTRON WIDTH
(L=1, J=3.0)
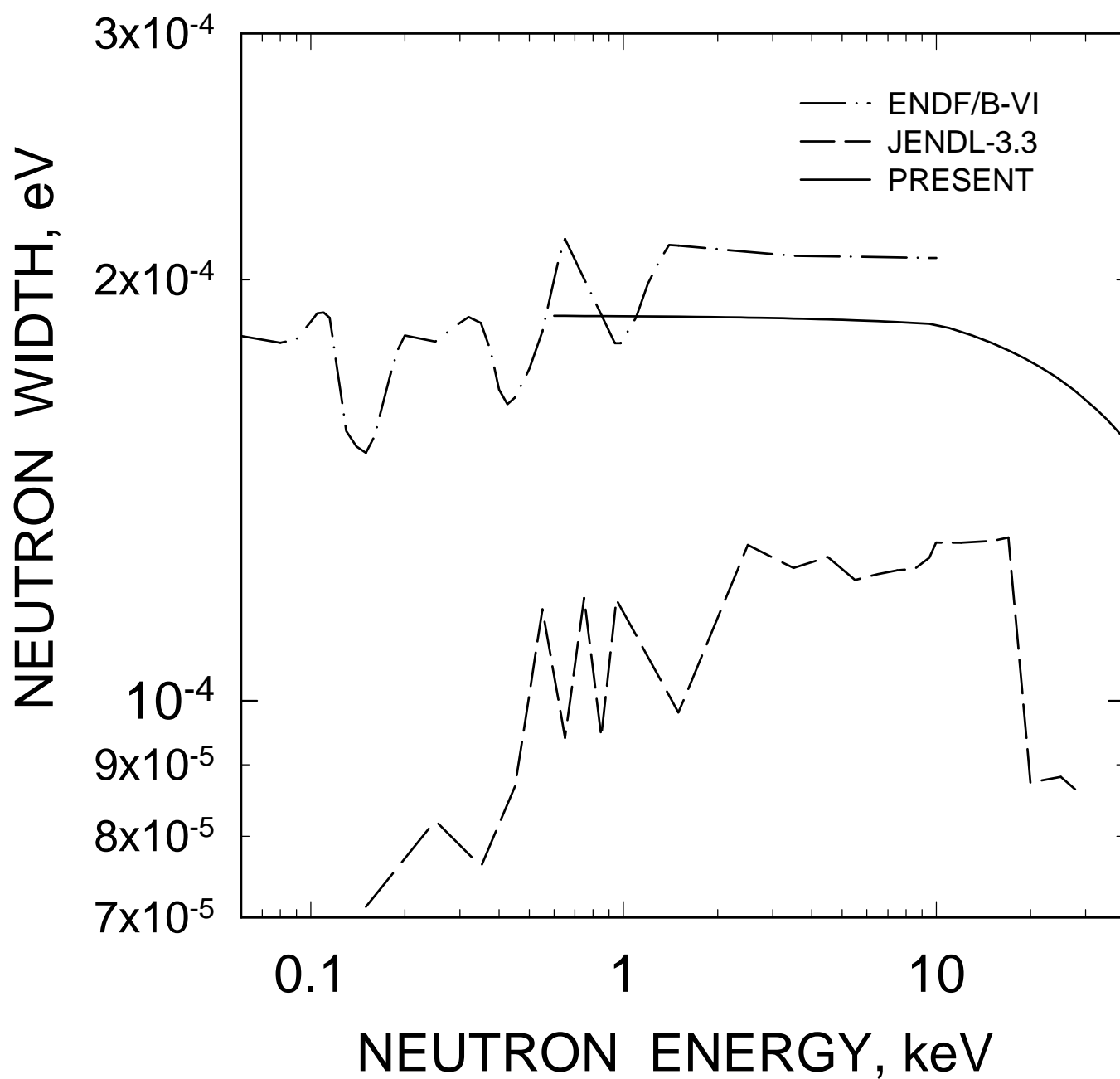
FIG. 16
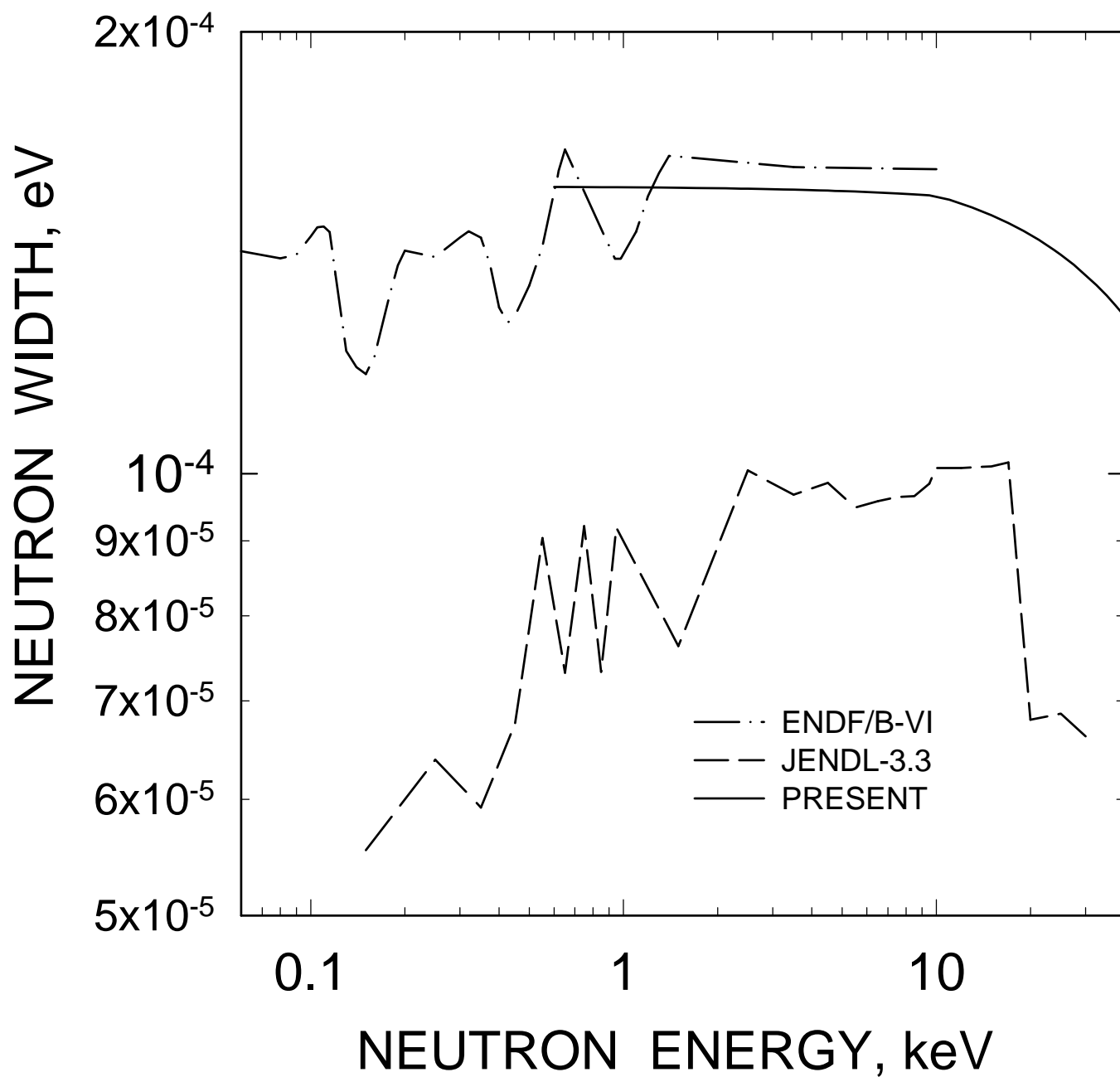
FIG. 17

^{233}U: AVERAGE REDUCED
FISSION WIDTH
(L=0, J=2.0)
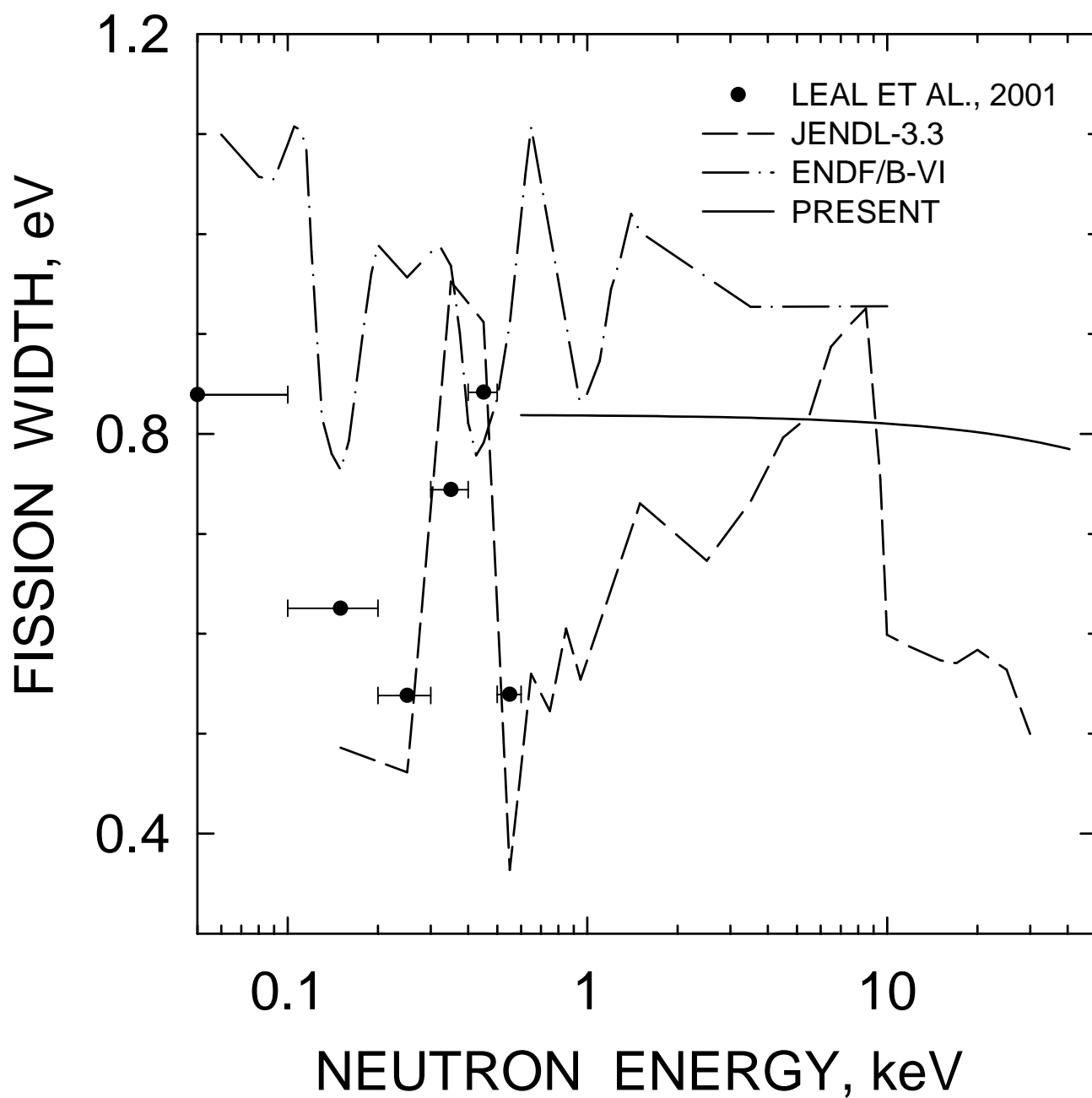
FIG. 18

^{233}U: AVERAGE REDUCED
FISSION WIDTH
(L=0, J=3.0)
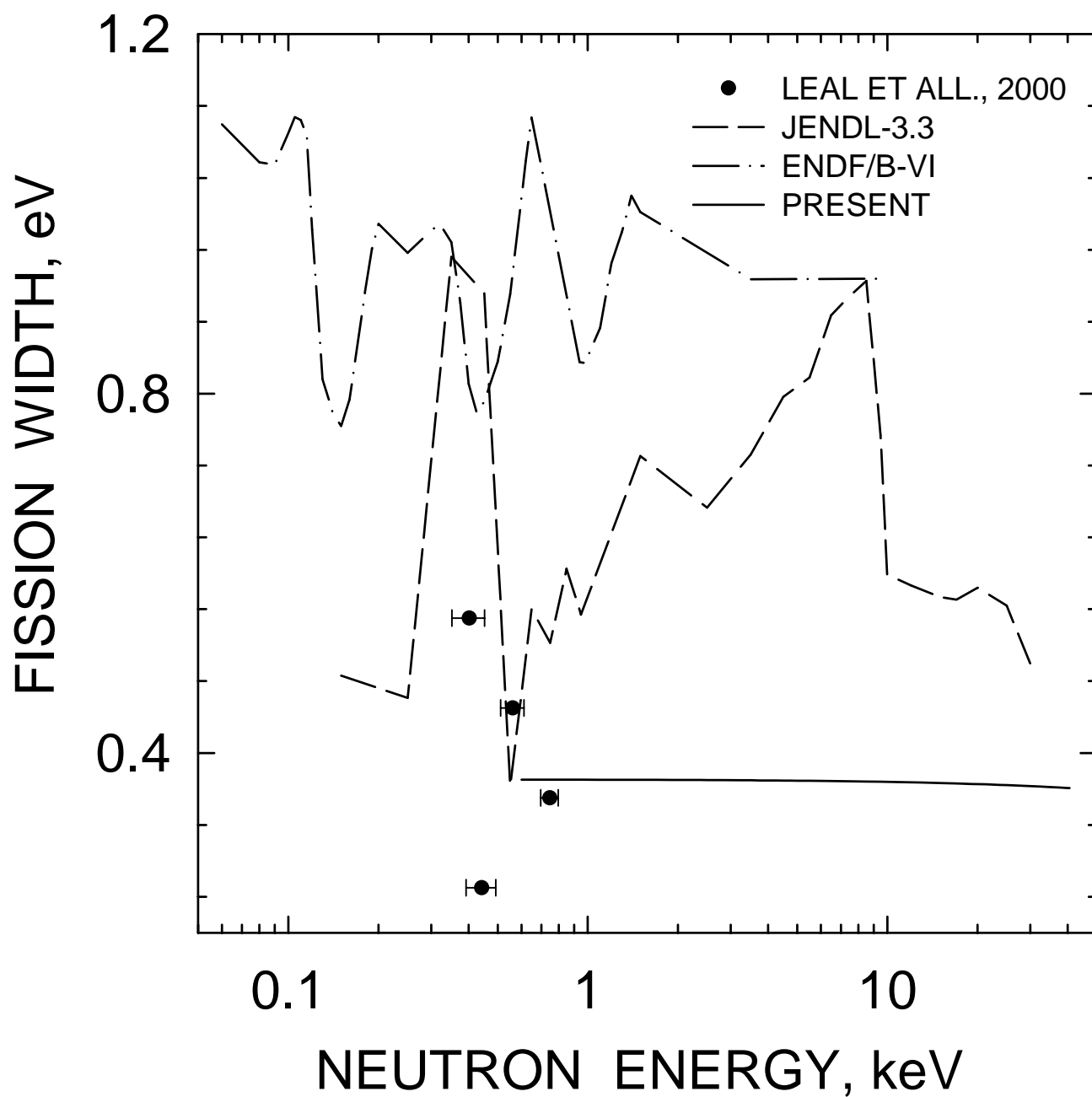
FIG. 19

^{233}U: AVERAGE REDUCED
FISSION WIDTH
(L=1, J=1.0)
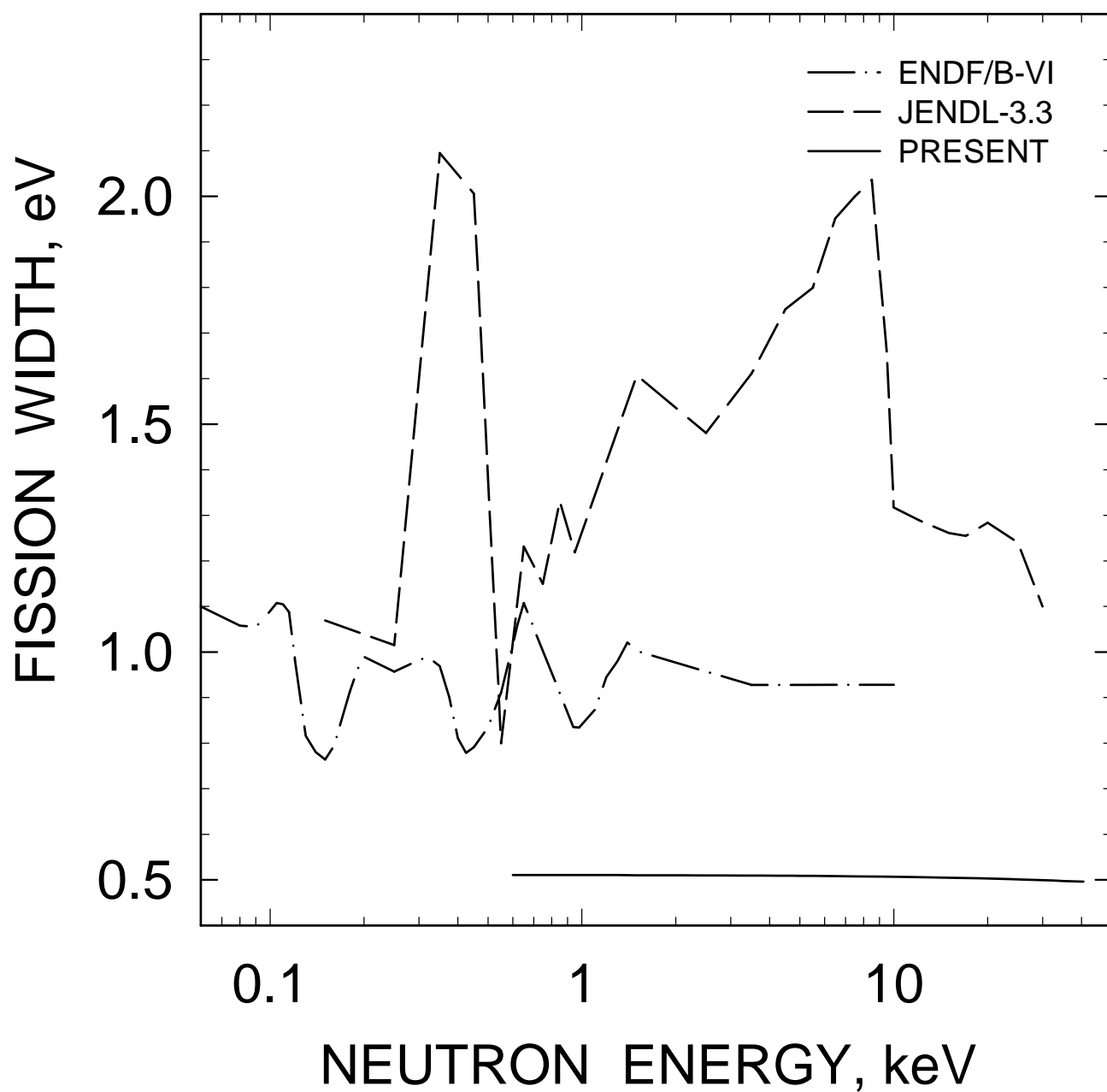
FIG. 20

^{233} U: AVERAGE REDUCED
FISSION WIDTH
(L=1, J=2.0)
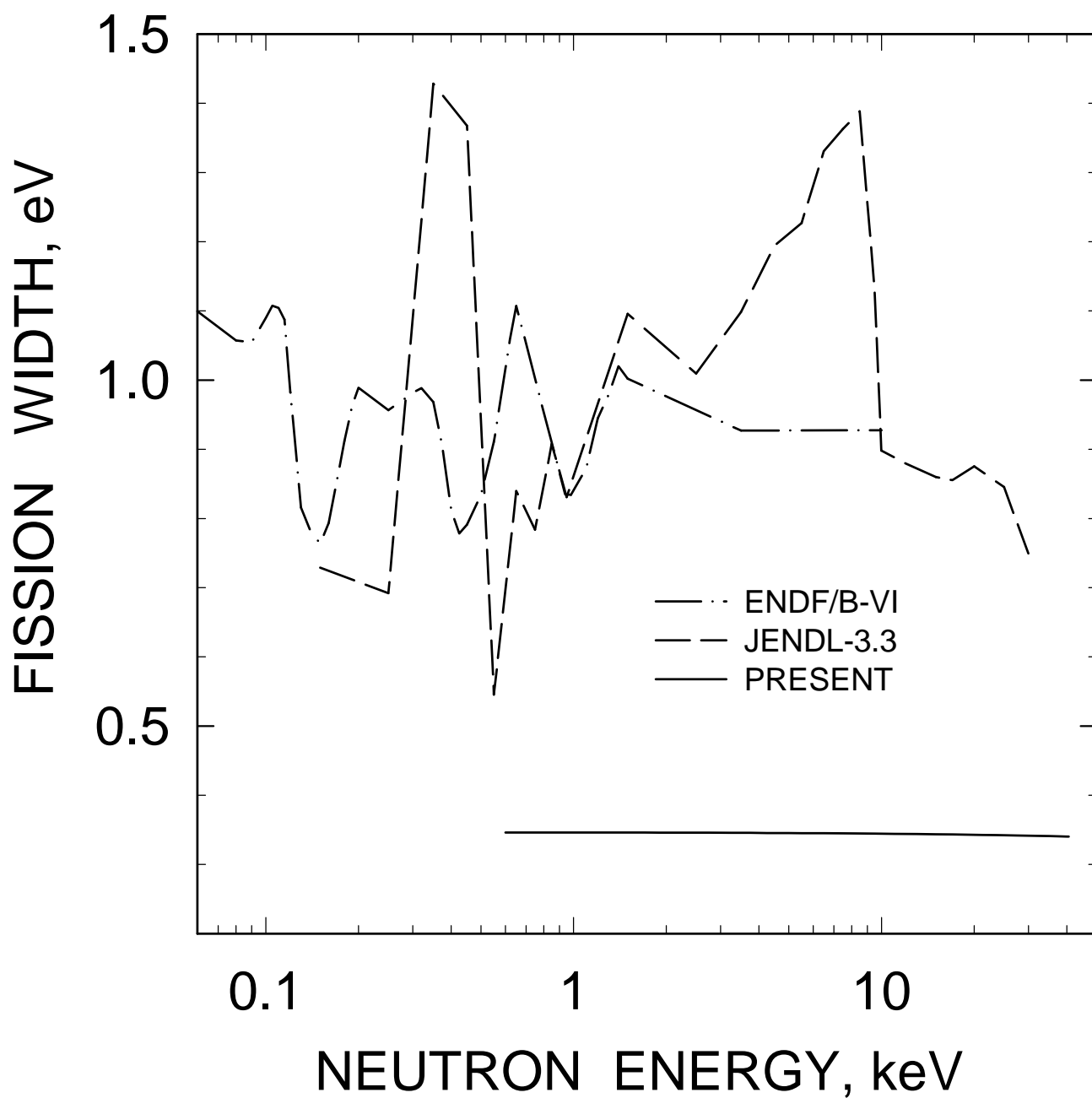
FIG. 21

^{233}U: AVERAGE REDUCED FISSION WIDTH (L=1, J=3.0)
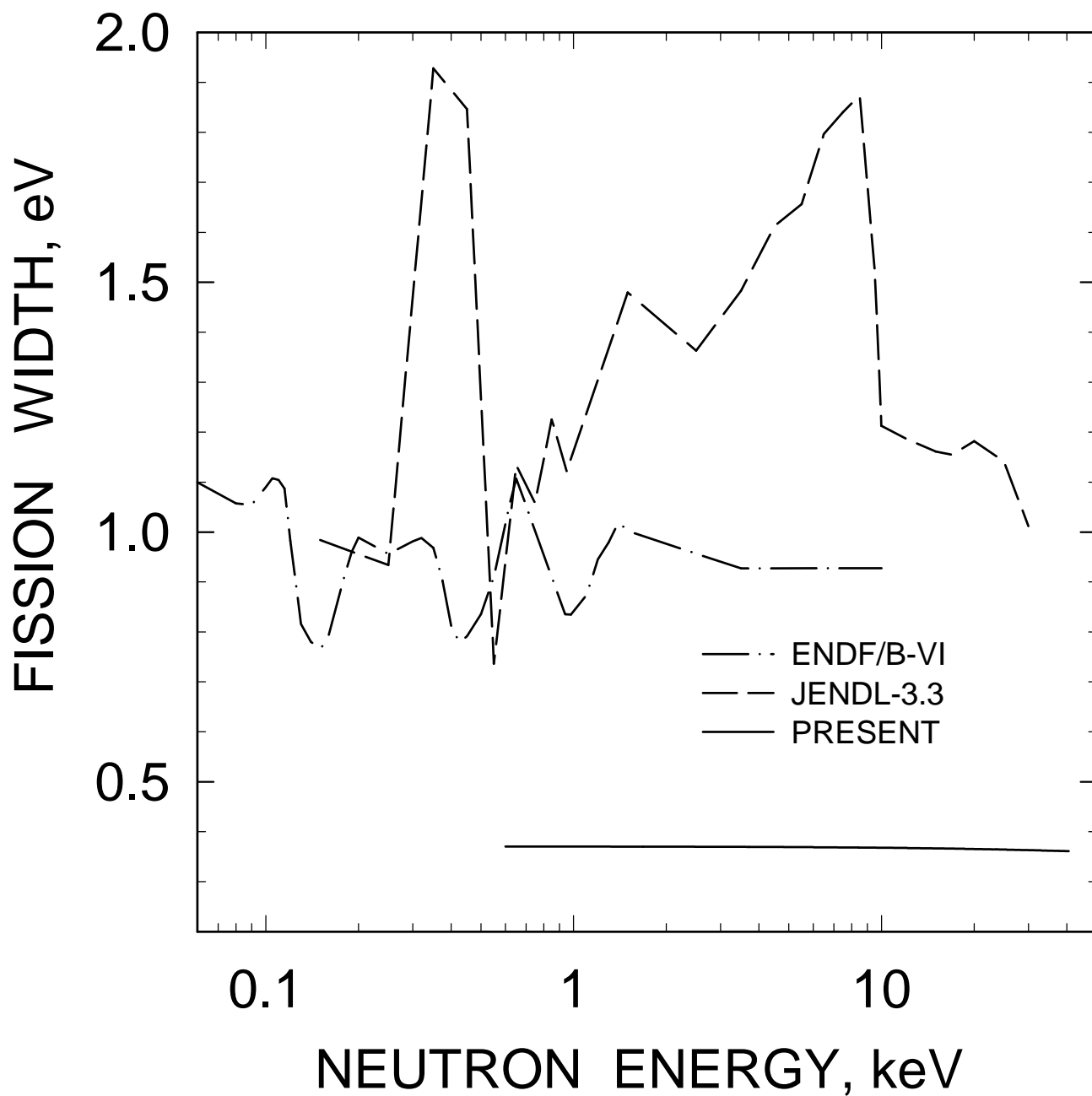
FIG. 22

^{233} U: AVERAGE REDUCED
FISSION WIDTH
(L=1, J=4.0)
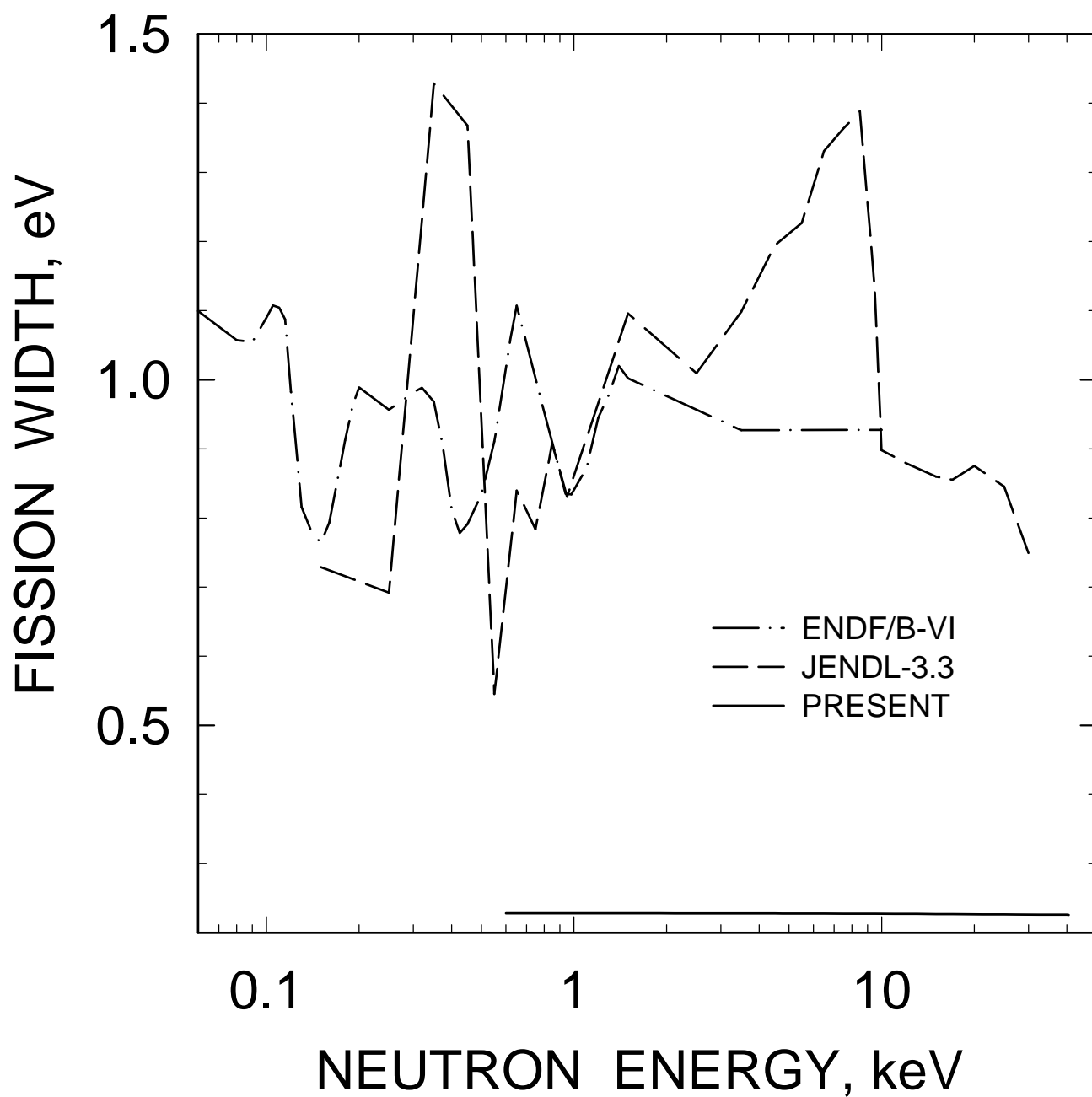
FIG. 23

^{233}U: AVERAGE LEVEL SPACING
(L=0, J=2.0)
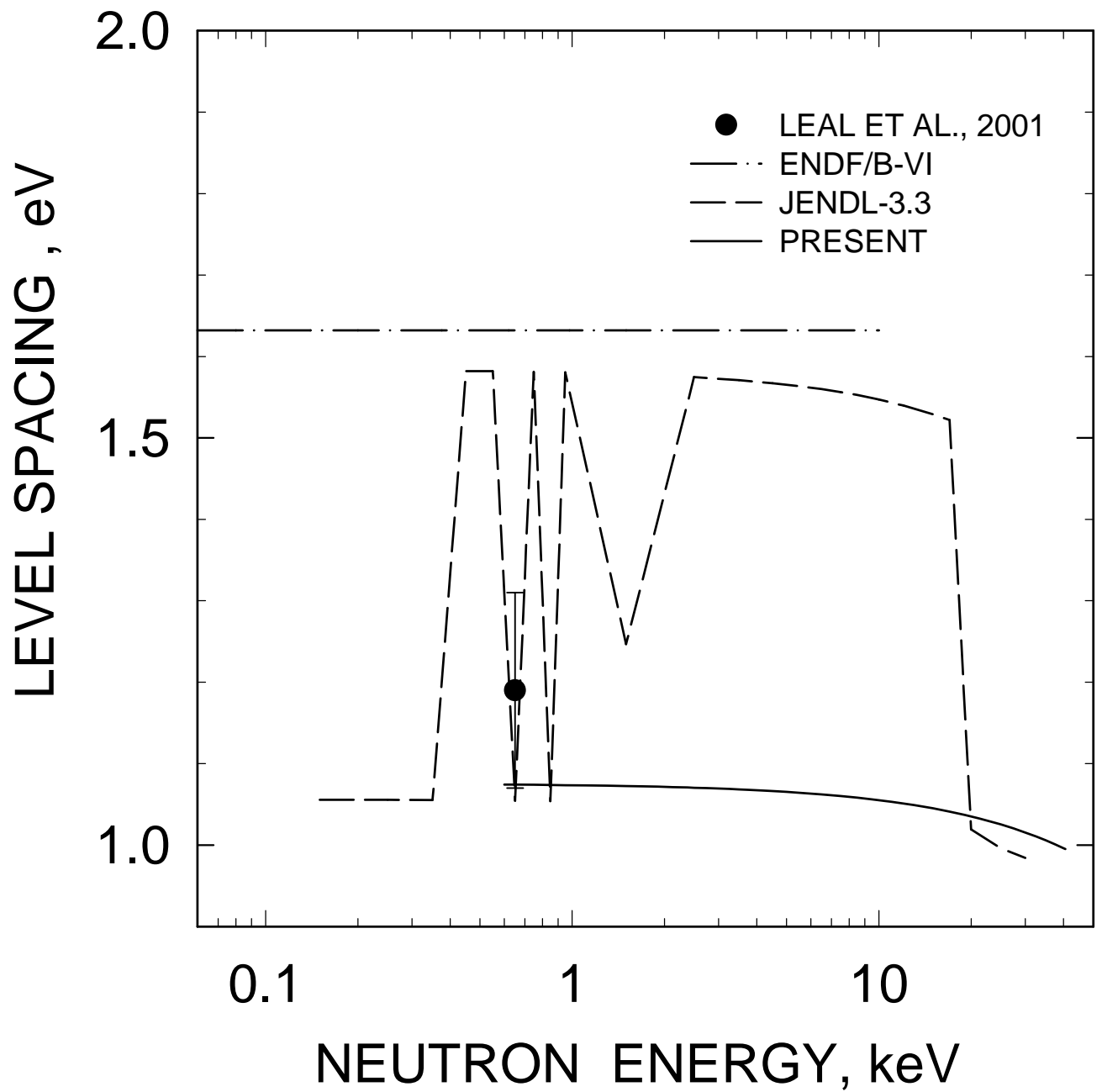
FIG. 24

^{233} U: AVERAGE LEVEL SPACING
(L=0, J=3.0)

● LEAL ET AL., 2001
— · ENDF/B-VI
— — JENDL-3.3
—— PRESENT

LEVEL SPACING , eV

NEUTRON ENERGY, keV
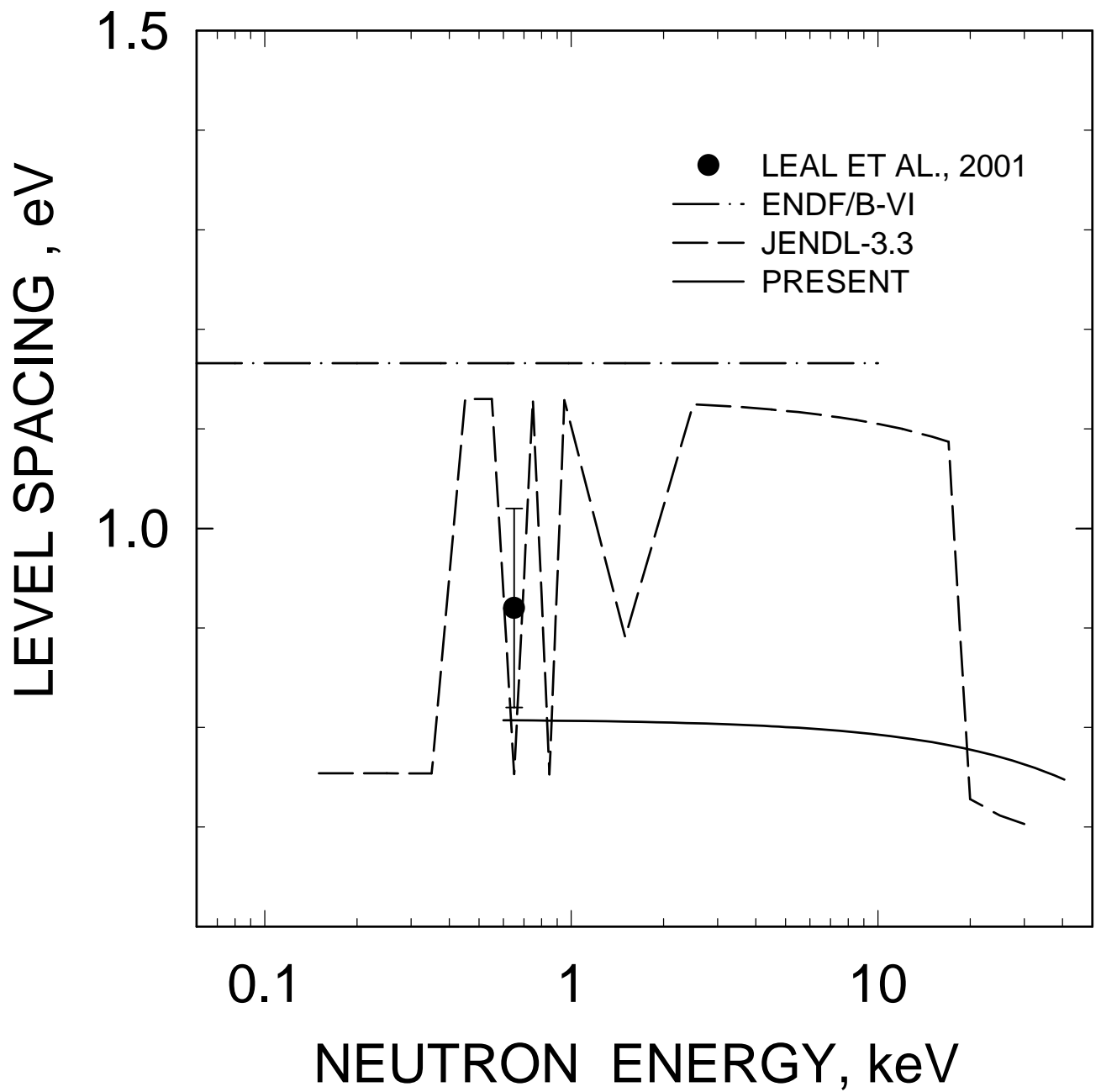
FIG. 25

^{233} U: AVERAGE LEVEL SPACING
(L=1, J=1.0)

ENDF/B-VI
JENDL-3.3
PRESENT
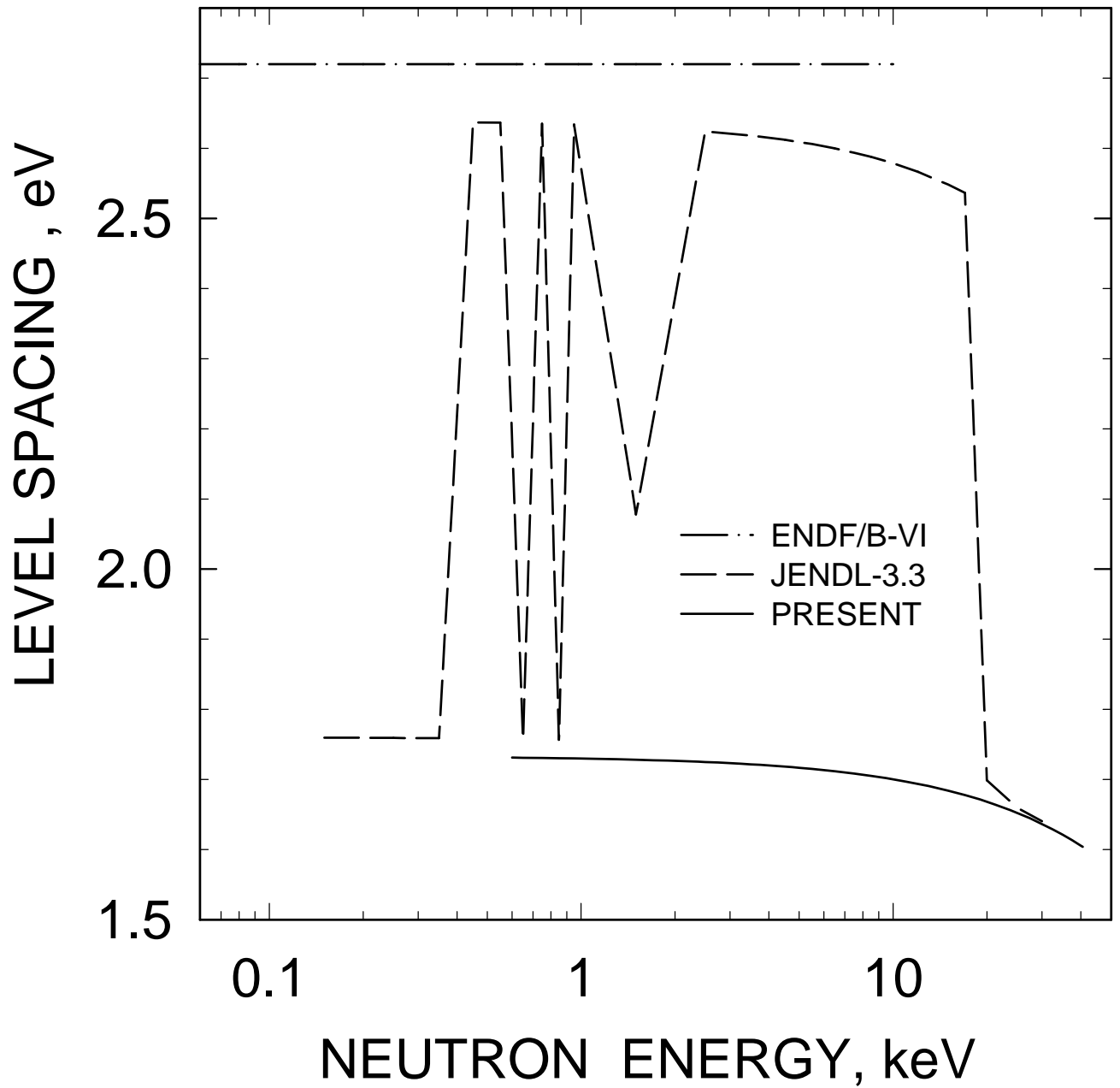
FIG. 26

^{233} U: AVERAGE LEVEL SPACING
(L=1, J=4.0)

FIG. 27
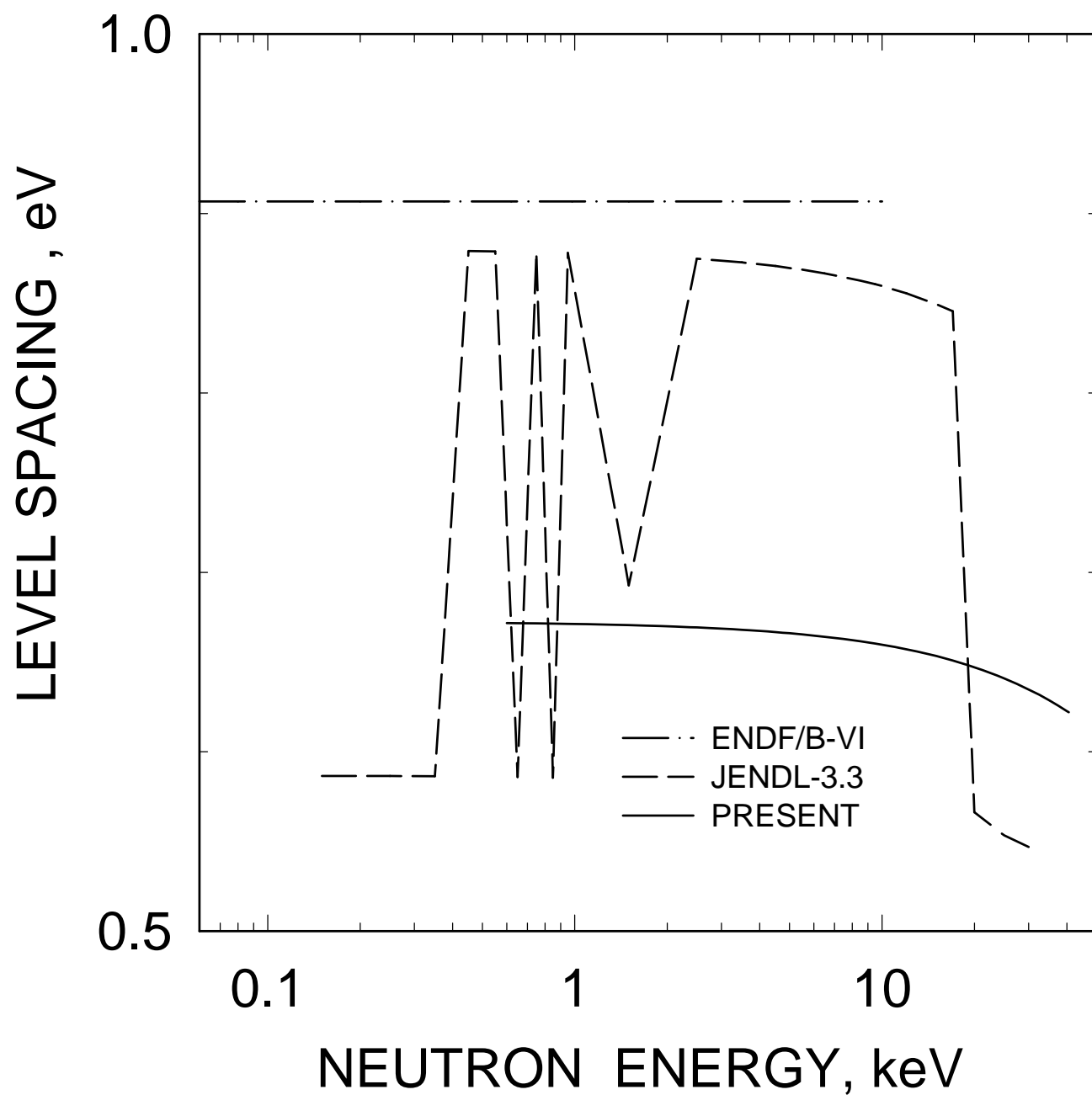
²³³U TOTAL CROSS SECTION

FIG. 28

^{233}U TOTAL CROSS SECTION
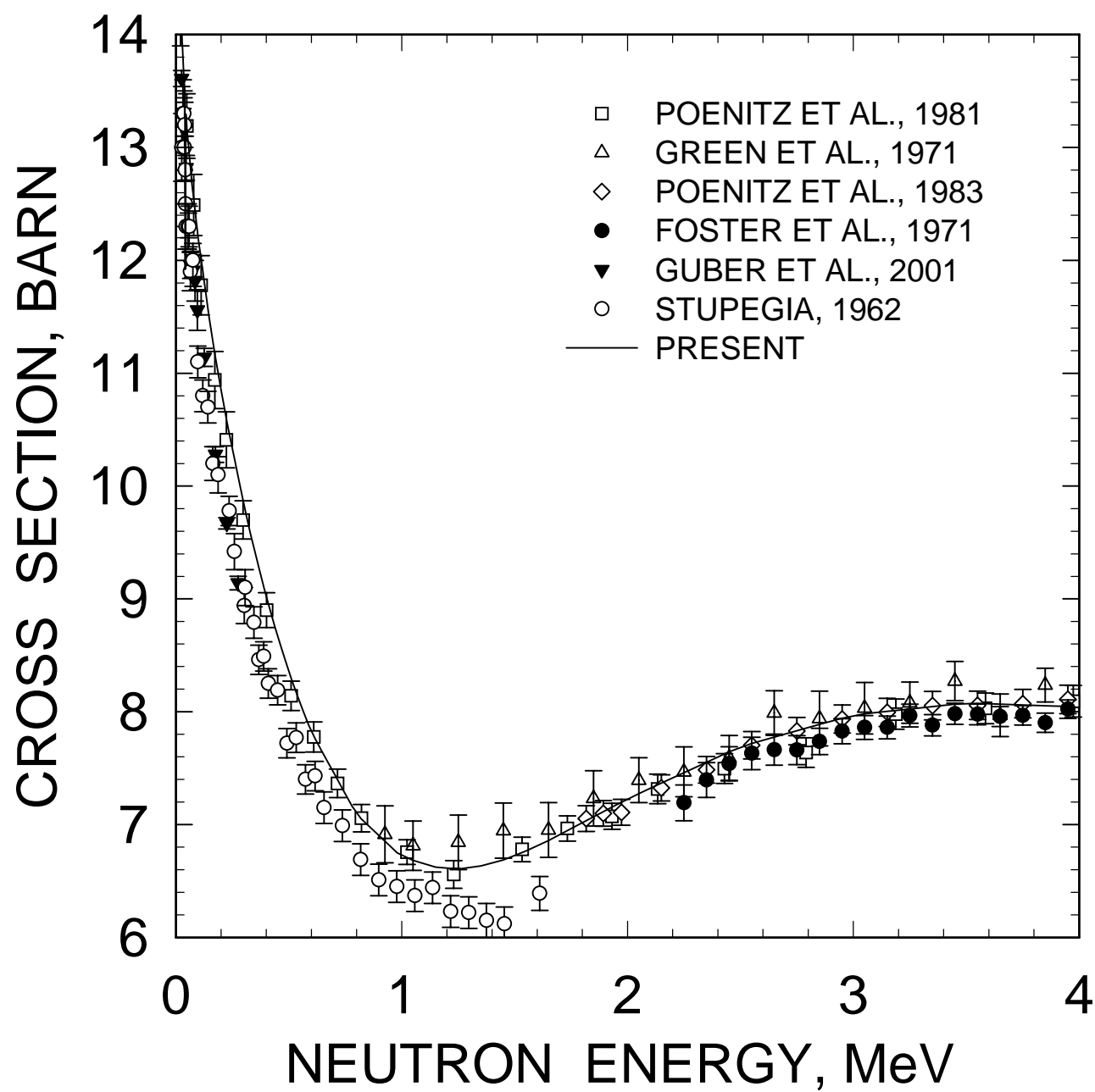
FIG. 29

^{233}U TOTAL CROSS SECTION

FIG. 30

^{233}U TOTAL CROSS SECTION

POENITZ ET AL., 1981
GREEN ET AL., 1971
POENITZ ET AL., 1983
FOSTER ET AL., 1971
——— PRESENT
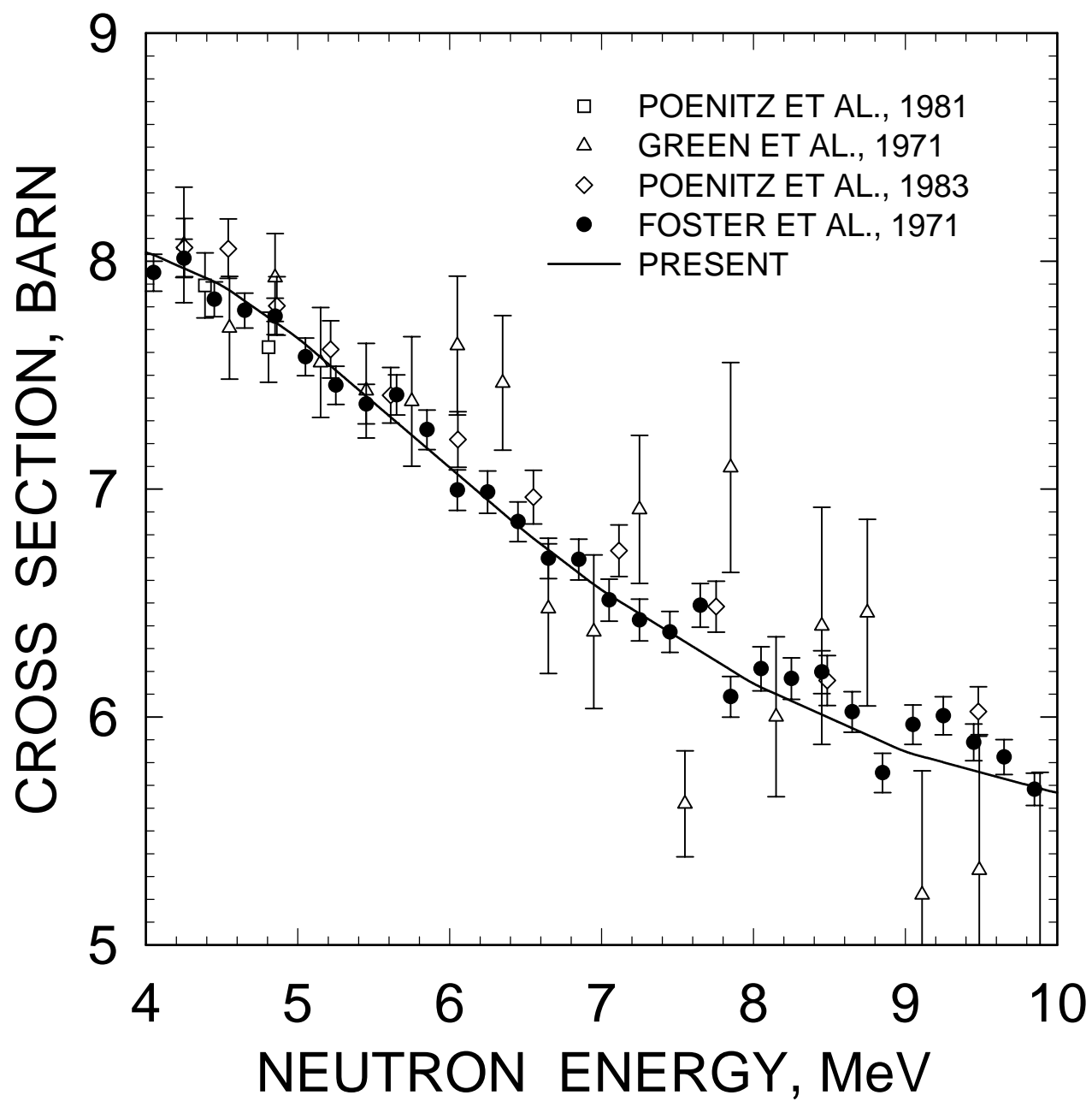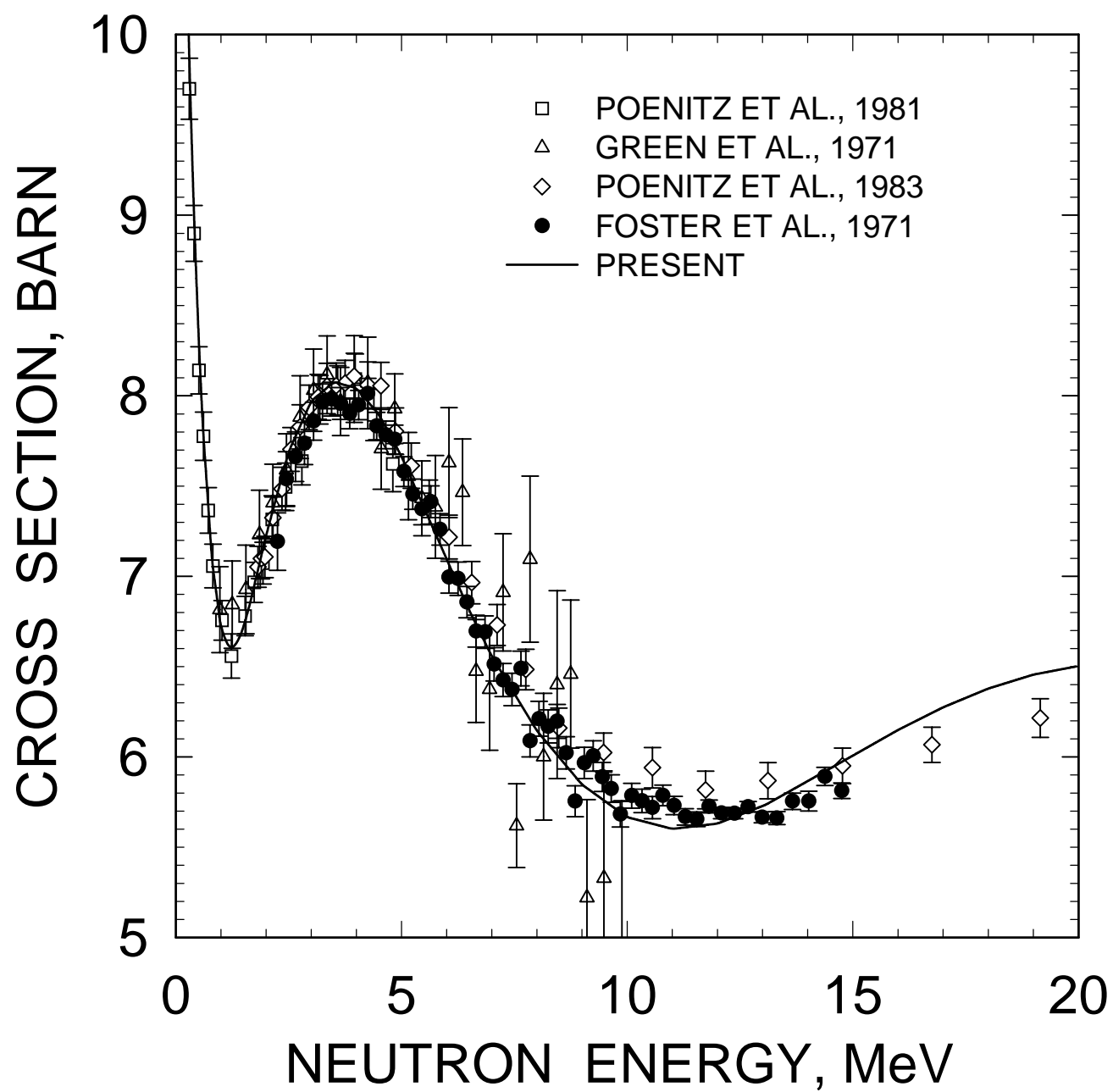
FIG. 31

^{233}U TOTAL CROSS SECTION
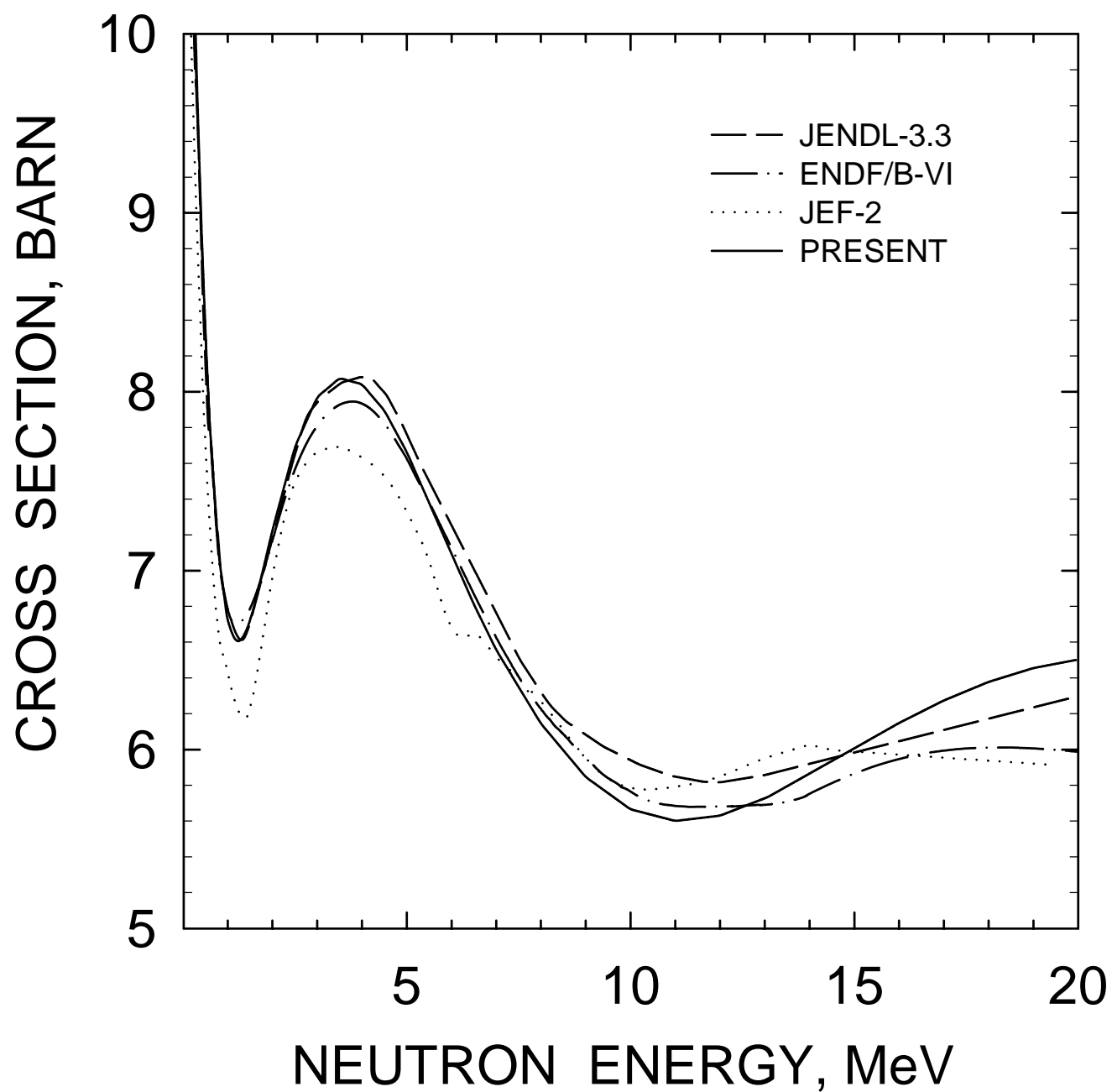
FIG. 32

^{233}U ELASTIC CROSS SECTION

FIG. 33

^{233}U E$_n$=0.7 MeV (5/2$^+$)

HAOUAT ET AL., 1982
— — 4 levels coupled
—·· 3 levels coupled
······· 5 levels coupled
—— PRESENT

dσ/dΩ(b/sr)

Θ(deg.)

FIG. 34

^{233}U E_n=1.5 MeV (5/2$^+$)

□   HAOUAT ET AL., 1982
— —   4 levels coupled
— · —   3 levels coupled
········   5 levels coupled
———   PRESENT

$d\sigma/d\Omega$(b/sr)

Θ(deg.)
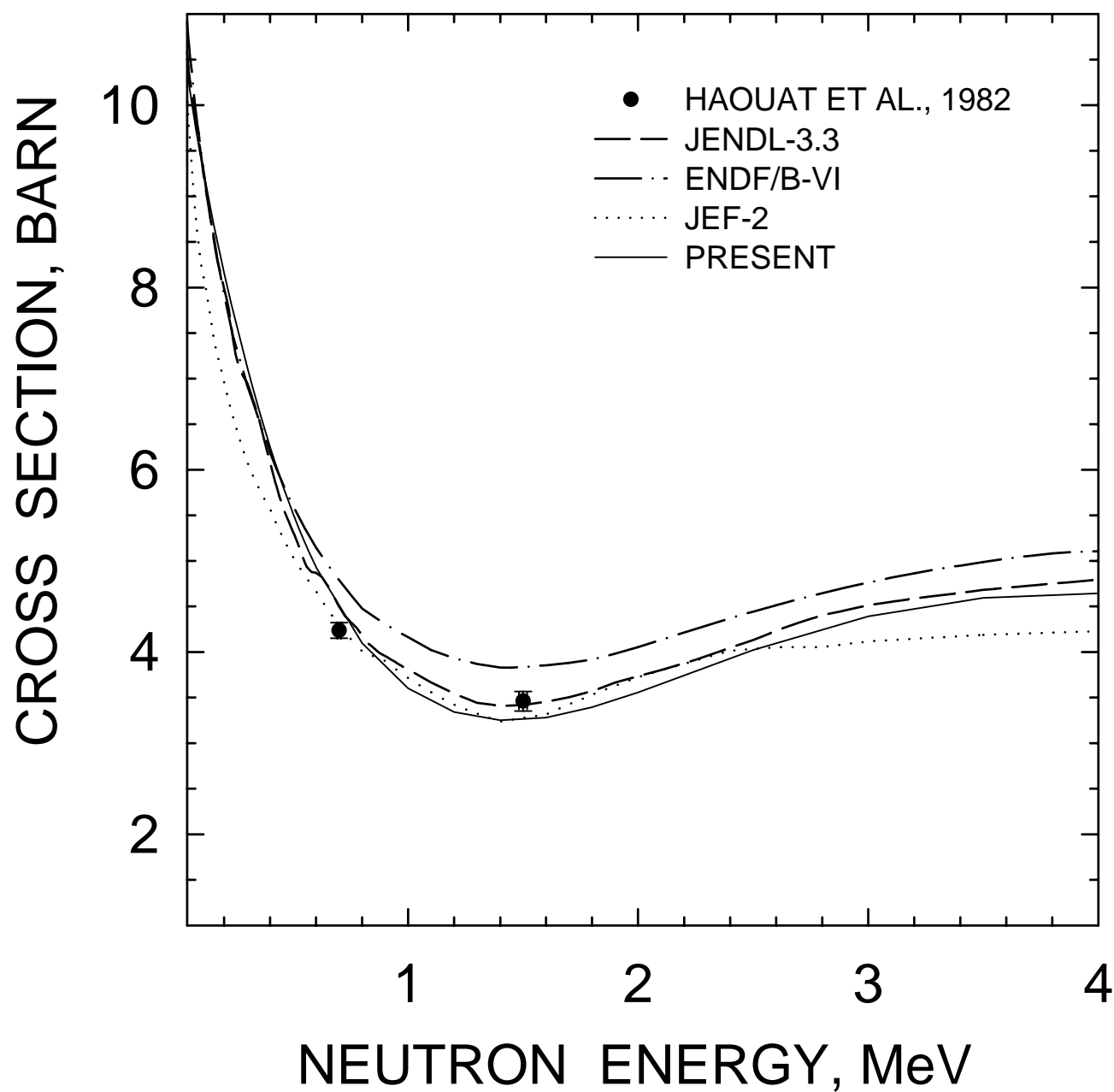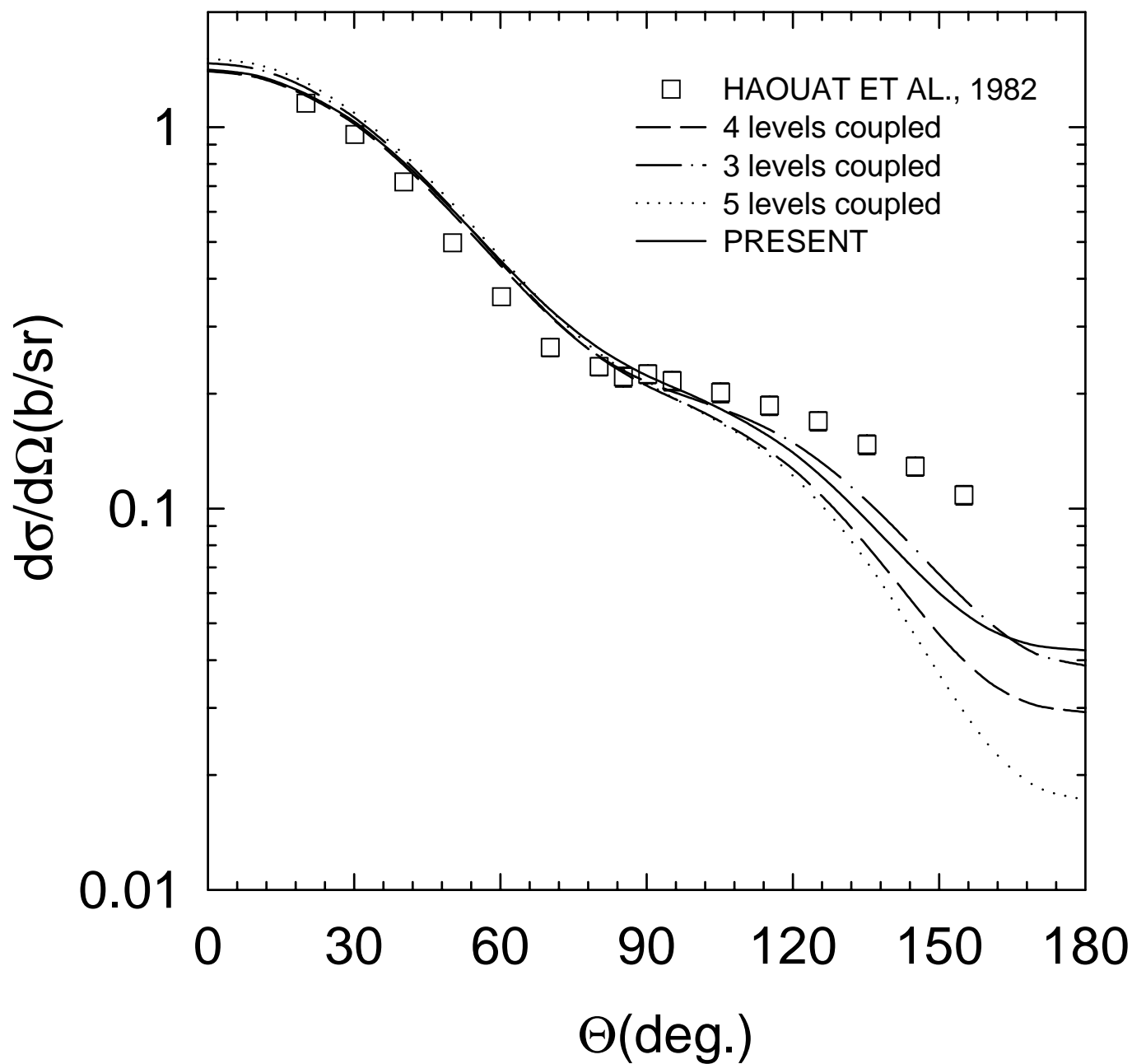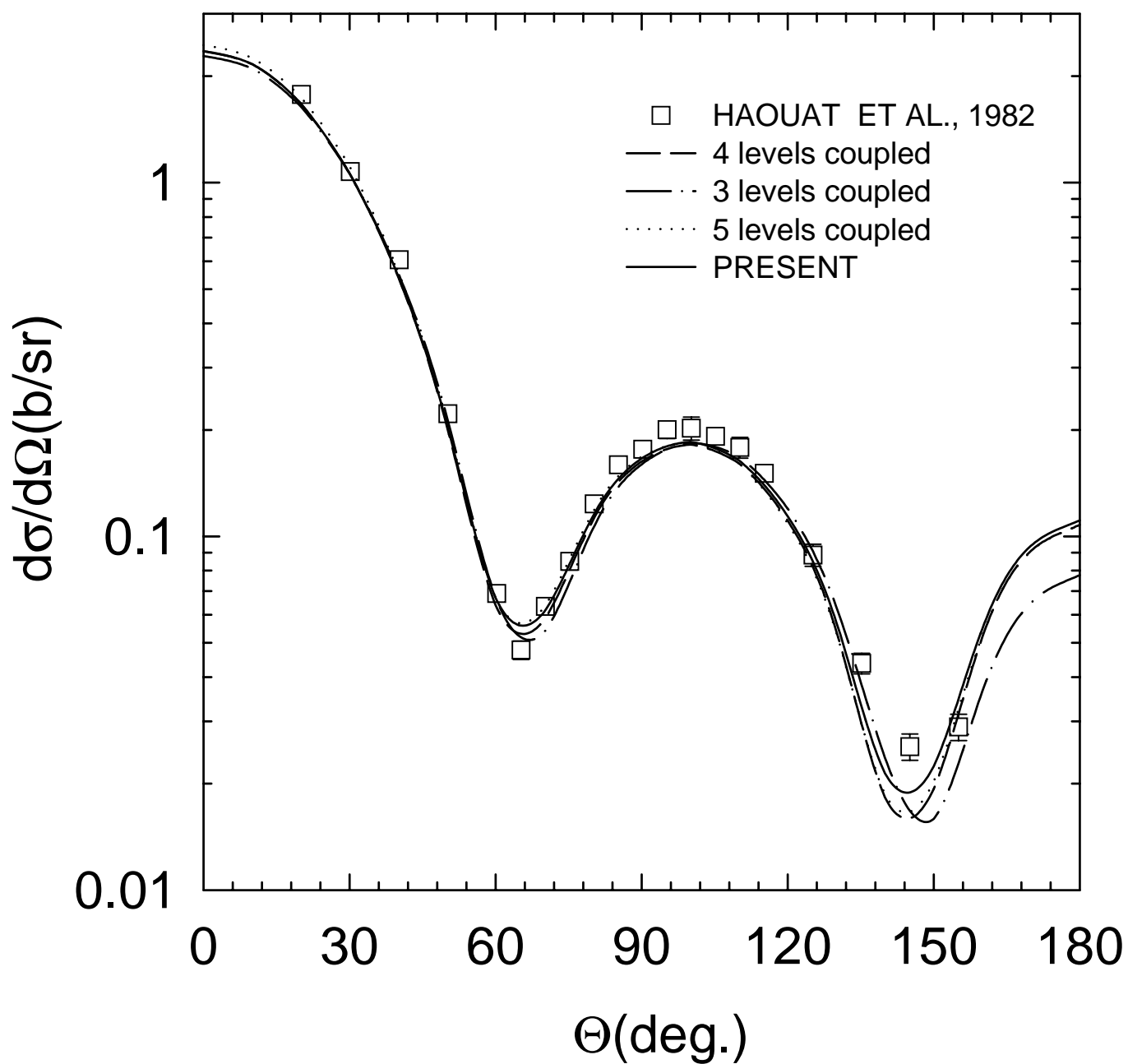
FIG. 35

^{233}U E_n=0.7 MeV (7/2$^+$)

FIG. 36

^{233}U E_n=1.5 MeV (7/2$^+$)

dσ/dΩ(b/sr)

0.01

□   HAOUAT ET AL., 1982
– – 4 levels coupled
– · – 3 levels coupled
· · · · · 5 levels coupled
——— PRESENT

0   30   60   90   120   150   180

Θ(deg.)

FIG. 37

^{233}U E_n=1.5 MeV ($9/2^+$)

□ HAOUAT ET AL, 1982
— — 4 levels coupled
— · — 3 levels coupled
· · · · · 5 levels coupled
—— PRESENT

$d\sigma/d\Omega$(b/sr)

0.01

Θ(deg.)

0   30   60   90   120   150   180
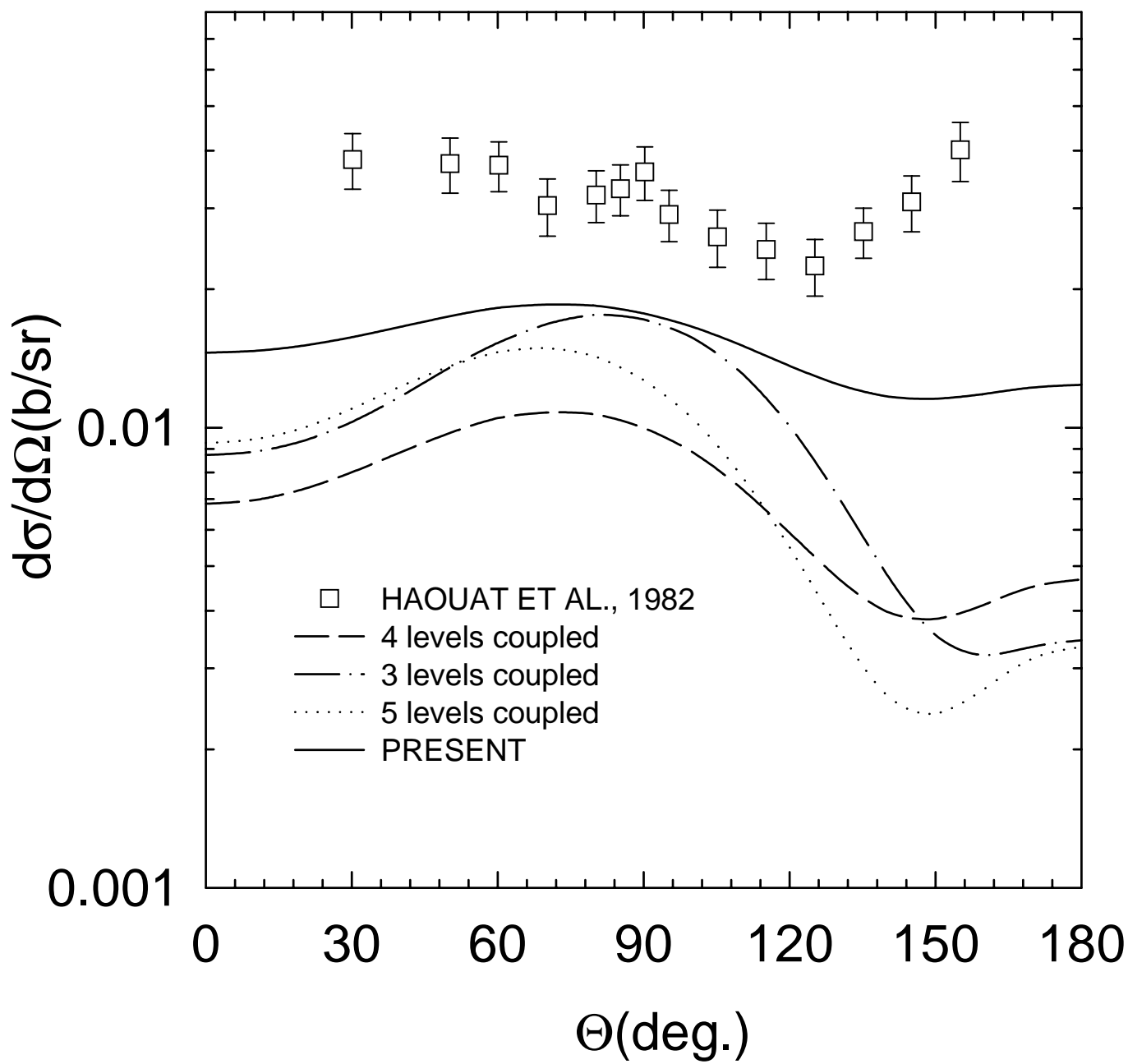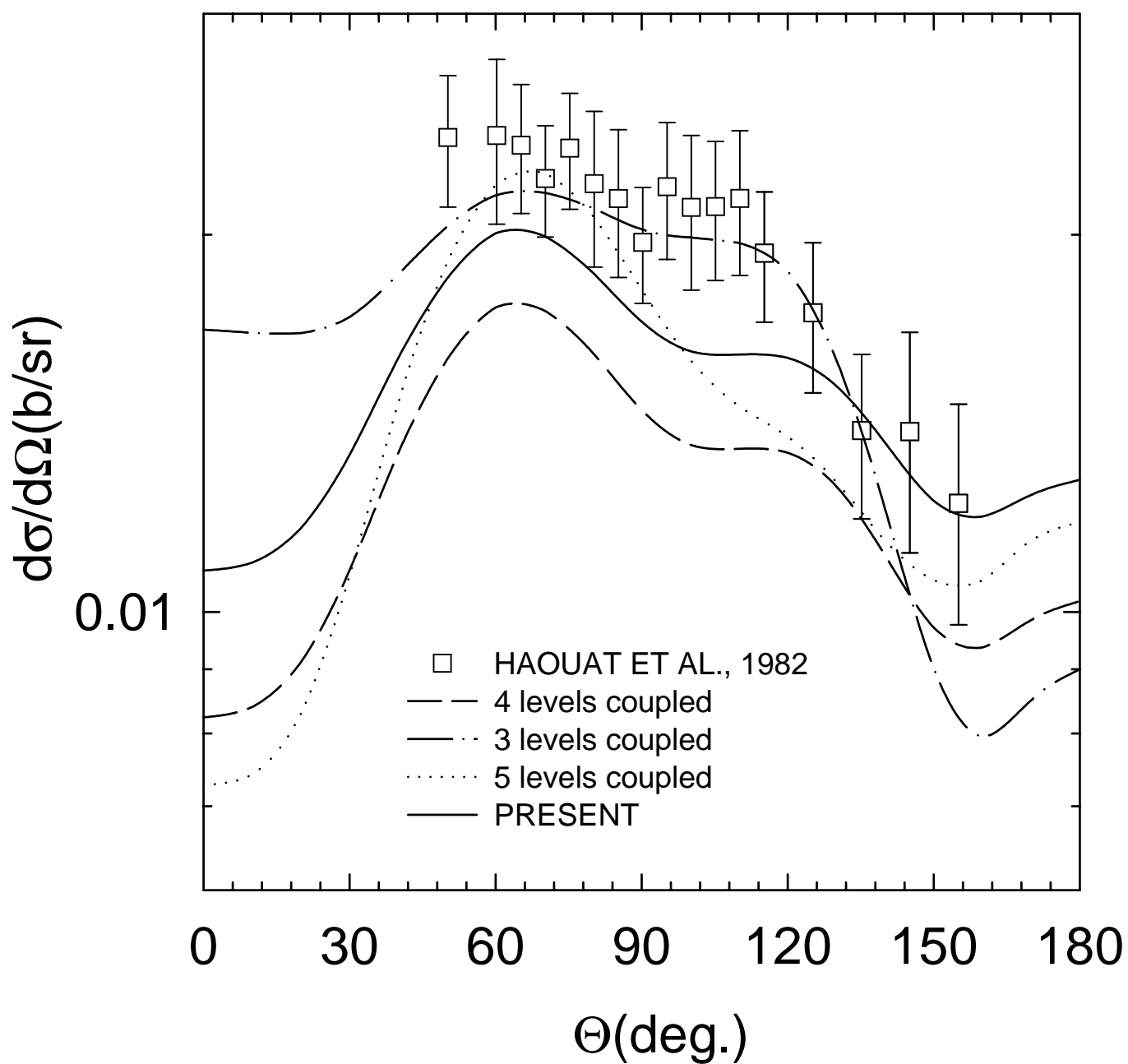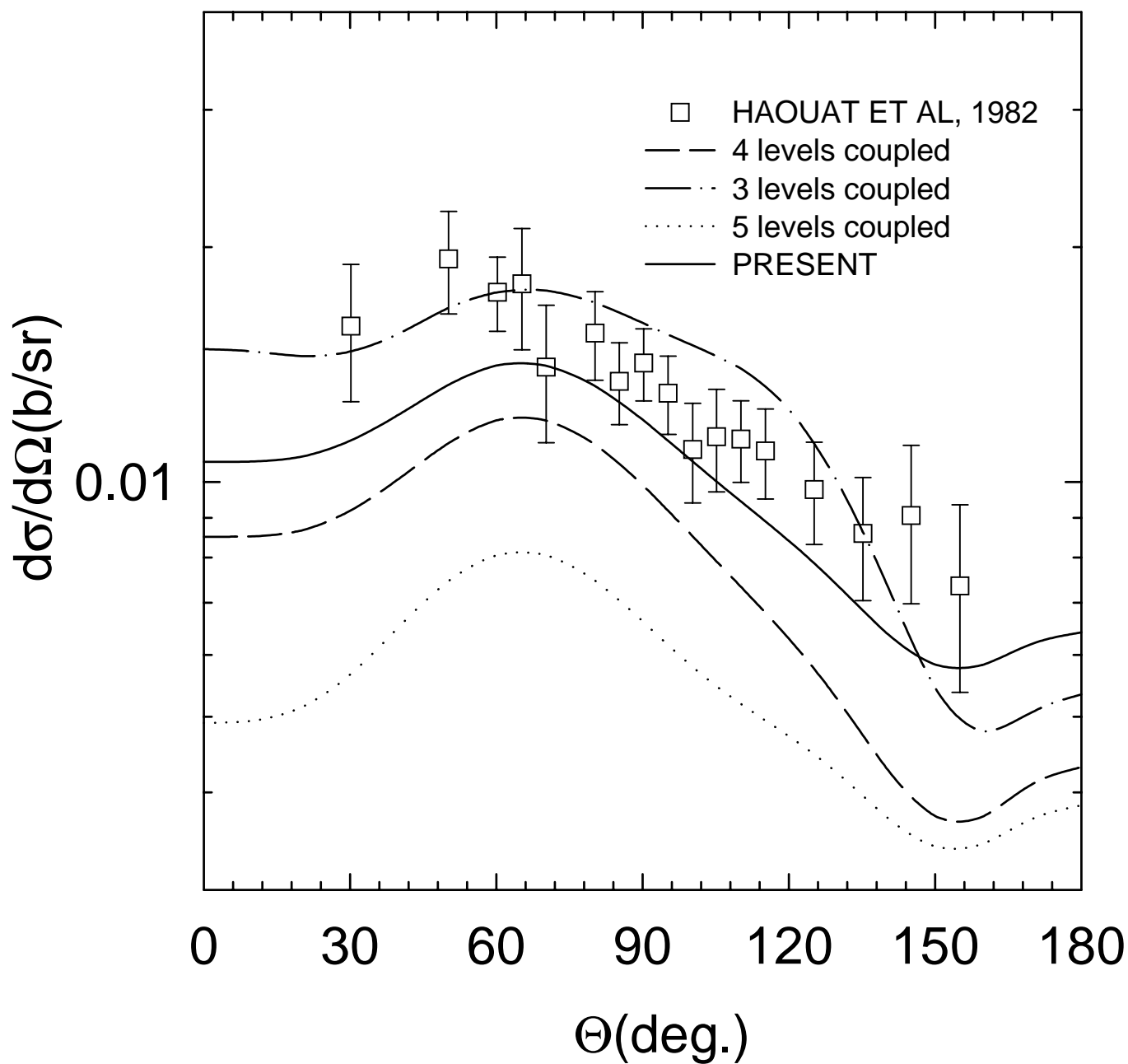
FIG. 38
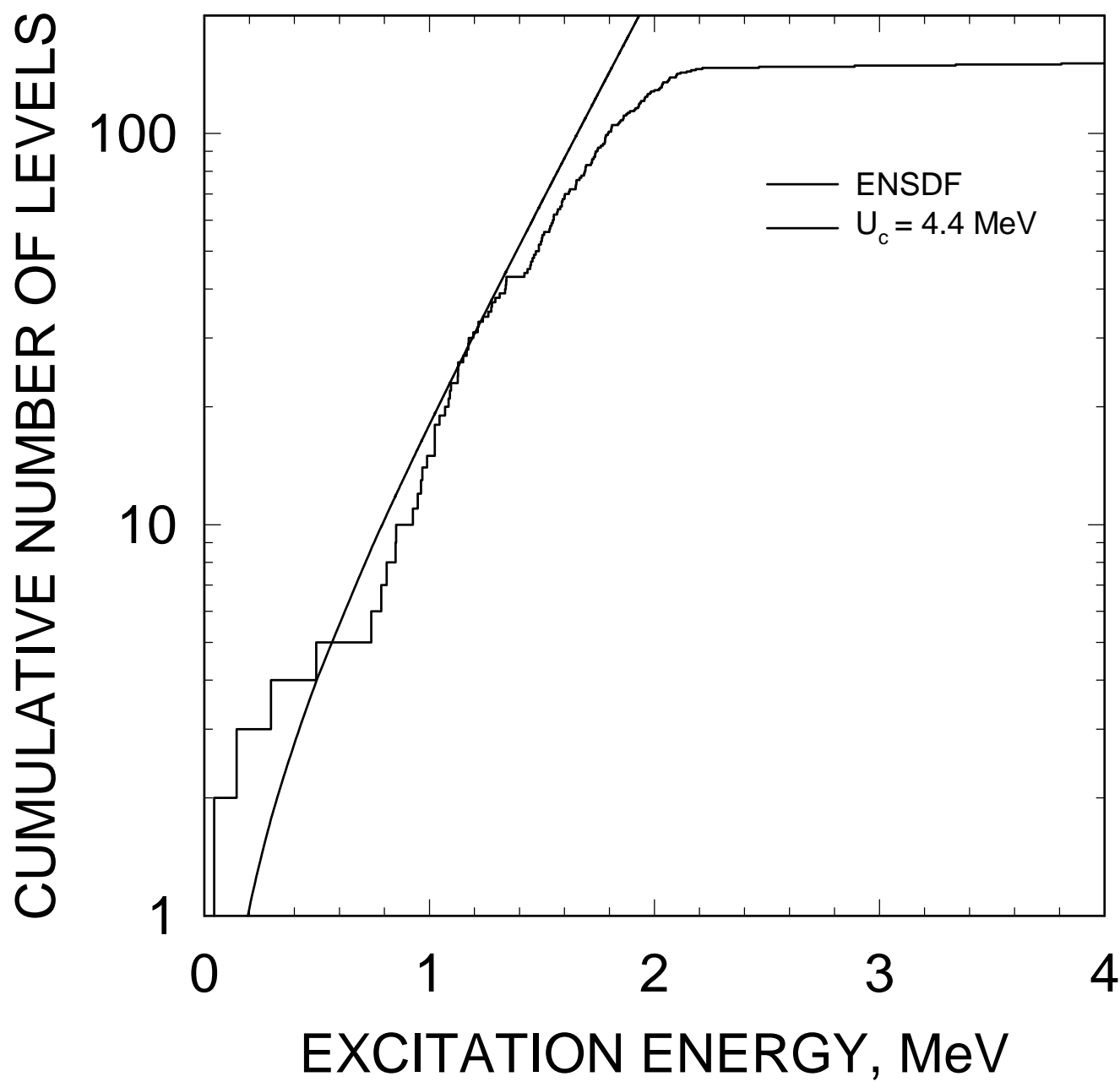
FIG. 39
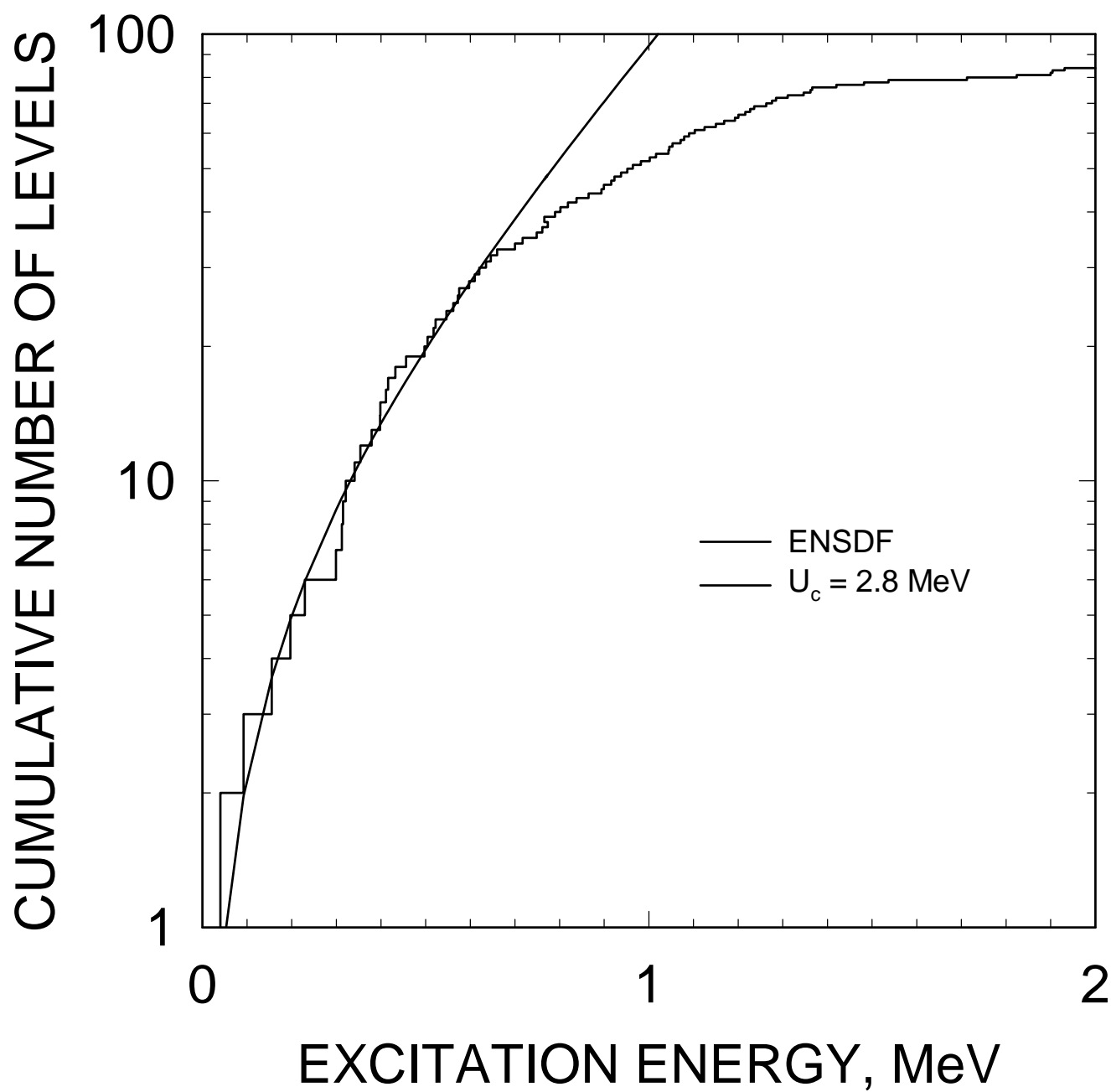
FIG. 40

^{234}U, OUTER SADDLE

FIG. 41

FIG. 42

^{233}U FISSION CROSS SECTION

CROSS SECTION, BARNS

NEUTRON ENERGY, eV

- △ CARLSON ET AL., 1978
- ○ GUBER ET AL., 2000
- □ WESTON ET AL., 1968
- ◇ BLONS, 1973
- ▽ GWIN ET AL., 1976
- ▲ MEADOWS, 1974
- ■ POENITZ, 1978
- ⬡ FURSOV ET AL., 1978
- —— PRESENT
- – – without $K^{\pi} = 2^{+}_{2}$ band
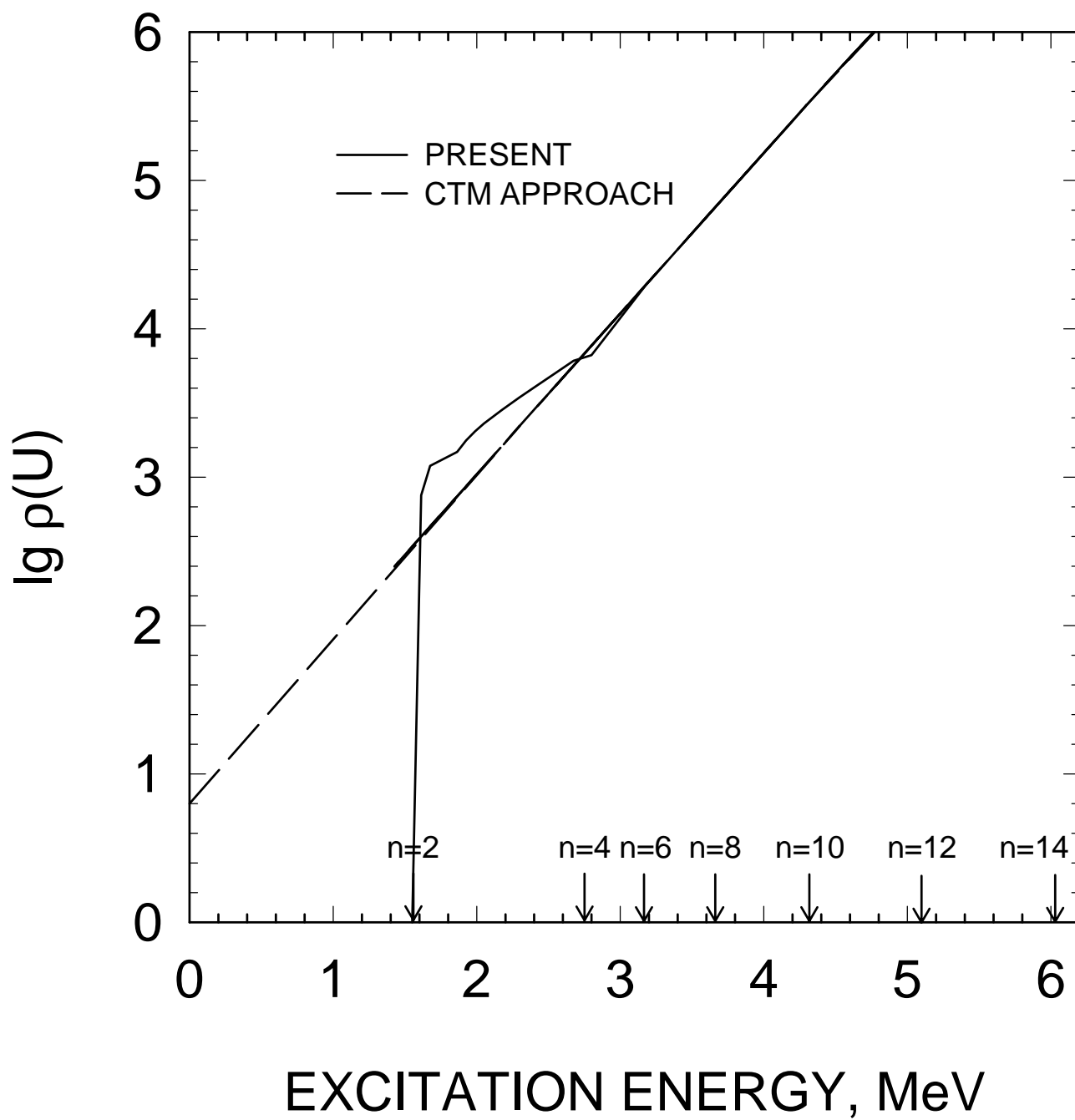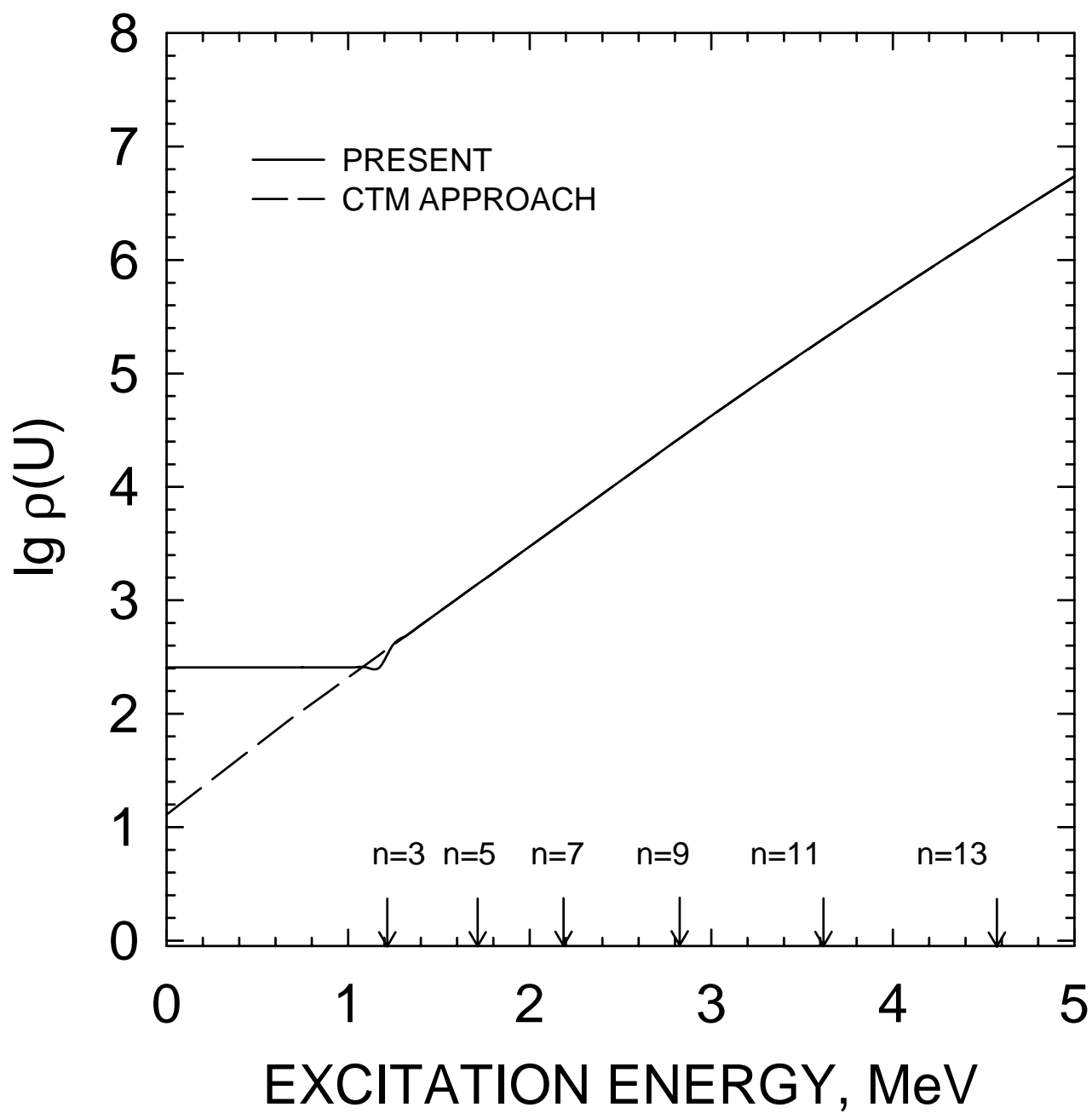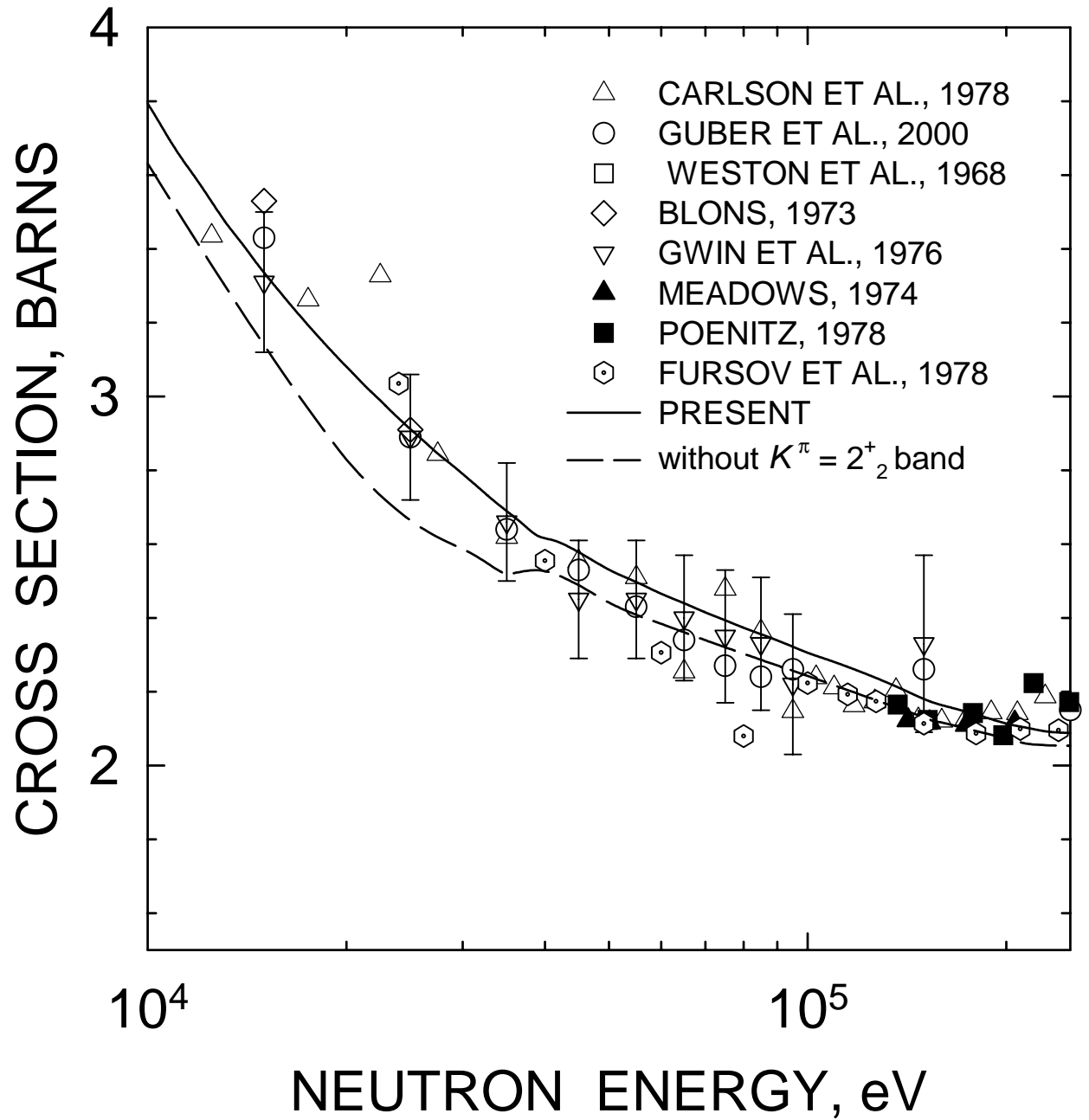
FIG. 43

^{233}U FISSION CROSS SECTION

FIG. 44

^{233}U FISSION CROSS SECTION

FURSOV ET AL., 1978
CARLSON ET AL., 1978
MEADOWS, 1974
KANDA ET AL., 1986
POENITZ, 1978
KALININ ET AL., 1987
GUBER AT AL., 2001
JENDL-3.3
ENDF/B-VI
JEF-2
PRESENT

CROSS SECTION, BARNS

NEUTRON ENERGY, MeV

FIG. 45

^{233}U FISSION CROSS SECTION

FURSOV ET AL., 1978
CARLSON ET AL., 1978
MEADOWS, 1974
KANDA ET AL., 1986
POENITZ, 1978
KALININ ET AL., 1987

GUBER ET AL., 2001
SHCHERBAKOV ET AL., 2001
JENDL-3.3
ENDF/B-VI
JEF-2
PRESENT
ω_4 increased
CTM APPROACH

CROSS SECTION, BARNS

2.0

1.5

0.1

1

NEUTRON ENERGY, MeV

FIG. 46

^{233}U FISSION CROSS SECTION

Legend:
- ⬡ FURSOV ET AL., 1978
- △ CARLSON ET AL., 1978
- □ MEADOWS, 1974
- ○ KANDA ET AL., 1986
- ▽ POENITZ, 1978
- ■ KALININ ET AL., 1987

- —○— GUBER ET AL., 2001
- ◇ SHCHERBAKOV ET AL., 2001
- — — JENDL-3.3
- —·· ENDF/B-VI
- ···· JEF-2
- —— PRESENT
- —△— ω_4 increased
- —·· CTM APPROACH

CROSS SECTION, BARNS

2.0

1.5

NEUTRON ENERGY, MeV

1   2   3   4   5

FIG. 47

^{233}U: 0.04035, 7/2$^+$ LEVEL EXCITATION
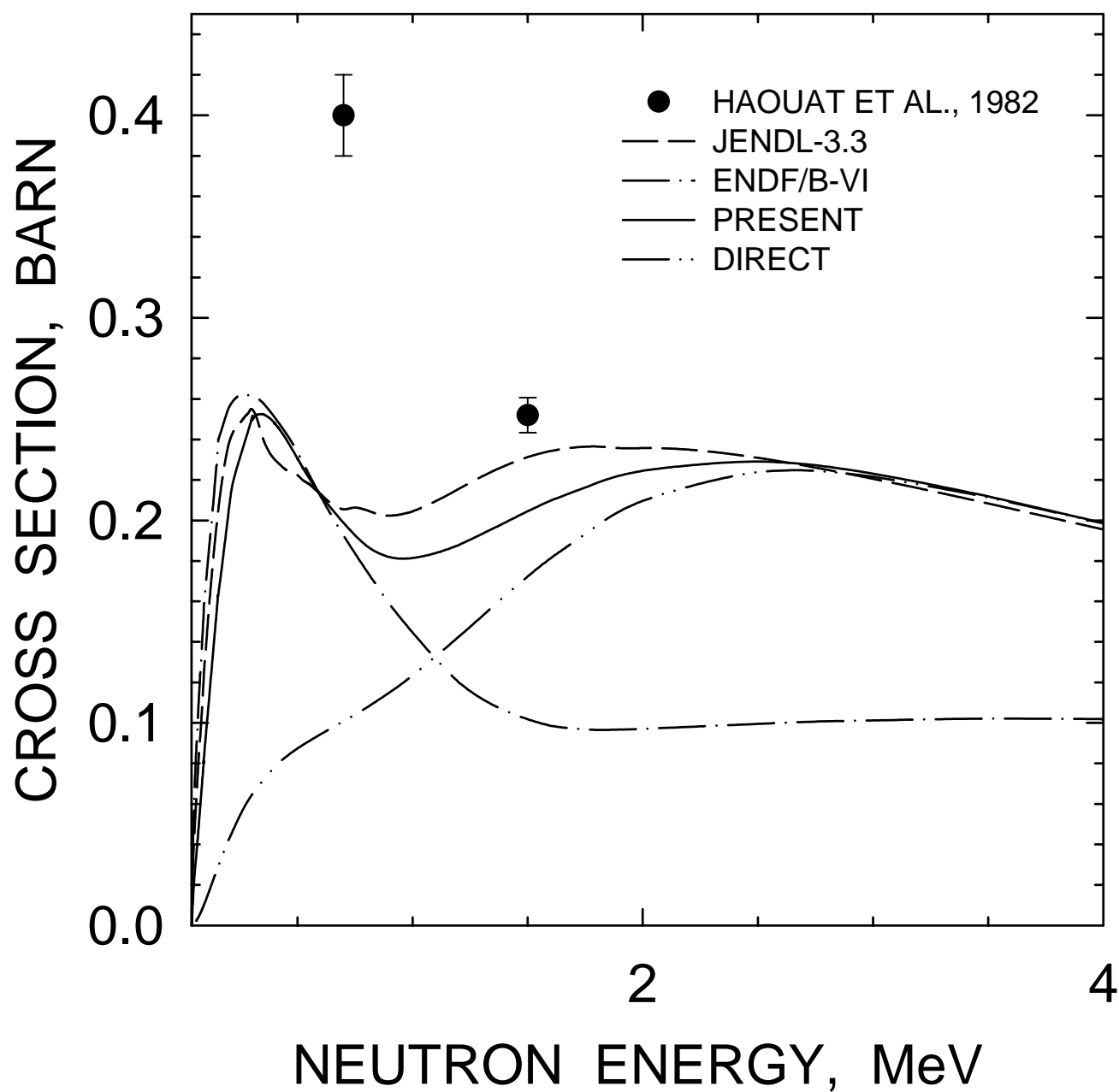
FIG. 48

^{233}U: 0.09219, 9/2$^+$ LEVEL EXCITATION
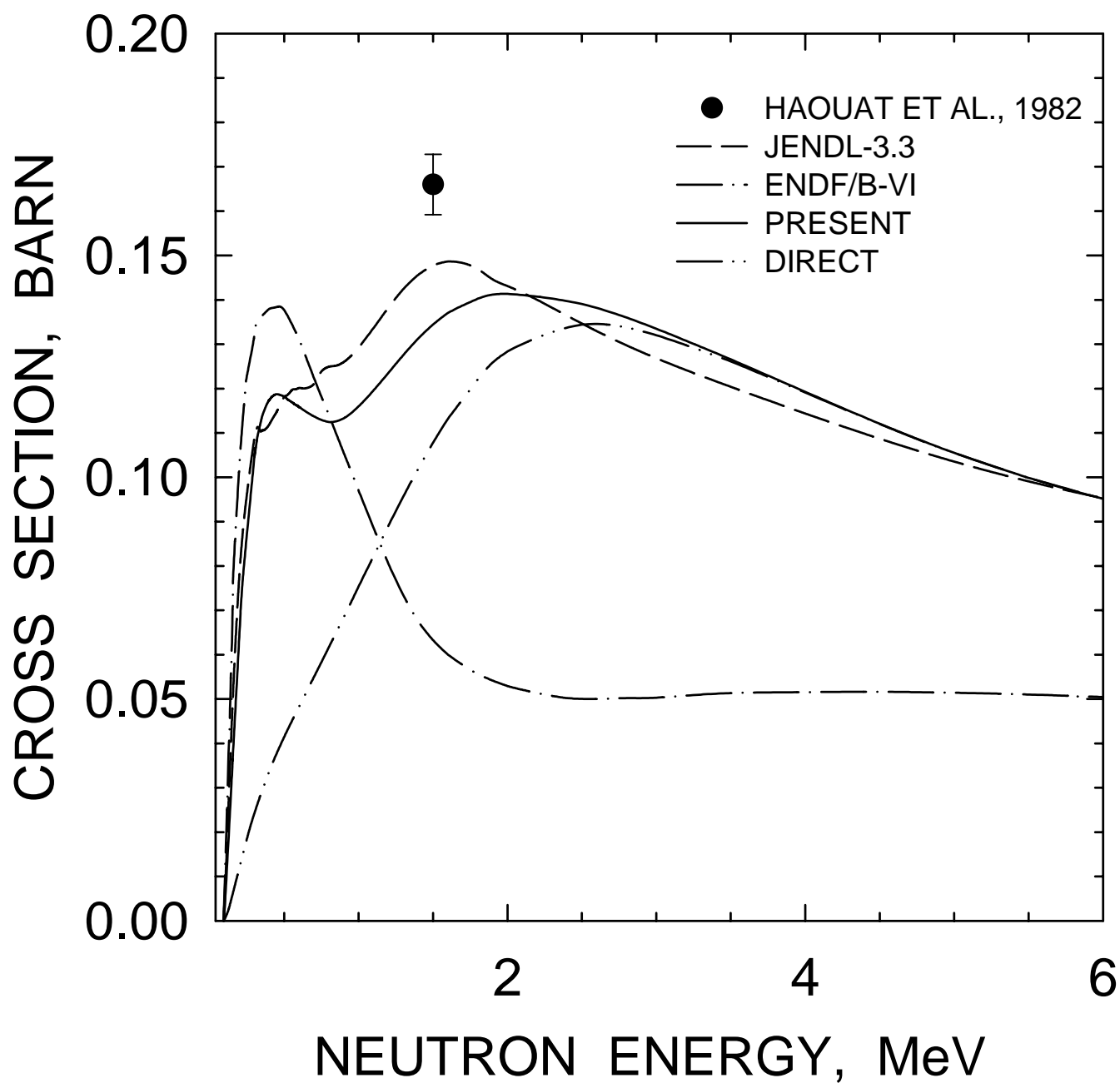
FIG. 49

^{233}U: 0.15527, 11/2$^+$ LEVEL EXCITATION
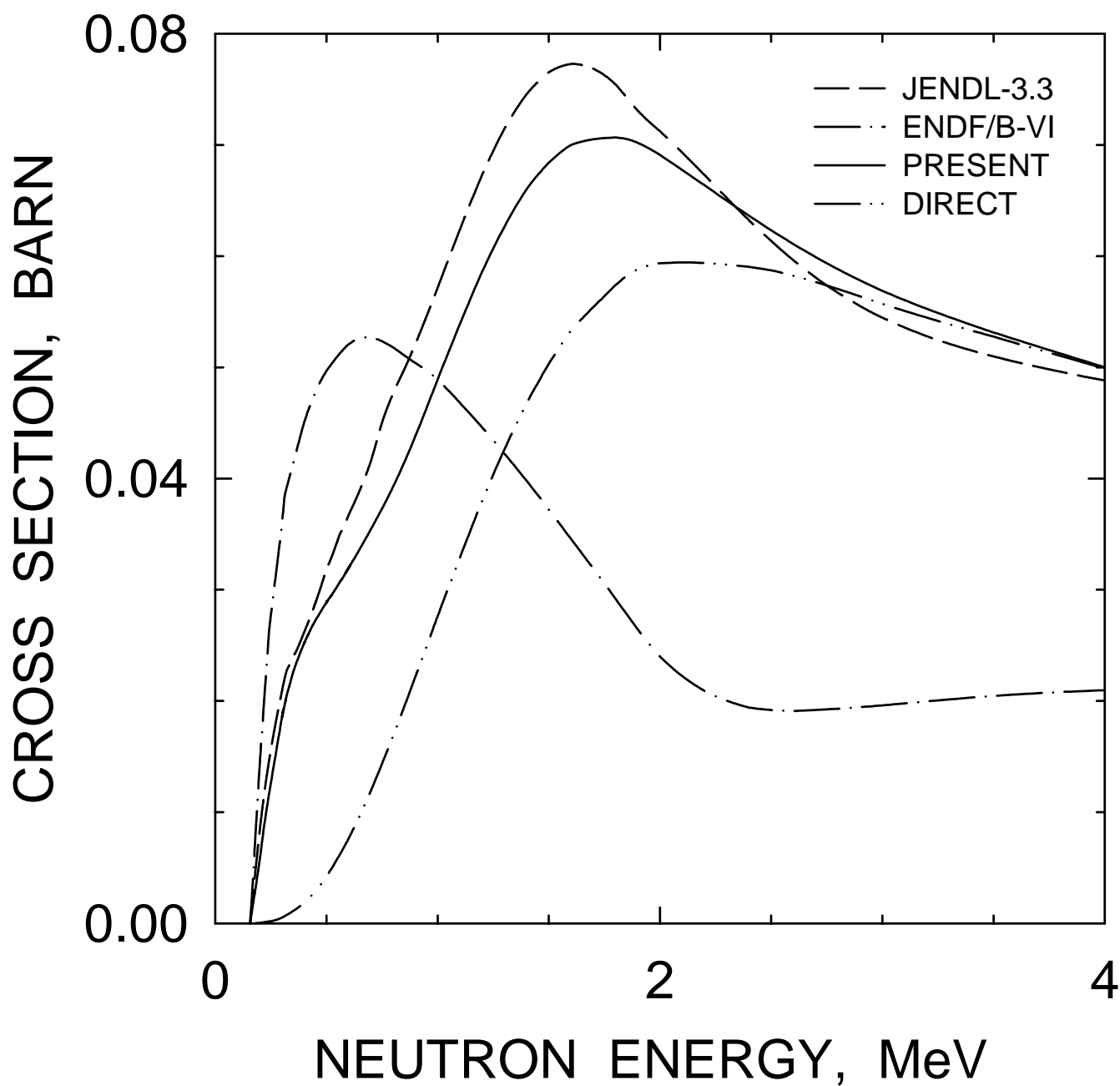
FIG. 50

^{233}U: 0.2294, 13/2$^+$ LEVEL EXCITATION
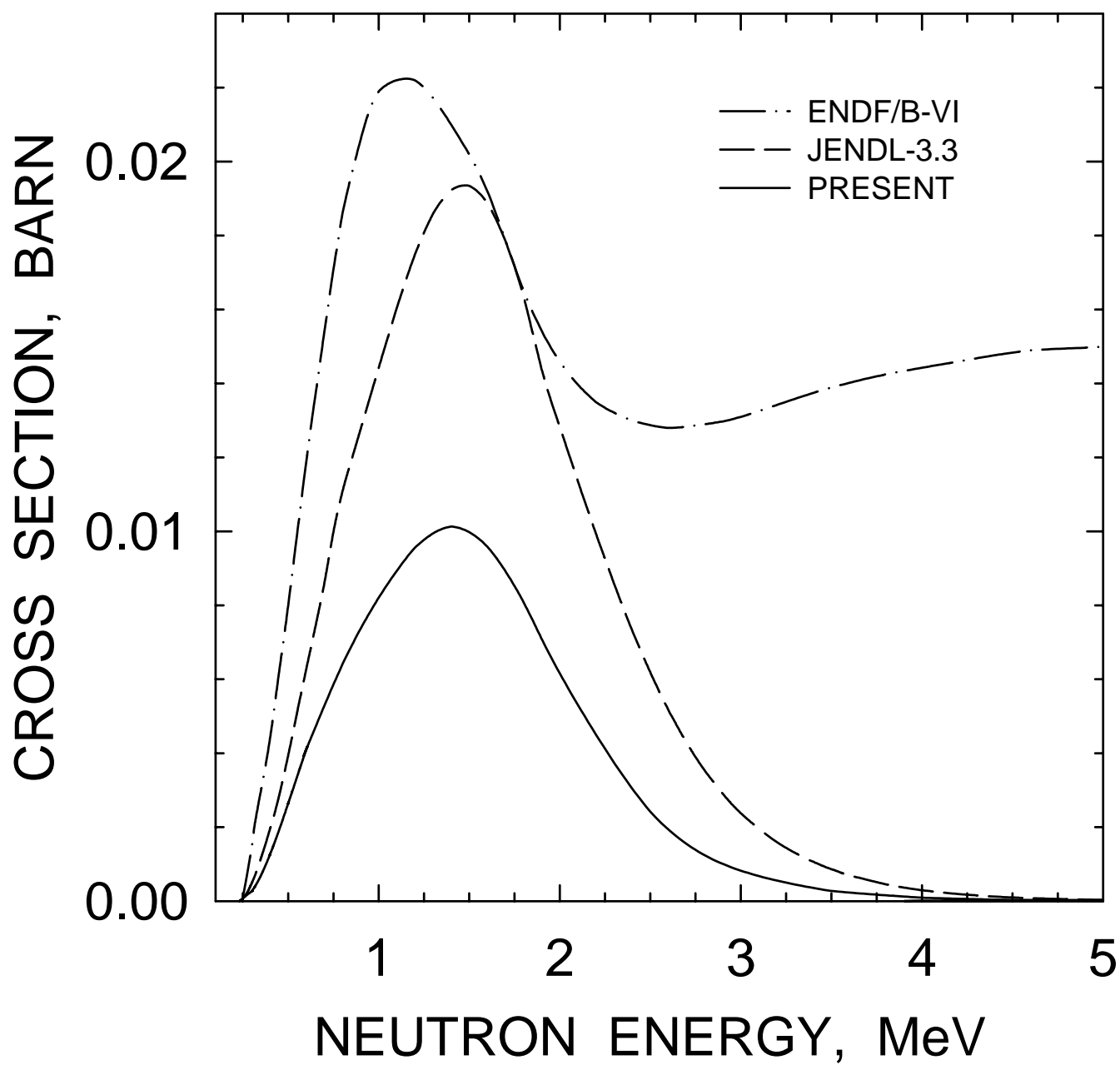
FIG. 51

^{233}U: 0.31217, 3/2$^+$ LEVEL EXCITATION
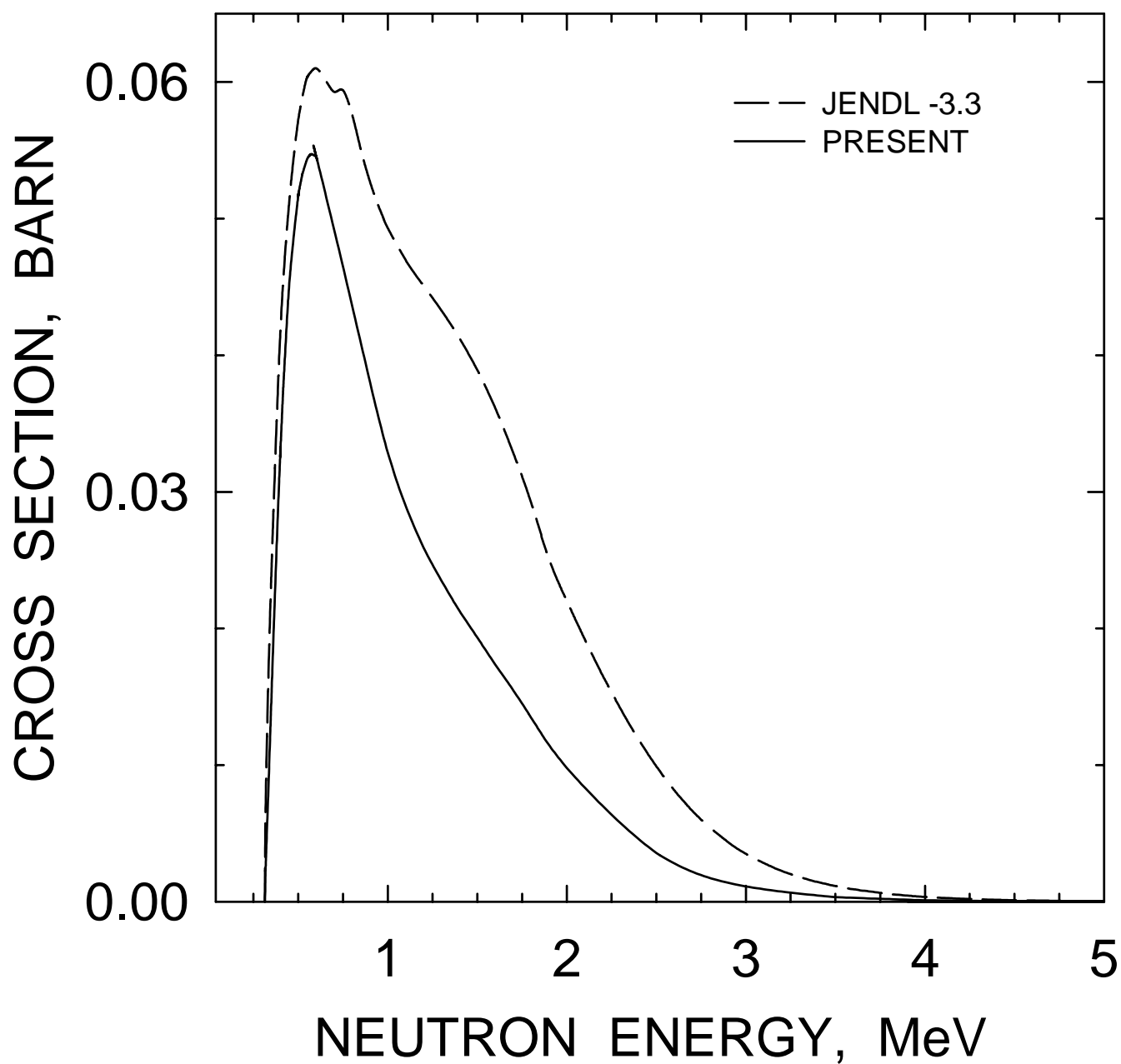
FIG. 52

^{233}U: 0.3147, 15/2$^+$ LEVEL EXCITATION
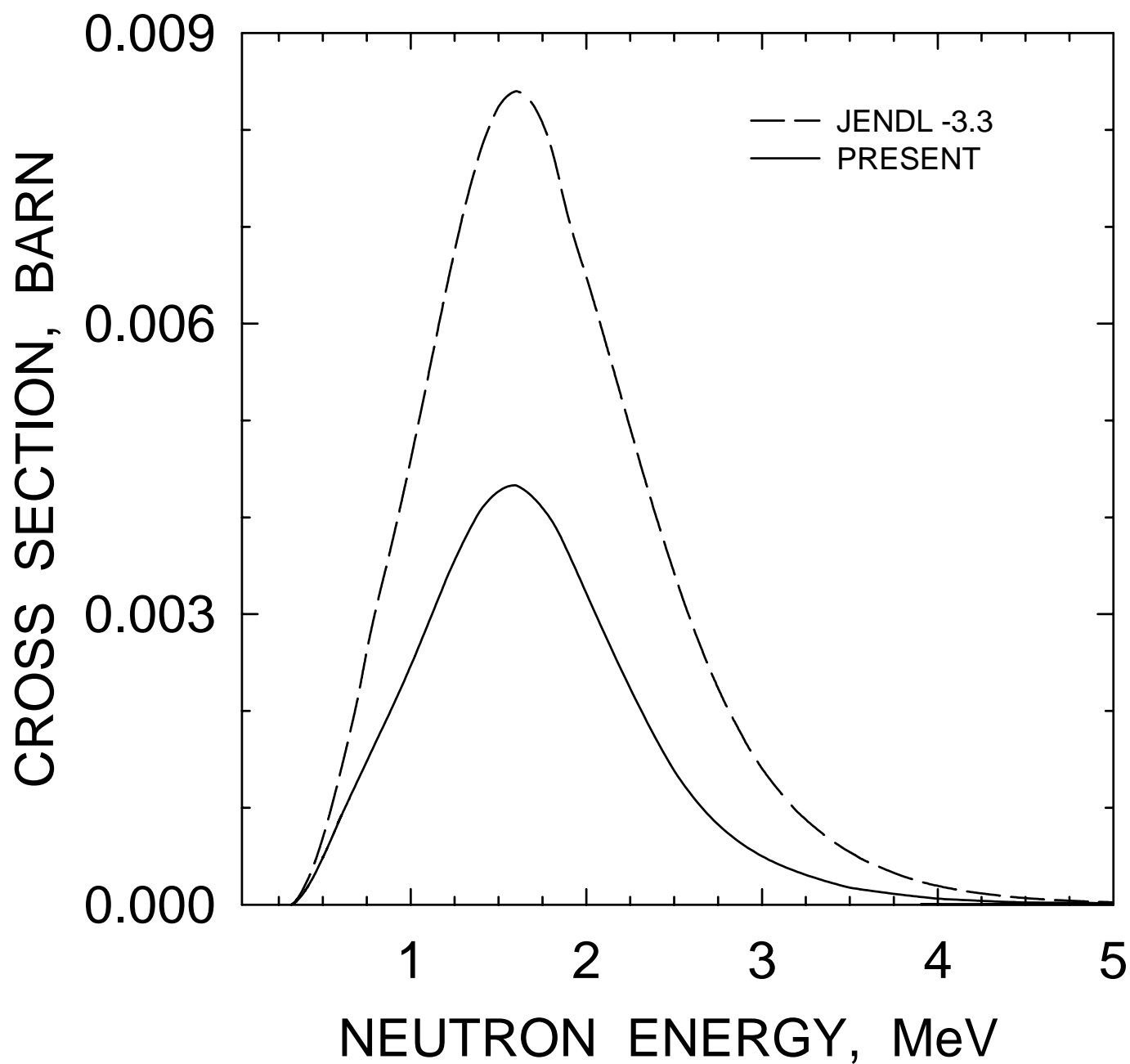
FIG. 53

^{233}U: 0.32075, 7/2$^-$ LEVEL EXCITATION
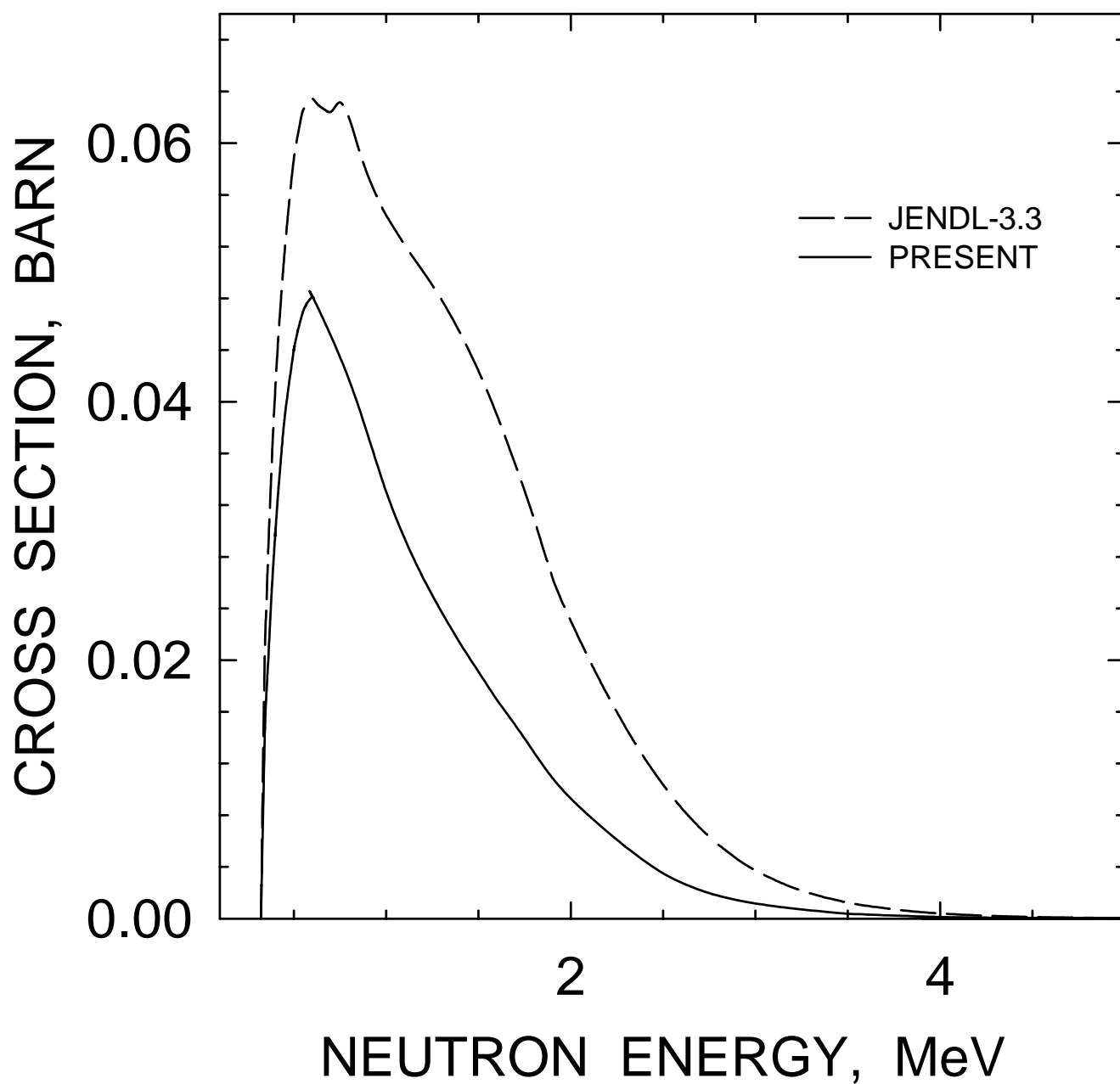
FIG. 54

^{233}U: 0.3976, 11/2$^-$ LEVEL EXCITATION

CROSS SECTION, BARN

NEUTRON ENERGY, MeV

JENDL-3.3
PRESENT
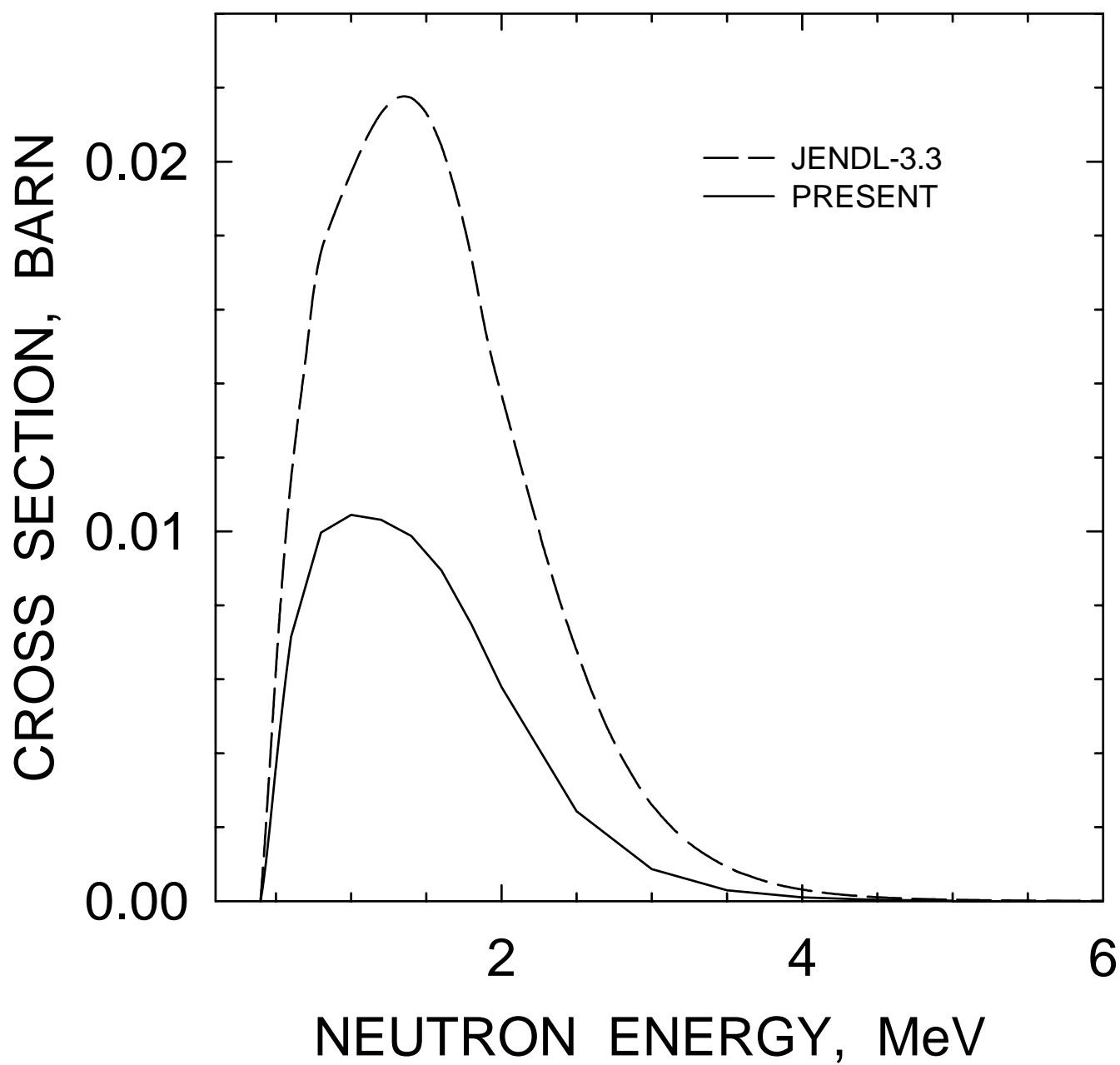
FIG. 55

^{233}U: 0.3985, 1/2$^+$ LEVEL EXCITATION
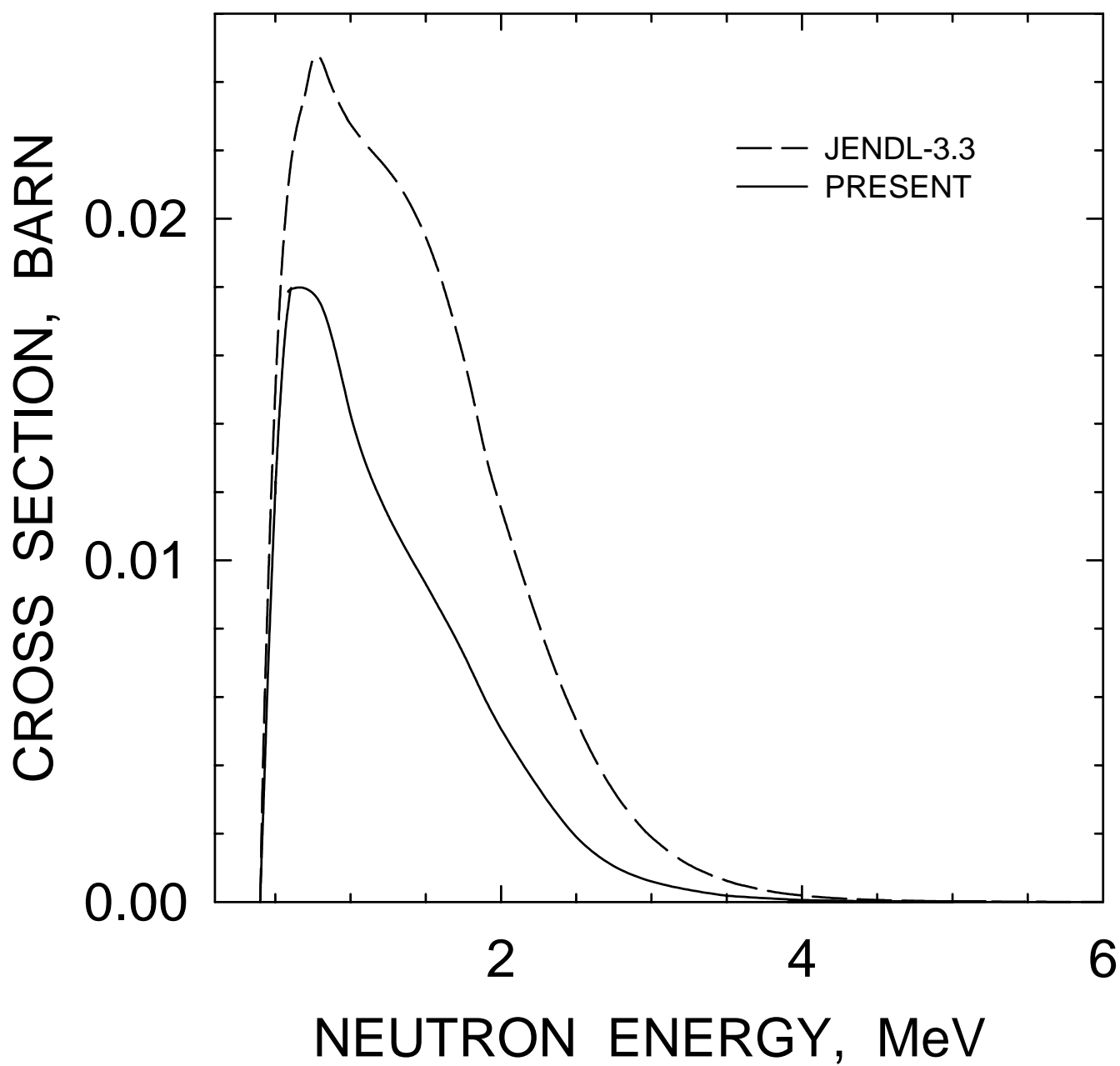
FIG. 56

^{233}U: 0.4158, 3/2$^+$ LEVEL EXCITATION

CROSS SECTION, BARN

NEUTRON ENERGY, MeV

JENDL-3.3
JEF-2
PRESENT
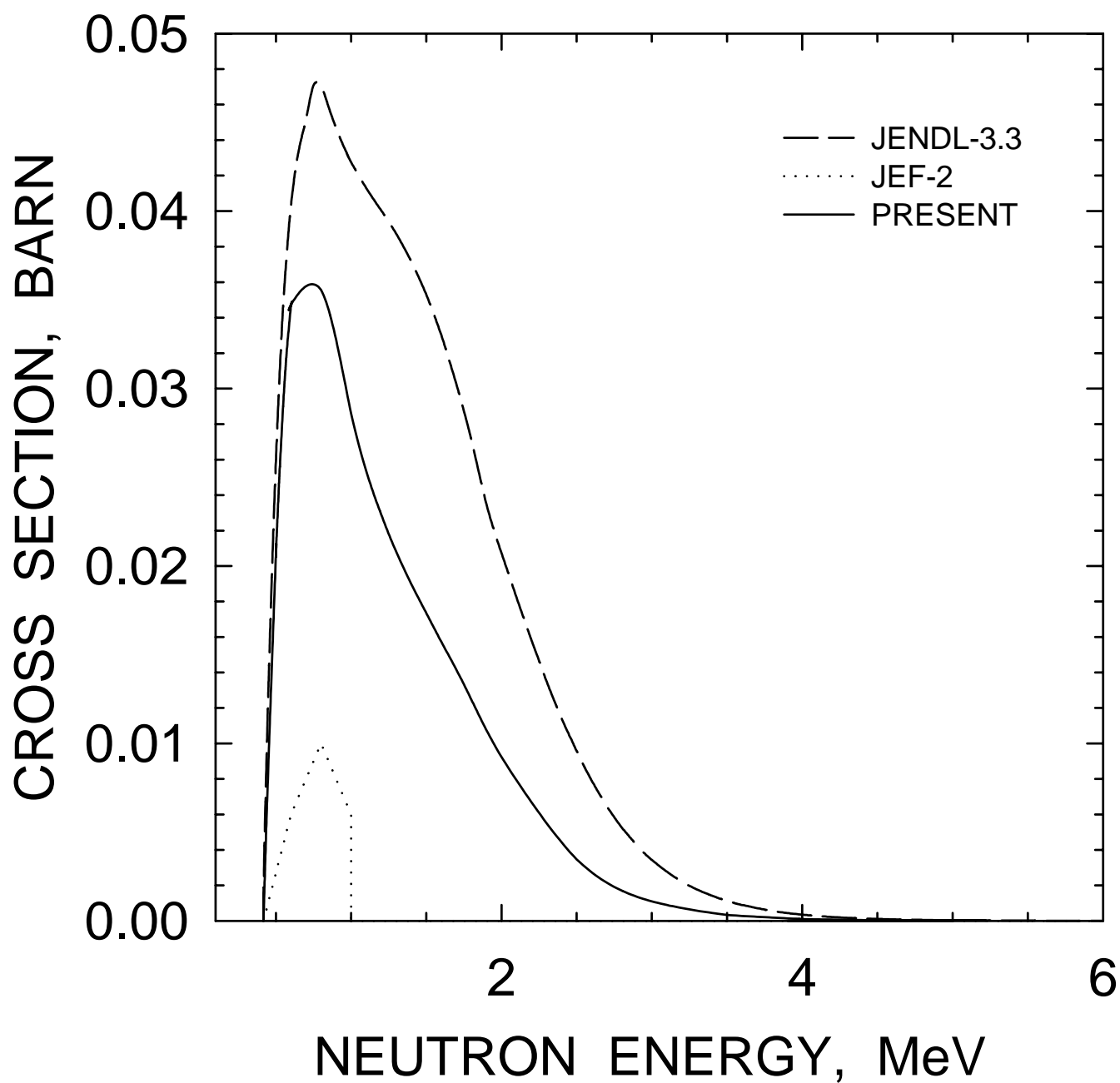
FIG. 57

^{233}U: 0.5038, 7/2$^-$ LEVEL EXCITATION
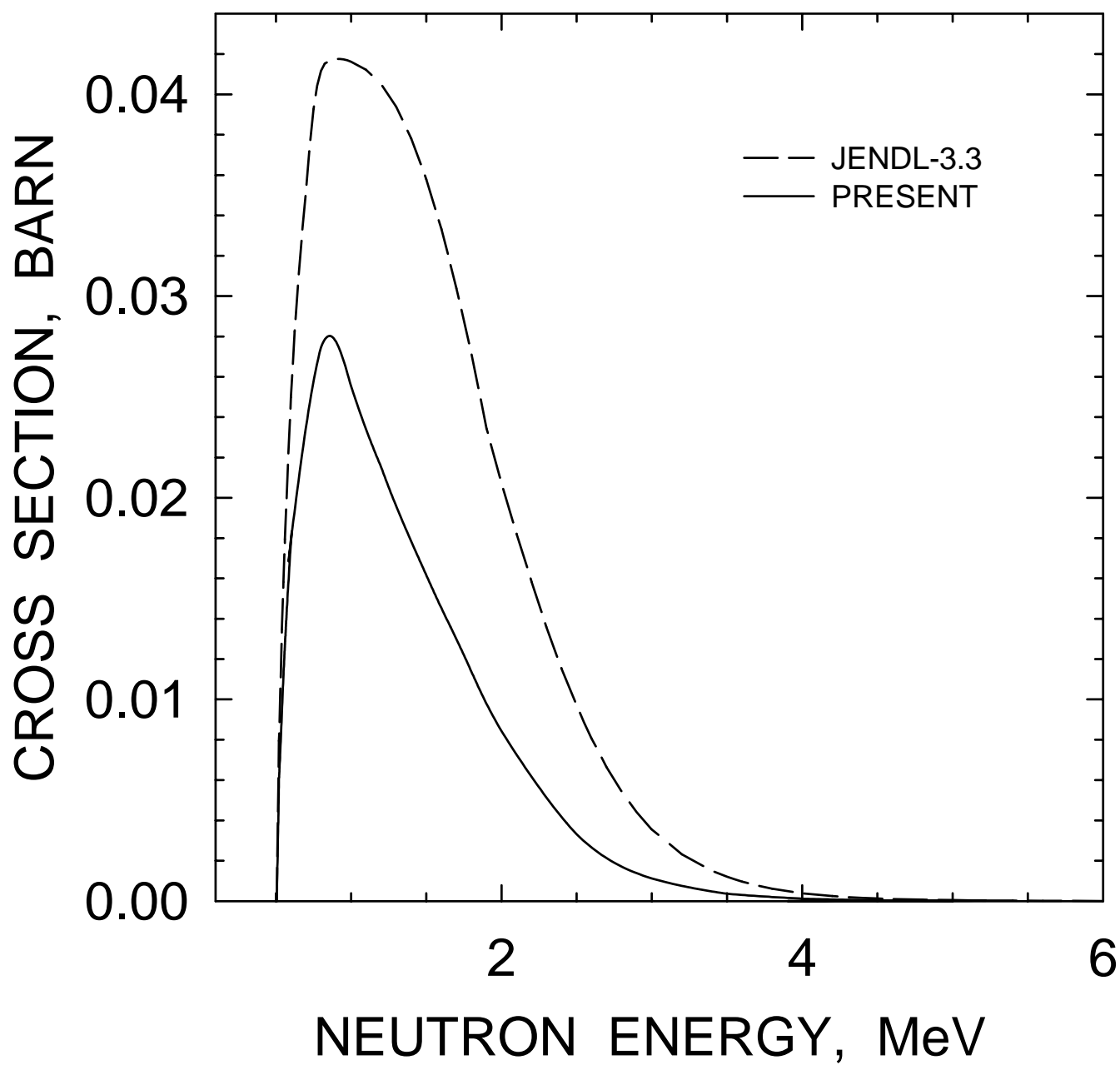
FIG. 58

^{233}U: 0.5466, (5/2$^+$) LEVEL EXCITATION
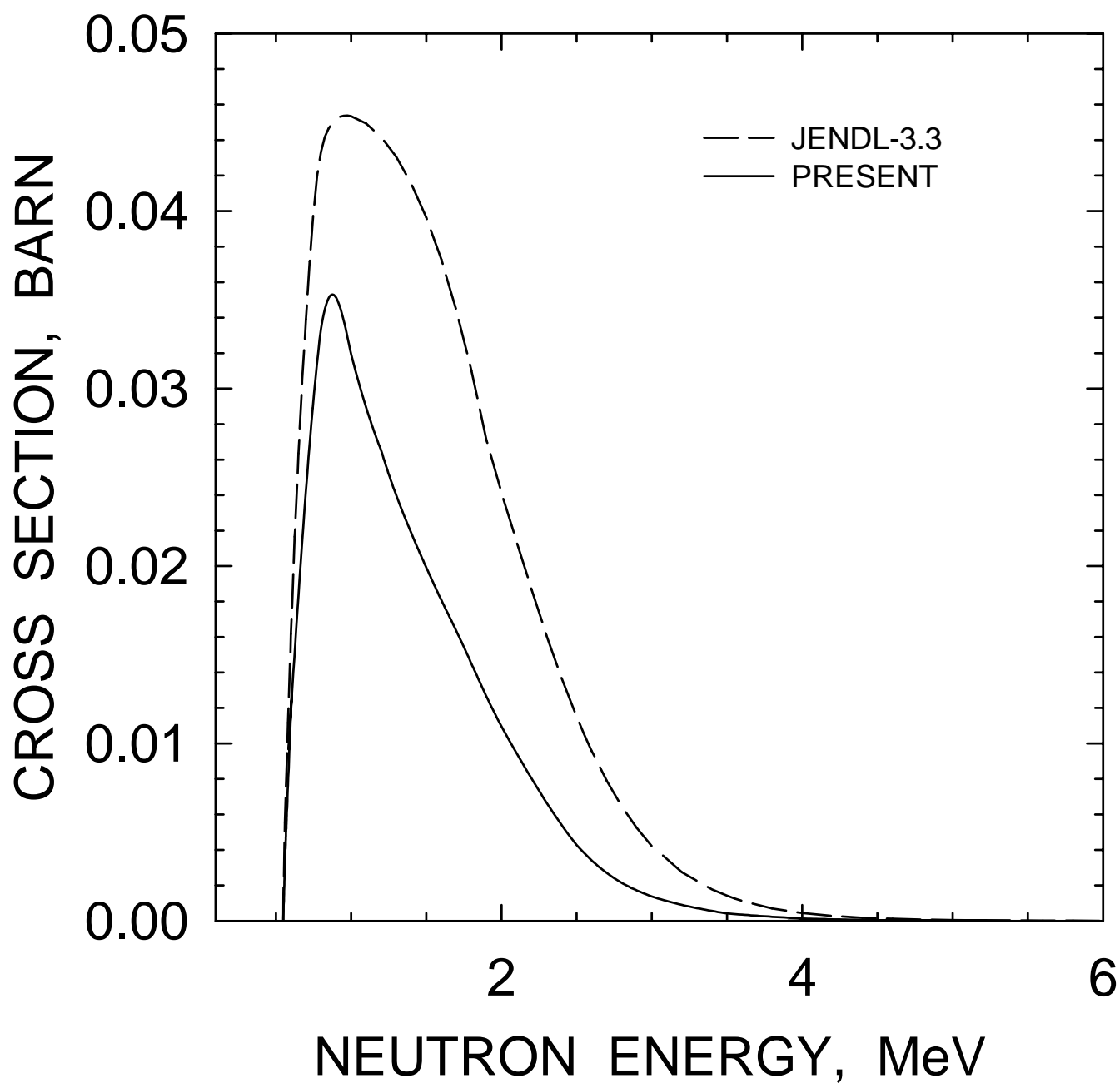
FIG. 59

^{233}U: 0.5615, (9/2$^-$) LEVEL EXCITATION
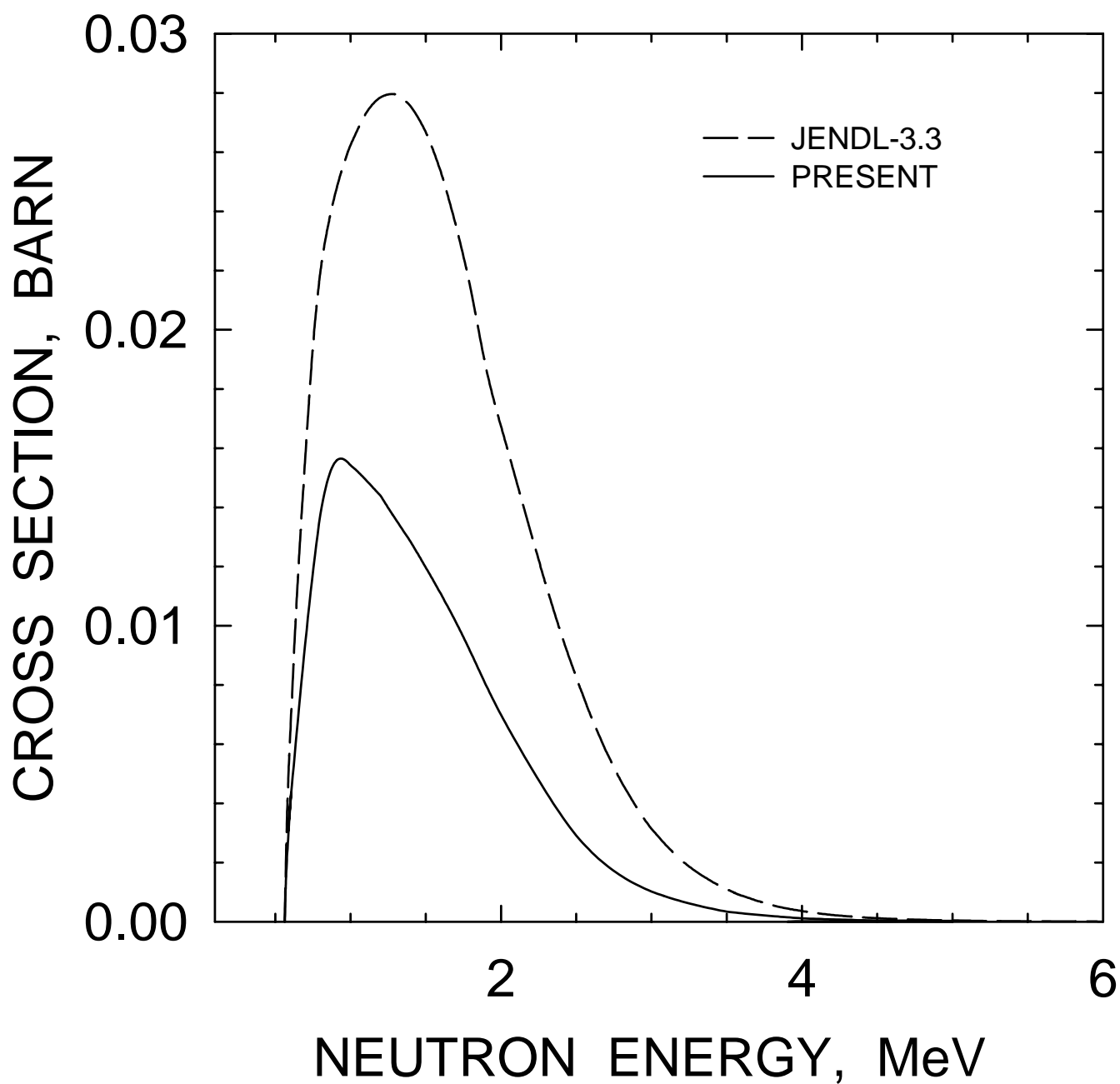
FIG. 60

^{233}U: 0.5972, (7/2^{+}) LEVEL EXCITATION

CROSS SECTION, BARN

NEUTRON ENERGY, MeV

JENDL-3.3
PRESENT

FIG. 61

^{233}U INELASTIC CROSS SECTION

▲ SMITH ET AL., 1983
— — JENDL-3.3
—·— ENDF/B-VI
········· JEF-2
——— PRESENT
—··— DIR. CONTR.GR.STATE BAND

CROSS SECTION, BARN

NEUTRON ENERGY, MeV
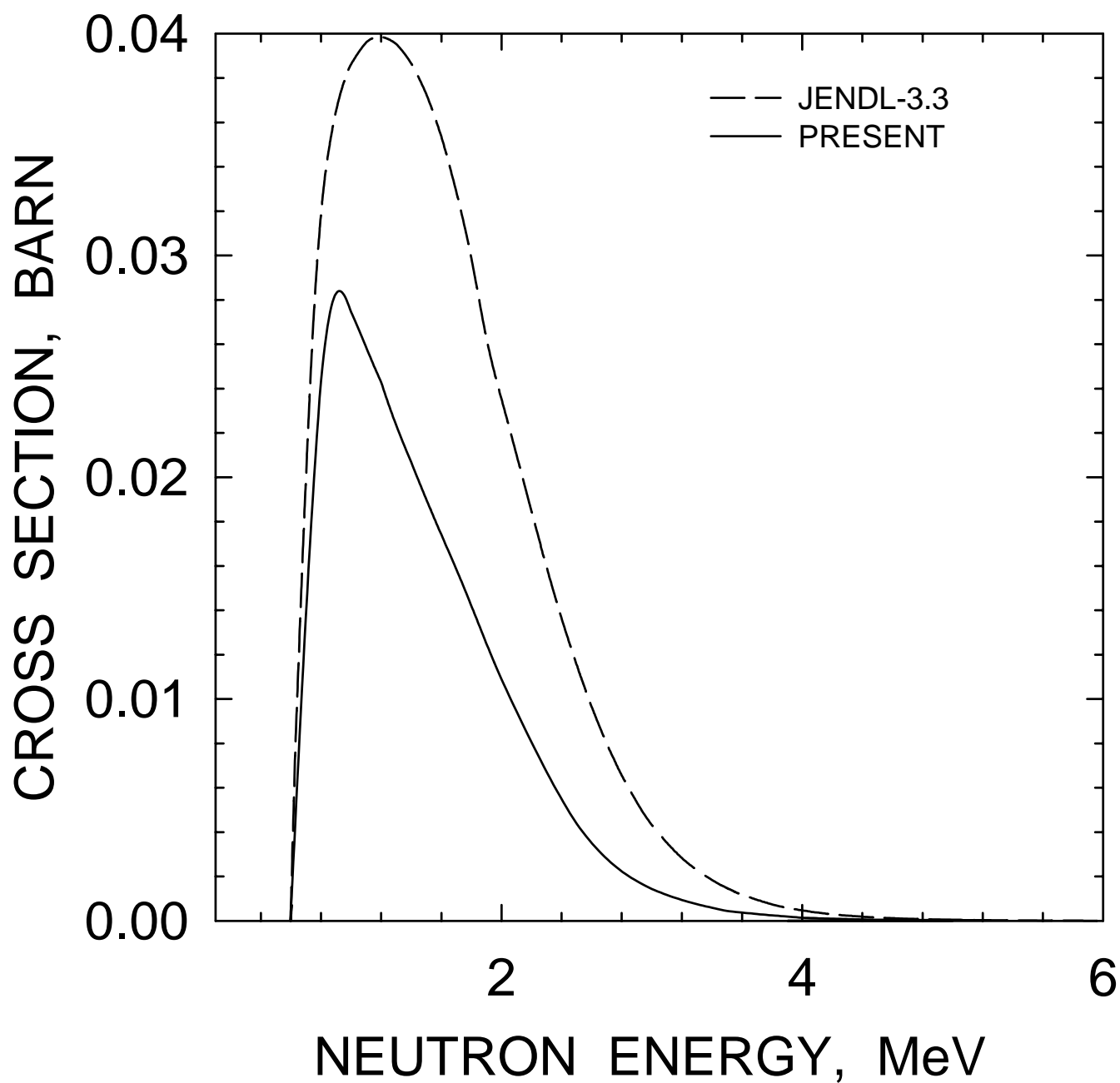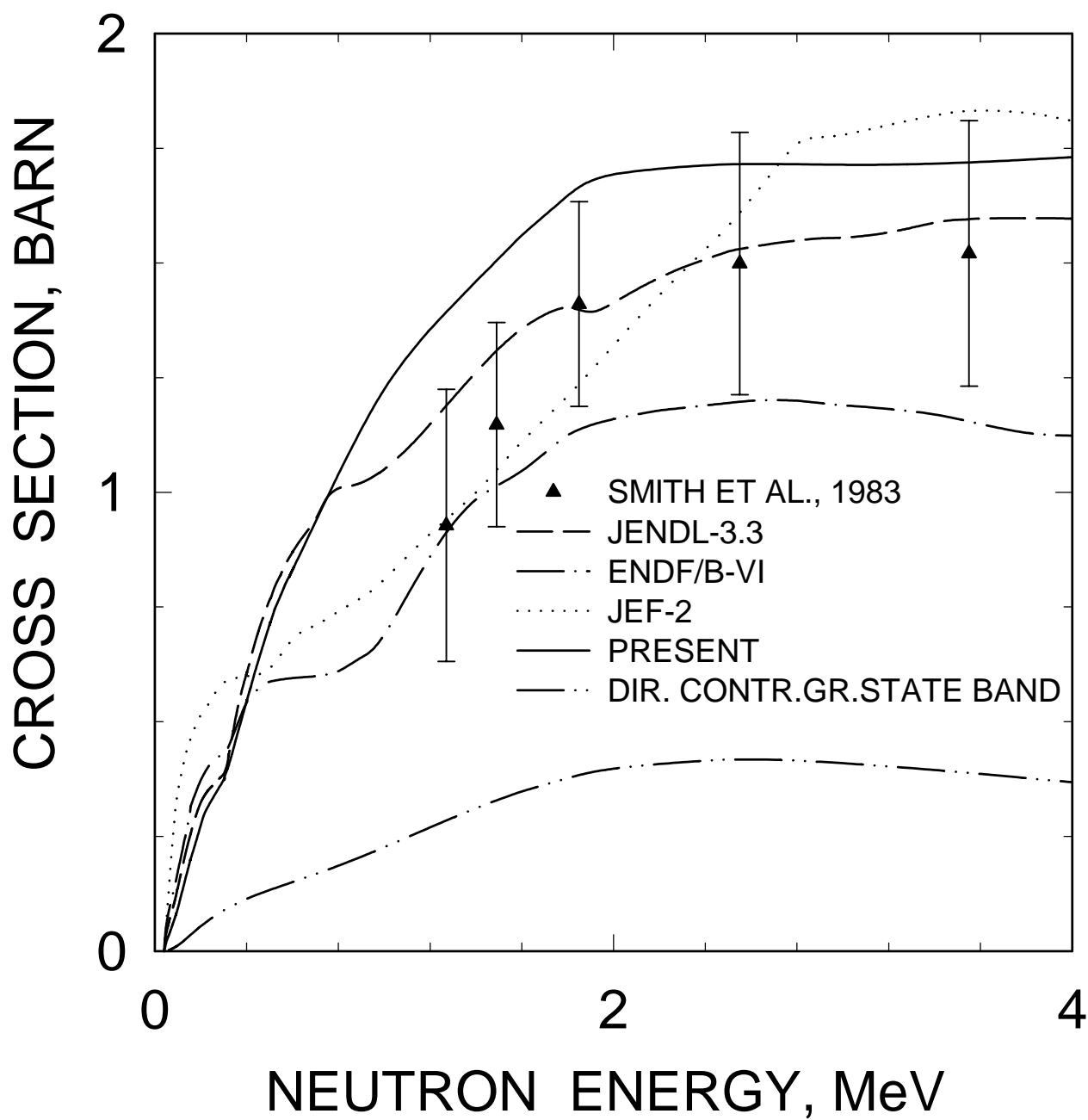
FIG. 62

^{233}U INELASTIC CROSS SECTION
(CONTINUUM CONTRIBUTION)

FIG. 63

^{233}U INELASTIC CROSS SECTION

▲   SMITH ET AL., 1983
— —   JENDL-3.3
— · —   ENDF/B-VI
· · · · ·   JEF-2
———   PRESENT
— · · —   DIR. CONTR.GR.STATE BAND
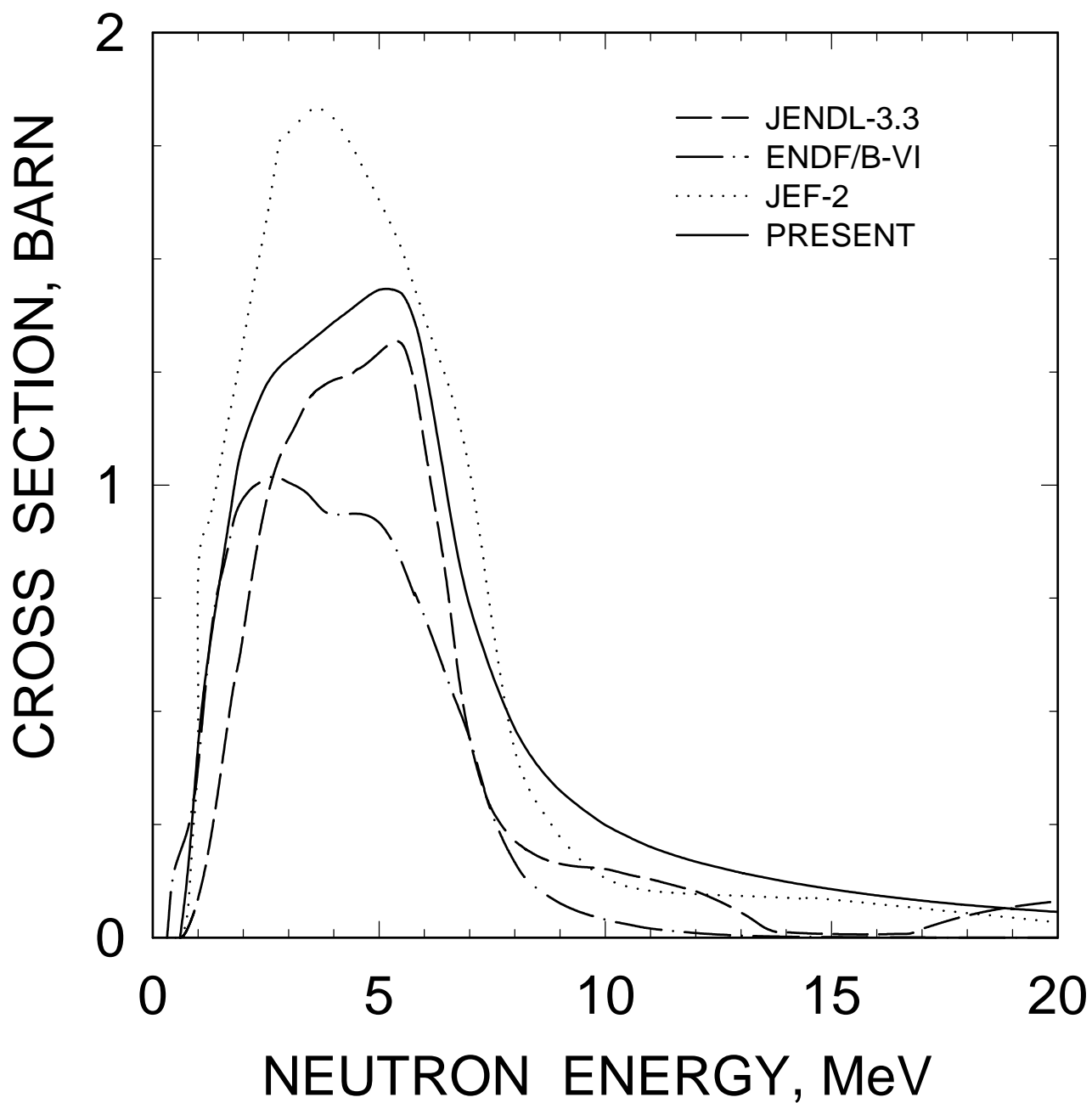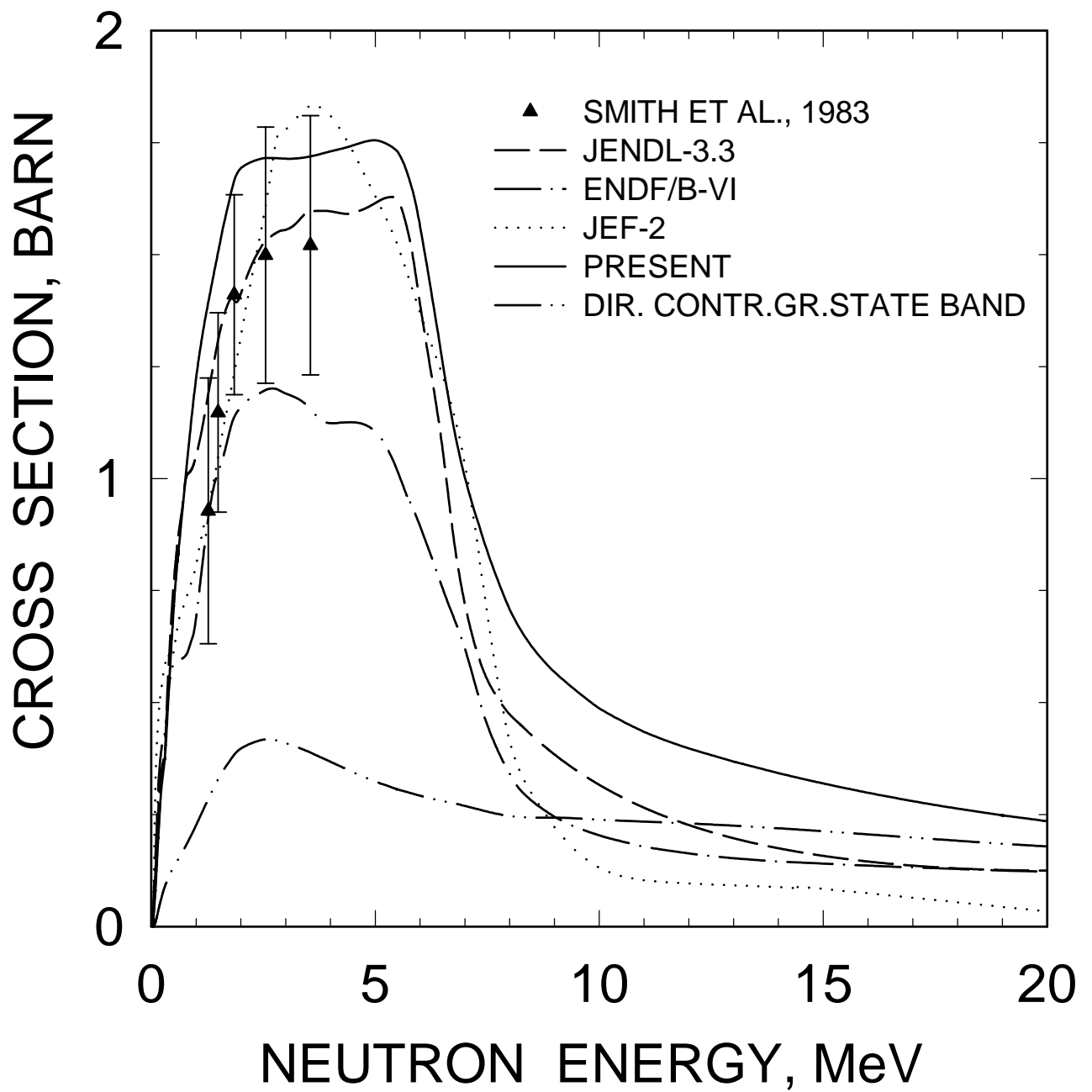
FIG. 64

^{233}U CAPTURE CROSS SECTION
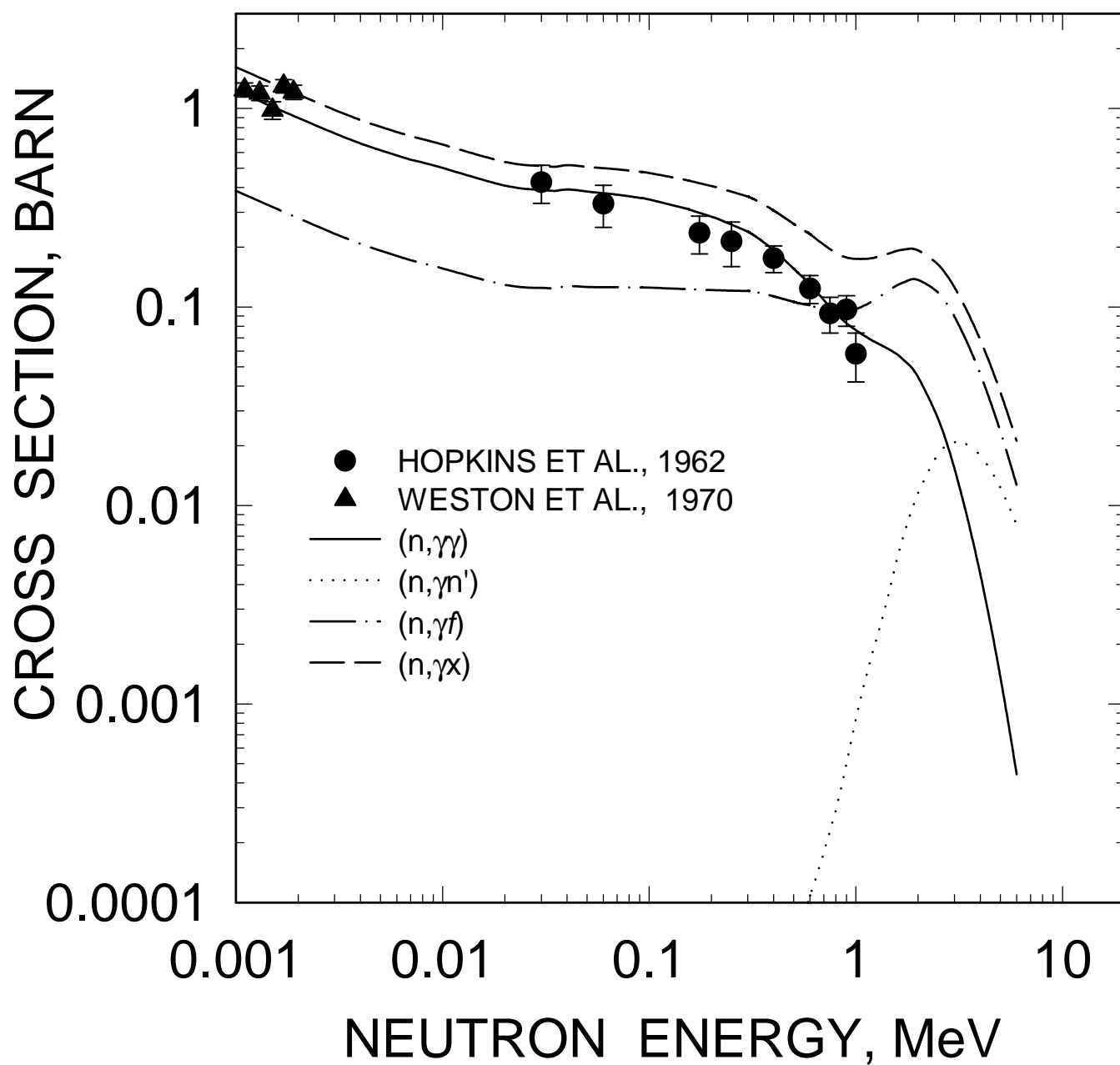
FIG. 65

^{233}U CAPTURE CROSS SECTION
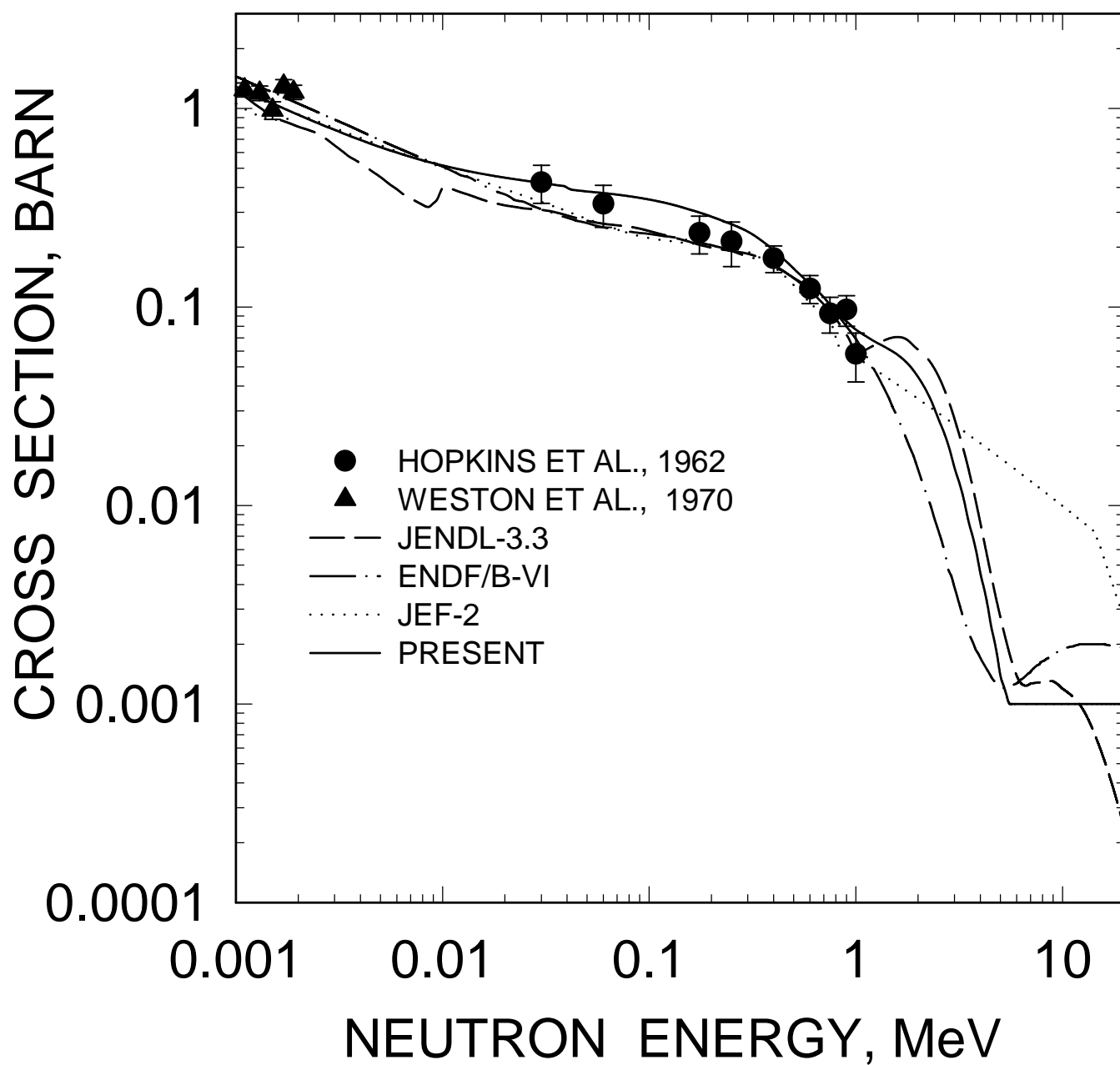
FIG. 66

^{233}U FISSION CROSS SECTION
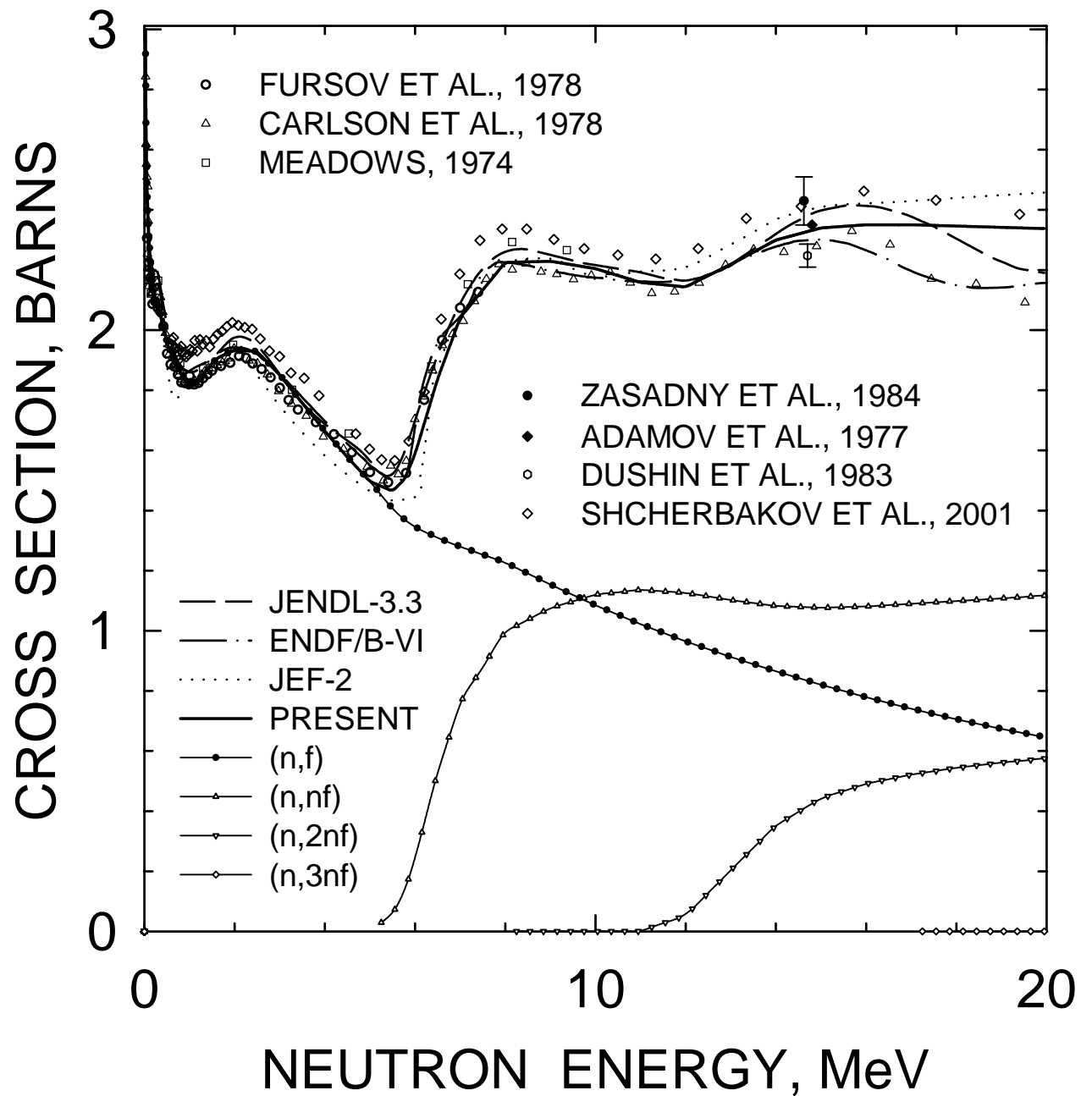
FIG. 67

^{233}U(n,f) CHANCE FISSION CONTRIBUTIONS
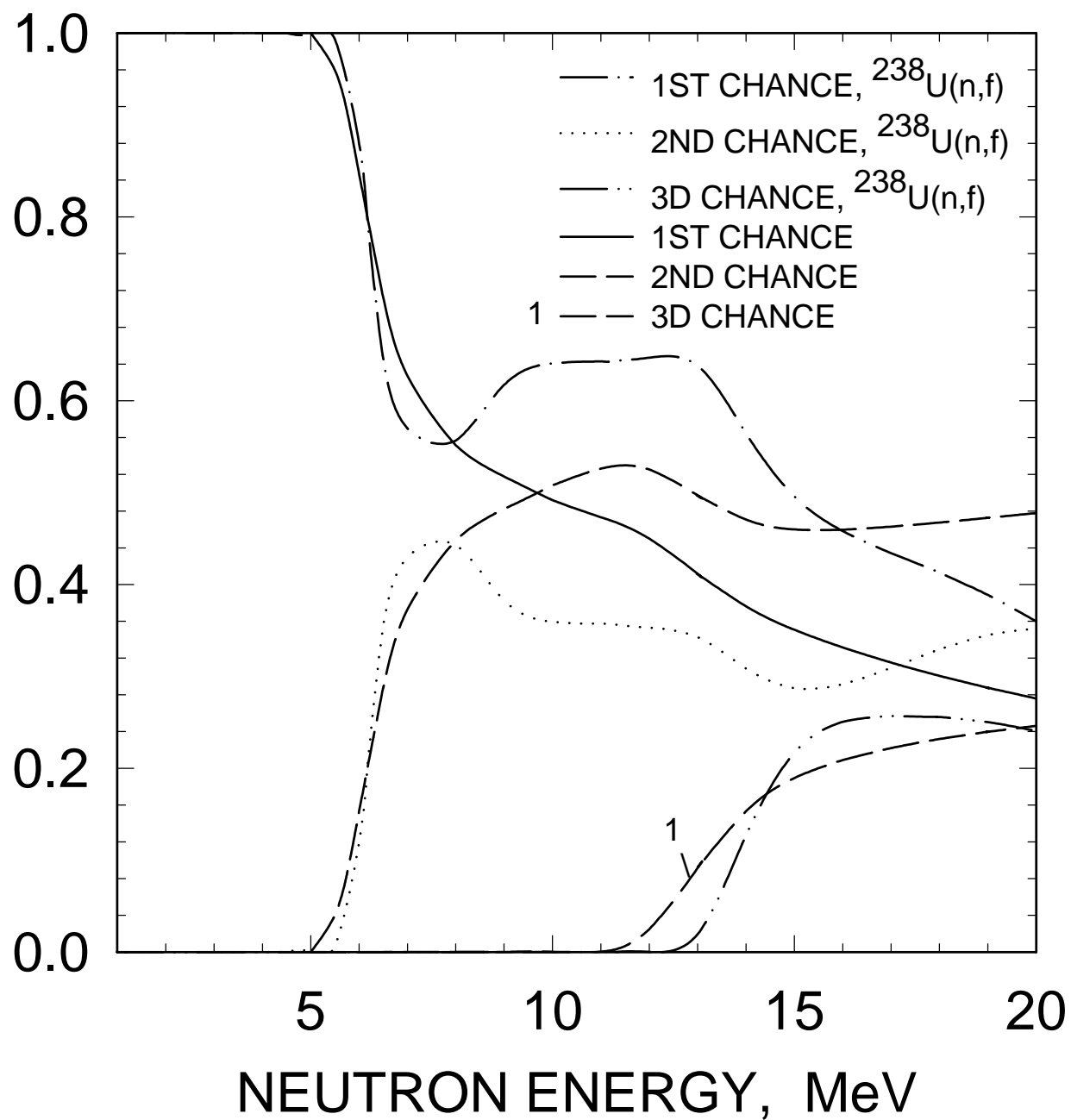
FIG. 68

^{232}U FISSION CROSS SECTION

- □ FURSOV ET AL.,1986
- ○ VOROTNIKOV ET AL.,1970
- — — JENDL-3.2
- — · — ENDF/B-VI
- —— PRESENT
- 1 —— (n,f)
- 2 ········ (n,nf)
- 3 — — (n,2nf)

CROSS SECTION, BARN

NEUTRON ENERGY, MeV
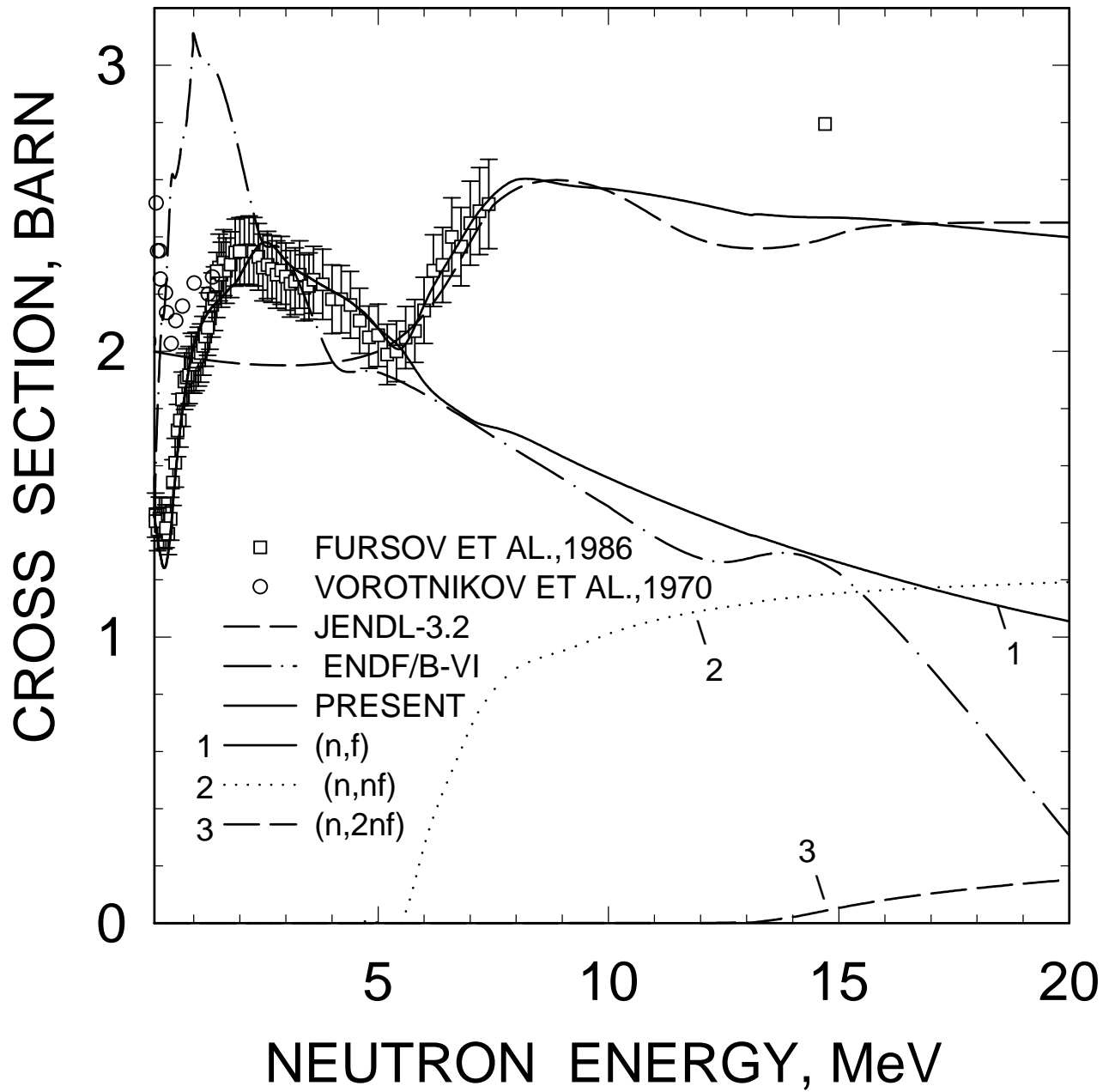
FIG. 69

^{233}U (N,2N) CROSS SECTION
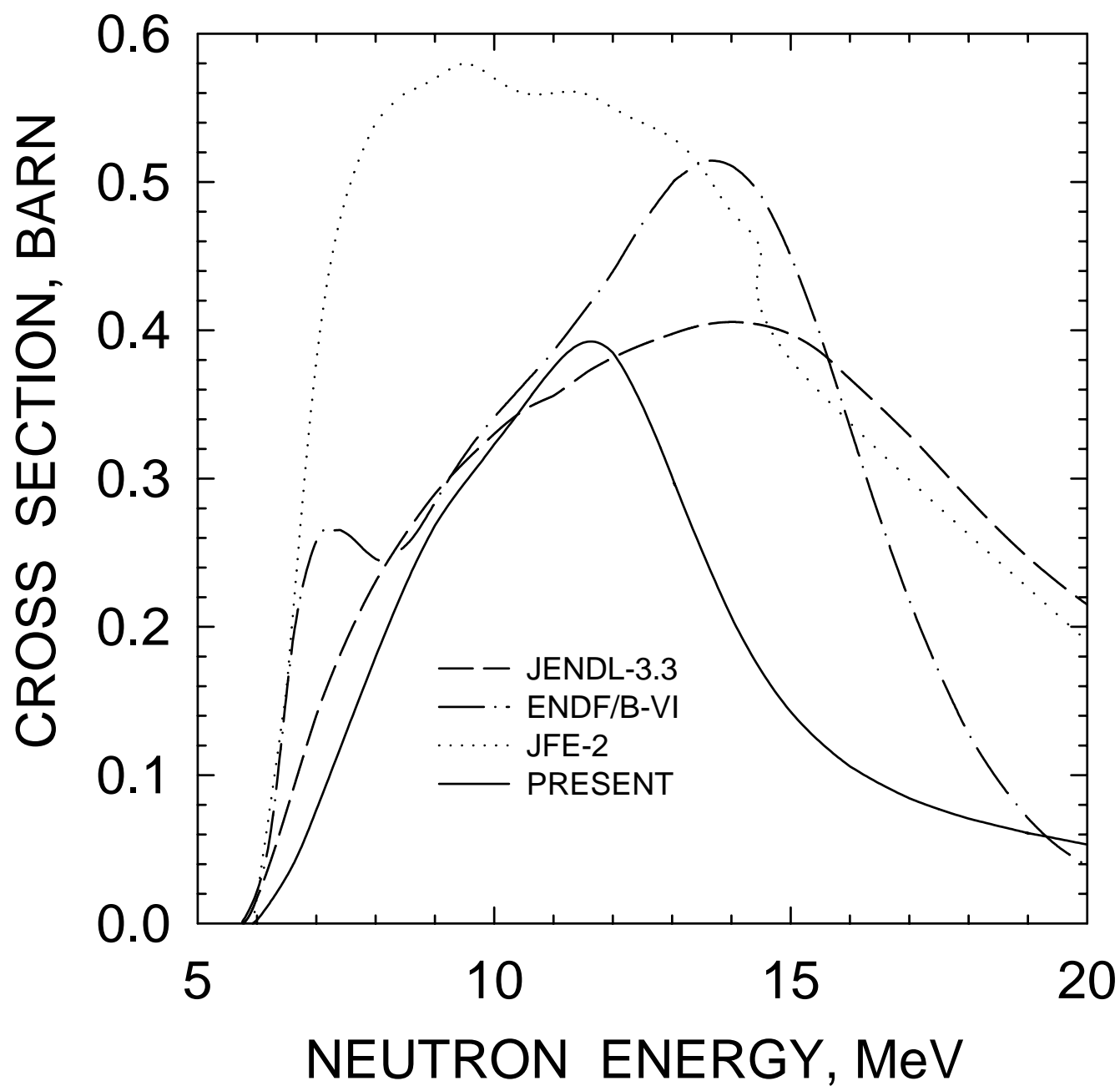
FIG. 70

^{233}U (N,3N) CROSS SECTION
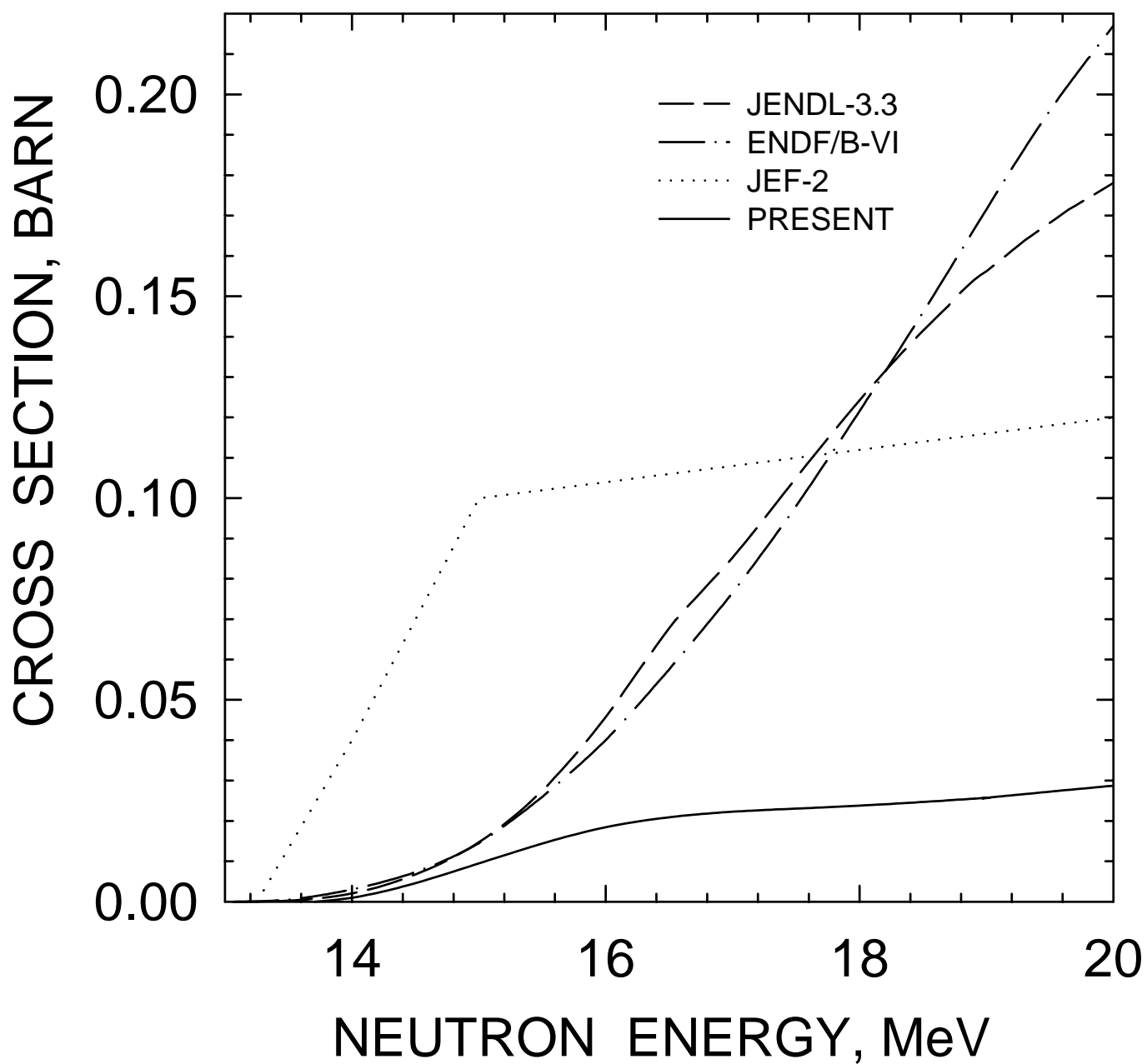
FIG. 71

^{233}U NEUTRON MULTIPLICITY

FIG. 72
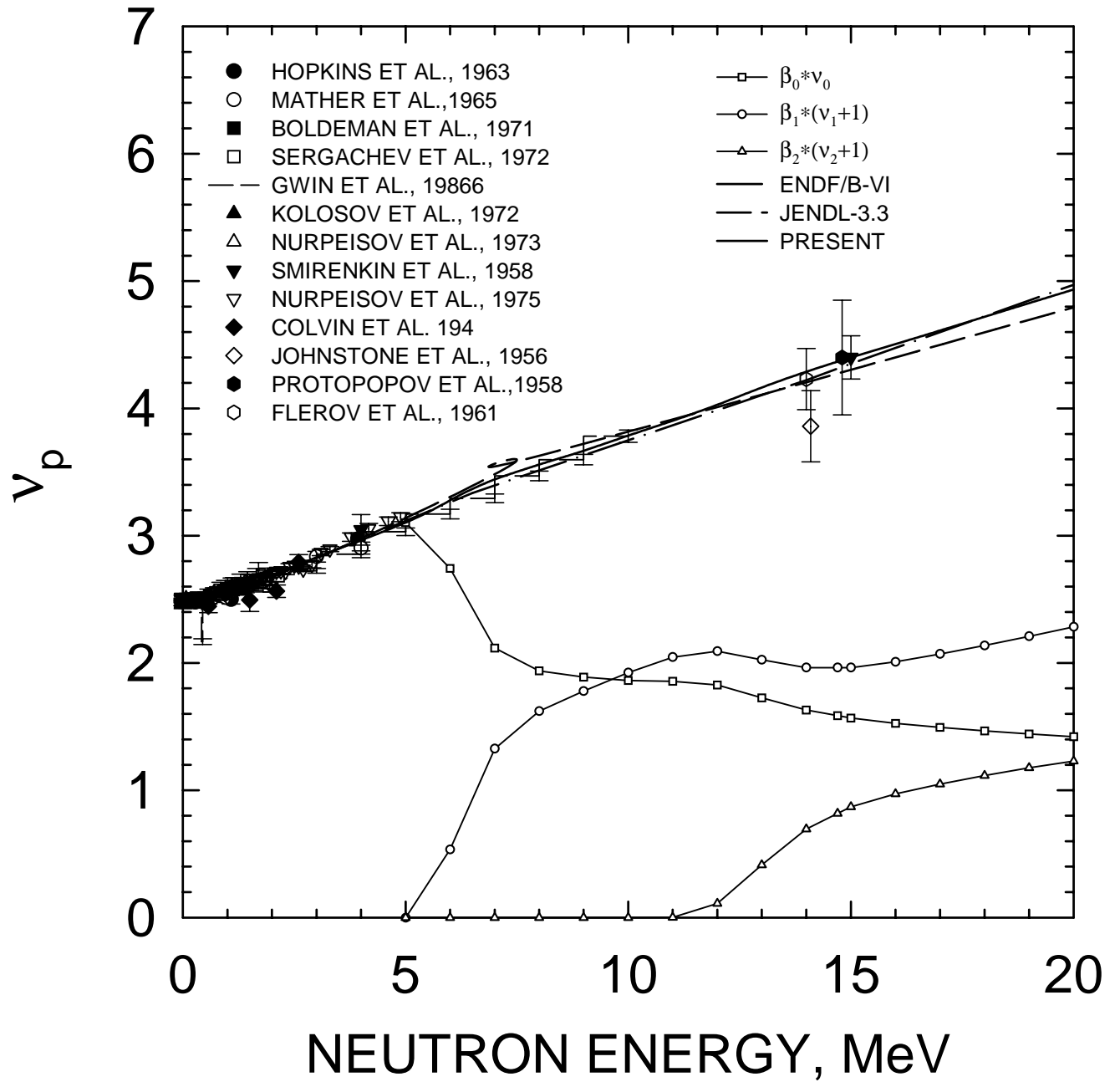
FIG. 73

^{233}U E_n=20 MeV
COMPONENTS OF FIRST NEUTRON SPECTRUM
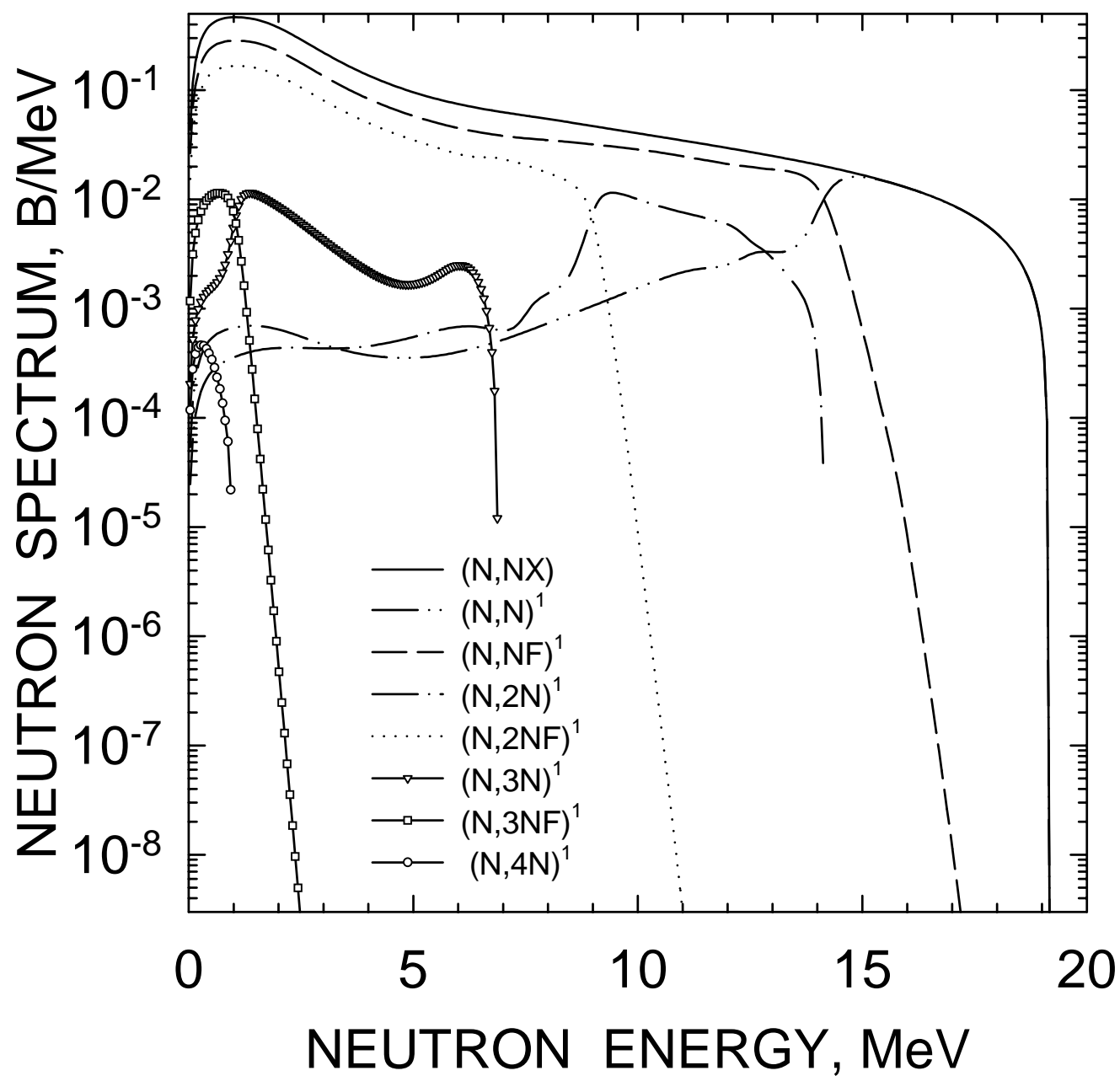
Legend:
- (N,NX)
- (N,N)[1]
- (N,NF)[1]
- (N,2N)[1]
- (N,2NF)[1]
- (N,3N)[1]
- (N,3NF)[1]
- (N,4N)[1]

X-axis: NEUTRON ENERGY, MeV
Y-axis: NEUTRON SPECTRUM, B/MeV

FIG. 74

^{233}U E_n=20 MeV
COMPONENTS OF SECOND NEUTRON SPECTRUM

Legend:
- (N,2NX)^2
- (N,2N)^2
- (N,2NF)^2
- (N,3N)^2
- (N,3NF)^2
- (N,4N)^2

NEUTRON SPECTRUM, B/MeV

NEUTRON ENERGY, MeV

FIG. 75

^{233}U E_n=20 MeV
COMPONENTS OF THIRD NEUTRON SPECTRUM

Legend:
- $(N,3NX)^3$
- $(N,3N)^3$
- $(N,3NF)^3$
- $(N,4N)^3$

Y-axis: NEUTRON SPECTRUM, B/MeV
X-axis: NEUTRON ENERGY, MeV

FIG. 76

FIG. 77

^{233}U E_n=14 MeV
COMPONENTS OF FIRST NEUTRON SPECTRUM

Legend:
- (N,NX)
- (N,N')
- (N,NF)[1]
- (N,2N)[1]
- (N,2NF)[1]
- (N,3N)[1]

Y-axis: NEUTRON SPECTRUM, B/MeV
X-axis: NEUTRON ENERGY, MeV
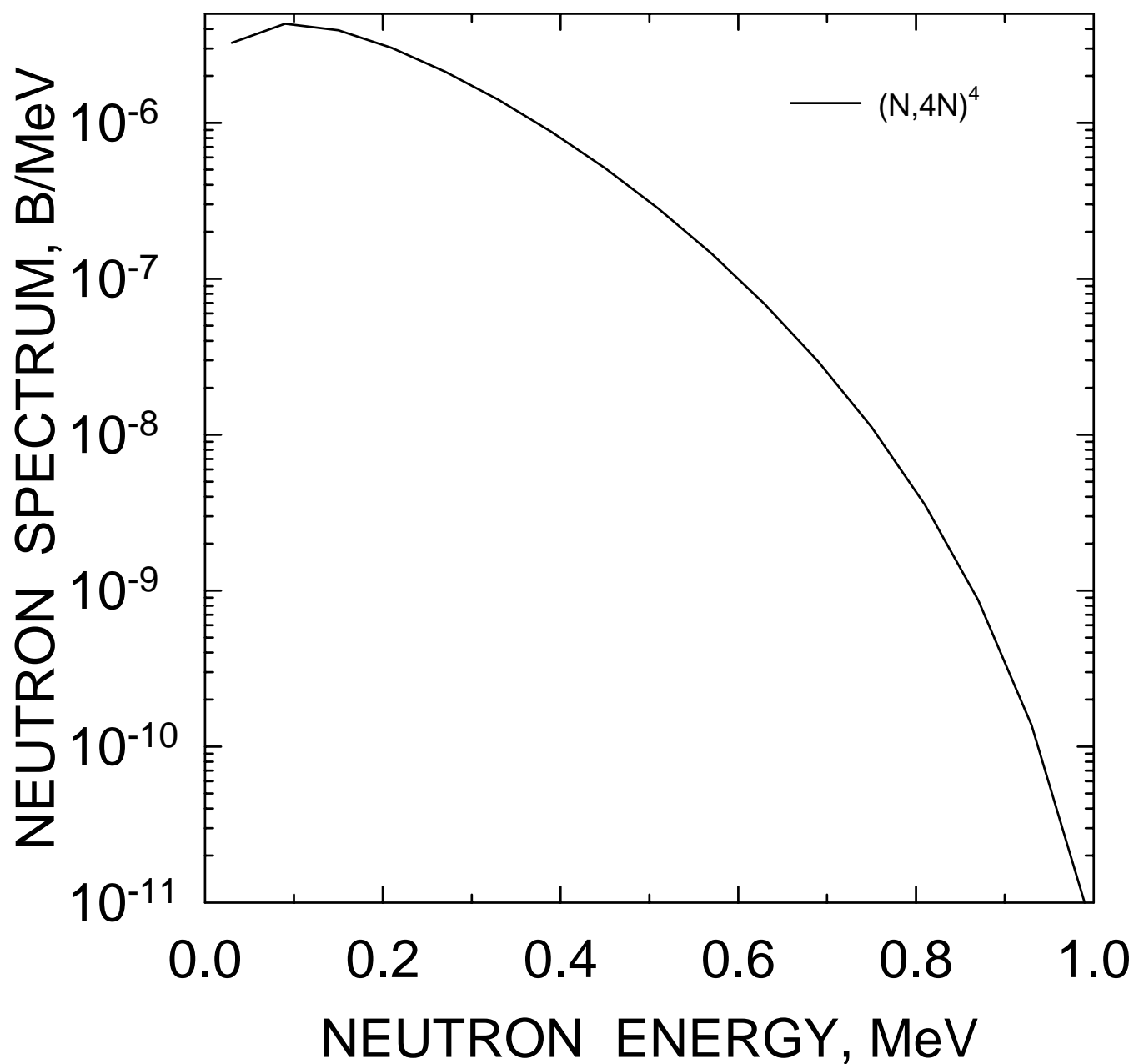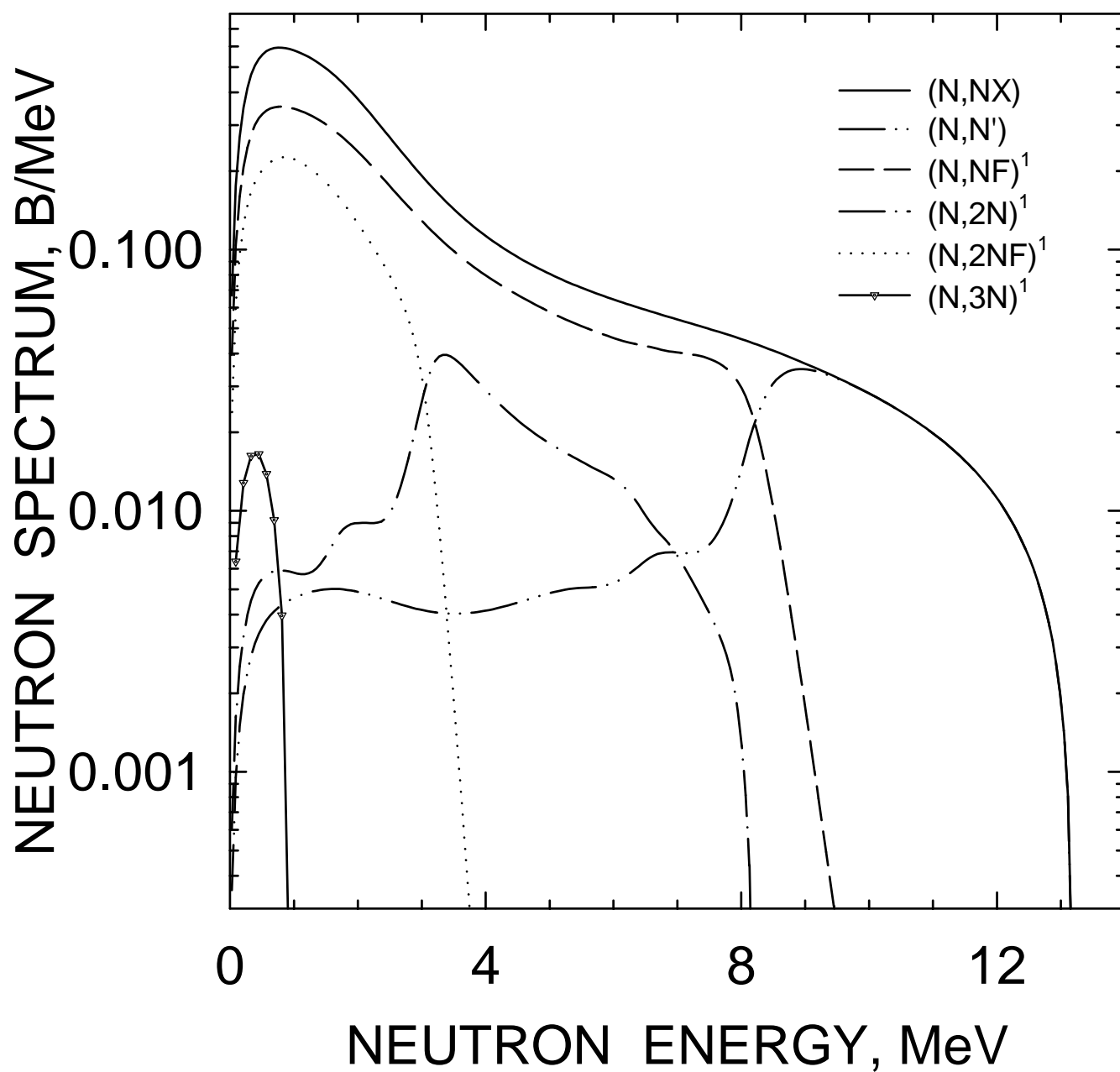
FIG. 78

^{233}U E_n=14 MeV
COMPONENTS OF SECOND NEUTRON SPECTRUM

Legend:
- $(N,2NX)^2$
- $(N,2N)^2$
- $(N,2NF)^2$
- $(N,3N)^2$

NEUTRON SPECTRUM, B/MeV (vertical axis)
NEUTRON ENERGY, MeV (horizontal axis)
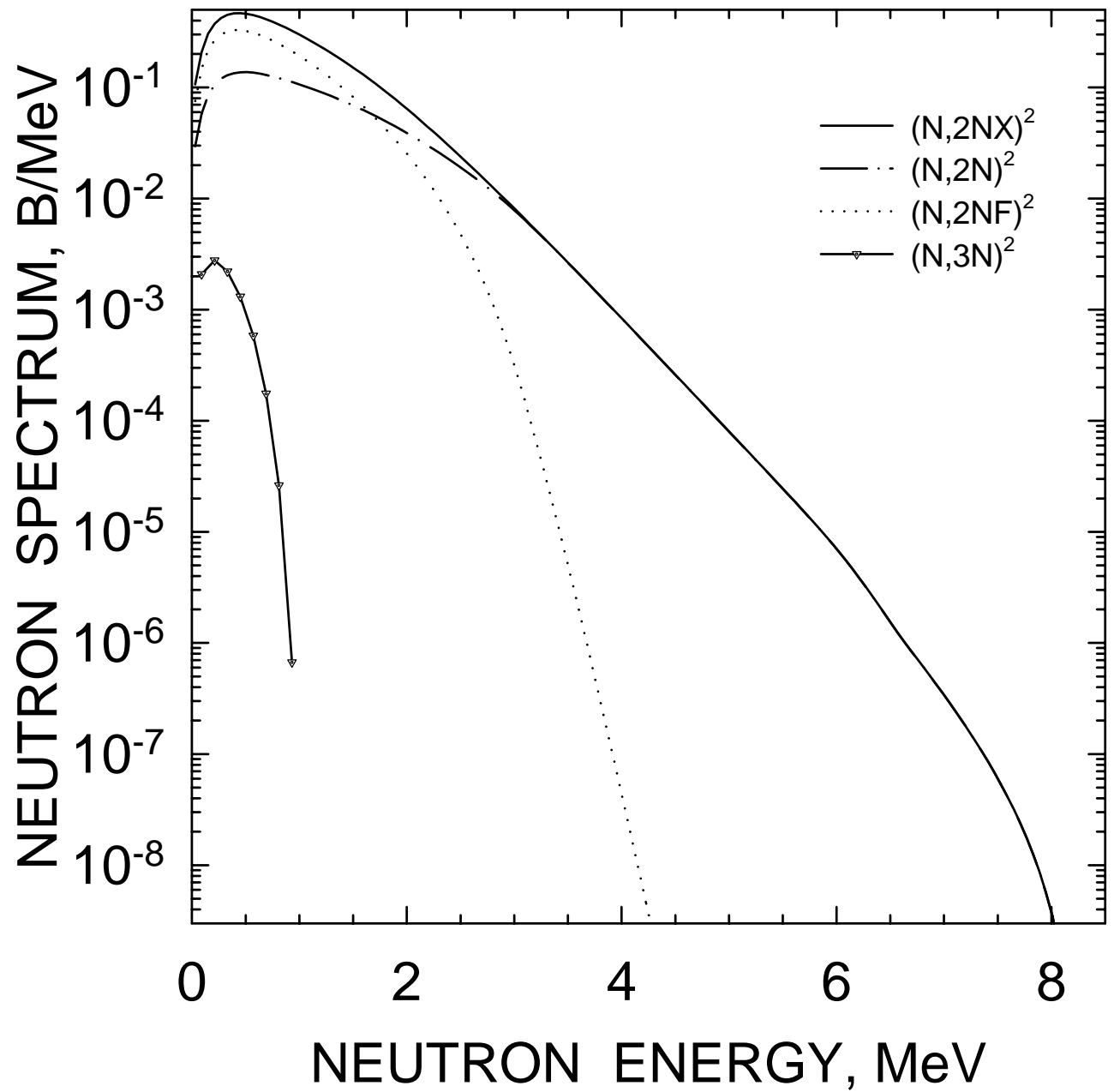
FIG. 79

^{233}U E_n=14 MeV
COMPONENTS OF THIRD NEUTRON SPECTRUM

FIG. 80

^{233}U E_n=8 MeV
COMPONENTS OF FIRST NEUTRON
SPECTRUM
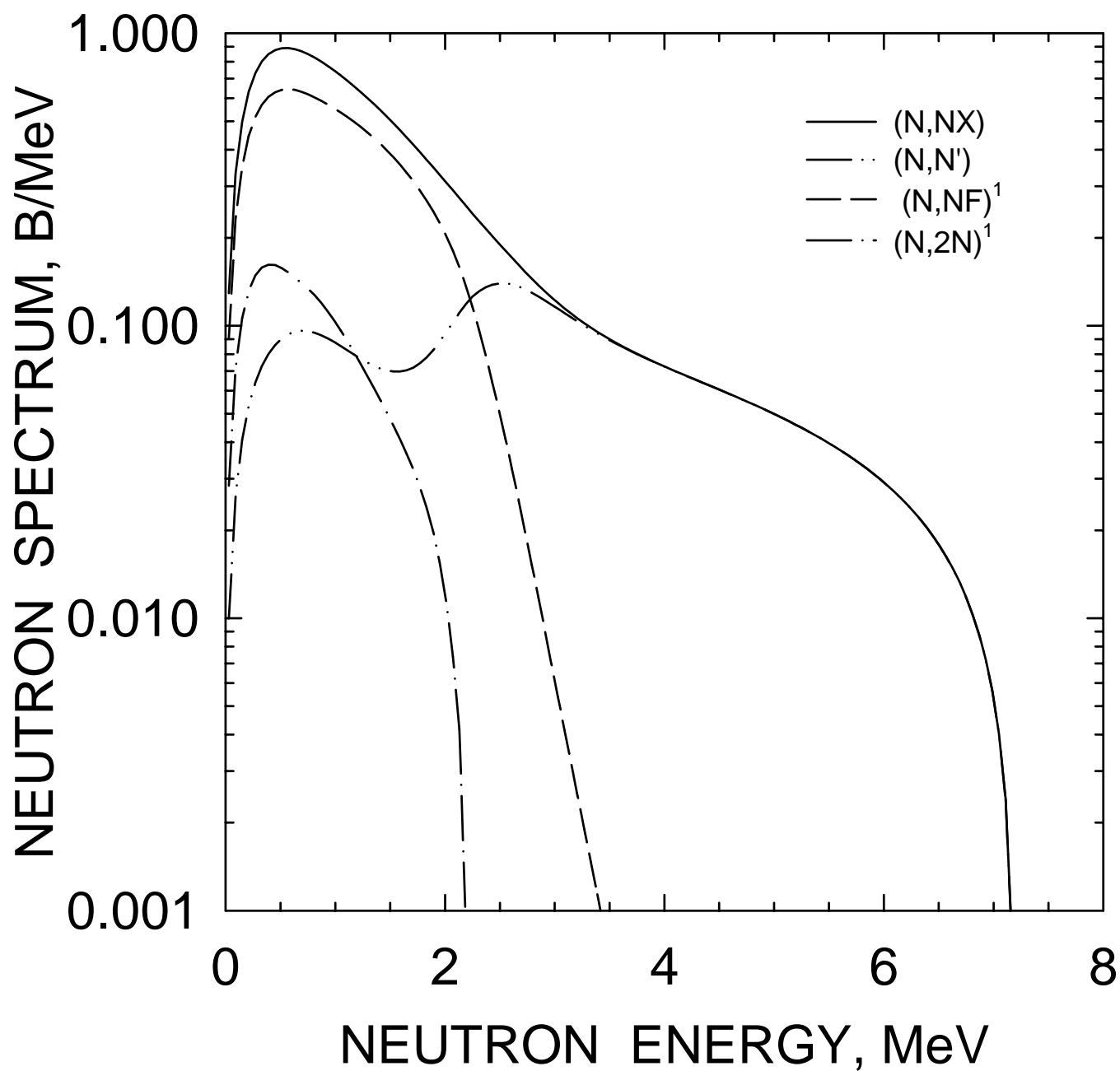
Legend:
- (N,NX)
- (N,N')
- (N,NF)[1]
- (N,2N)[1]

X-axis: NEUTRON ENERGY, MeV
Y-axis: NEUTRON SPECTRUM, B/MeV

FIG. 81

^{233}U E_n=8 MeV
COMPONENTS OF SECOND NEUTRON SPECTRUM
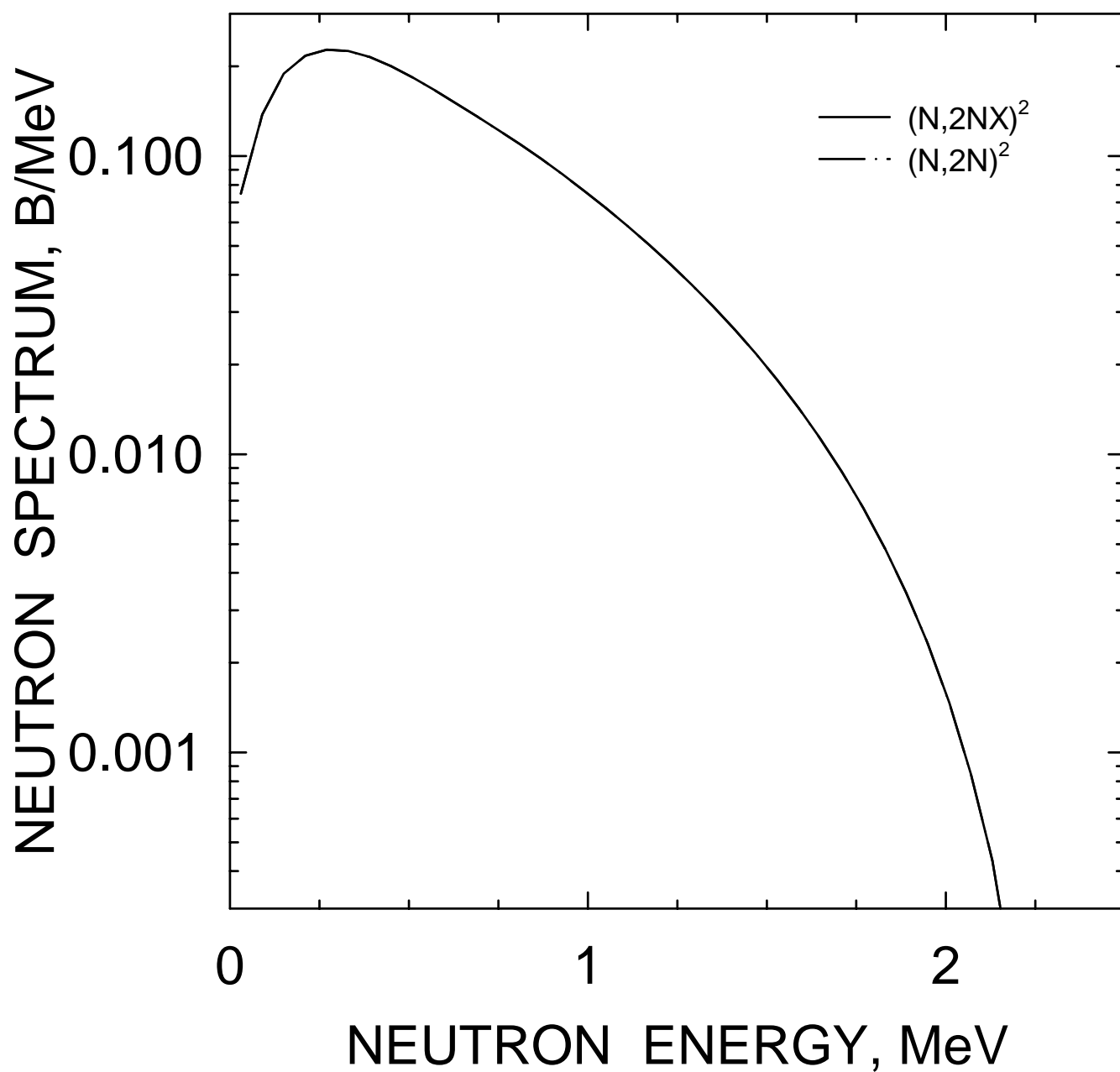
Legend:
— $(N,2NX)^2$
— ·· $(N,2N)^2$

NEUTRON SPECTRUM, B/MeV (y-axis: 0.100, 0.010, 0.001)
NEUTRON ENERGY, MeV (x-axis: 0, 1, 2)

FIG. 82

^{233}U FISSION NEUTRON SPECTRUM
E_n=0.025eV

- STAROSTOV ET AL., 1983
- — JENDL-3.3
- — ·· ENDF/B-VI
- —— PRESENT

FIG. 83

^{233}U FISSION NEUTRON SPECTRUM
E_n=0.025eV

R(E_n,E)

○   LAJTAI ET AL., 1984
— —   JENDL-3.3
— ·   ENDF/B-VI
———   PRESENT
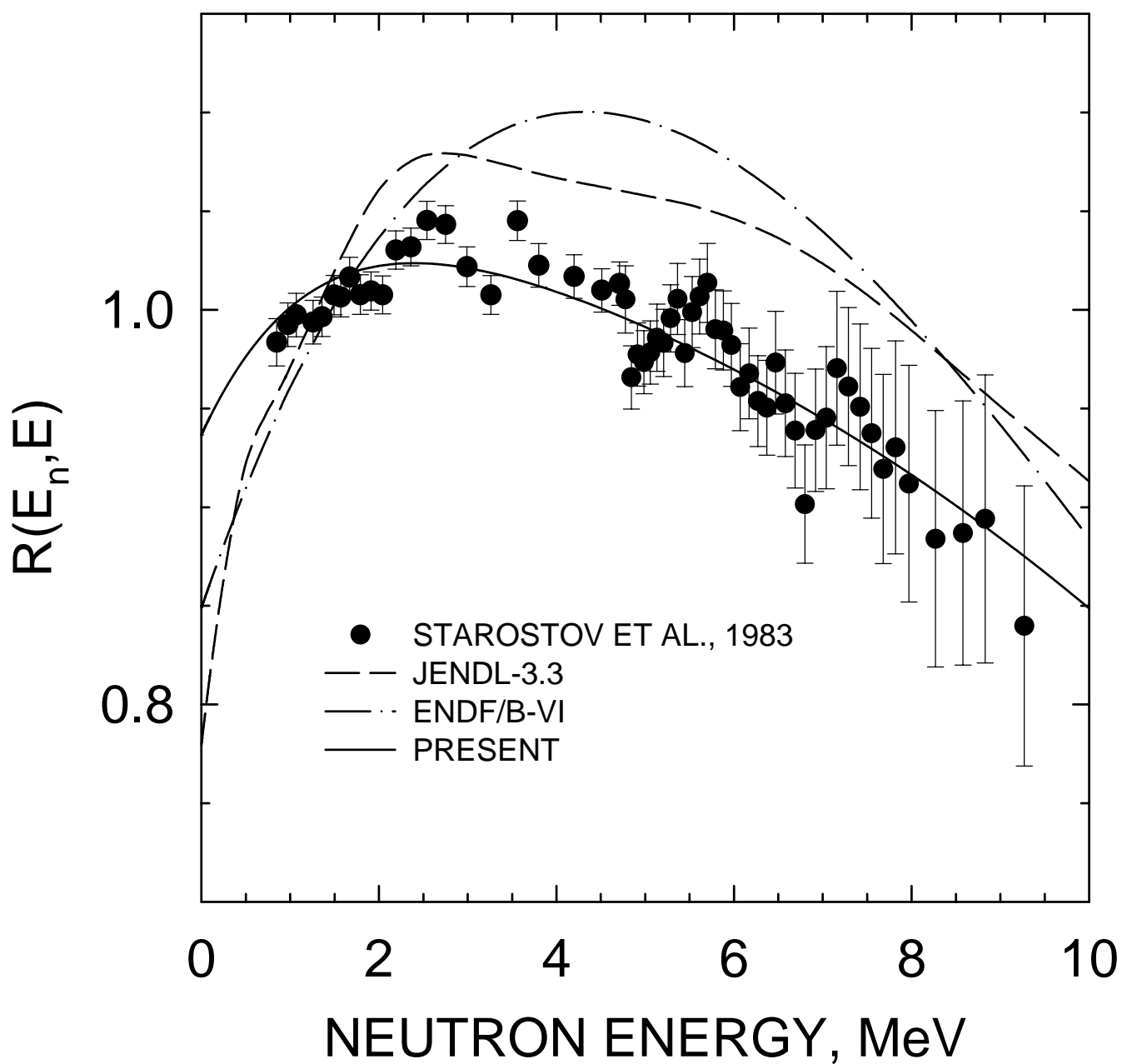
NEUTRON ENERGY, MeV
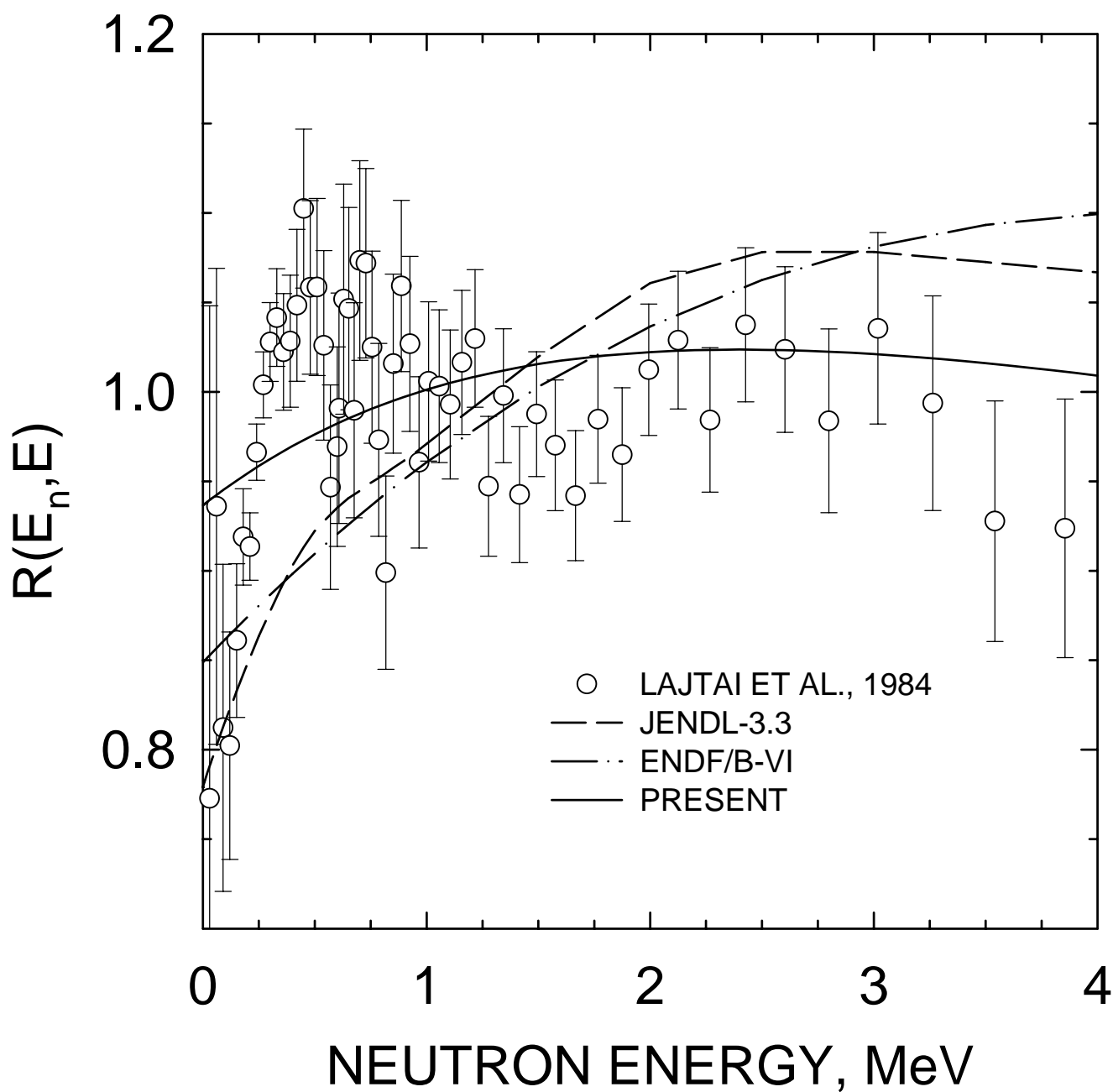
FIG. 84

^{233}U FISSION NEUTRON SPECTRUM
E_n=0.55MeV
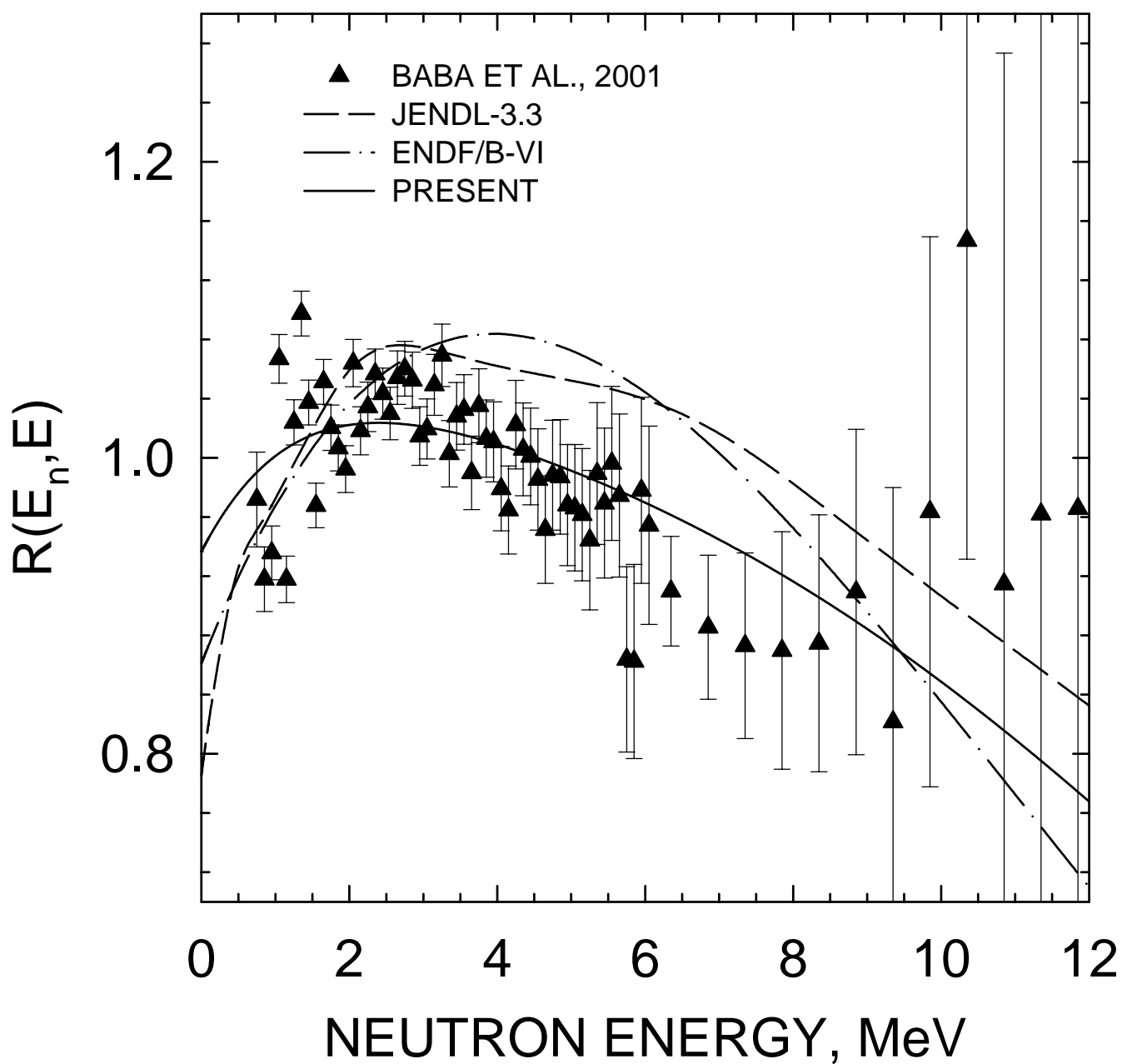
FIG. 85

^{233}U FISSION NEUTRON SPECTRUM
E_n=1.9MeV

- ● MIURA ET AL., 2001
- — — JENDL-3.3
- —·— ENDF/B-VI
- —— PRESENT

R(E_n,E)

NEUTRON ENERGY, MeV
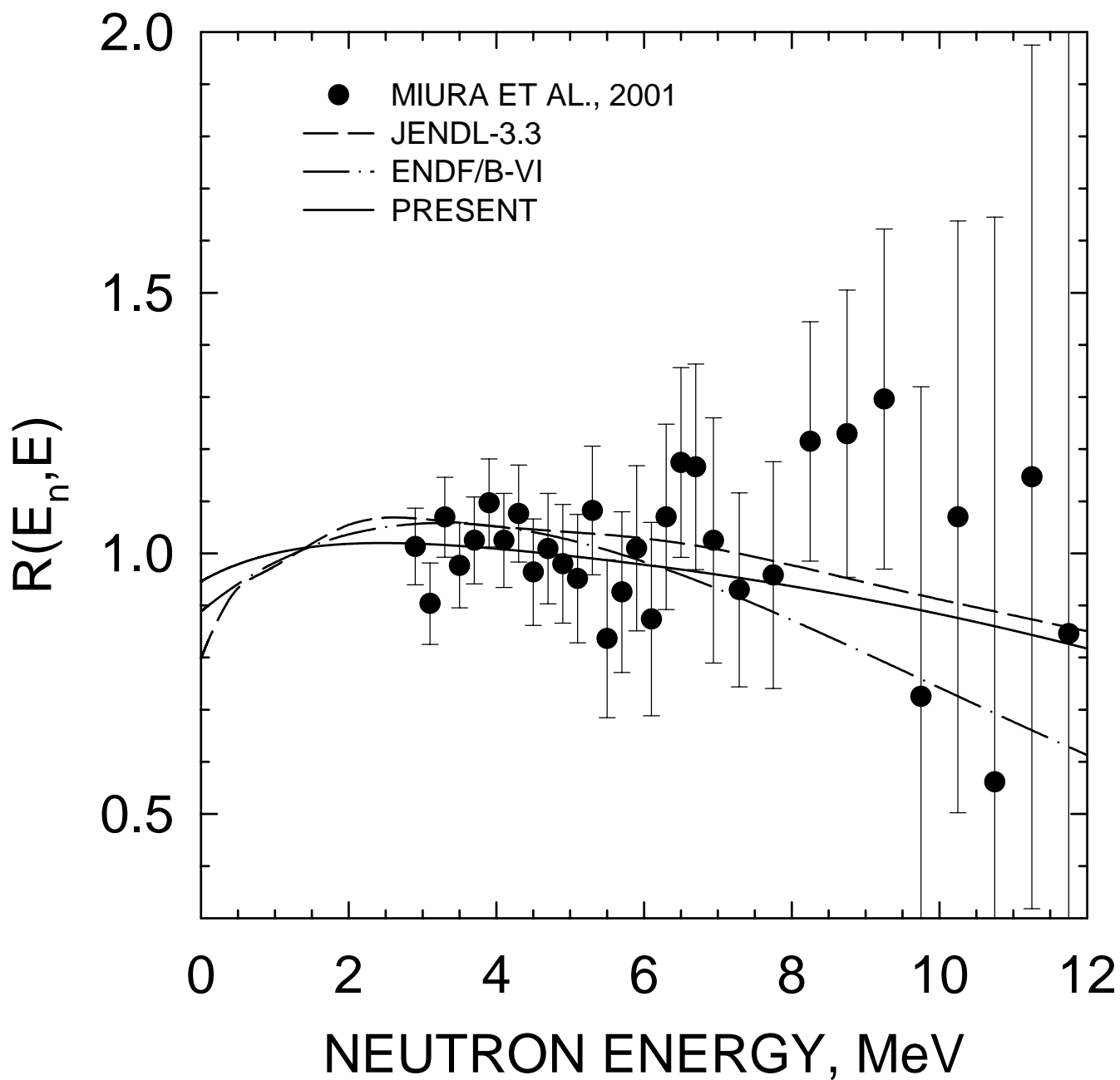
FIG. 86

^{233}U FISSION NEUTRON SPECTRUM
E_n=4.1MeV
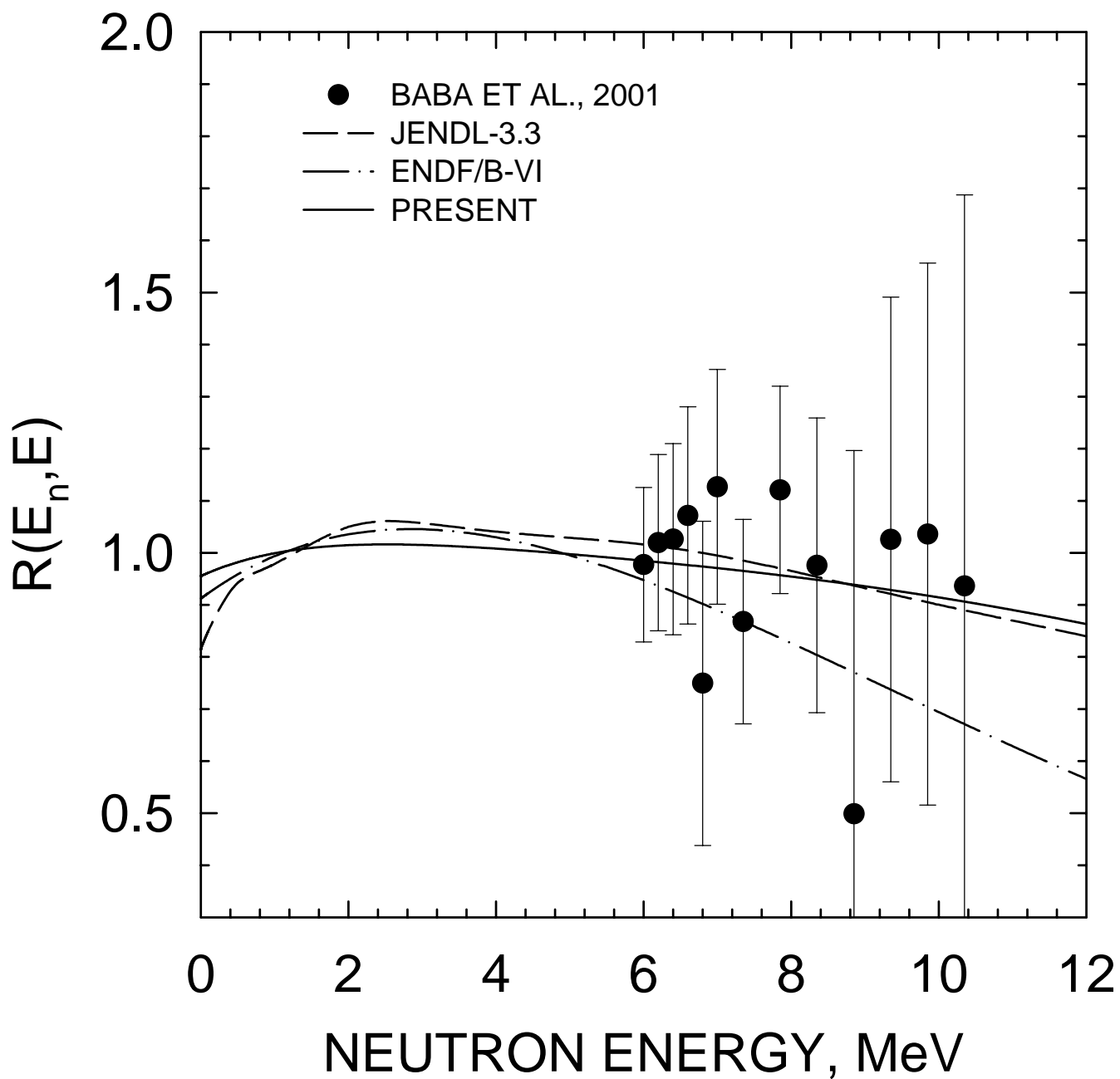
FIG. 87
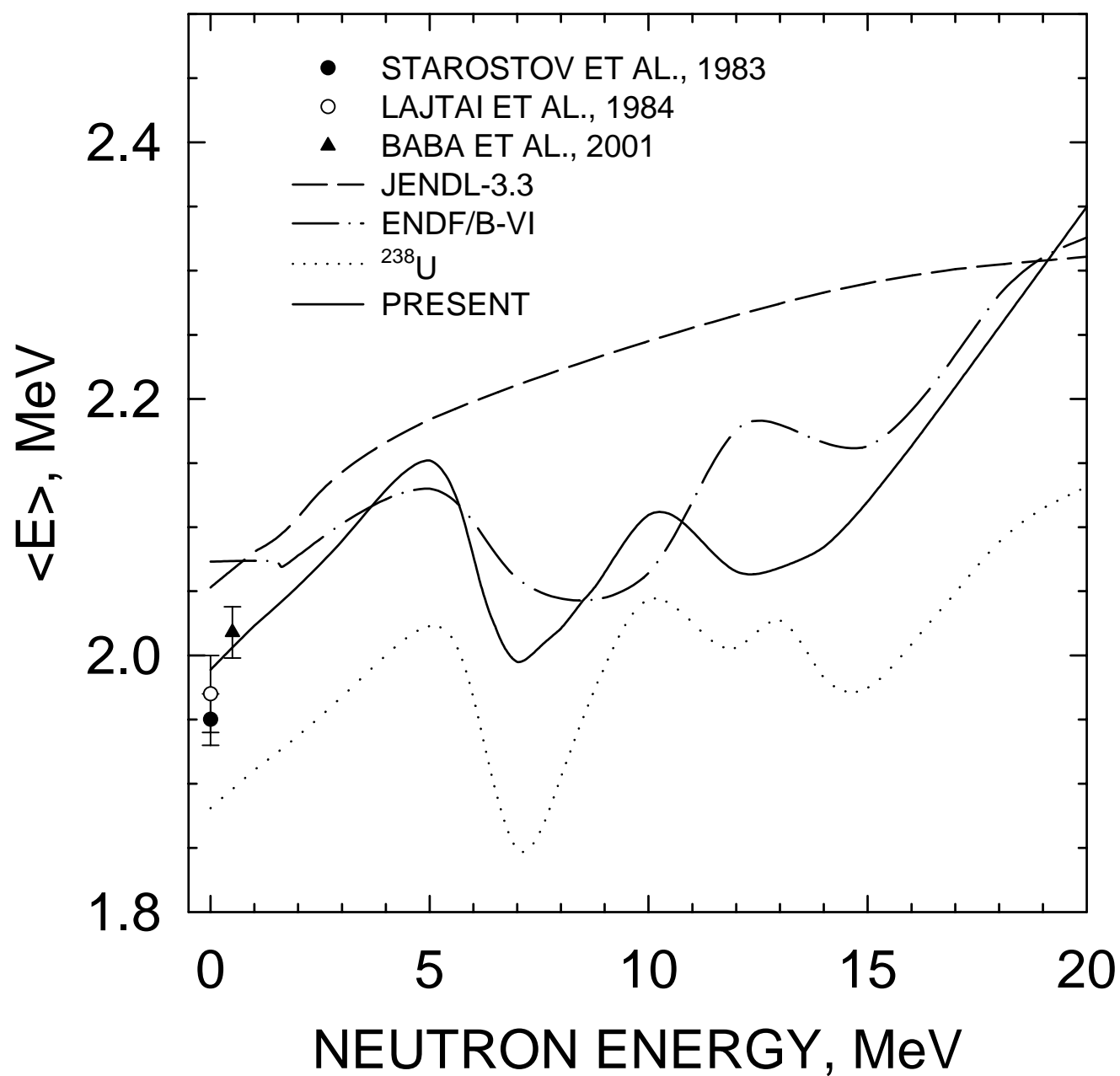
FIG. 88

^{233}U FISSION NEUTRON SPECTRUM
E_n=7MeV
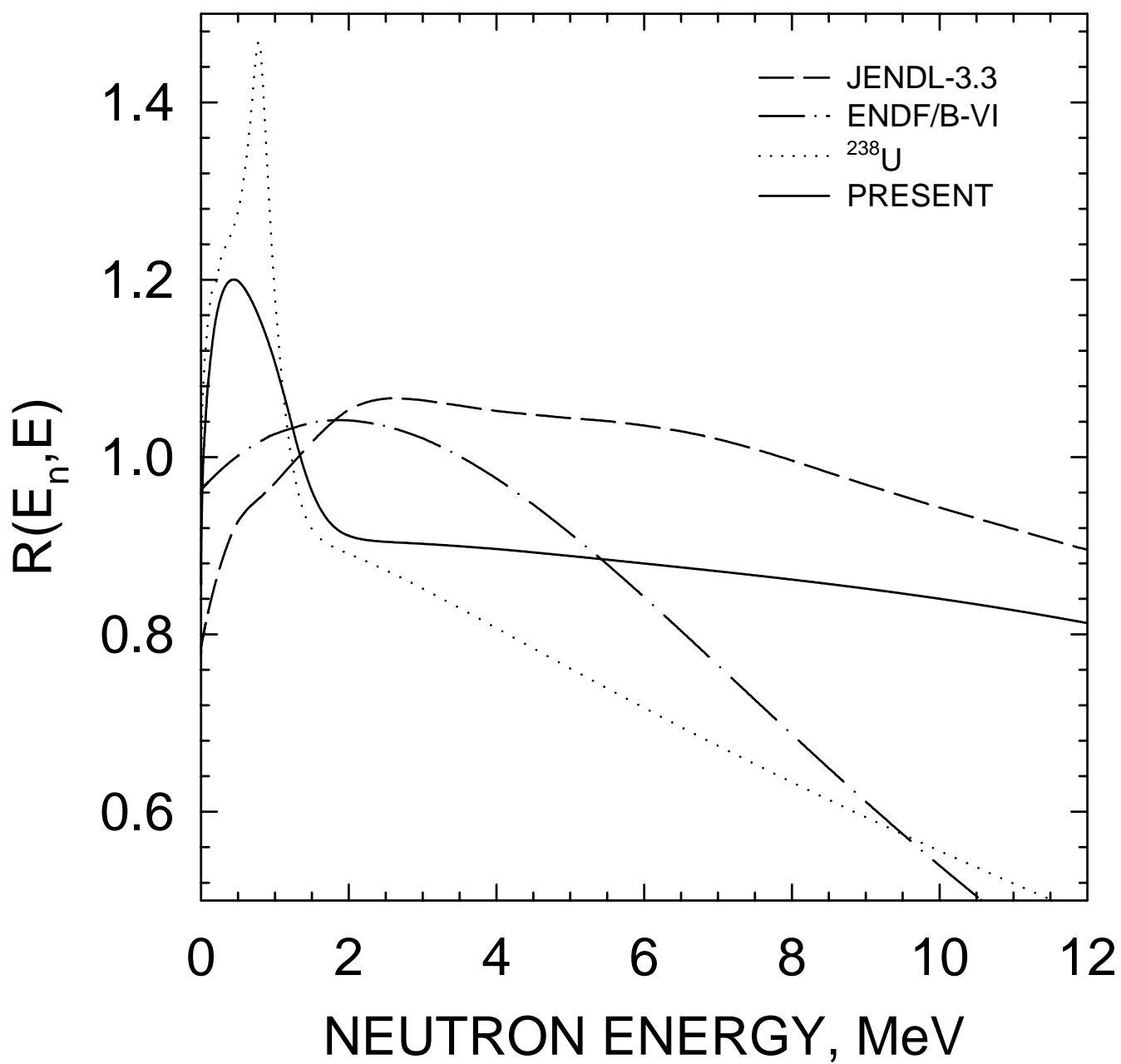
FIG. 89

^{233}U FISSION NEUTRON SPECTRUM
E_n=14MeV
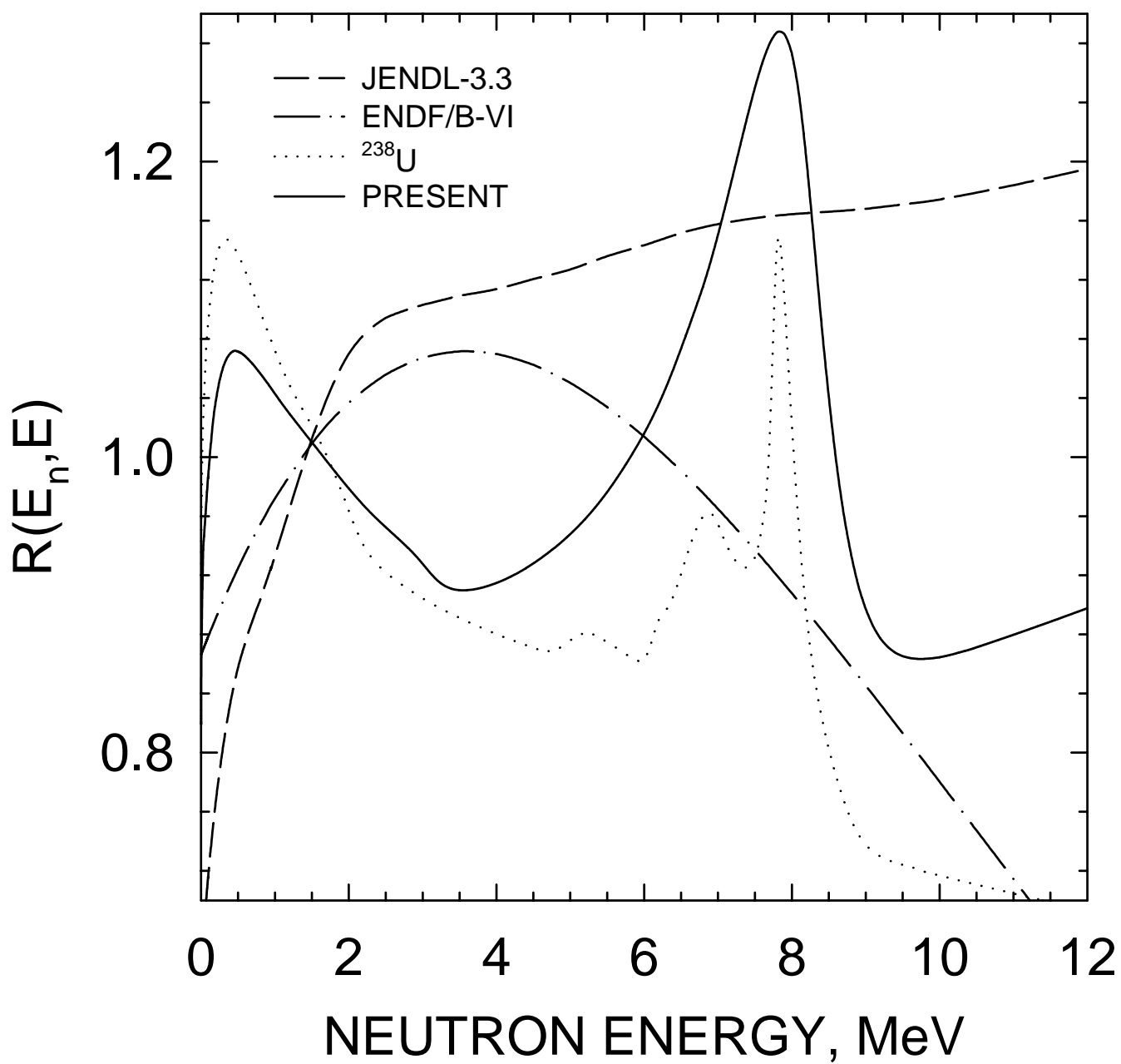
FIG. 90

^{233}U FISSION NEUTRON SPECTRUM
E_n=20MeV
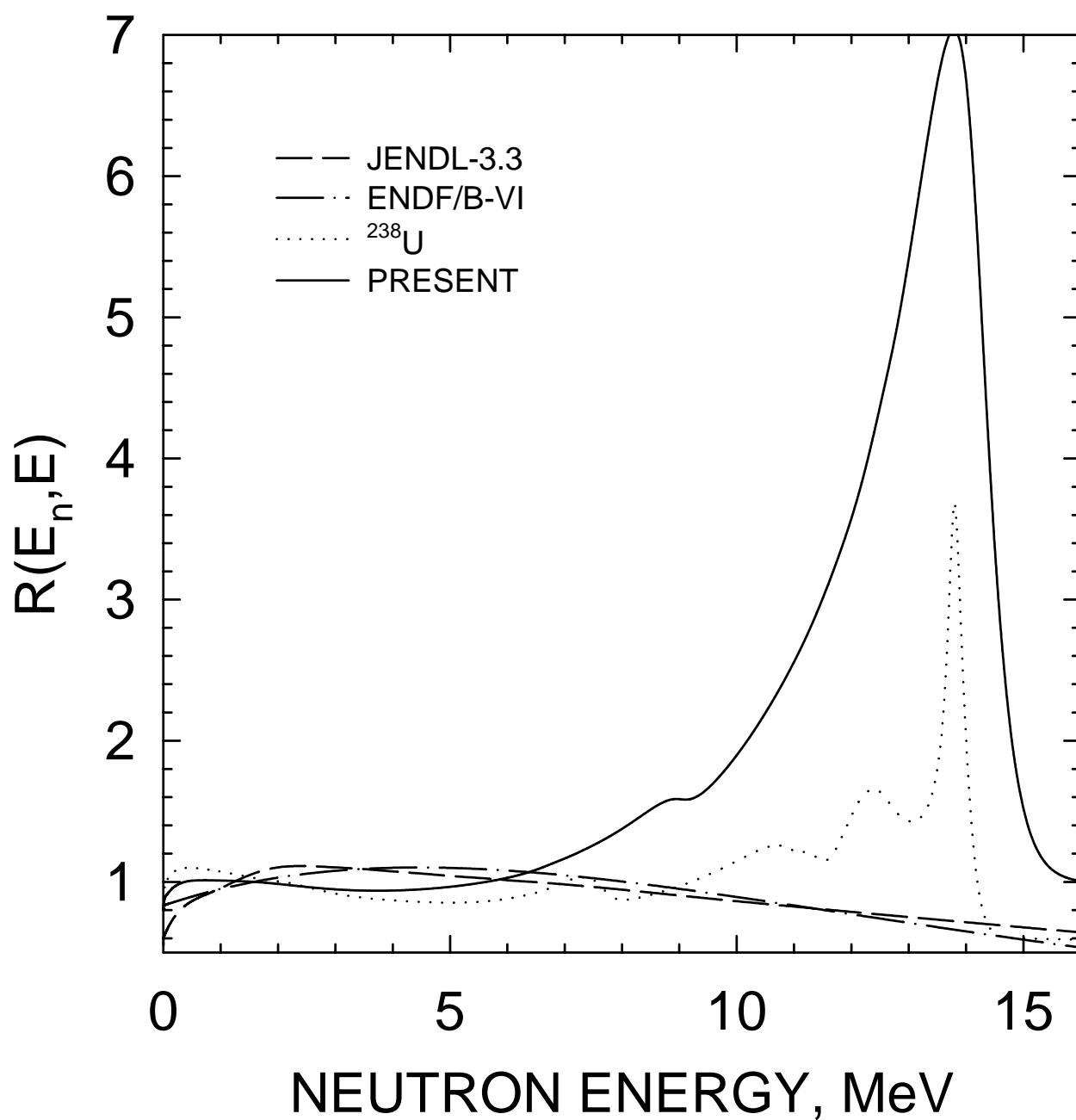
FIG. 91

^{233}U PARTIAL FISSION NEUTRON SPECTRA, E_n=20MeV
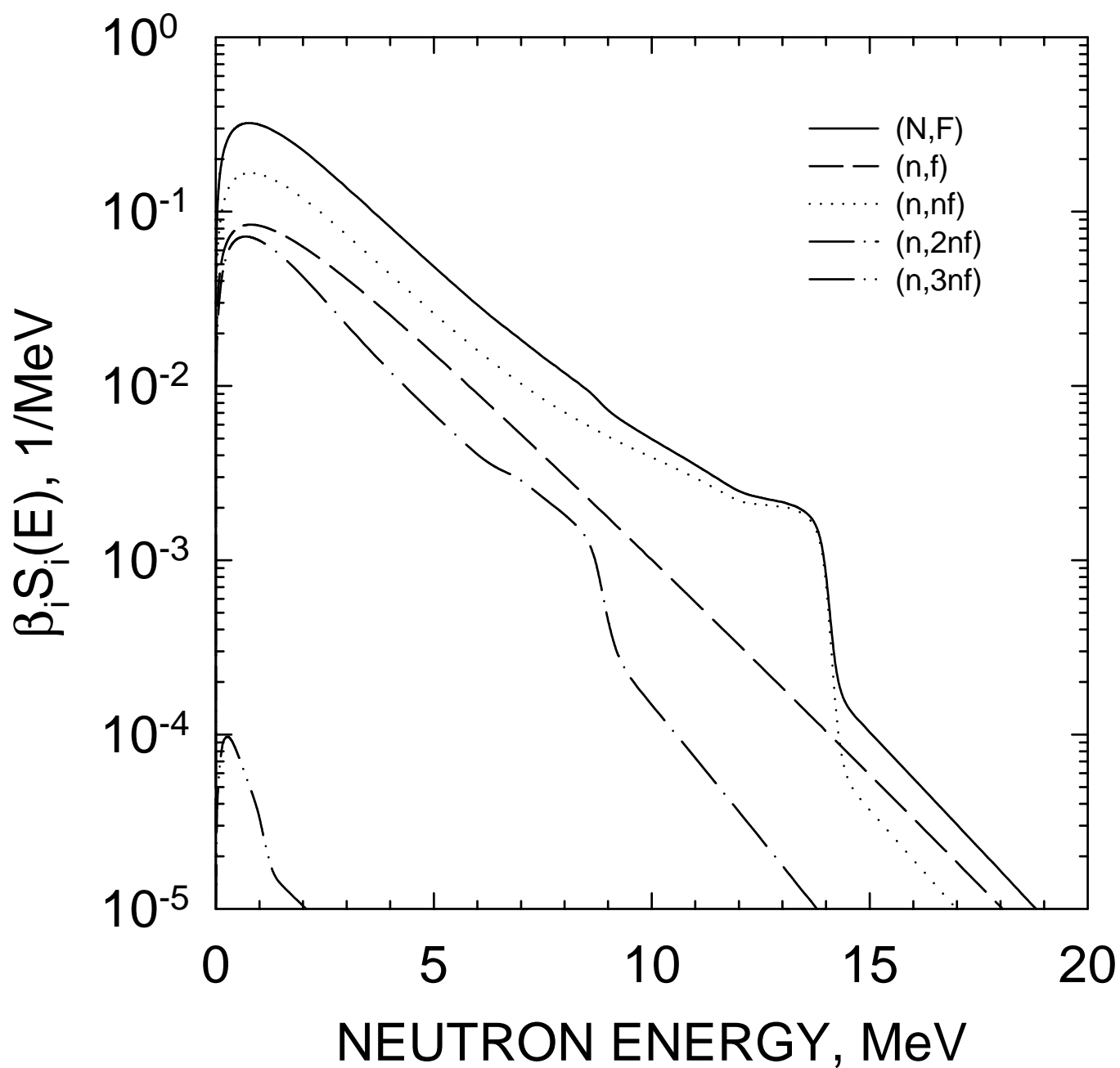
FIG. 92

^{233}U PARTIAL FISSION NEUTRON SPECTRA, E_n=14MeV

Legend:
- (N,F)
- (n,f)
- (n,nf)
- (n,2nf)

y-axis: $\beta_i S_i(E)$, 1/MeV

x-axis: NEUTRON ENERGY, MeV
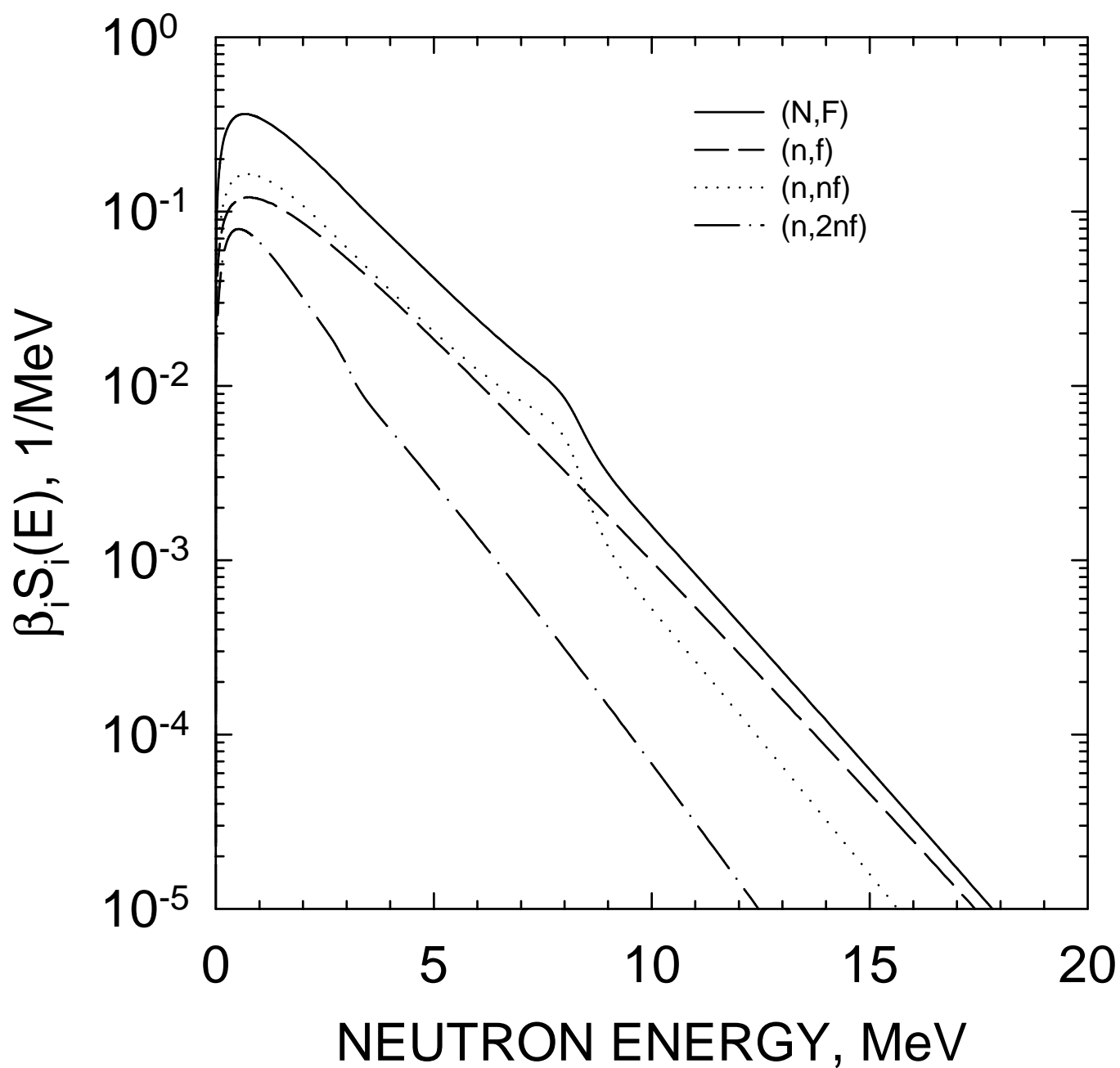
FIG. 93

^{233}U PARTIAL FISSION NEUTRON SPECTRA, E_n=7 MeV

FIG. 94

^{233}U E_n= 20 MeV
COMPARISON WITH JENDL-3.3
AND ENDF/B-VI

Legend:
JENDL-3.3
ENDF/B-VI
PRESENT

Y-axis: SPECTRUM OF (N,N'), ARB. UNITS/MeV
X-axis: NEUTRON ENERGY, MeV

FIG. 95

^{233}U E_n= 14 MeV
COMPARISON WITH JENDL-3.3
AND ENDF/B-VI

JENDL-3.3
ENDF/B-VI
PRESENT

SPECTRUM OF (N,N'), ARB. UNITS/MeV

NEUTRON ENERGY, MeV
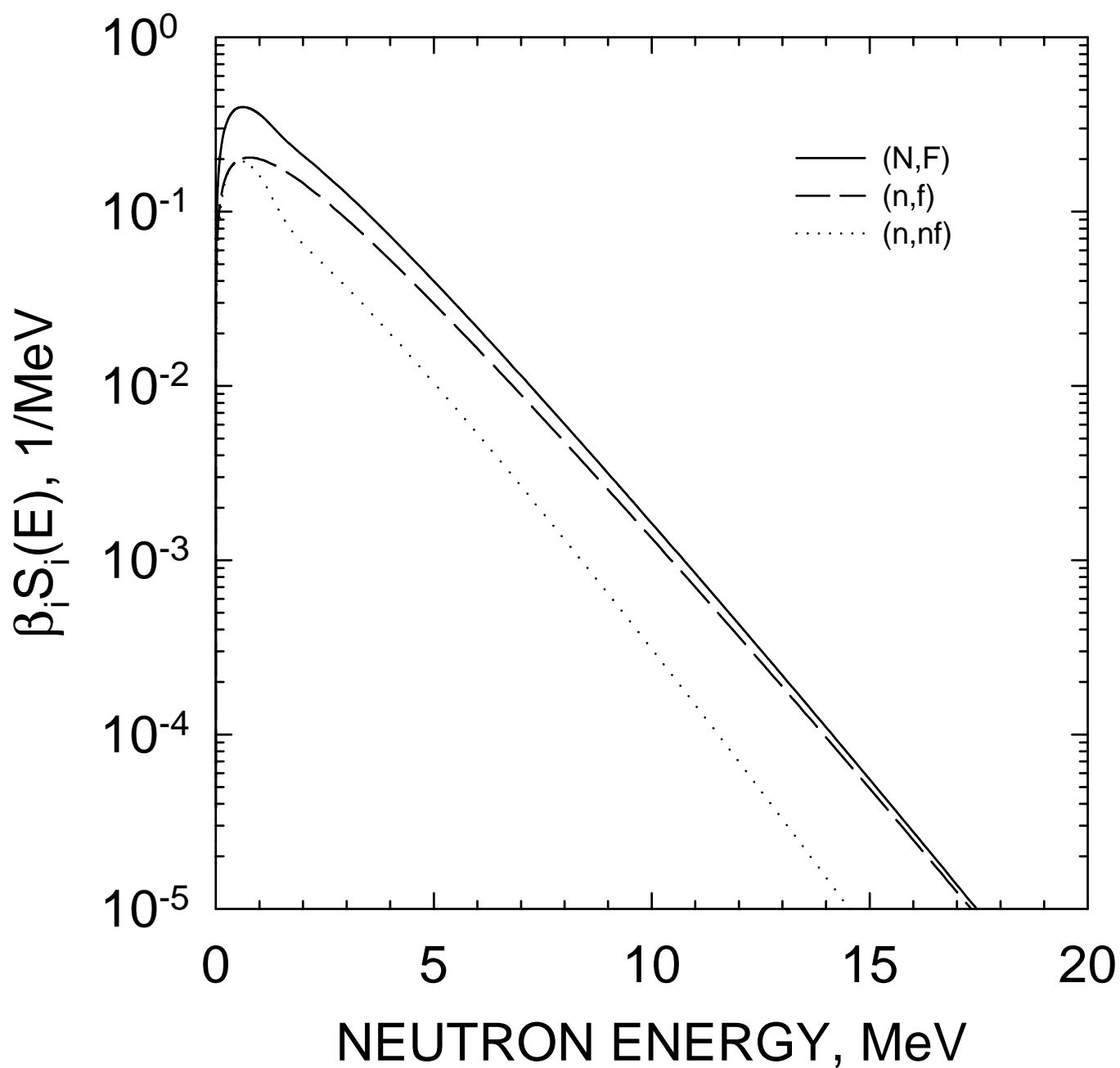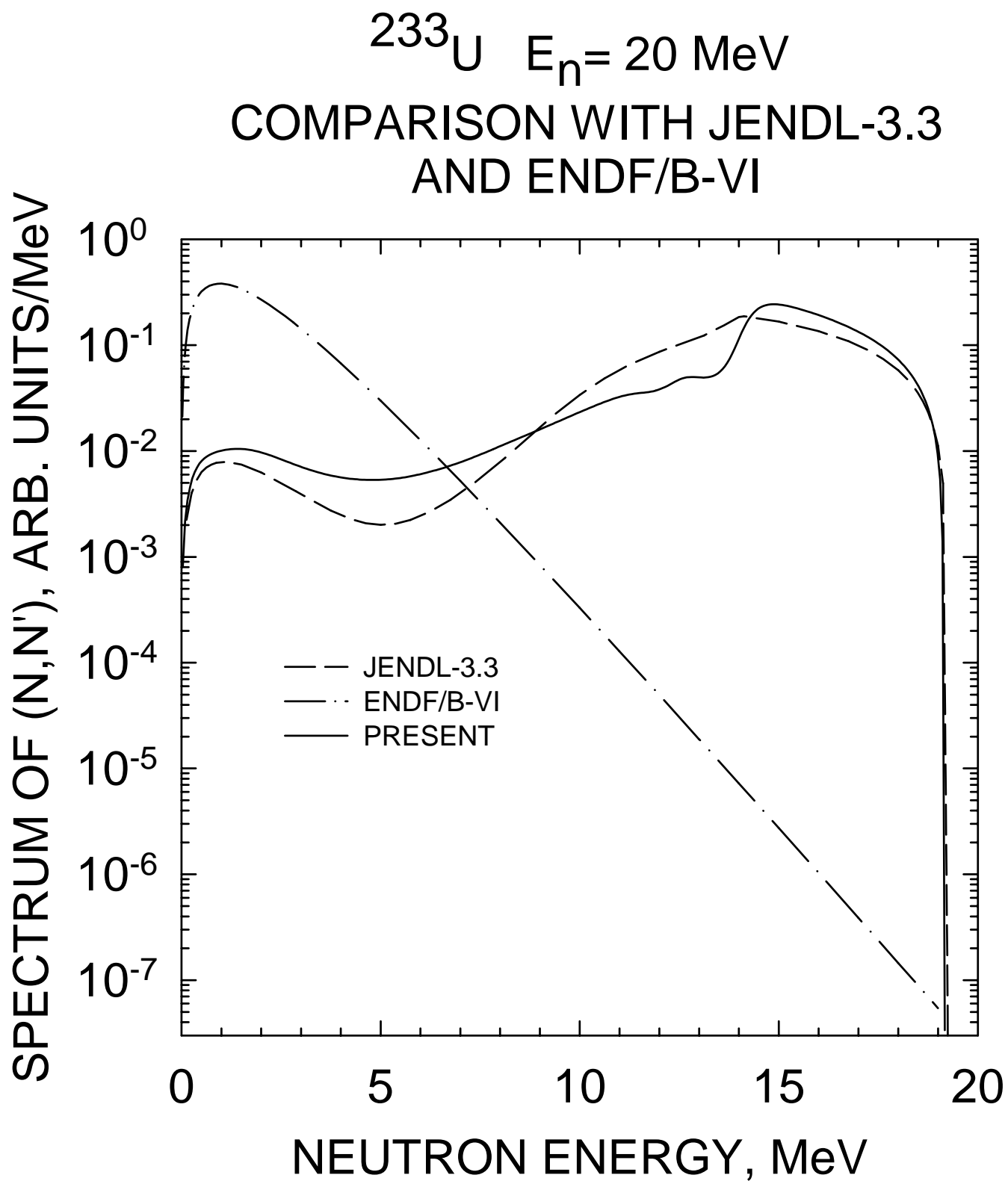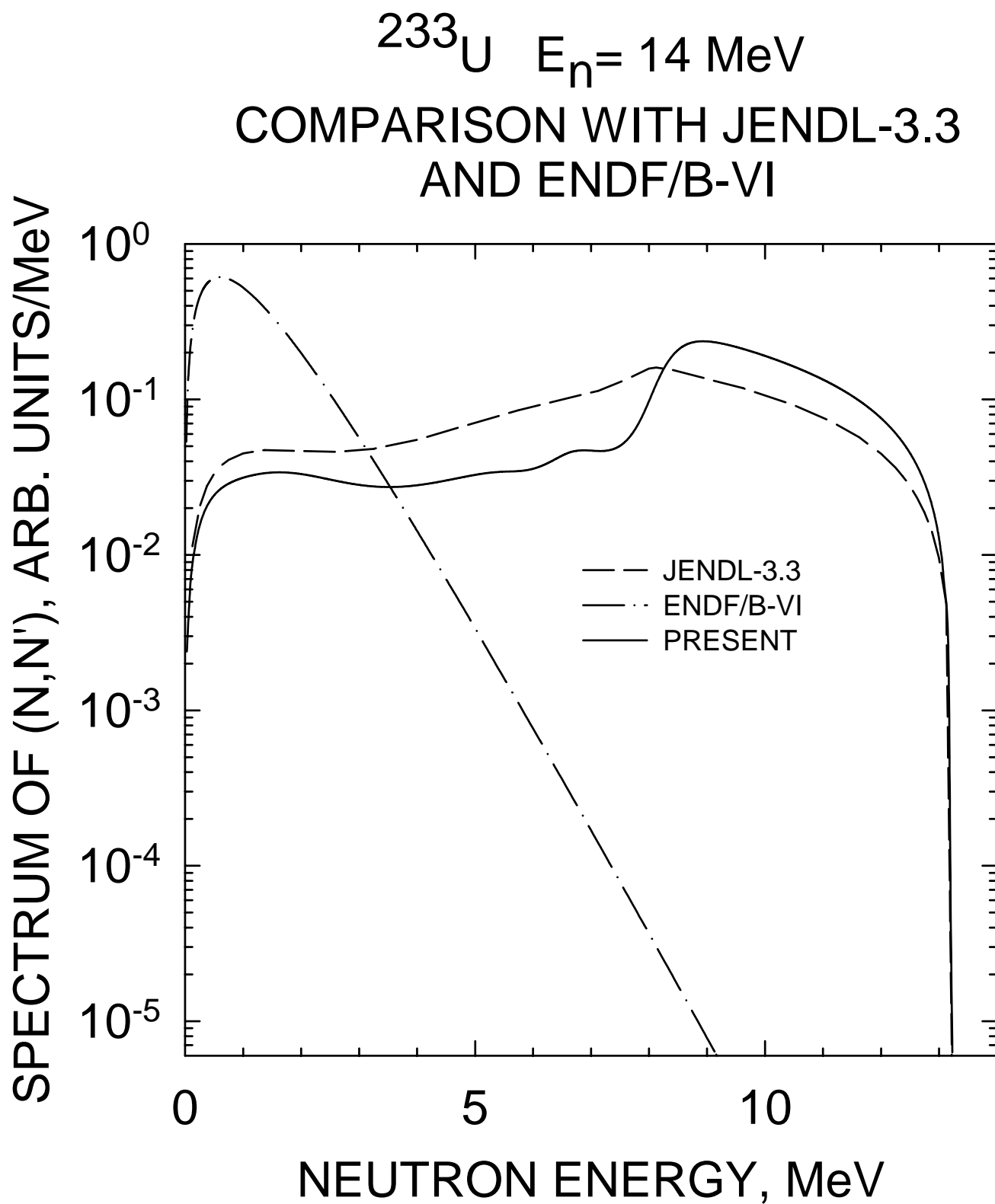
FIG. 96

^{233}U E_n= 10 MeV
COMPARISON WITH JENDL-3.3
AND ENDF/B-VI
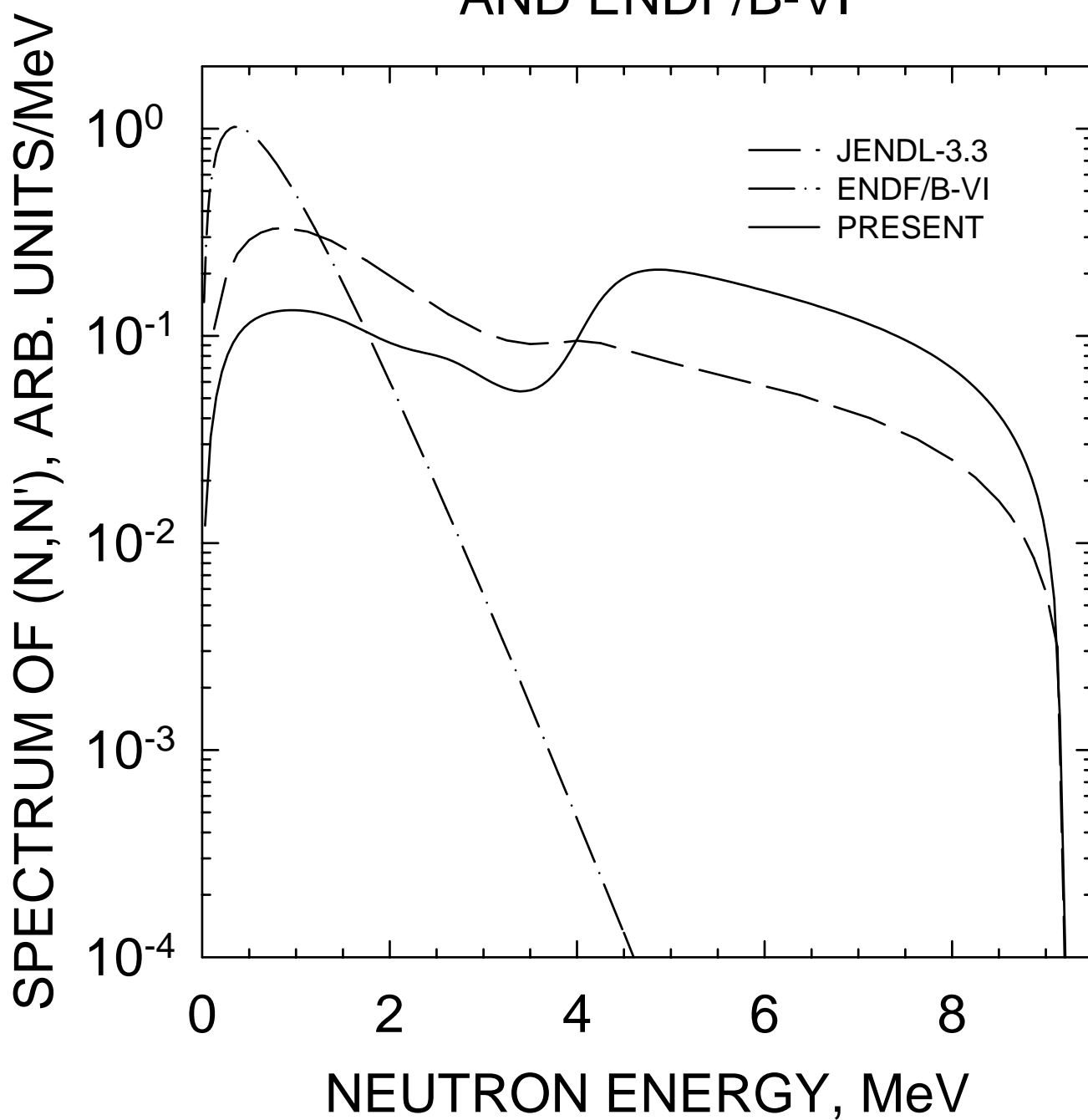
FIG. 97

^{233}U E_n= 8 MeV
COMPARISON WITH JENDL-3.3
AND ENDF/B-VI
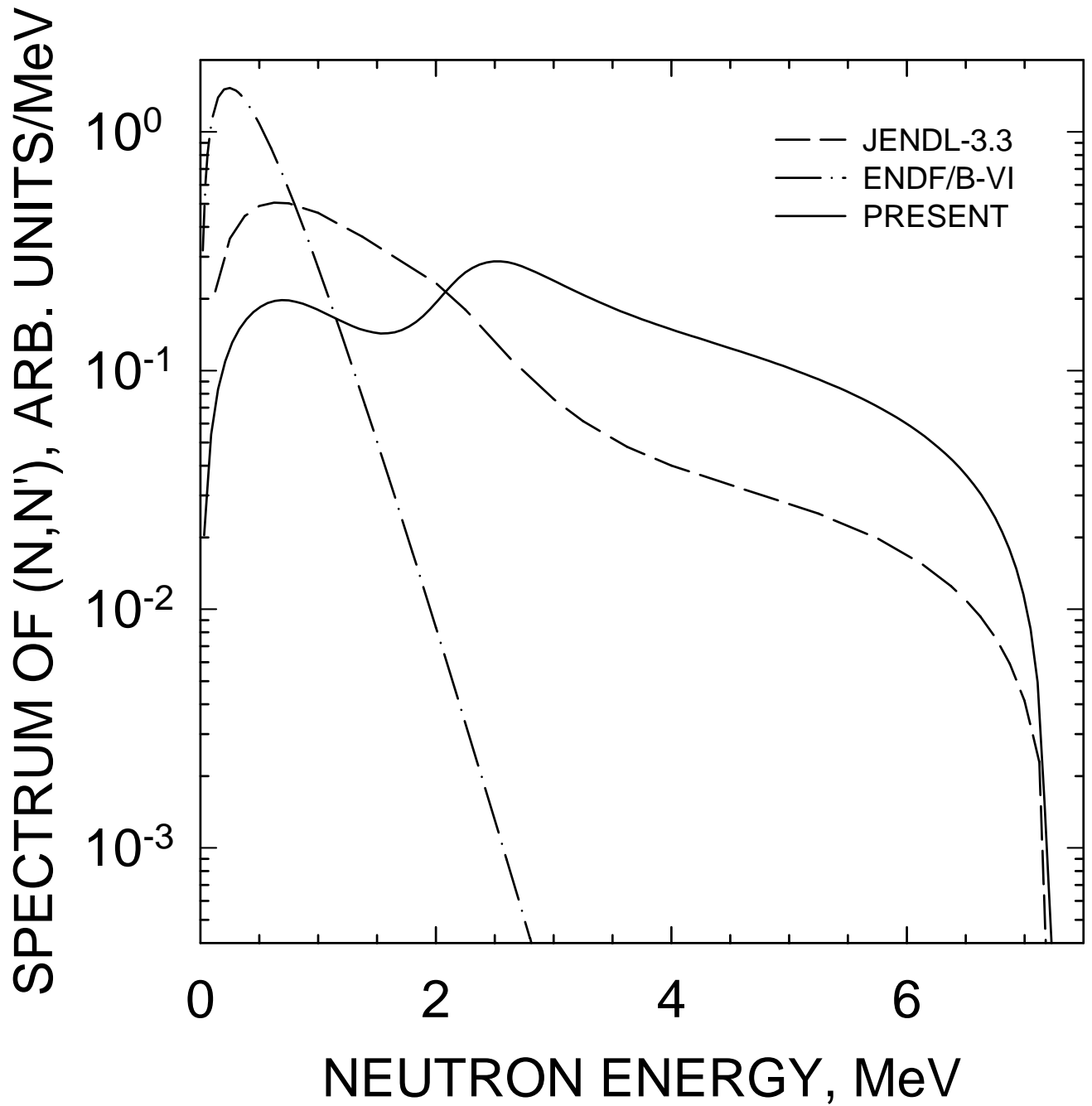
FIG. 98

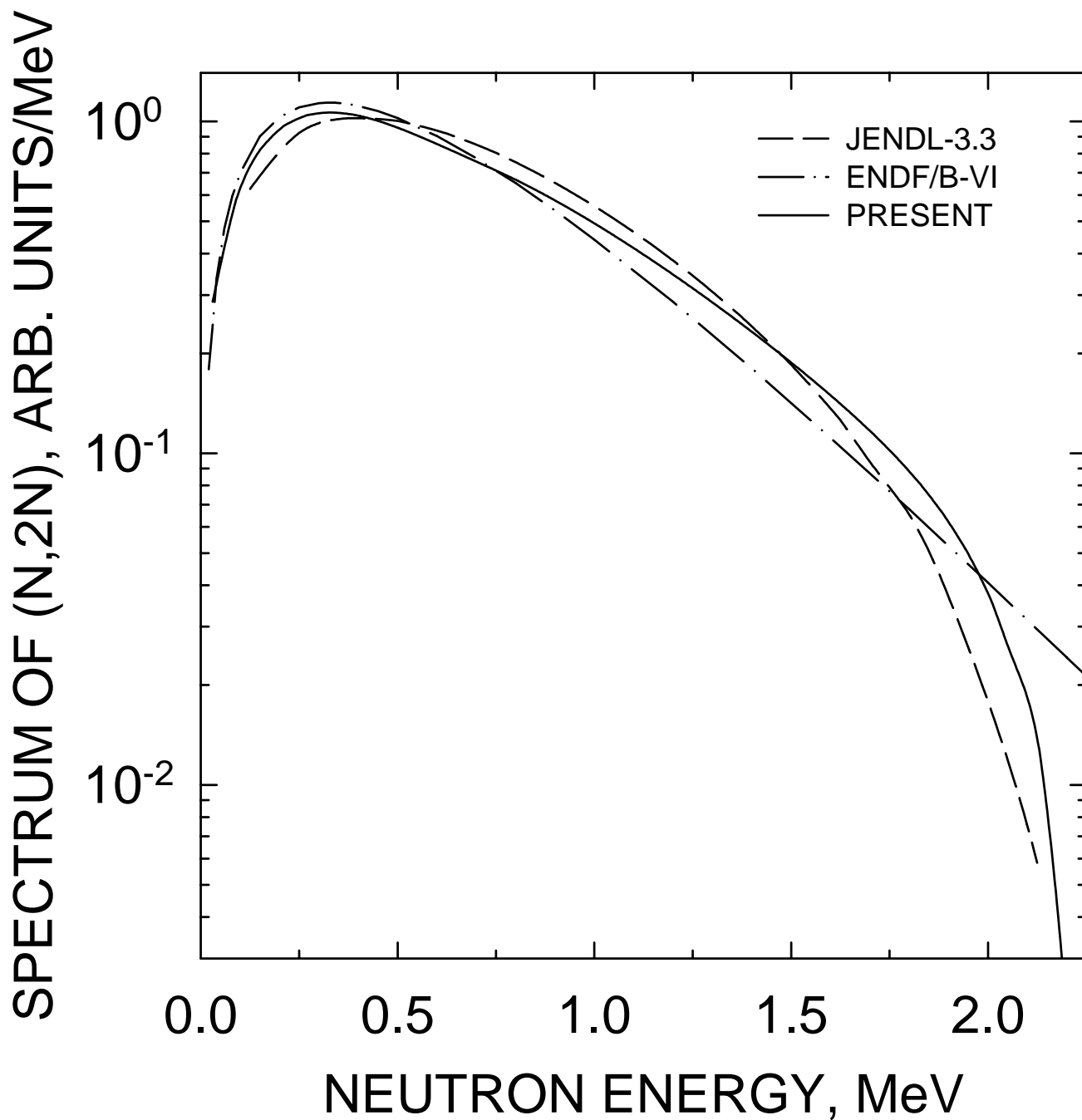^{233}U E_n= 6 MeV
COMPARISON WITH JENDL-3.3
AND ENDF/B-VI

FIG. 99

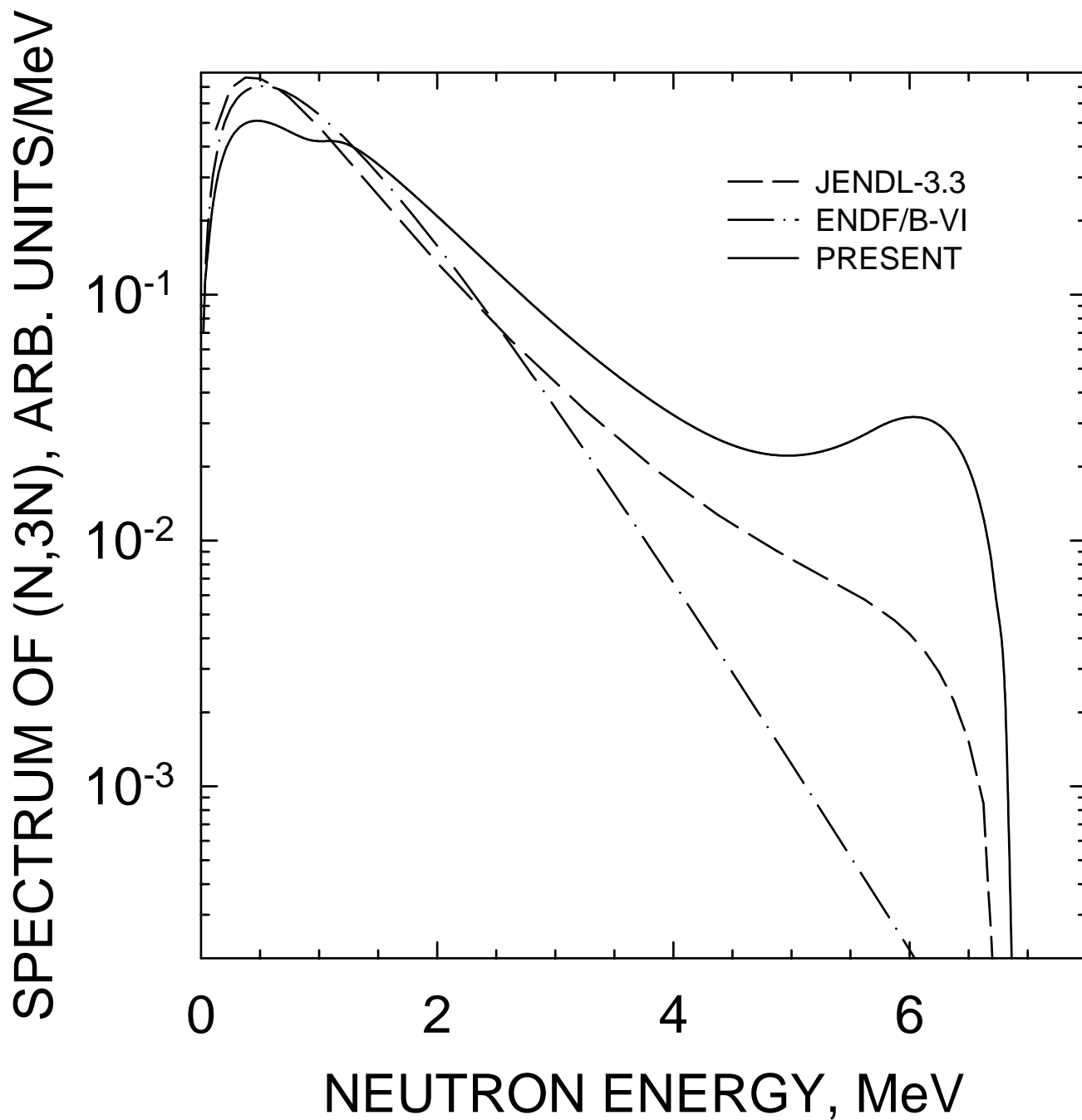^{233}U E_n= 20 MeV
COMPARISON WITH JENDL-3.3
AND ENDF/B-VI

JENDL-3.3
ENDF/B-VI
PRESENT

SPECTRUM OF (N,2N), ARB. UNITS/MeV

NEUTRON ENERGY, MeV
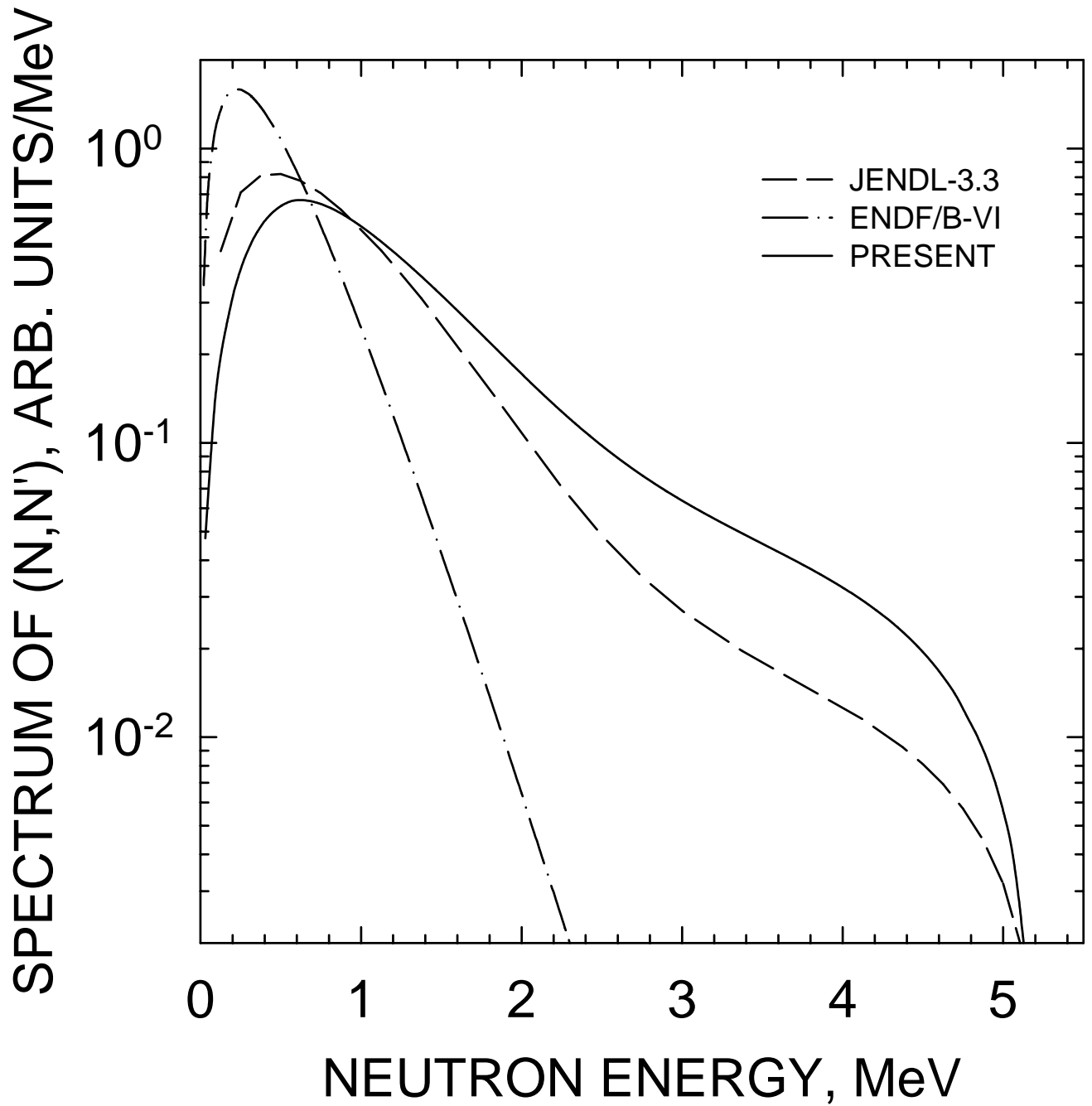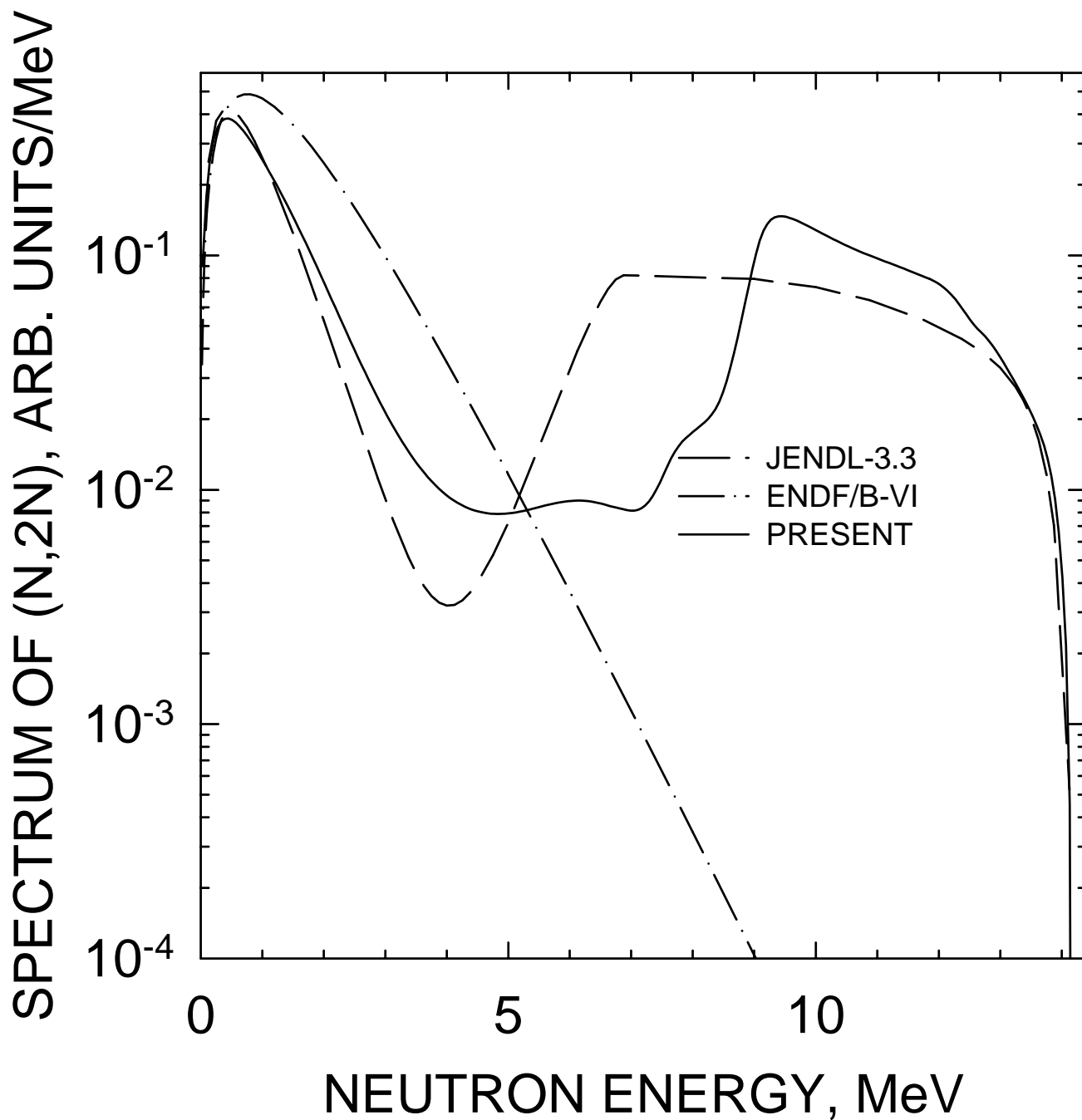
FIG. 100

^{233}U E_n= 14 MeV
COMPARISON WITH JENDL-3.3
AND ENDF/B-VI
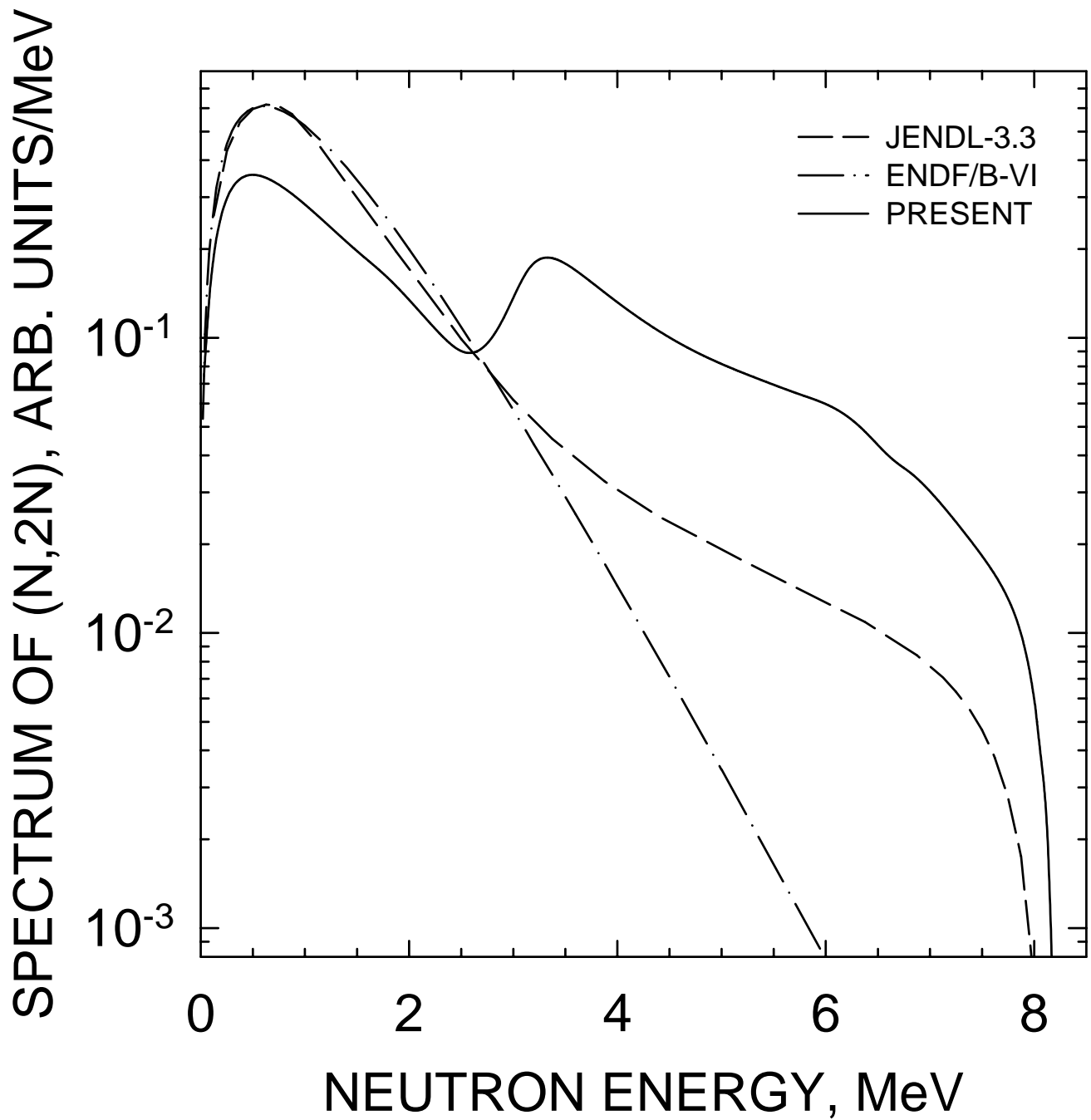
FIG. 101

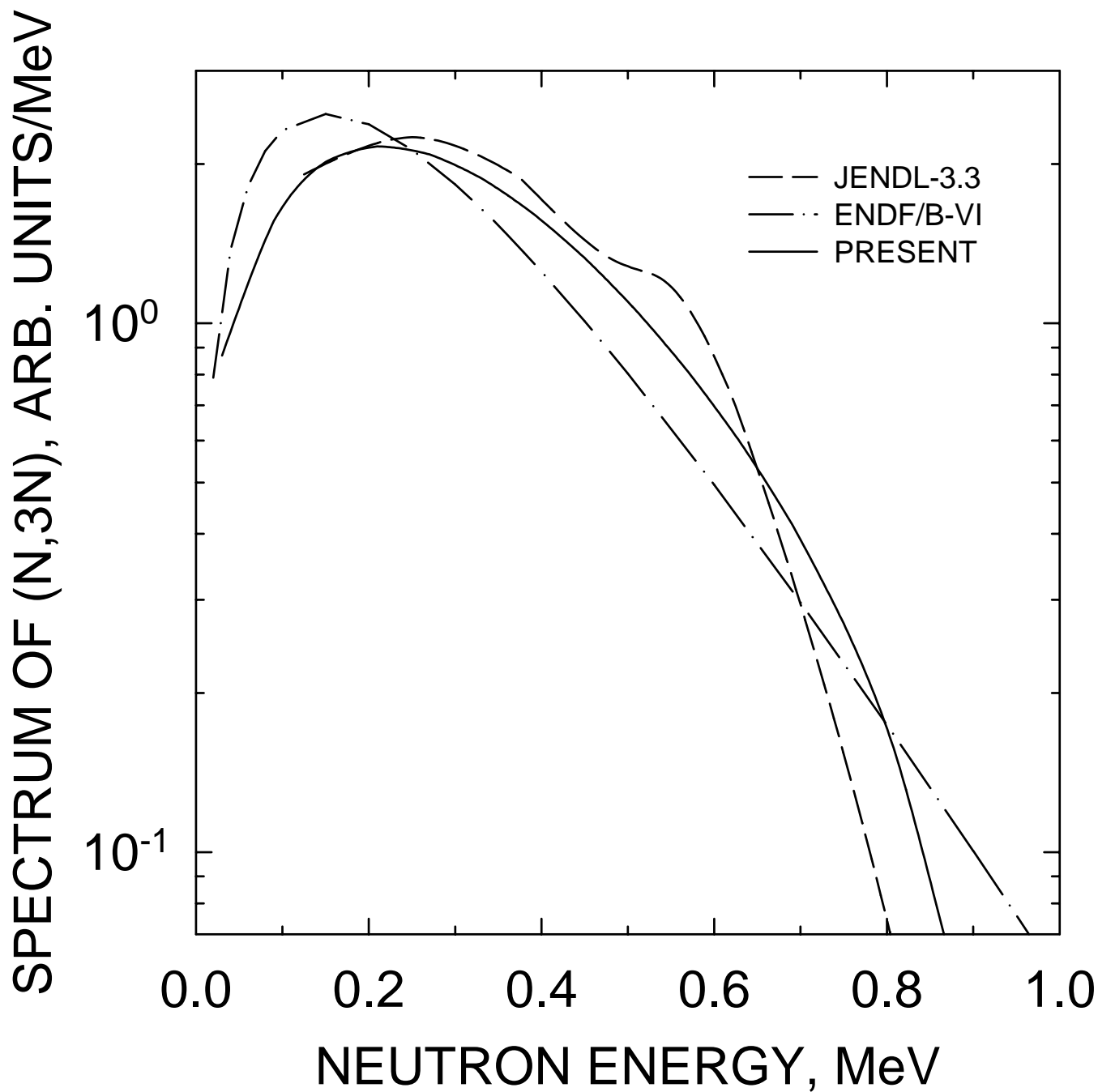^{233}U E_n= 10 MeV
COMPARISON WITH JENDL-3.3
AND ENDF/B-VI
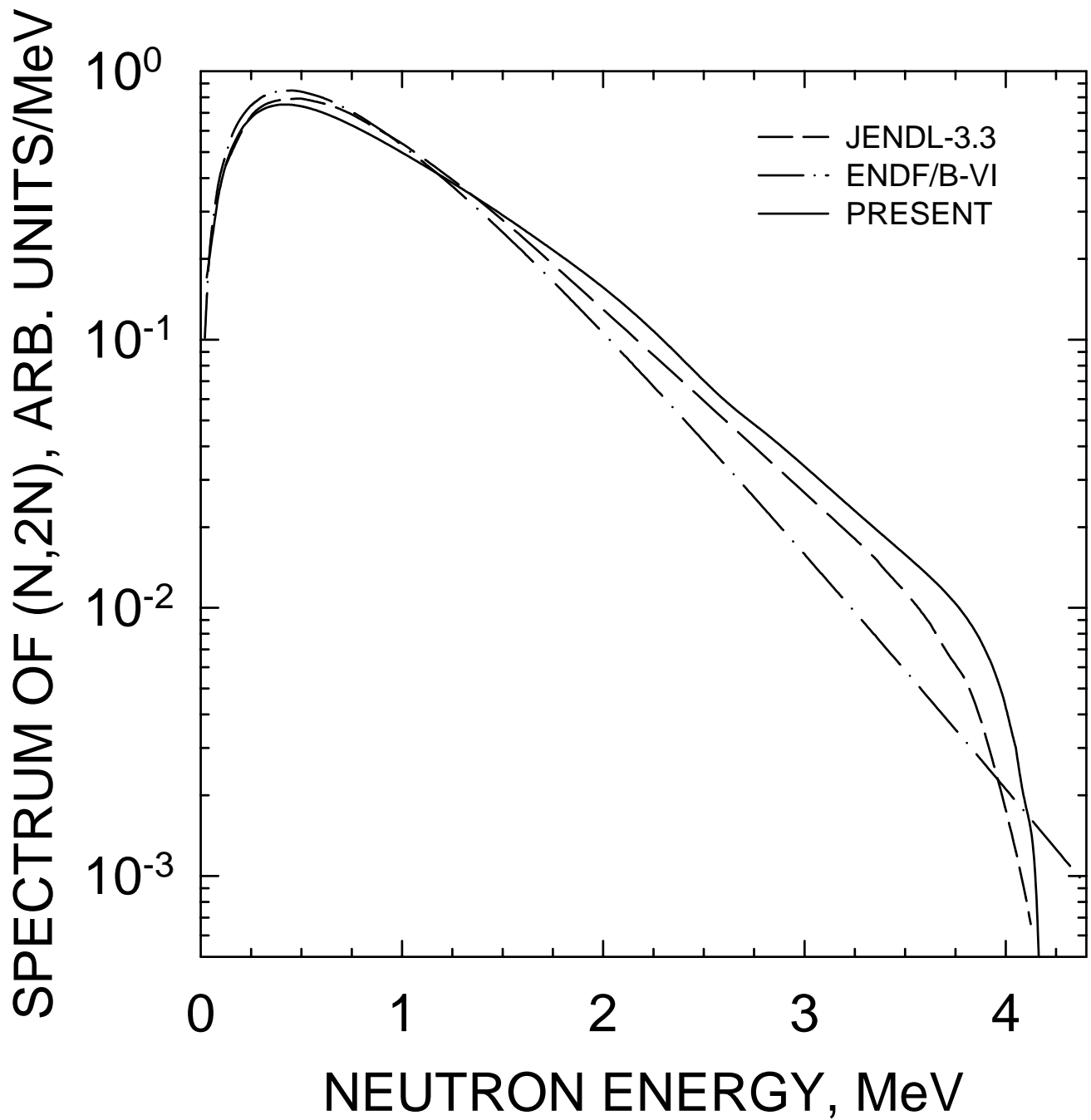
FIG. 102

^{233}U E_n= 8 MeV
COMPARISON WITH JENDL-3.3
AND ENDF/B-VI

FIG. 103

^{233}U E_n= 20 MeV
COMPARISON WITH JENDL-3.3
AND ENDF/B-VI

FIG. 104

^{233}U E_n= 14 MeV
COMPARISON WITH JENDL-3.3
AND ENDF/B-VI

FIG. 105